Design of Frequency-Selective Surfaces for Advanced Applications

by

Deisy Formiga Mamedes
B.Sc., Federal Institute of Paraiba, 2016
M.Sc., Federal Institute of Paraiba, 2018

A Dissertation Submitted in Partial Fulfillment of the
Requirements for the Degree of

DOCTOR OF PHILOSOPHY

in the Department of Electrical and Computer Engineering

Design of Frequency-Selective Surfaces for Advanced Applications

by

Deisy Formiga Mamedes
B.Sc., Federal Institute of Paraiba, 2016
M.Sc., Federal Institute of Paraiba, 2018

Supervisory Committee

Dr. Jens Bornemann, Supervisor
(Department of Electrical and Computer Engineering)

Dr. Thomas Darcie, Departmental Member
(Department of Electrical and Computer Engineering)

Dr. Afzal Suleman, Outside Member
(Department of Mechanical Engineering)

ABSTRACT

The advancement of mobile technology is driven by the requirements for wider bandwidth, higher data rates, a large number of users, and reliable connectivity. The fifth generation (5G) mobile network is currently in its early stages of commercialization with two frequency bands allocated for its technology. Frequency-selective surfaces (FSS) form a promising technology to help meet these requirements. Extensive research has been conducted on the use of FSSs as spatial filters in the sub-6GHz and millimeter-wave (mm-wave) spectra, as they are able to impart screening properties in the spatial domain. Therefore, this dissertation presents works focused on FSS technology to demonstrate and verify its advantages.

First, a new polarization converter system using only a single-layer FSS is proposed. Design equations are introduced for the four-arms star geometry which is used as polarizing element. Polarization converters have become popular in different communication systems due to their characteristics of mitigating the effects of polarization mismatching, thus improving signal strength.

Second, an ultra-wide band-stop FSS operating at K- and Ka-bands for mm-wave applications is presented. This structure comprises of double-layer FSS with simple modeling, where a series of basic equations are implemented and described. When the proposed resonators are cascaded, they offer wide bandwidth, eliminating the need for extra layers.

Third, a new beam-tilting and gain enhancement system operating at 28 GHz is proposed. The system is composed of a bio-inspired bow-tie antenna as excitation source and a single-layer FSS positioned at the bottom of the antenna. The effect of FSS panel size is investigated to achieve the better antenna performance.

Fourth, a system of closely coupled complementary and passive FSSs that achieves dual- and triple-band operations is presented. Four configurations of the elements are investigated, which can present two and three transmission bands in one or both polarizations by inducing an electromagnetically induced transparency effect.

Fifth, a novel reconfigurable complementary-inspired FSS with reconfigurable frequency response is described. The proposed structure consists of two resonators with immersed biasing network, and only a single PIN diode per unit cell as active device. Single- and dual-passband performance is achieved by switching the diode's state from off to on. When the threshold voltage is applied, no passband appears.

Sixth, two high-gain beam-switching antenna systems are presented. Both systems

comprise of a dipole antenna as excitation source and single-layer PIN-diode-switched FSS panels as mechanism of reconfiguring the radiation pattern. The first system is configured as a reconfigurable corner antenna with large beam-switching range. The second system can steer the beam in the azimuth and elevation planes.

Therefore, the works developed in this dissertation prove the FSS' reliability in the sub-6GHz and mm-wave frequency ranges for different and advanced applications.

Table of Contents

List of Tables

List of Figures

ACKNOWLEDGEMENTS

When I got accepted into the doctoral program, I knew many challenges and adventures would come, and I was urging to live them all. This opportunity opened many doors for my professional career and personal development. Completing this dissertation was only possible with the support and encouragement of many people.

I would like to extend my sincere gratitude and thank those who have helped me along the way:

Dr. Jens Bornemann for the opportunity to join his research team and being a great mentor. I am grateful for his continuous support, wise advice, the freedom to pursue different projects, and the freedom to teach and engage with students. His dedication to teaching inspires me in the search for constant learning. I hope someday I can be as enthusiastic and energetic as Dr. Bornemann is to command an audience as well as he can.

The Supervisory Committee members, Dr. Thomas Darcie and Dr. Afzal Suleman, for their time to administer the doctoral examination, and their constructive feedback in reviewing this dissertation.

Dr. Alfredo Gomes Neto and the Group of Telecommunications and Applied Electromagnetism – Federal Institute of Paraiba for their generous help with the fabrication and measurements of some prototypes presented in this dissertation, as well as for the many enriched discussions that we had.

Skyworks Solutions Inc. for offering me the 12-month co-op opportunity in their design office in Ottawa, where I had the chance to work with such an amazing team that led me to work on diverse exciting projects.

My friends, for all the moments we shared, great chats and laughs, for all the lessons we learned together, and for celebrating each accomplishment.

My family, especially my mother, for their unlimited love, unconditional support and tireless efforts they have given me to follow my dreams. I am honored to be a first-generation Doctor of Philosophy in my family. As an important member of my family, I would like to give a heartfelt acknowledgment to my precious cat, Mia, that gave me endless love and vigilant dedication, and for her purrfect performance as a furry research assistant.

DEDICATION

To my family: past, present, and future.

Chapter 1

Introduction

Emerging mobile communication systems will require wider bandwidth, ultra-high speeds, and low latency [1]. Currently, the communication networks are advancing to fifth generation (5G), which operates in multiple frequency bands. 5G aims to use frequencies that lie in the sub-6GHz spectrum and millimeter-wave bands [2]. The latter has become a research hotspot due to its potential to meet the higher mobile communication performance requirements. The upcoming generation intends to provide 1000 times higher data volume per area, 10 to 100 times higher number of connected devices, 5 times reduced end-to-end latency, and 10 to 100 times higher data rates [3], [4]. In other words, 5G offers more connections, sending more data, while consuming less energy from devices, which makes batteries last longer. There are several challenges to be addressed to meet these demands that requires research on increasing spectral efficiency, energy efficiency and high reliability of networks connectivity.

In this new wireless communication network, improved antenna performance plays an important role for its implementation. It requires that antennas must have high gain and beam steering function, being able to focus the signal to a specified target, which reduces the energy consumption for data transfer. To satisfy these demands, several research projects have been reported in the development of reconfigurable antennas, which can improve the transmission capacity of systems by steering their signal, favoring a better use of the electromagnetic spectrum, preventing the electromagnetic signal from being radiated in unwanted directions [5]–[7]. This generation also requires that RF front-end systems can handle numerous frequencies and communication protocols, which makes multi-band systems desirable.

Another challenge in millimeter-wave systems is that they are impaired by atmo-

spheric attenuation, which reduces the range and strength of waves [8]. Antennas with circular polarization technology present a good solution to address this issue due to their capacity to overcome some obstructions such as polarization mismatch, multi-path effects, and phasing issues occasioned by weather conditions [9].

As mentioned above, depending on the type of communication, the system requires to provide desired actions. In some of these systems, the antennas are bulky and require a complicated fabrication process, adding costs, e.g., phased arrays that need to be integrated to a large number of radio frequency (RF) phase shifters, feed networks, and control systems. It is important to investigate low-cost and low-power alternatives, and one of the favoured solutions that has become the most suitable and effective candidate to be incorporated in these antenna systems is the use of electromagnetic (EM) periodic structures, such as frequency-selective surfaces (FSSs), due to their typical EM characteristics. FSSs are well-known for being powerful and practical tools in microwave, millimeter-wave and terahertz filtering [10]. FSSs are fabricated from conductive patches or aperture elements, which can enable EM wave transmission or reflection in determined bands [11].

1.1 Motivation

FSSs are versatile and their characteristics of efficiently manage frequency resources can optimize spectral efficiency, as well as make a compact system. With the advantages that FSSs have to offer in the sub-6GHz and mm-wave regimes, a series of FSS models in various frequency ranges are proposed, designed, and fabricated in this dissertation. These FSSs are designed for different applications to verify the performance of FSSs in designing different advanced communication system components.

1.2 Contributions

The contributions of this dissertation lie in investigating the applicability of FSSs in advanced communication systems to enhance their performance. It aims to address some of the challenges and concerns of radiation and scattering properties of the upcoming networks. The following specific contributions are identified:

- Proposing a simpler polarization converter system using a single-layer FSS. The proposed system provides a wideband 3-dB axial ratio by using a simple-to-

design unit-cell element. This FSS polarization converter can be easily designed for mm-wave frequencies.

- An ultra-wide bandwidth FSS is introduced for covering the K- and Ka-band frequency range applications. The proposed cascaded structure can have its bandwidth and resonance frequencies independently adjusted by optimizing each resonator individually. A thorough overview of equivalent circuit modeling techniques for FSSs provides a model for cascaded FSSs. An investigation of Fano resonance occurrence in this system is performed.

- A high gain, beam-tilting antenna system is presented for mm-wave applications. This system consists of an FSS at the bottom of a microstrip antenna. This novel beam-tilting system uses simpler geometry for the antenna and FSS design in comparison to other systems, but it is also compact, easy to assemble, and provides high tilting angle and gain.

- A multi-band FSS based on Babinet's principle is proposed and investigated. The structure is formed by complementary elements that present two passbands. By offsetting the resonators, a third passband arises which eliminates the need for another resonator/layer. This system can be polarization dependent or independent and exhibit dual- and/or triple-band operations.

- A reconfigurable FSS that offers single-, dual- or no-passband response is presented. This system is composed of a stack of complementary elements, and its reconfiguring characteristic is achieved by switching off-, on- and threshold states of a single PIN diode per unit cell with immersed biasing network.

- Two beam steering/switching antenna systems are designed using only a single-layer FSS. The FSS unit cell includes only a single PIN diode for electronically steering the beam. The rows of the FSS used in these systems can be independently controlled, which permit the beam to be steered in the elevation plane. The first system offers ± 60-degree switching range in the azimuth plane, while the second system allows 360° and $\pm 22^\circ$ steering range in the azimuth and elevation planes, respectively.

1.3 Academic activities

1.3.1 Thesis contributions

- **D. F. Mamedes** and J. Bornemann, "Using an Equivalent-Circuit Model to Design Ultra-Wide Band-Stop Frequency-Selective Surface for 5G mm-Wave Applications," in IEEE Open Journal of Antennas and Propagation, vol. 3, pp. 948-957, 2022, doi: 10.1109/OJAP.2022.3198290.

- **D. F. Mamedes**, J. Bornemann, A. G. Neto, and Sérgio L. M. Sales Filho, "Dual- and Triple-Passband Coupled-Complementary FSSs Based on the Four-Arms Star Geometry," accepted in IET Microwaves, Antennas & Propagation.

- **D. F. Mamedes**, J. Bornemann, A. G. Neto, and Sérgio L. M. Sales Filho, "Frequency-Selective Surface With Reconfigurable Response Based on Duality Theorem," submitted to IEEE Transactions on Antennas and Propagation.

- **D. F. Mamedes**, A. G. Neto and J. Bornemann, "Reconfigurable Corner Reflector Using PIN-Diode-Switched Frequency Selective Surfaces," IEEE International Symposium on Antennas and Propagation and North American Radio Science Meeting, Montreal, Canada, 2020, pp. 127-128,
doi: 10.1109/IEEECONF35879.2020.9329791.

- **D. F. Mamedes** and J. Bornemann, "High-Gain Reconfigurable Antenna System Using PIN-Diode-Switched Frequency Selective Surfaces for 3.5 GHz 5G Application," SBMO/IEEE MTT-S International Microwave and Optoelectronics Conference (IMOC), Fortaleza, Brazil, 2021, pp. 1-3,
doi: 10.1109/IMOC53012.2021.9624918.

- **D. F. Mamedes** and J. Bornemann, "Gain Enhancement of Bio-inspired Antenna Using FSS for 28 GHz 5G Application," SBMO/IEEE MTT-S International Microwave and Optoelectronics Conference (IMOC), Fortaleza, Brazil,

2021, pp. 1-3, doi: 10.1109/IMOC53012.2021.9624742.

- **D. F. Mamedes**, J. Bornemann and A. G. Neto, "Linear-to-Circular Polarization Converter Based on Four-Arms Star FSS at 5.2 GHz for 5G Applications," 16th European Conference on Antennas and Propagation (EuCAP), Madrid, Spain, 2022, pp. 1-4, doi: 10.23919/EuCAP53622.2022.9768954.

- **D. F. Mamedes** and J. Bornemann, "Polarization-selective Fano resonance in cascaded frequency-selective surfaces," Proc. URSI Int. Symp. Electromagn. Theory, pp. 1-4, Vancouver, Canada, 2023 (invited).

- **D. F. Mamedes**, J. Bornemann and A. G. Neto, "Single- and Dual-Band FSS With Switchable Characteristics," accepted in IEEE International Symposium on Antennas and Propagation and USNC-URSI Radio Science Meeting (AP-S/URSI), Florence, Italy, 2024.

1.3.2 Other contributions

- Z. Liu, J. Bornemann, **D. F. Mamedes**, S. Liu, X. Kong and X. Zhao, "A Wideband Fabry-Pérot Antenna With Enhanced Gain in the High-Frequency Operating Band by Adopting a Truncated Field Correcting Structure," in IEEE Transactions on Antennas and Propagation, vol. 69, no. 12, pp. 8221-8228, Dec. 2021, doi: 10.1109/TAP.2021.3090841.

- Y. Zhu, Y. Dong, J. Bornemann, L. Gu and **D. F. Mamedes**, "An Inline Compact SIW Bandpass Filter With Quasi-Elliptic Response Using Microstrip Extracted-Pole Resonators," in IEEE Transactions on Circuits and Systems II: Express Briefs, vol. 70, no. 6, pp. 1856-1860, June 2023, doi: 10.1109/TCSII.2022.3231577.

- Y. Zhu, Y. Dong, J. Bornemann, L. Gu and **D. F. Mamedes**, "SIW Triplets Including Meander-Line and CRLH Resonators and Their Applications to Quasi-

Elliptic Filters," in IEEE Transactions on Microwave Theory and Techniques, vol. 71, no. 5, pp. 2193-2206, May 2023, doi: 10.1109/TMTT.2022.3225447.

- T.S. Evangelista, **D. F. Mamedes**, A. J. R. Serres, and A. G. Neto. "A Reconfigurable Frequency Selective Surface for Wi-Fi Application." in Journal of Microwaves, Optoelectronics and Electromagnetic Applications, pp. 33-46, 2023, DOI: 10.1590/2179-10742023v22i1260442.

- Y. Zhu, Y. Dong, J. Bornemann, L. Gu and **D. F. Mamedes**, "A Compact Dual-Band Quasi-Elliptic Filter Using Meander-line- and CRLH-Based SIW Triplets," submitted to Electromagnetic Science.

- A. G. Neto, J. C. E. Silva, J. N. de Carvalho, **D. F. Mamedes**, M. C. de Andrade and J. A. da Costa, "Compact Matryoshka DGS Using Dielectric Resonator," in IEEE Access, vol. 12, pp. 21947-21953, 2024, doi: 10.1109/ACCESS.2024.3363874.

- T. R. de Sousa, **D. F. Mamedes**, A. G. D'Assunção and V. P. Da Silva Neto, "Convoluted Frequency Selective Surface with Dual and Trial-Band Response," SBMO/IEEE MTT-S International Microwave and Optoelectronics Conference (IMOC), Fortaleza, Brazil, 2021, pp. 1-3, doi: 10.1109/IMOC53012.2021.9624876.

- **D. F. Mamedes** and J. Bornemann, "Substrate Integrated Waveguide Single-Pole Dual-Double-Throw (SPDDT) Switch for K-Band Applications," IEEE Asia-Pacific Conference on Applied Electromagnetics (APACE), Penang, Malaysia, 2021, pp. 1-4, doi: 10.1109/APACE53143.2021.9760636.

- **D. F. Mamedes**, A. G. Neto, J. Bornemann, J. C. e Silva and F. A. Teixeira Abreu, "A Sensor Using a Matryoshka Geometry Defected Ground Structure," 16th European Conference on Antennas and Propagation (EuCAP), Madrid, Spain, 2022, pp. 1-4, doi: 10.23919/EuCAP53622.2022.9768950.

- **D. F. Mamedes** and J. Bornemann, "Band-pass Hairpin Filter Using C-shaped DGS With Wide-band Rejection," IEEE International Symposium on Antennas and Propagation and USNC-URSI Radio Science Meeting (AP-S/URSI), Denver, USA, 2022, pp. 277-278, doi: 10.1109/AP-S/USNC-URSI47032.2022.9886114.

- T. R. Sousa, **D. F. Mamedes**, A. G. Neto, and V. P. S. Neto, "Reconfigurable Convoluted Frequency-Selective Surface with Single- and Dual-Band Response," Proc. URSI Int. Symp. Electromagn. Theory, pp. 1-4, Vancouver, Canada, May 2023.

- **D. F. Mamedes** and T. Darcie, "Laboratory Manual: ECE 404 – Microwave Engineering and Fiber Optics," University of Victoria, 2020.

- **D. F. Mamedes**, P. So and J. Bornemann, "Laboratory Manual: ECE 216 - Electricity and Magnetism," University of Victoria, 2021.

1.4 Dissertation overview

This dissertation is organized into nine chapters, including this introduction, and one appendix, covering different topics of FSSs modeling and their characterizations for sub-6GHz and mmWave ranges, as follows:

Chapter 2 describes the fundamental concepts and theory of frequency-selective surfaces, and delivers an overview of traditional FSS applications. This contains a literature review and basic principles governing the operation of FSSs, and methods of analysis.

Chapter 3 encompasses a simple but effective approach to convert a linearly polarized wave into a circularly polarized one using a single-layer FSS with a simple geometry shape. The main geometry used in the designs for this dissertation is introduced in this chapter, where equations for the initial design are provided. The design of the FSS polarization converter is explained, which works for low-

and high-frequency applications. Its numerical and experimental characterizations are discussed.

Chapter 4 formulates and provides an equivalent circuit model for a multi-layer FSS to characterize its transmission response. The proposed structure combines two different elements to achieve a wide-band response in the mm-wave range which is confirmed by experimental characterization. It also contributes an insightful analysis of the generation of a Fano resonance.

Chapter 5 presents a tilted-beam antenna with its gain enhanced by using an FSS. The superformula of Gielis is applied to generate a geometry of the microstrip antenna, bio-inspired by the Wayfaring-tree leaf, and its design is described in detail. Numerical results are discussed, showing the gain enhancement when an FSS is applied, as well as beam-tilting.

Chapter 6 discusses the use of complementary elements to provide multi-passband for multi-band applications. This design takes advantage of the Electromagnetically Induced Transparency Effect by offsetting the elements to create an extra resonance.

Chapter 7 describes a novel reconfigurable FSS composed of complementary elements that offer switchable reflection and transmission characteristics. The effect of the biasing network and threshold voltage applied in the diodes are investigated.

Chapter 8 describes the development of two high-gain reconfigurable antenna systems. The first one uses two reconfigurable FSS panels combined with aperture angles of 45° and 90° as a corner reflector that provide wider switching angle of the beam. The fabrication process and measurements are explained. The second system is a reconfigurable sectoral antenna that consists of four FSS panels, which provides different configurations to steer the antenna's beam in the azimuth and elevation planes.

Chapter 9 lists the conclusions of every project and presents avenues for future work.

Chapter 2

Background of Frequency-Selective Surfaces

This chapter introduces the fundamental concepts of frequency-selective surfaces (FSSs), systematically covering parameters that affect the FSS response as well its structuring. Reconfigurability techniques and FSS applications are discussed. A brief review of relevant literature is presented for a better understanding of FSS functionality. Also, some of the numerical methods for analysis of FSSs and typical experimental setups are described.

2.1 Introduction

FSSs are, in essence, arrays of periodic structures, which provide frequency filtering of the incident electromagnetic waves, thus exhibiting reflection or transmission in free space for different frequencies [12], [13], in two and three dimensions. The earliest use of an FSS dates back to 1919, patented by Marconi and Franklin, where they developed a parabolic reflector grid using an array of resonant dipoles [14]. Research into FSSs did not gain momentum until the 1960s, when its potential for military applications was demonstrated. It had applications in stealth systems, intensifying the research in this field, and various applications in communication systems. Many methods were adopted to model FSSs with accuracy in the late 60's [15], and more sophisticated FSSs were designed with the advance of computational electromagnetic codes in the 90's [16].

Contrary to classical microwave filter, the transmission properties of FSSs are

more complex to analyze. In traditional filters, the frequency is varied at the input port and the response is quantified at the output. In spatial filters, the incident wave can arrive at different angles of incidence and polarizations. Moreover, the FSS frequency response depends on the thickness and electromagnetic characteristics of the dielectric material, and geometry and periodicity of the elements [12], [17], as shown, as an example, in Figure 2.1.

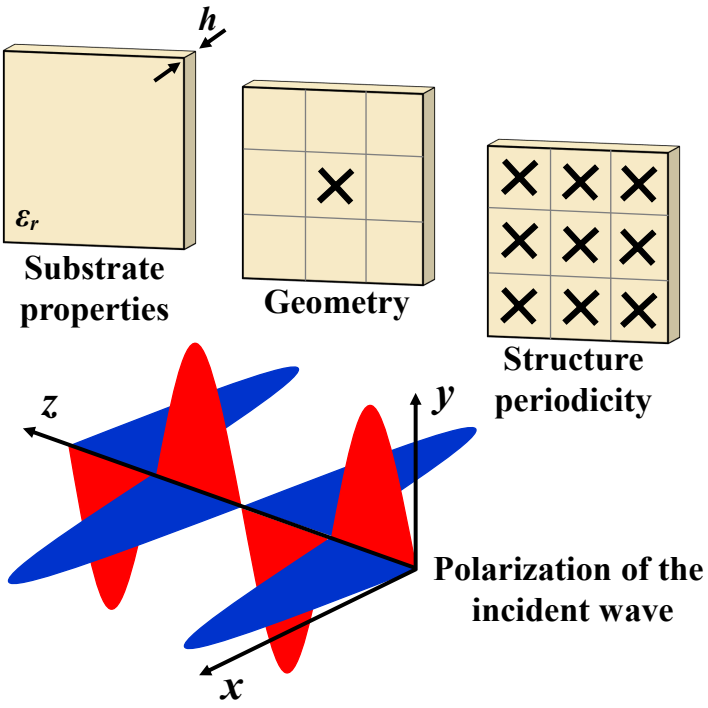

Figure 2.1: Parameters that affect the FSS frequency response.

2.2 Parameters that affect the FSS response

2.2.1 Unit cell filling

The FSS can be characterized as a function of how the basic elements of the periodic array are filled, which can be conductive (patch) type or aperture (slot) type. Figure 2.2 and Figure 2.3 exhibit frequency filtering properties of FSSs similar to those of frequency filters in traditional radiofrequency (RF) circuits. Depending on its physical construction, material, and geometry, they can be classified into band-stop and band-pass filtering characteristics. When the FSS is freestanding (without dielectrics), the

filtering performance of the patch element and aperture FSS are complementary to one another [17].

An array of conducting patches, as shown in Figure 2.2a, behaves as a series LC circuit (Figure 2.2b), presenting characteristics of a band-stop filter (Figure 2.2c). Thus, considering an incidence on the surface, as the elements go into resonance, the incident power radiation occurs in the direction of reflection, until at the resonance frequency of the structure, it will ideally behave as a conductor, reflecting the incident wave [12]. On the contrary, in a periodic array of slot elements (Figure 2.3a), the FSS behaves similar to a parallel LC circuit (Figure 2.3b), with band-pass characteristics (Figure 2.3c). When the structure is subjected to an incident wave perpendicular to its surface, as the elements go into resonance, the structure becomes transparent to the incident wave, until, ideally at the resonance frequency, wave transmission occurs.

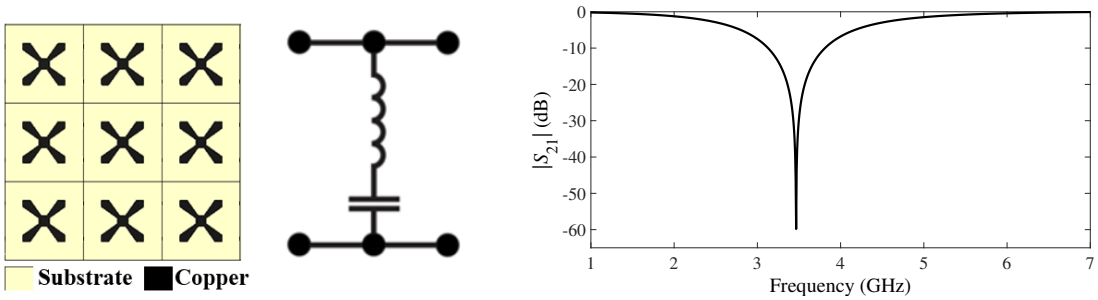

(a) Patch element. (b) Equivalent circuit. (c) frequency response.

Figure 2.2: Typical filtering characteristics of patch element FSS.

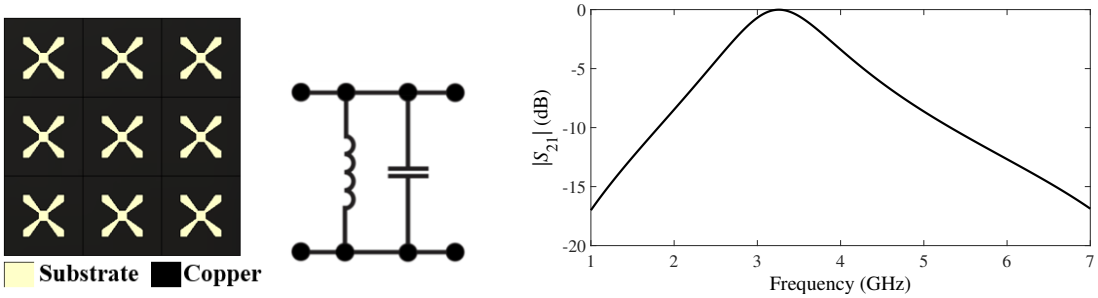

(a) Aperture element. (b) Equivalent circuit. (c) frequency response.

Figure 2.3: Typical filtering characteristics of aperture element FSS.

2.2.2 Geometry of basic element

Traditional elements

The characteristics of the FSS, such as resonance frequency, bandwidth, polarization and angular coverage, depend mainly on the unit cell element type. There is a variety of shapes of conducting and resonating elements, some of them are independent of polarization and offer wider bandwidth than others. According to Munk [12], the elements can be categorized in four possible configurations: center-connected or N-poles (Figure 2.4), loop structures (Figure 2.5), solid interior (Figure 2.6) and hybrid elements (Figure 2.7) [12]. The first group is formed by elements with N-poles connected at the center. The well-known elements are the straight dipole (Figure 2.4a), crossed dipole (Figure 2.4b), tripole (Figure 2.4c), Jerusalem cross (Figure 2.4d), among others. For this type of elements, their length for the first dominant resonance is about a half-wavelength and can be packed tightly with enhanced bandwidth, which also pushes grating lobes to higher frequencies [18].

(a) Dipole. (b) Cross dipole. (c) Tripole. (d) Jerusalem cross.

Figure 2.4: Center-connected or N-poles elements [12], [17], [18].

Loop-type elements correspond to the second group. The typical shape elements are the square loop (Figure 2.5a), double square (Figure 2.5b), gridded square (Figure 2.5c), double ring (Figure 2.5d), etc. These configurations have stable resonance frequencies in response to oblique incidence of waves. The length of loop elements is about a wavelength at the dominant resonance frequency. Moreover, they offer a broad range of bandwidth variation depending on the geometry chosen.

In the third group, the elements have a solid interior, which can assume various geometric shapes such as square (Figure 2.6a), rectangle (Figure 2.6b), hexagon (Figure 2.6c), circular patches (Figure 2.6d), and others. The size of the elements is about a half-wavelength, which further imposes inter-element spacing to be large, leading to an early onset of grating lobes and high sensitivity to oblique incidence [12], [18].

The fourth group is composed of hybrid elements by combinations of the three

(a) Square. (b) Double square. (c) Gridded square. (d) Double ring.

Figure 2.5: Loop elements [12], [17]–[19].

(a) Square. (b) Rectangle. (c) Hexagon. (d) Circle.

Figure 2.6: Solid interior elements [12], [17], [18].

previous groups. Figure 2.7 exemplifies some of these combinations. The combined elements are designed to overcome specific drawbacks from the traditional elements for a desired application.

Figure 2.7: Hybrid elements [12], [18].

Fractal elements

As the design, method of analysis and fabrication technologies have improved, new types and applications of FSSs have been introduced, such as the fractal elements. Fractals possess self-similarity and space-filling properties in the sense that a very long line or a large surface can be built over a limited area [20], [21]. The use of fractal elements in FSSs has proved to be effective in designing FSSs with higher frequency compression factor that ensures its miniaturization and a good angular stability. The use of fractal motifs in FSSs was originally proposed in [22] to reduce the overall size of the FSS. Since then, many geometric fractals have been applied to FSS designs,

e.g., to obtain a multiband response. Figure 2.8 shows an overview of some fractal shapes used as elements of FSSs.

(a) Sierpinski gasket [23].

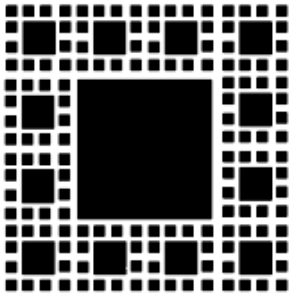

(b) Sierpinski carpet [24].

(c) Dürer's pentagon [25].

(d) Vicsek [26].

(e) T-Shaped [27].

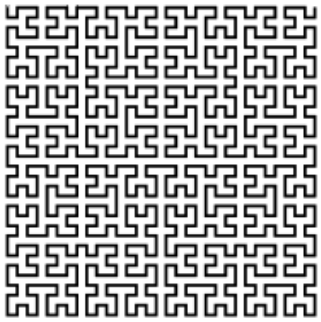

(f) Hilbert curves [28].

Figure 2.8: Examples of fractal FSS geometries.

To obtain a fractal geometry, two main parameters are required: the iteration factor and the number of iterations. The initial geometry (level 0) is divided by the iteration factor and a set of geometric transformations is applied in each segment (Equation (2.1)) [29].

$$W\begin{pmatrix} x \\ y \end{pmatrix} = \begin{pmatrix} a & b \\ c & d \end{pmatrix} \begin{pmatrix} x \\ y \end{pmatrix} + \begin{pmatrix} e \\ f \end{pmatrix} \tag{2.1}$$

where a, b, c and d control rotation and scaling transformation and e and f control linear translation. The new geometry produced by the new level applied to an initial geometry can be represented by the sum of the segments as in Equation (2.2)

$$W(A) = \bigcup_{n=1}^{N} w_n(A) \tag{2.2}$$

Reference [23] presents an FSS designed by arraying a second-iteration Sierpinski dipole (Figure 2.8a). These dipoles are built after the Sierpinski gasket or Sierpinski

triangle. They show that the self-similarity of the Sierpinski dipole translates into a dual-band behavior of an FSS that allows its geometry resonators to operate at different frequencies. The design of three surfaces based on the Minkowski and Sierpinski Carpet (Figure 2.8b) fractals is demonstrated in [24]. The FSSs exhibit two or three stop-bands depending on how many iterations are used and are dual-polarized due to the symmetry of the geometry. Figure 2.8c shows a level 2 Dürer's pentagon pre-fractal patch element. Reference [25] discusses Dürer's pentagon applied to an FSS as its basic element with levels of iteration starting from 0 up to 3. When the fractal used in the FSS starts presenting a dual-band response and when the level of iteration is increased, the resonance frequencies decrease.

The application of Vicsek fractal elements (Figure 2.8d) to design FSSs is described in [26]. They present a new EM-optimization technique for the optimal design of the FSS. The fractal motifs proposed here present some desirable features such as dual polarization and angular stability for oblique incidence of plane waves. When increasing the fractal iteration factor, the resonance frequency decreases and its bandwidth becomes narrower. The characteristics of FSSs with T-shaped pre-fractals patch elements (Figure 2.8e) are investigated in [27] from level 0 (square patch) to level 3. It is verified again that once the number of iteration increases so does the frequency compression factor in relation to level 0 (in order of 60% for this fractal) and it results in the lower bandwidth, allowing higher selectivity.

The Hilbert curves are a family of space filling curves, and they offer the property of being able to compact an electrically long wire within a very small space. In [28] the fifth generation of the Hilbert curve FSS (Figure 2.8f) is generated by way of the Lindenmayer system, and the results shows a reduction of the unit cell size. As the Hilbert curve begins and ends at adjacent corners, the element is not symmetrical and therefore is singly polarized.

2.2.3 Dielectric loading effect

In practice, the conductive pattern of an FSS must be supported by dielectric substrates for mechanical strength. Moreover, the substrates contribute to the flatness of bandwidth, roll-off rate and controlling the drift of the resonance frequency with incident angle variations [12], [30], [31]. The periodic array elements can be embedded within dielectric slabs as in Figure 2.9a, or etched on one side of the dielectric slab as in Figure 2.9b.

The frequency response of an FSS embedded in dielectric slabs is reduced by a factor of $\sqrt{\epsilon_r}$, where ϵ_r is the relative permittivity of the dielectric substrate [30]. The resonance frequency f_0 of the transmission response of the FSS is shifted down to

$$f_0' = \frac{f_0}{\sqrt{\epsilon_r}} \tag{2.3}$$

When an FSS is bonded on one side of the dielectric slab, the frequency shifts downwards (Equation 2.4) with a ratio of $\sqrt{\epsilon_e}$ [30], where $\epsilon_e \approx \frac{\epsilon_r+1}{2}$ [12], [32].

$$f_0' = \frac{f_0}{\sqrt{\epsilon_e}} \tag{2.4}$$

The thickness of the dielectric substrate contributes to the angular stability and the polarization of the FSS. In other words, the use of a dielectric substrate makes the FSS structures less angle sensitive. This is supported by Snell's law; obliquely incident waves on a dielectric layer are refracted towards the normal direction of incidence as shown in Figure 2.9. Higher dielectric permittivity leads to a higher bending of waves towards the normal direction for a single interface.

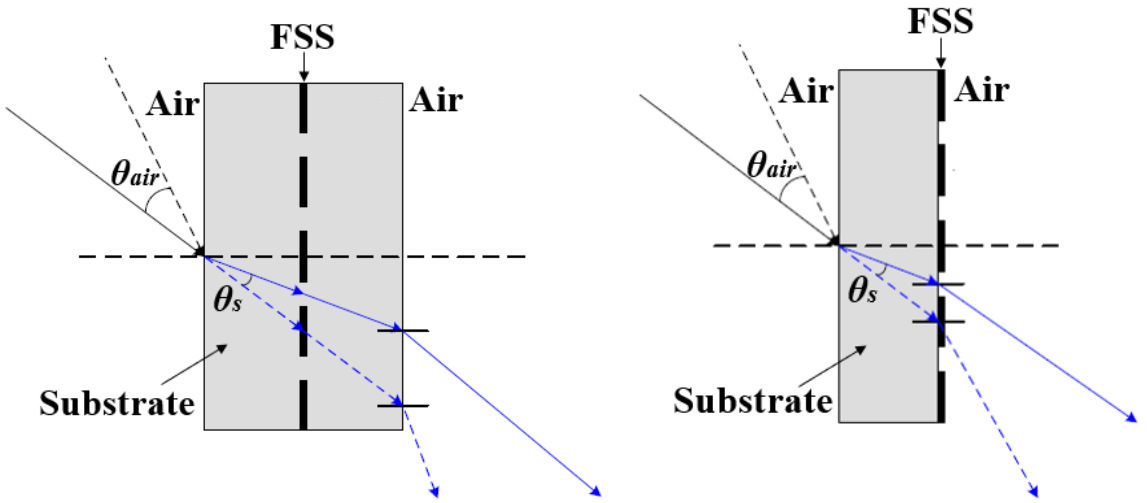

(a) FSS embedded within dielectric substrates. (b) FSS etched on a dielectric substrate.

Figure 2.9: Dielectric arrangements.

2.2.4 Periodicity and grating lobes

The lattice pattern or periodicity of the conducting elements is another key parameter that affects the transmission and reflection response of an FSS. Depending on the

spacing between the elements and the geometrical position of adjacent elements, the resonance frequency, bandwidth, cross-polarization level, and angular sensitivity are varied [12], [33]. Therefore, the periodicity directly influences the appearance of grating lobes in the FSS frequency response. Grating lobes are undesired secondary lobes in the transmission and reflection coefficients that can occur at angles with higher order constructive interference when the spacing between elements is electrically large [17] compared to the wavelength of the incoming waves. Furthermore, the onset of grating lobes is dictated by the geometrical lattices such as square, triangular, and the brick lattices, etc. Table 2.1 [17] lists the criteria to avoid grating lobes for those lattice patterns, considering cases when the incident angle is $\theta = 0°$ and $= 45°$.

Lattice type	Maximum spacing	$\theta = 0°$	$\theta = 45°$
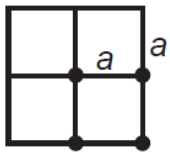	$\frac{a}{\lambda_0} < \frac{1}{1+\sin\theta_0}$	$\frac{a}{\lambda_0} < 1$	$\frac{a}{\lambda_0} < 0.59$
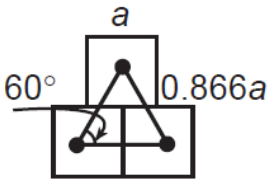	$\frac{a}{\lambda_0} < \frac{1.15}{1+\sin\theta_0}$	$\frac{a}{\lambda_0} < 1.15$	$\frac{a}{\lambda_0} < 0.67$
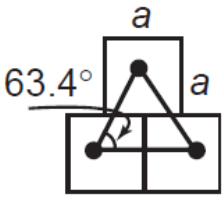	$\frac{a}{\lambda_0} < \frac{1.12}{1+\sin\theta_0}$	$\frac{a}{\lambda_0} < 1.12$	$\frac{a}{\lambda_0} < 0.65$

Table 2.1: FSS lattice types and grating lobe criteria [17].

By respecting these criteria, the onset of grating lobes is moved to higher frequencies. From Table 2.1, it can be seen that the square lattice offers the most closely packed elements, while the triangular one has the largest inter-element spacing. In practice, it is recommended for the lattice size to be two-thirds or less of the value given in Table 2.1, to avoid wasted energy. Moreover, by reducing the grid spacing, the bandwidth of the FSS can be increased [17]. When decreasing this distance, the real part of the array self-impedance is increased, while its imaginary part remains almost the same, and the transmission coefficient will be close to unity over a larger frequency band [12].

2.2.5 Angle of incidence and polarization

Incident waves can strike the FSS at any angle. When an incident wave arrives at an off-normal or oblique angle ($\theta \neq 0°$) to an FSS formed with periodic conducting strips spaced by g, as illustrated in Figure 2.10, the width w and the separation between the elements will be effectively reduced by a factor of $\cos\theta$. The effective element dimensions seen by the wave with oblique incidence, and consequently the current induced in these elements, are different from the wave that reaches the FSS with normal incidence ($\theta = 0°$) [34], resulting in a variation in the scattering response of the FSS under angular incidence [35]–[39].

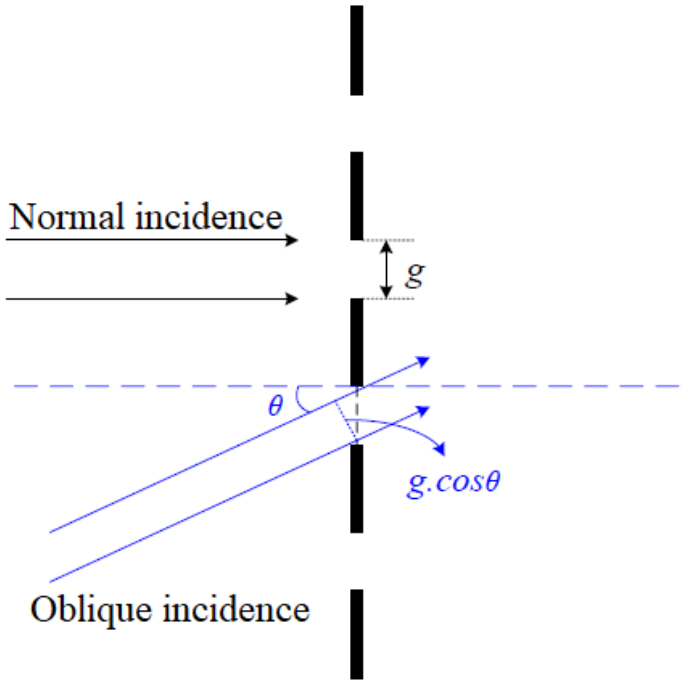

Figure 2.10: Normal and oblique incident wave on FSS.

The variation in the FSS response due to the angle of incidence of the incoming wave can also be demonstrated by an equation of the equivalent circuit, as presented by Marcuvitz [40]. This will be discussed in Section 2.6.2, which basically says that conducting strips in parallel with an incident electric field behave as inductors, while the gap between conductors act as capacitors [40]. The equations for the equivalent circuit calculate the inductance and capacitance of the periodic array as a function of the angle of incidence.

The polarization of the incident wave can also affect the transmission response of

the FSS. A polarized wave can be described as the superposition of the electric field components:

- when the electric field is perpendicular ($E_{\perp}$) to the plane of incidence, it is called transverse electric (TE) polarization.
- and when an electric field is parallel ($E_{\parallel}$) to the plane of incidence, it is called transverse magnetic (TM) polarization.

Depending on the polarization used, the impedance of the FSS will change, thus also changing its scattering response. Figure 2.11 exemplifies an FSS with square-loop elements separated into vertical and horizontal strips [41]. When a TE wave strikes the FSS, the vertical strips will contribute to the inductive impedance. While in the TM polarization, the horizontal gratings correspond to the capacitive component [42]. In the TE mode (Figure 2.11a), the polarization of the E-field is parallel to the strip, exciting it to its total length, independent of the incident angle. However, for the TM mode (Figure 2.11b), the E-field arrives obliquely to the strips. When the angle of incidence increases, the length seen by the wave is shorter than the one designed.

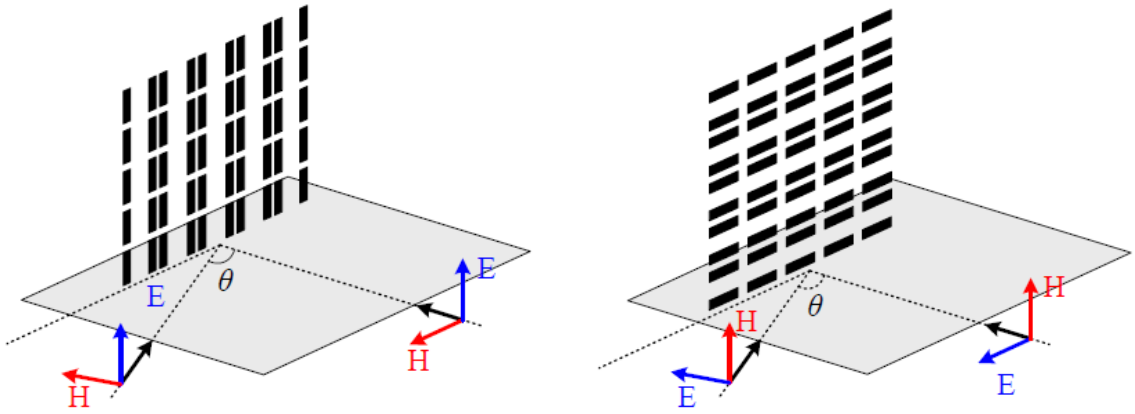

(a) TE waves incident.

(b) TM waves incident.

Figure 2.11: Polarization of the incident wave on a square loop separated into vertical and horizontal strips.

The effect of the incident angle and polarization on the FSS response cannot be neglected; however their influences will vary between designs. Depending on the application requirements, the microwave engineer should choose a geometry with less deviation between the normal and off-normal incidence.

2.3 FSS structuring

2.3.1 Single-layer and multi-layers FSS

A traditional single-layer FSS is comprised of a two-dimensional (2D) periodic array of elements that can be implemented by commercial lamination and etching techniques on a supporting dielectric layer, which has the benefit of easy fabrication, low profile and low cost [12]. As was explained in Section 2.2.1, an FSS can exhibit a band-pass or stop-band response, depending on whether its elements are shaped as apertures or patches. Single-layer structures have been used in many applications in microwave, millimeter-wave and terahertz ranges [43]. This type of FSS is easy to synthesize, but it presents single-band and narrow bandwidth responses as it behaves as a first-order filter. Many techniques are applied to address some of the limitations, and miniaturization is one that has recently emerged.

A range of planar single-layer FSSs have been reported with insensitivity to incidence angle. A single-layer pass-band FSS working at 2.6 GHz is proposed in [44], suppressing the grating lobe and achieving miniaturization. From the perspective of the bandwidth, the FSS remains stable at 60° under TE and TM polarization. Two free-standing single-layer FSSs are presented in [45] to be used as dichroic filters with a high transmission in the atmospheric window between 602–725 GHz. They used an aperture flower-type geometry, which showed to increase the transmitted frequency range by 24% at non-normal beam incidence. Also, they demonstrated the advantage of using a single-layer system over more complicated layer configurations.

The high inductance and low capacitance in single-layer FSSs provides a narrow bandwidth, as mentioned before, which is very difficult to improve on. Multilayered FSS structures have shown to be a good alternative to this limitation, achieving higher order filter performance, which provides a multi-band or broadband response [46], [47]. In this configuration, single-layer structures are cascaded with the inclusion of dielectric spaces. In addition to the geometry of the element and lattice configuration, the inter-layer coupling is an important parameter to be considered, in order to achieve the required performance.

A two-layer absorber based on a two resistor-loaded square loop FSS array is proposed in [48] with an ultrawide absorption band. A large absorption bandwidth of 171.2% is achieved with the designed absorber. A fully inkjet-printed multi-layer Miura FSS structure, with dipole resonant elements and a specialized origami-inspired

shape reconfigurable spacer layer, is described in [49]. The bandwidth of this structure is more than double as compared to the single-layer Miura FSS and can be varied by simply changing the design parameters of the spacer layer.

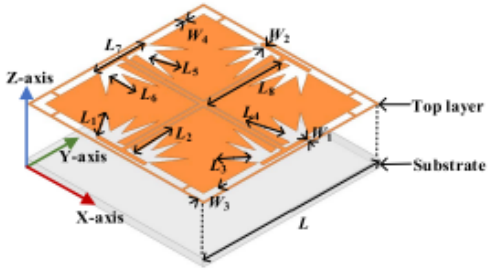

(a) Single-layer FSS proposed in [44].

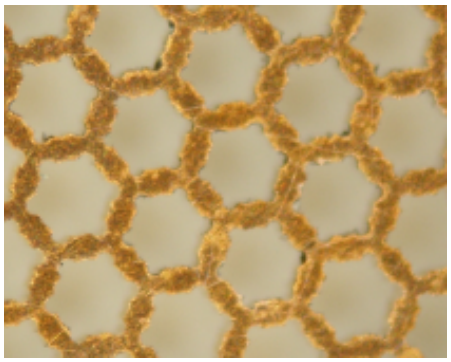

(b) Single-layer FSS proposed in [45].

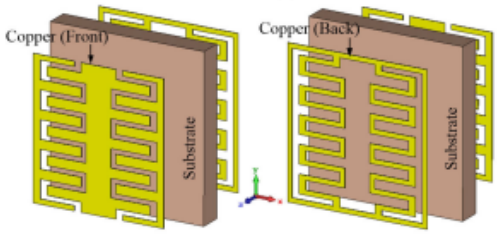

(c) Multi-layer FSS proposed in [46].

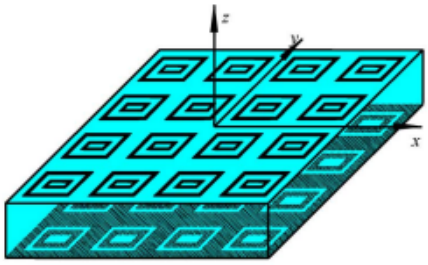

(d) Multi-layer FSS proposed in [47].

Figure 2.12: Examples of 2-D FSS structures.

2.3.2 3-D FSS

In some applications, FSSs require some characteristics such as wideband performance, fast roll-off, and insensitivity to incident angles and polarization of the incoming EM wave. As scrutinized previously, 2-D planar FSS elements in their single- or multi-layer configurations have shown to be inefficient with respect to the required features, e.g., they are inherently sensitive to the incoming wave angles, even though some studies reported in the literature aimed at improving the characteristics of traditional FSSs [50]. Recently, a new type of FSS formed by three-dimensional (3D) periodic volumetric elements has been introduced and has demonstrated better performance features when compared to the 2-D FSSs [32]. 3-D FSSs can achieve stable frequency responses at oblique incidences [51] and provide more flexibility. The techniques used to deduce the scattering characteristics of 2-D FSSs can be applied to design 3-D structures, considering that the volumetric elements are built based on

planar ones. However, 3-D FSSs have some difficulties in implementation and fabrication [52]; also its size and weight are larger than 2-D ones.

The fabrication of 3-D FSSs presents many challenges, due to the complex geometry of the elements. In [53] this issue is addressed by proposing PolyJet 3-D printing for the fabrication of the elements. The printed elements are metallized and encapsulated in a Sylgard-527 substrate over a polymethylmethacrylate lattice resulting in a low-loss, low-cost, low-profile, and light-weight array. Figure 2.13a shows the proposed multiband polarization independent FSS that was optimized using the MOLACO algorithm. Eightfold symmetry guarantees identical response of the structure at TE and TM polarizations for normal incidence. To validate the fabrication technique, measurements were carried out in two different setups, one in a WR-284 waveguide and the other using two broadband horn antennas and focusing lenses. These experimental characterizations will be described in Section 2.7.

A 3-D FSS using symmetrical tapered resonator elements (Figure 2.13b) is presented in [54]. The proposed structure produces a stable angular response up to 80° with $< 0.5\%$ frequency deviation. The tapered geometry enables a stable cavity resonance to be matched at a single frequency for both TE and TM incident angles without the need for external dielectric matching layers.

Reference [50] implements an assembled-type 3-D FSS with replaceable unit cells using a 3-D printing technique, providing a reconfigurable behavior. The structure is designed to operate at 6.45 GHz using conducting cross-dipoles as basic elements on a square pyramid shaped dielectric substrate. The structure exhibits a stable response for incident angles up to 45° for the TE and TM modes. The reconfiguration of the structure is done by structurally replacing and reconstructing the unit structure (Figure 2.13c), which varies the frequency response.

The concept of substrate integrated waveguide (SIW) cavity technology is applied to develop a 3-D FSS in [55]. They use a hexagonal-shape geometry due to its stable resonance performance in 2-D planar form. The 2-D structures are coupled through a series of periodically spaced metallic vias, separated by a finite gap, as shown in Figure 2.13d. The vias will act as virtual walls and ensure the design of the 3-D FSS. The proposed FSS shows two sharp roll-off performance characteristics. Furthermore, as the length of metallic vias increases, the band-stop response is converted to a higher frequency, and another stop-band is generated in a lower frequency region as an effect of mutual coupling.

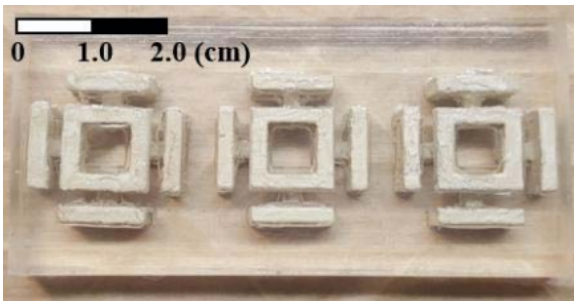

(a) 3-D hybrid elements [53].

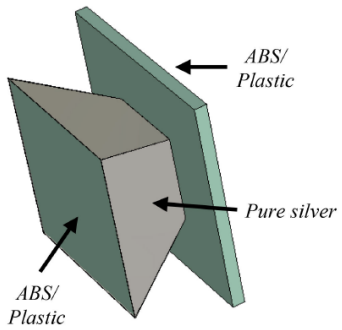

(b) Tapered resonators [54].

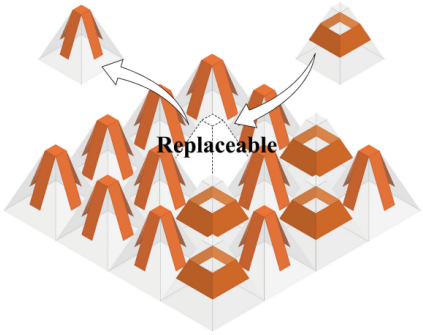

(c) Assembled-type FSS [50].

(d) SIW hexagonal FSS [55].

Figure 2.13: Examples of 3-D FSS structures.

2.3.3 2.5-D FSS

As described previously, 3-D structures assume volumetric shapes/elements. Lately, a new concept or nomenclature of non-2-D nor 3-D FSS has attracted the interest of researchers; these structures are denominated 2.5D. The miniaturization into the domain of 2-D planar structures is limited. Using higher dimensional structures can improve FSS miniaturization. The methods applied to miniaturize 3-D FSSs increase their complexity and cost. Contrastingly, 2.5-D structures can offer an easier way to achieve the miniaturization. A 2.5-D FSS consists of 2-D geometries interlayer-coupled by metallic vias [56], [57]. The inclusion of via holes increases the capacitance and inductance of the unit cell, offering a simple and low-cost solution to miniaturize FSSs [58], [59]. What distinguishes a 3-D SIW FSS from a 2.5-D one is that in the 2.5-D structures, the elements have different geometries in each layer and they close the loop by knitting the segment with the vias [60].

The design of a 2.5-D FSS is proposed in [61]. They use 2-D convoluted and interweaved lines in the form of square spirals incorporated with vertical vias, as illustrated in Figure 2.14a, giving a unit cell size of 0.027λ. The resonators are

combined in such a way that results in polarization independence. Also, the FSS provides a stable frequency response for incidence angles, up to 75°, for both the TE and TM polarizations.

Reference [62] presents a multilayer hexagonal 2.5-D closed loop FSS. The structure consists of three layers of dielectric substrates and four layers of metallic patches. The three-layer dielectric substrates are closely connected, and the adjacent two-layer patches are connected through metallic vias (Figure 2.14b). The structure shows a good miniaturization performance with a unit cell size of 0.041λ. It also shows an outstanding stability under different polarization modes and incident angles (up to 80°) of the EM wave.

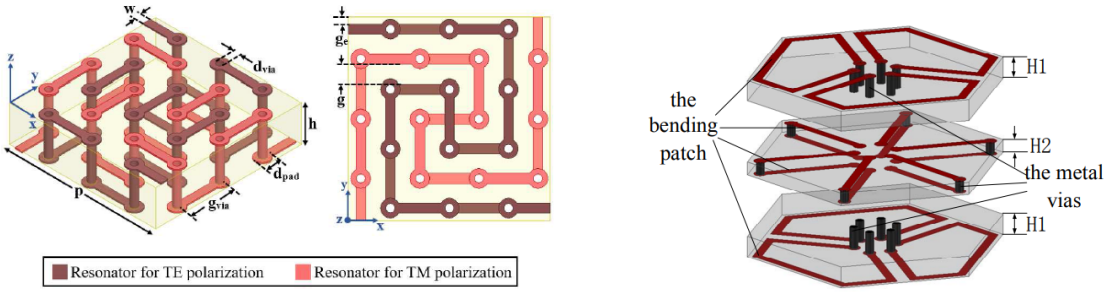

(a) 2.5-D convoluted square spirals [61]. (b) Multilayer hexagonal 2.5D [62].

Figure 2.14: Examples of 2.5-D FSS structures.

2.4 Reconfigurable FSSs

Conventional passive FSSs (consisting of conducting patches and/or apertures) are fabricated on a dielectric substrate for a particular transmission or reflection. Once they are manufactured, the electromagnetic characteristics such as the resonance frequency and bandwidth cannot be changed, due to their permanent physical characteristics. The advantage of these FSSs is that their design and fabrication are simple.

In certain applications altering the FSS' frequency response is a requirement. The active FSS or reconfigurable FSS (RFSS) has proved to be an alternative in order to provide mechanical and/or electrical tuning. In the mechanical reconfiguring method, movable parts and mechanical modifications are applied to the panel by stretching [63], folding [64], [65] or rotating [66], [67] the FSS elements to achieve tuning of the frequency response. In the electrical reconfiguring method, active components,

such as PIN diodes [68]–[70], varactors [71]–[73], Schottky diodes [74], and others, are incorporated on the FSS to manipulate the magnitudes and phases of the reflection and transmission coefficients by altering the element's geometry and effective size. The active elements are tuned by external excitation, e.g., a DC power supply [75]. The disadvantage of this type of structure is the added cost of manufacturing, power consumption and complexity to the system.

Table 2.2 briefly shows some recent tuning methods applied in RFSSs along with configurations and frequency ranges. In [76] each unit cell has four PIN diodes across the aperture at 90° intervals, providing symmetry to the structure for TE and TM polarization, while switching the diodes from off- to on-state. Using varactor diodes, a wide tuning range of resonance from 3.5 to 5.7 GHz is achieved in [77]. An FSS with cantilever-arms is presented in [78], and by adjusting the height of the bending of the arms, the capacitance between the top and ground layers gets changed, thus influencing the resonance frequency of the structure. The proposed 3-D FSS in [79] achieves its reconfigurability by sliding the outer cylinder over the inner cylinder. Reference [80] presents a mechanical tunable FSS by folding and unfolding the structure, resulting in a shift in resonance frequency.

2.5 Applications

The application of periodic structures has contributed to the development of new technologies. These applications involve designs that enhance the electromagnetic compatibility. The common FSS applications explore its filtering properties, preventing interfering signals between antennas, reducing radar noise, improving the security of wireless communication, etc. FSSs have been widely used in a variety of frequency ranges of the electromagnetic spectrum, with applicability from microwave to terahertz frequencies. One of the most well-known examples of FSS applications is the shielding in the door of a standard household microwave oven (Figure 2.15). The perforated metal screen door blocks the microwave at 2.45 GHz and allows the visible light to pass through.

FSSs have been used as sub-reflectors in multi-band reflector antenna systems [81]–[84], where the FSS diplexes two different frequency bands, reflecting one and passing another. Therefore, two feeds are placed at different location, but sharing the reflector antenna simultaneously. Figure 2.16 shows a Cassegrain reflector system with an FSS as dichroic sub-reflector, isolating the feeds. Feed #1 is located at the

Reference	Frequency (GHz)	Tuning method	Configuration
[76]	3	PIN diode	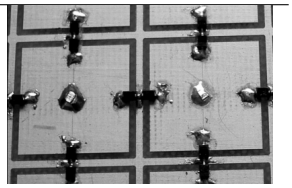
[77]	3.5 to 5.7	Varactor diode	
[78]	30	Cantilever	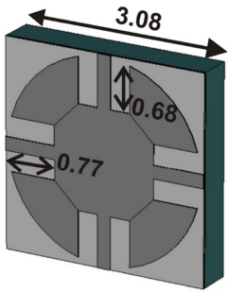
[79]	1.86 to 3.10	Sliding cylinders	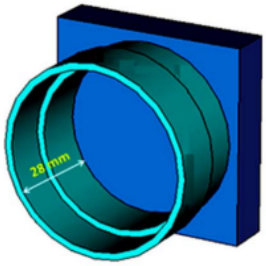
[80]	10 to 12	Folding angle	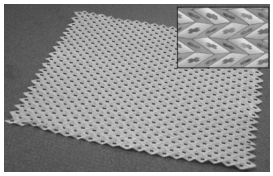

Table 2.2: An overview of tuning methods for RFSS.

Cassegrain focus and feed #2 at the prime focus. The sub-reflector is transparent to the frequency range of feed #2 and reflective to that of feed #1. This configuration has only one main reflector at two different operating frequencies, providing the system with a reduction in mass, volume and cost.

The FSS radome has been used to reduce the radar cross section (RCS) of large

Figure 2.15: FSS embedded in the door of a microwave oven.

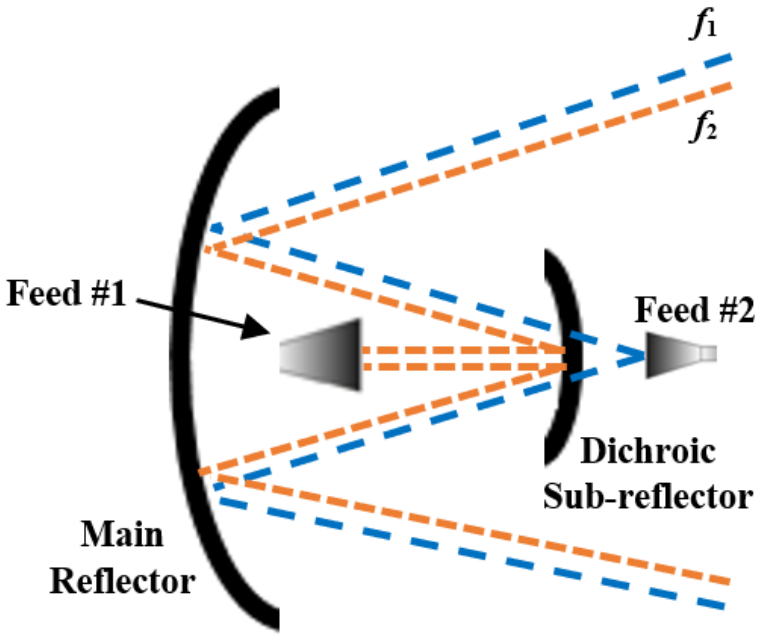

Figure 2.16: Configuration of a dual antenna system with FSS dichroic sub-reflector. The FSS acts as a reflector for one frequency band and is transparent for the other.

antennas in airborne system. RCS is described as the product of geometric cross section, fraction of power scattered (reflectivity) and the direction in where the power is scattered (directivity) by the target. The FSS radome is designed to be in-band transparent in the antenna's operating frequency band, passing the EM wave through to the antenna, and is reflective (or absorbent) in the out-band, reducing RCS [12], [85]. To ensure the radiation performance of the system, the FSS radome must be stable and transparent over a range of angles of oblique incidence for both TE and

TM polarizations [86], [87]. Figure 2.17 illustrates an FSS radome on the surface of an aircraft with a pointed nose shape. It is demonstrated that the transmitted and received EM waves passing through the FSS radome have incident angles that can vary from 0° (normal incidence) to 75° or even higher [88].

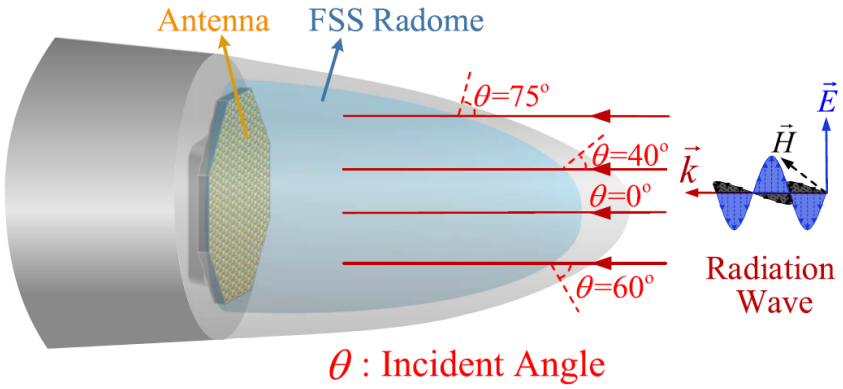

Figure 2.17: Application of FSS as radome on the aircraft's nose cone [89].

FSSs have been used in designing structures of high-impedance surfaces such as the artificial magnetic conductor (AMC) and electromagnetic bandgap (EBG) material. The most well-known example of AMC structures was designed by Sievenpiper, presented systematically in [90]. Due to their unusual boundary conditions, the high-impedance surfaces work as a unique new type of ground plane, which suppresses the propagation of surface waves within the substrate [91]. The image currents are in-phase allowing radiating elements to lie directly adjacent to the surface, at a distance as low as $\lambda/50$, while still radiating efficiently.

A thin metallic-oxide coating is used in modern window design for saving energy. The coating provides thermal isolation while blocking the electromagnetic radiation in the infrared region and being almost transparent to the visible part of the spectrum [92]. It rejects the heat transfer from the outdoor to indoor environment in the warmer seasons and vice versa during the colder ones. FSSs are used in the metallic coating of an energy-saving glass to pass the frequency bands of desired signals, without degrading the thermal response of the window (Figure 2.18) [93]. Moreover, the FSS offers a radio shielding application from external signals in buildings [94]. With advances in communication systems, just a few transparent FSSs operate in 5G millimeter-wave communications. A transparent FSS on a glass window is proposed in [95] for a signal selectivity of 5G communication, operating at 28 GHz, based on a transparent and low-loss material cyclic olefin copolymer. The FSS has a spatial

filtering function for electromagnetic pollution prevention and information security in 5G millimeter-wave communication scenarios, with maximum loss of 2.98 dB in the frequency range of 27.5 $\sim$ 29.5 GHz.

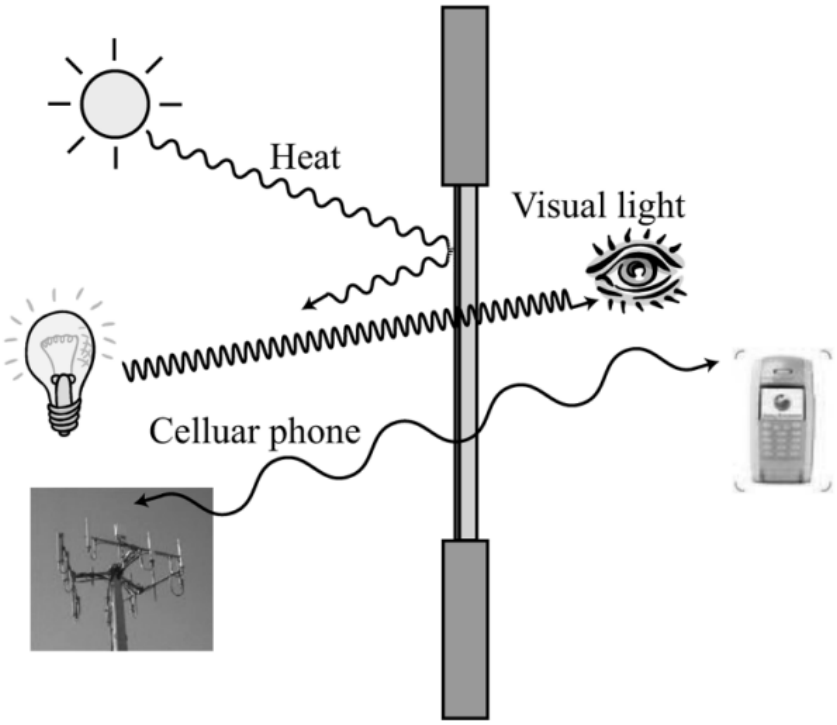

Figure 2.18: Energy-saving glass window showing transmission properties of different frequencies and blocking infrared rays [93].

In recent years, research on wearable FSSs is found in the literature. This technology is commonly used in wireless body area networks for communication among sensor nodes operating in contact, or close to a live body, which permits a continuous and unobtrusive examination of patients' state of health, i.e., monitoring blood pressure or heart rate [96]. FSSs have been used as electronic bandgap and artificial magnetic conductors to reduce the height of antennas and communicate with the body in wearable systems. Also, FSSs have been used as transponders in radio frequency identification (RFID) applications. Reference [97] proposed a semi-passive RFID based on a low-power consumption modulated FSS for on-body wearable applications (Figure 2.19) using back-scattering communication in the 2.45 GHz ISM band.

Advances in manufacturing techniques (e.g., computerized knitting [98], embroidery [99], and weaving machines [100]) have permitted the fabric-based FSS using

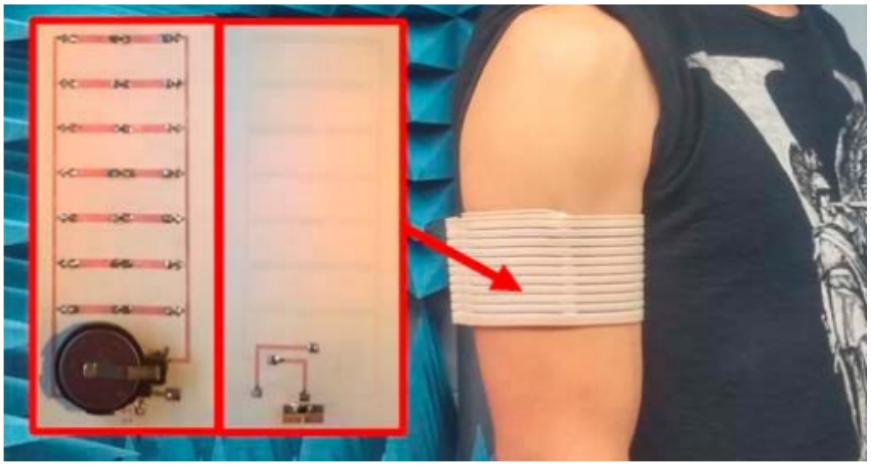

Figure 2.19: Example of FSS for wearable RFID and sensor applications [97].

textiles as substrate materials. These structures offer light weight, flexibility, and softness [99] and can be integrated into clothes to provide on-body and off-body communications [98]. Figure 2.20 presents an example of the fabrication process of textile FSSs and fabric substrates.

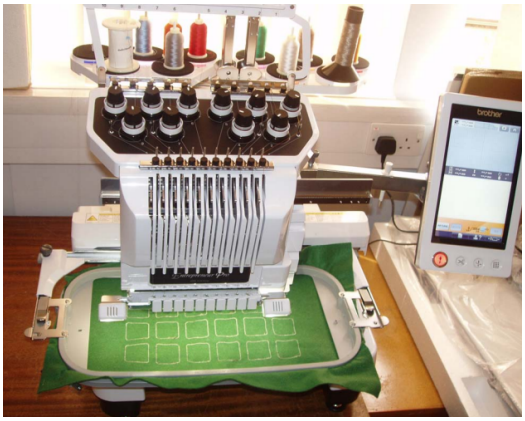

(a) Fabrication of a textile FSS using a digital embroidery machine [99].

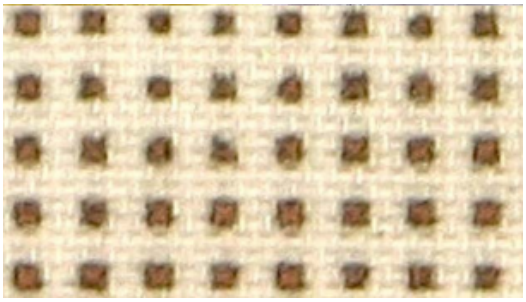

(b) Copper square FSS on nylon fabric [101].

Figure 2.20: Examples of fabric-based FSSs.

FSSs with slot elements, with rectangular or circular shape, have been designed for collecting solar energy [102]. The band-pass FSS screen is transparent in the frequency band where the solar cell is more efficient and reflecting in frequencies out-of-band. Moreover, the use of solar cells incorporated in reconfigurable FSSs for biasing has been reported. Reference [103] presents a fully inkjet-printed electronically tunable FSS with an on-package solar cell to bias varactors. The solar cell changes its output

voltage with variation in light intensities that leads to a change in capacitance of the varactor and, hence, frequency response of the FSS.

2.6 Numerical methods for analysis

Techniques of analysis are used to understand and obtain the FSS characteristics, i.e., its design parameters. In the variety of techniques published, the design engineers have to chose one that balances their requirements in the results, such as accuracy, type of elements (simple or complex geometry), computational time, etc. This section presents some of the most performed methods in FSS analysis, which are divided in three technique categories: theory of circuits, modal expansion and interactive.

A bibliometric study was carried out through the IEEE Xplore database on November 26, 2021, considering the method applied to analyze FSSs. The numbers of publications in IEEE periodicals having the index terms "Frequency Selective Surface" combined with the numerical methods "Mode Matching", "Equivalent Circuit", "Method of Moments", "Finite Element", "Finite-Difference Time-Domain", "Wave Concept Iterative Procedure", found in IEEE Xplore are shown in Figure 2.21. According to this bibliometric study, the equivalent circuit method is the most popular method, among the others to analyze FSSs, in the number of scientific publications. This result is probably due to the fact that this method is easy to implement and uses less computational effort compared to full-wave ones.

2.6.1 Mode-matching technique

The Mode-Matching (MM) Technique was originally developed to solve bifurcated waveguide problems [104], [105] by expanding the fields on the side of the discontinuities in terms of vector wave functions. The performance of periodic structures can be predicted using mode-matching by matching the expansions in the regions of discontinuity, according to the boundary conditions, into Floquet modes [106]. The integral equation is reduced to matrix form.

The Floquet theorem is an extension of the Fourier series for periodic structures, which provides the description of modes of any electromagnetic field or function that repeats periodically, only differing by a phase factor. Considering an incident plane wave towards an FSS, the transmission and reflection coefficients can be calculated, where the Floquet modes are defined as a set of discrete components of this plane

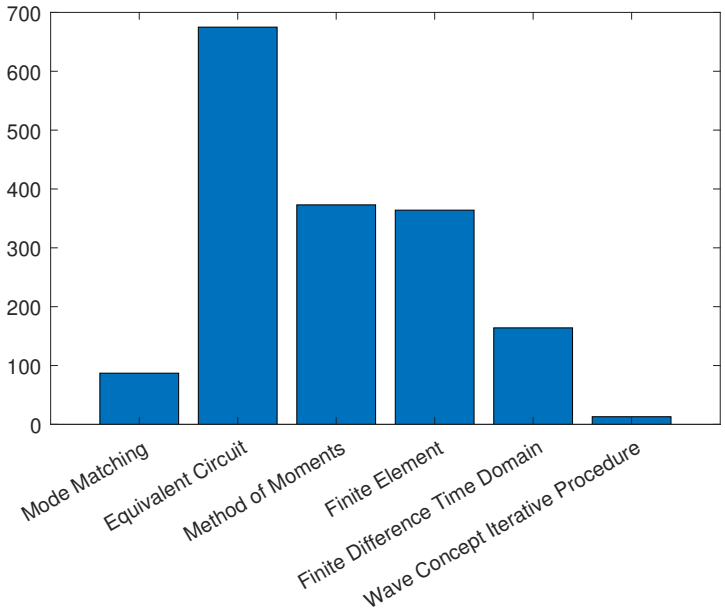

Figure 2.21: Number of publications in IEEE periodicals with index terms of numerical methods for FSS analyses.

wave with spacing as function of its periodicity.

The matching of modes is a powerful technique for analyzing periodic structures and waveguides with varying cross-section. This method is usually combined with other techniques. Reference [107] presents a hybrid approach of mode-matching with finite-elements (FE) method for a rigorous analysis of thick-screen inductive FSSs. It uses the computational efficiency of the MM analysis with the versatility and flexibility of the FE method. It employs an edge-based FE approach for determining the modal expansion in the case of arbitrarily shaped apertures and a standard Floquet modal expansion in free space.

A mode-matching generalized scattering matrix technique is applied to analyze a cascaded rectangular aperture-type thick FSS in [108]. The technique is used for identifying the modes that contribute to the transmission characteristics of the FSS structure, providing an accurate prediction of its performance with less computational complexity.

2.6.2 Equivalent circuit

Studies of fundamental equations have been published to determine the transmission and reflection coefficients of FSSs. In 1946, MacFarlane [109] demonstrated that the scattering problem of a parallel wire grid could be solved using a transmission line model (TLM). Marcuvitz [40] showed that FSS structures can be represented by an equivalent circuit (EC), considering the TE and TM incidence on conductive strips, which uses less computational effort compared to full-wave methods. Chen [110] and Ulrich [111] improved the EC to consider resonant effects of the structures. Reference [112] presented a refined version of Chen's and Ulrich's formulas. Furthermore, the formula was extended to approximate solutions for cascading screens and dielectric slabs. In the 80s, derivate formulas have been reported for more complex FSS geometries and achieved accurate results, as demonstrated by Langley [38], [39], [113], [114].

Marcuvitz [40] demonstrated that an FSS is modelled as an infinite array of parallel conducting strips, and it can be represented by capacitive and inductive elements. Figure 2.22a shows the EC for a TE incidence when the conducting strips are parallel to the electric field; in this configuration, the FSS is represented by an inductance. In the other case, Figure 2.22b, the conducting strips are parallel to the magnetic field, and the FSS is associated with a capacitance. The strip parameters are width w, periodicity p, spaced distance g, and incidence angles of ϕ and θ for incident plane waves, TE and TM, respectively.

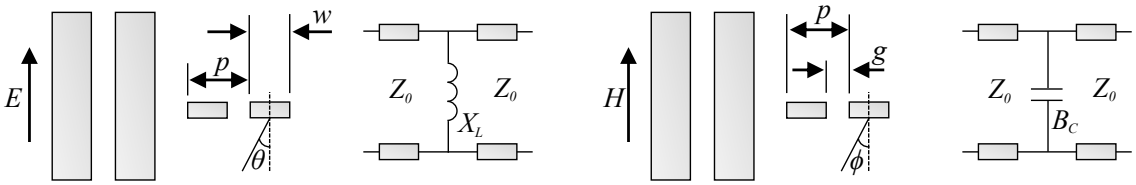

(a) TE polarization (b) TM polarization

Figure 2.22: Incidence parameters considering strip arrangement and angle, and equivalent circuit.

A complementary FSS (CFSS) is proposed in [115], which is defined as patch and slot elements of same size and shape arranged on either side of a substrate, based on Babinet's principle. An equivalent circuit method (ECM) compounded with TLM was employed to analyze the CFSS response. The method presented a good accuracy

of the scattering parameters, for normal and oblique incidence, allowing to estimate the frequency response with less error. The efficacy of the ECM results was verified with commercial software.

A wideband FSS operating in Ka-band is presented in [116]. A multi-layer structure was adopted to enhance the passband, and coupling between the capacitive and inductive surfaces was employed to miniaturize the structure to 0.26λ. The ECM was applied to give a better understanding of the structure's behavior and its frequency response.

The ECM is introduced in [117] to explain the effect of a convoluted geometry structure on the frequency response of an FSS. Measured and simulated results showed that the proposed FSS has a good stability under different polarizations and incidence angles.

An accurate analytical procedure is described in [118] for wideband nonmagnetic absorbers operating at lower microwave frequencies. An ECM was designed, based on the simulated data and synthetic asymptotes for single and double-layer FSSs. Several designs of broadband absorbers were demonstrated by employing the ECM and genetic algorithm-based optimization. Those results were compared to full-wave methods, showing more than 95% accuracy.

2.6.3 Method of moments

The Method of Moments (MoM) is a technique that models the field along the substrate and the surface currents and volumetric polarization currents along patches. The method is based on solving the electrical field integral equation. It consists in reducing a function equation into a matrix one, and then solving this matrix with other known techniques. It can be performed in the time or spectral domain. The procedure consists of solving linear equations, taking moments by multiplying with appropriate basis functions and then integrating, i.e., the method is used to solve the integral equation, reducing the number of unknown coefficients to a finite number of equations containing the same number of unknown coefficients [119]. The convergence properties are determined by the choice of basis functions used to expand the quasi-periodic form of the induced surface current [16]. Further, the Green's function is employed to account for the presence of the dielectric substrate.

Skokic and Sipus [120] present a program for analyzing spherical FSSs using the Moment Method in the spectral domain. In their model, a plane wave is impinging

on a dipole array lying in free space. The plane wave is expanded into a series of spherical harmonics while the Green's functions of the spherical structure are found using an algorithm.

An improved interpolation approach known as model-based parameter estimation is applied to the wide-band interpolation of the periodic method of moments (PMM) impedance matrices in [121]. They introduce an efficient spectral-domain PMM formulation to accelerate analysis of FSS problems with a large number of unknowns, employing a one-dimensional FFT-based method to speed up the computation of matrix-vector products within the bi-conjugate gradient. The accuracy and efficiency of the proposed techniques for large FSS problems are demonstrated by several design examples for both the normal and oblique incidence cases.

2.6.4 Finite element method

The Finite Element Method (FEM) is a numerical technique used to solve partial differential equations and has its origin in solving problems in solid-state mechanics; its concept was first introduced by Courant [122]. The method was not applied to electromagnetic problems until 1969 [123], but since then, it has been implemented for solving a wide variety of problems in all areas of engineering.

In the FEM, the domain of the problem is discretized into a finite number of small elements, and the characteristics of the continuous domain are estimated by assembling the similar properties of discretized elements per node. In this technique, the region of interest is divided into n finite surfaces or volume elements, the set of these finite elements is called mesh. The discrete elements are represented for well-defined geometry shapes, e.g., triangles for 2-D structures, and tetrahedras and prisms for 3-D ones. The FEM has similarity to the MoM, both methods do the conversion of either a differential or an integral equation into a matrix equation. The distinction between FEM and MoM is the fact that FEM is based on the physical principle of minimizing the energy of a system [124]. The analysis and modeling of an infinite periodicity is simplified by the geometrical information of a single unit cell. Figure 2.23 illustrates an example of a unit cell of an infinite periodic array discretized with triangular prismatic elements. By enforcing Floquet's theorem and radiation boundary conditions at the top and bottom of the reference unit cell, numerical modeling can be applied, where its four vertical walls are identified as Γ_{Left}, Γ_{Right}, Γ_{Front} and Γ_{Back}, assuming that Γ_{Left} and Γ_{Front} are sidewalls opposite to Γ_{Right},

Γ_{Back}, respectively.

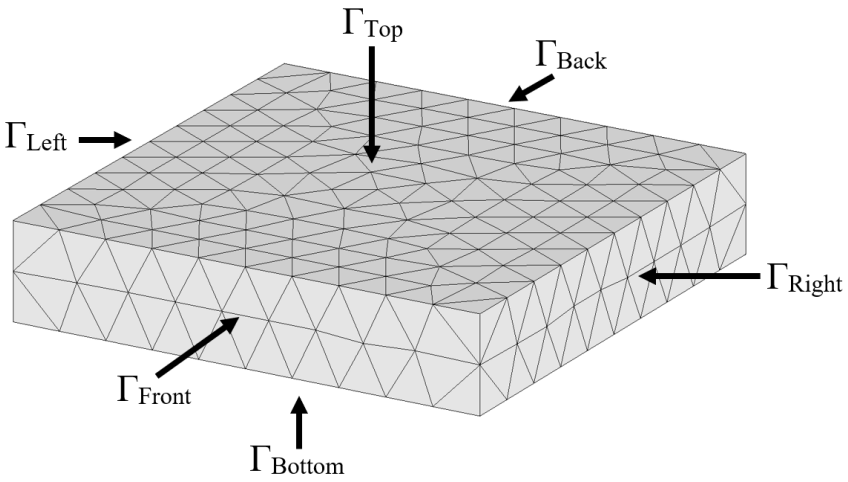

Figure 2.23: Periodic unit cell with mesh consisting of triangular prisms.

To solve some problems involving arbitrary three-dimensional periodic scatterers, hybrid techniques of FEM have been developed such as Boundary Element (FE/BE) [125] or Boundary Integral (FE/BI) [126]. A 3-D vector variational hybrid finite element boundary element method for the general nonself-adjoint infinite periodic array problem is introduced in [125]. The vector variational formulation applies and extends the variational electromagnetics methodologies from the perspective of the reaction reciprocity which exists between the direct and adjoint problem systems. The array polarization characteristics are naturally handled through the vector Floquet boundary element method procedure which also is absorbed into the stationary E-field functional. The tangential vector finite element method is used to discretize the periodic volume domain.

Eibert [126] presents a hybrid FE/BI modeling of 3-D doubly periodic structures utilizing triangular prismatic volume meshes with edge-based basis functions for the electric field intensity. The method starts from a functional description of the field problem where only a single unit cell of the array is considered. On the top and/or bottom boundary planes of the unit cell, the mesh is truncated by a boundary integral, and a periodic phase boundary condition is employed on the sidewalls of the unit cell mesh. The required space-domain periodic Green's function is calculated after applying the Ewald acceleration technique that converts the slowly converging series representation into two rapidly converging series.

2.6.5 Finite-difference time-domain method

The Finite-DifferenceTime-Domain (FDTD) method is one of the most widely used computational methods in electromagnetics. The FDTD is classified as a full-wave method and was developed by Yee [127] in 1966. FDTD is based on the discretization of Maxwell's curl equations directly in time and space, dividing the volume of interest into unit cells allowing the analysis of any type of element as well as analysis of inhomogeneous and lossy media [128]. The FDTD method solves these equations on a discrete spatial and temporal grid.

Staggered grids for the electric and magnetic fields are determined in space (Figure 2.24a), within the established computational domain, and in time (Figure 2.24b), in order to ensure a second-order accuracy. Each field component is solved at a different location within the Yee's grid cell. The material of each cell must be specified in the FDTD mesh, as well as its permeability, permittivity and conductivity. For simpler applications, the material is free space, a metal, or a dielectric. The method's output is usually the electric or magnetic field in a point or a series of points in the computational domain, obtaining these fields propagating in time [129]. It also allows the analysis of complex structures whose characteristics vary with time, such as FSSs that use semiconductor devices such as diodes. FDTD is an explicit method where the entire computational domain is discretized and there is no necessity to solve a set of linear equations. Therefore, it is mathematically less demanding and more intuitive than other numerical methods such as MoM.

Ko [130] shows a computational FDTD space with Floquet phase shift boundary condition created by exciting the space with phase-quadrature sinusoidal plane waves and extracting the phasor for Floquet phase shifting. The proposed method obviates the need of large memory storage, usually required in the FDTD approach implemented strictly in the time domain.

Reference [131] demonstrates the use of the FDTD method with periodic boundary condition to simulate the electromagnetic wave interaction with an FSS using a plasma tube as its basic element. The FDTD is combined with an auxiliary differential equation that offers a representation of the dispersion characteristics of the plasma. They use ten perfectly matched layers to truncate the front and back of the computational domain The incident, reflected, and transmitted fields of every time step are recorded and then transformed into the frequency domain to calculate the reflected and transmitted coefficients.

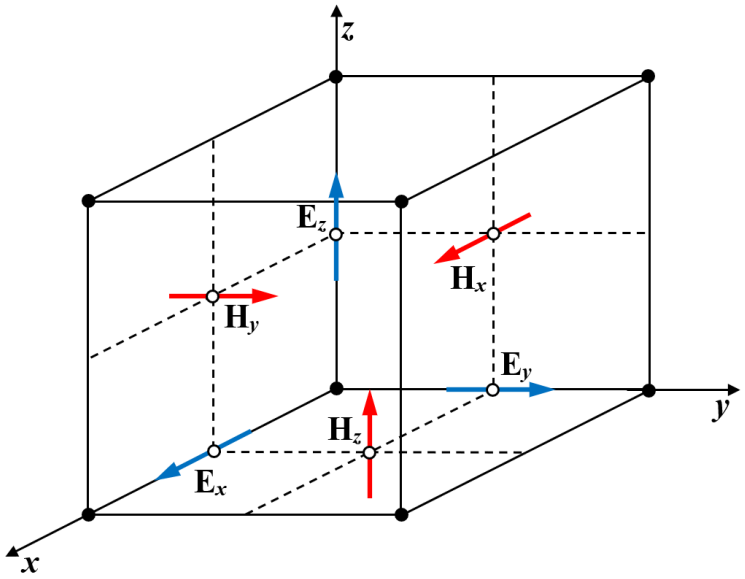

(a) Spatially discrete.

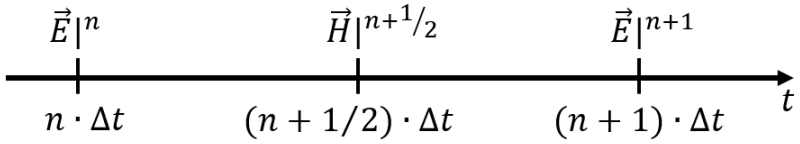

(b) Temporal increment.

Figure 2.24: Staggering of electric- and magnetic-field components of the Yee's grid cell.

2.6.6 Wave concept iterative procedure

The Wave Concept Iterative Procedure (WCIP) method was developed in late 90s and is based on the concept of electromagnetic waves to describe the boundary conditions and the field continuity on the circuit interface. This method uses a linear combination of tangential components of E- and H-fields, originated from incident waves at the interface of the analyzed structure and the reflected waves by this surface [132].

In FSSs, WCIP reduces the computation effort in the analysis, because it considers just the unit cell, which is limited by hypothetical periodic walls, characterizing the discontinued FSS interface between two media. The excitation is done using a distributed electromagnetic wave source. The formulation of this method consists of two operators that describe the incident (A_i) and scattered waves (B_i) in the spatial domain and spectral domain [133] given by Equation 2.5 and Equation 2.6. The iterative procedure is repeated until convergence is obtained as illustrated in Figure

2.25.

$$\begin{pmatrix} B_1 \\ B_2 \end{pmatrix} = \Omega \begin{pmatrix} A_1 \\ A_2 \end{pmatrix} \tag{2.5}$$

$$\begin{pmatrix} A_1 \\ A_2 \end{pmatrix} = \Gamma \begin{pmatrix} B_1 \\ B_2 \end{pmatrix} + \begin{pmatrix} A_0 \\ 0 \end{pmatrix} \tag{2.6}$$

- Ω: scattering operator defined in the spatial domain
- Γ: eflection operator defined in the spectral domain.
- A_0: incident wave source.

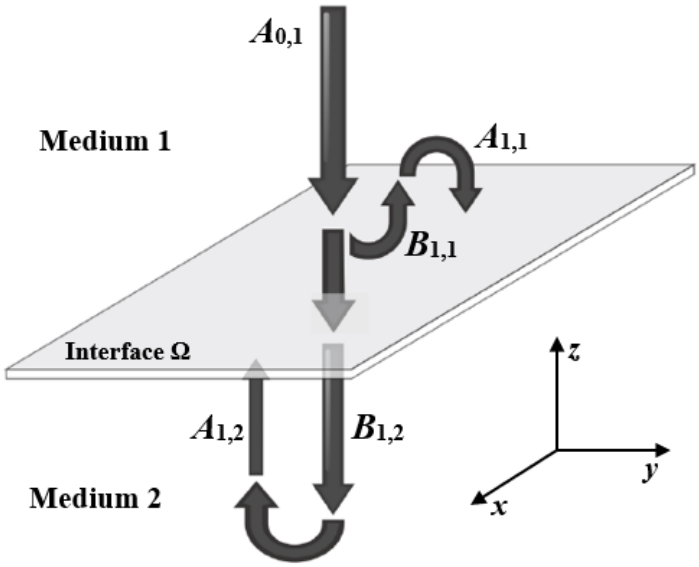

Figure 2.25: Transmitted and reflected waves iterative process.

WCIP has shown its applicability in FSS analysis, obtained reasonable results for different type of elements and topologies. Reference [134] presents the use of WCIP as a computational tool to analyze a quasi-fractal FSS. Even though the proposed geometry is a complex one, the method was able to investigate the effect on the distribution of electromagnetic fields, as well as the frequency response with a good agreement when compared to measured results.

A generalization of the wave concept iterative procedure (GWCIP) method is proposed in [135] to analyze a non-uniform FSS with finite size. The non-uniformity of the FSS is obtained by mixing different shapes of elements in the finite size FSS

structures. The results from the GWCIP show a good accuracy when compared to HFSS and measured ones.

A combination of the WCIP and scattering matrix (SM) method is described in [136] for analysis of a double-layer FSS. The WCIP-SM technique is compared to results of other methods given in the literature, for different values of the air gap spacing between the two cascaded structures, showing increased accuracy and less computational effort.

2.7 Measurement techniques

The transmission and reflection characteristics of FSSs can be measured by a few methods, which will be presented in this section. This process aims to validate the numerical results obtained from the numerical methods discussed in the previous section.

In order to measure the FSS transmissivity, the structure under test must be positioned between two directive antennas (e.g., horn antenna), where one acts as a transmitter and the other as a receiver. The antennas are placed facing each other at a fixed position, while the FSS plane can be rotated (Figure 2.26). The rotation of the FSS holder fixture with different angles θ allows measurements of oblique incidence. The electromagnetic signal transmitted from the antenna and arriving on the FSS is considered a plane wave. Therefore, the distance should be far enough to satisfy the far-field condition. Experimentally, the characterization of the TE and TM polarization of the FSS is done by changing the antenna polarization from vertical to horizontal or rotating the FSS by 90°. The data collection is done using a two-port vector network analyzer (VNA). The calibration in the transmission setup is done by removing the FSS and measuring the transmission coefficient, as the reference of the transmissivity ($|S_{21}| = 1$ or 0 dB). Then, the results of the FSS under test are normalised to the reference.

The numerical techniques assume that an FSS is an infinite doubly-periodic array. However, an FSS has finite dimensions in practice. Due to the finite size of the FSS and its distance to the antennas, diffraction at the edge of the FSS may occur. To circumvent this issue and have more accurate results, two basic increments can be employed in the setup. One of them is to use a pair of lens-corrected horn antennas (Figure 2.27a) so that the diffraction effects are minimized by the far-field focusing ability of these antennas, where the FSS is excited with a collimated beam. The

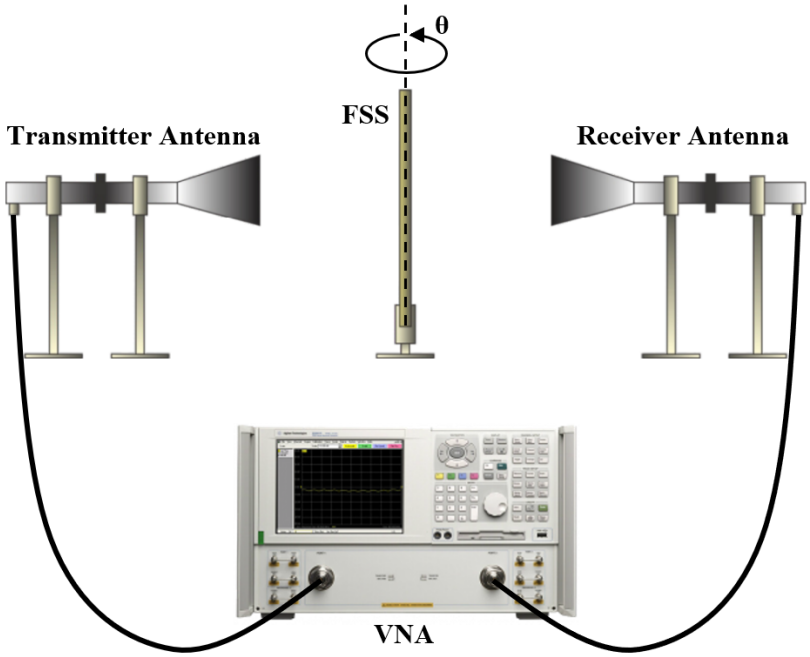

Figure 2.26: Standard FSS transmission measurement setup.

other technique to avoid spillover is using RF absorbing materials surrounding the FSS (Figure 2.27b).

Another method with precise results is performing measurements in an anechoic chamber, which is a confined environment with pyramid radiation-absorbent material all around to minimize reflections, as shown in Figure 2.28.

A method that emulates an infinite FSS in a free-space environment is equivalent to performing the measurement in a waveguide. In this procedure, the FSS under test must have the appropriate size to fit within the waveguide flanges, eliminating the effects of undesired diffractions (Figure 2.29a). Via holes are used on the perimeter of the FSS where the waveguide flanges meet to ensure the flow of the longitudinal conduction current on the waveguide walls (Figure 2.29b). This method is frequency-dependent, as the wave-number of the propagating wave inside the waveguide changes with frequency. Thus, the incidence angle of the wave that arrives at the FSS changes as the frequency varies, making it more suitable for single-frequency testing, as well as being limited to TE modes for the excitations.

To measure the reflectivity of the FSS, the transmitter and receiver antennas are positioned at the same side in relation to the FSS, as illustrated in Figure 2.30. An absorber screen is placed between the two antennas to eliminate their direct coupling. The calibration in this setup is performed by first measuring the reflection coefficient

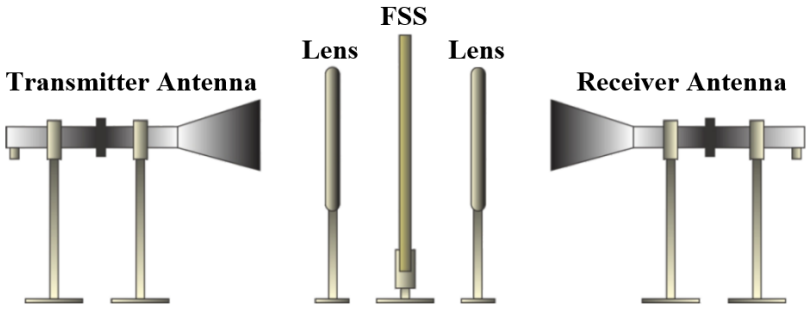

(a) Using lens-corrected horn antennas.

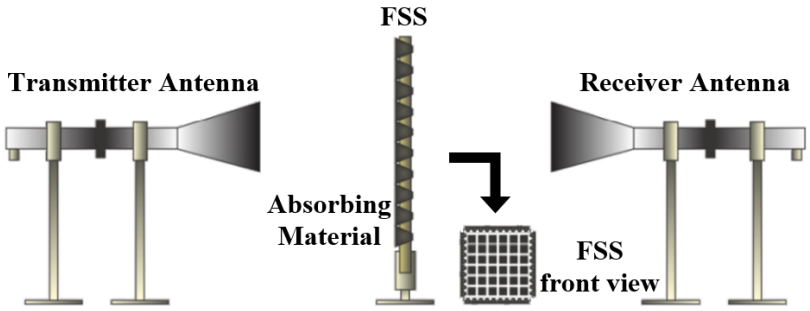

(b) Measurement window with absorbing materials.

Figure 2.27: FSS transmission measurement setup to avoid diffraction.

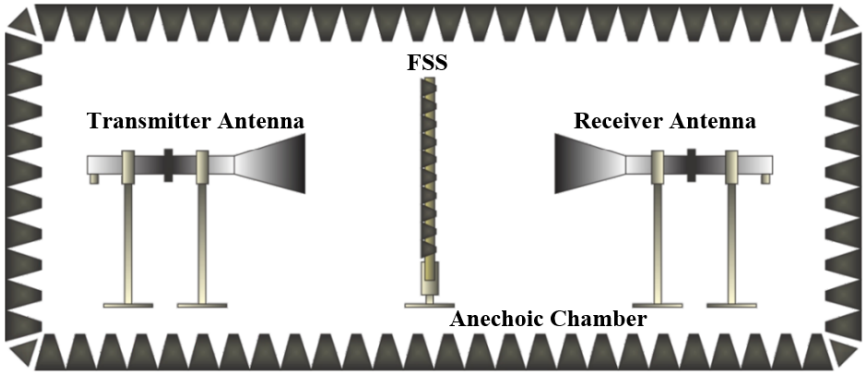

Figure 2.28: FSS transmission measurement setup in the anechoic chamber.

of plane metal screen (placed instead of the FSS) as the reference for 100% reflection ($|S_{11}| = 1$ or 0 dB). With the FSS under test, its reflection coefficient is normalised to the reference.

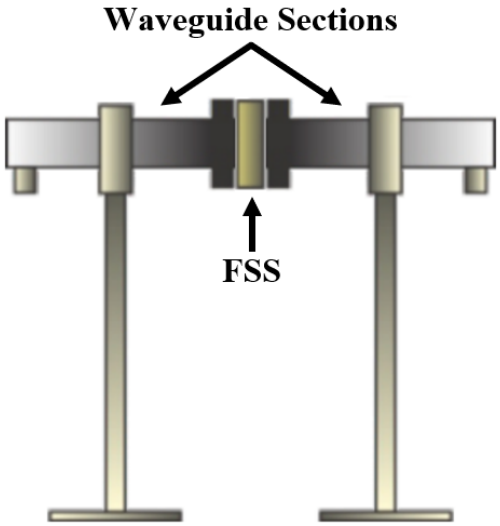

(a) Waveguide measurement setup.

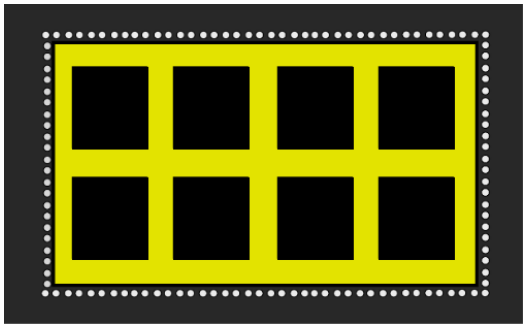

(b) FSS surround by via holes.

Figure 2.29: FSS measurement setup in waveguide environment.

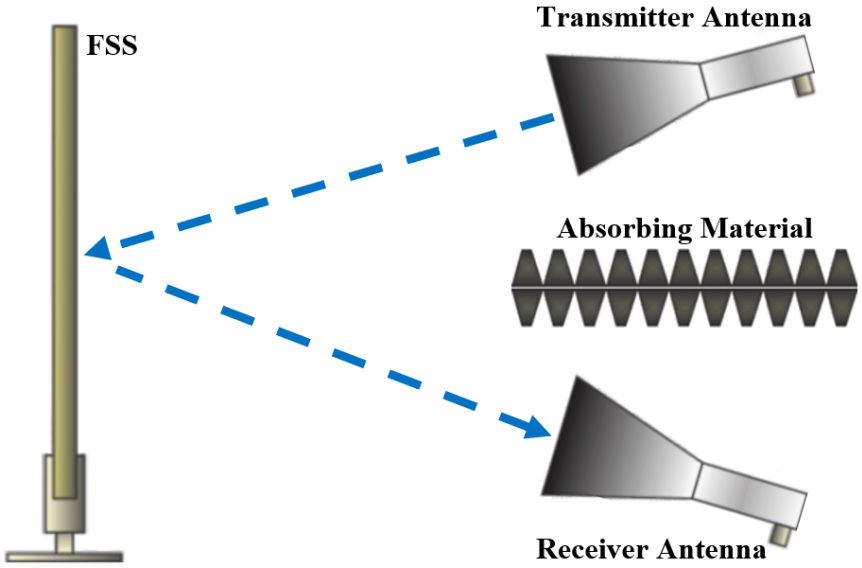

Figure 2.30: FSS reflection measurement setup.

Chapter 3

Linear-to-Circular Polarization Converter FSS

This chapter describes the design process of a single-layer FSS that acts as a polarization converter of a linear wave to circular one, operating at 5.2 GHz for 5G applications. The simulated and experimental performance of the proposed FSS converter is presented and its analyses are based on the magnitude and phase of the transmission coefficient of the electric field components.

This chapter contains material extracted from the following publication:

D. F. Mamedes, J. Bornemann and A. G. Neto, "Linear-to-Circular Polarization Converter Based on Four-Arms Star FSS at 5.2 GHz for 5G Applications," 16th European Conference on Antennas and Propagation (EuCAP), Madrid, Spain, 2022, pp. 1-4, doi: 10.23919/EuCAP53622.2022.9768954.

3.1 Introduction

In communication systems, the use of circular polarization (CP) circuitries has been demonstrated as a viable solution to overcome some disruptions such as susceptibility to multi-path fading, and ability to mitigate polarization mismatch [137], [138]. The conversion of linear polarization (LP) to CP has attracted the interest of engineers, and its principle consists of the use of two orthogonal linearly polarized field components with equal amplitude and 90° phase difference. To achieve the conversion to CP, different structures have been reported such as Fabry-Perot cavities [139], meander-line [140], [141] and SIW circuits [142], etc.

FSS converters offer low-profile and easy fabrication, making them favorable among periodic structures. The geometries among the types of FSS converter are mainly based on cross-dipole [143] or ring shapes [144], and also on cascaded structures [145], [146]. However, these geometries are simple to design and they offer maximum 3-dB axial ratio (AR) bandwidth of ∼10%.

In the following few paragraphs, a few published works on polarization converters based on FSS are described, highlighting the complexity of their designs and results. Reference [147] presents a polarization converter based on the multi-layer FSS operating in X-band, with center frequency at 10 GHz. The structure consists of four dielectric substrate layers, three square patch layers, and two grid line layers (Figure 3.1). The operational frequency and bandwidth are determined by the design of the square patches and grid lines. The phase difference is obtained by truncating the corners of the square patches. A fractional axial ratio bandwidth of 15% for circular polarization is obtained at the center frequency.

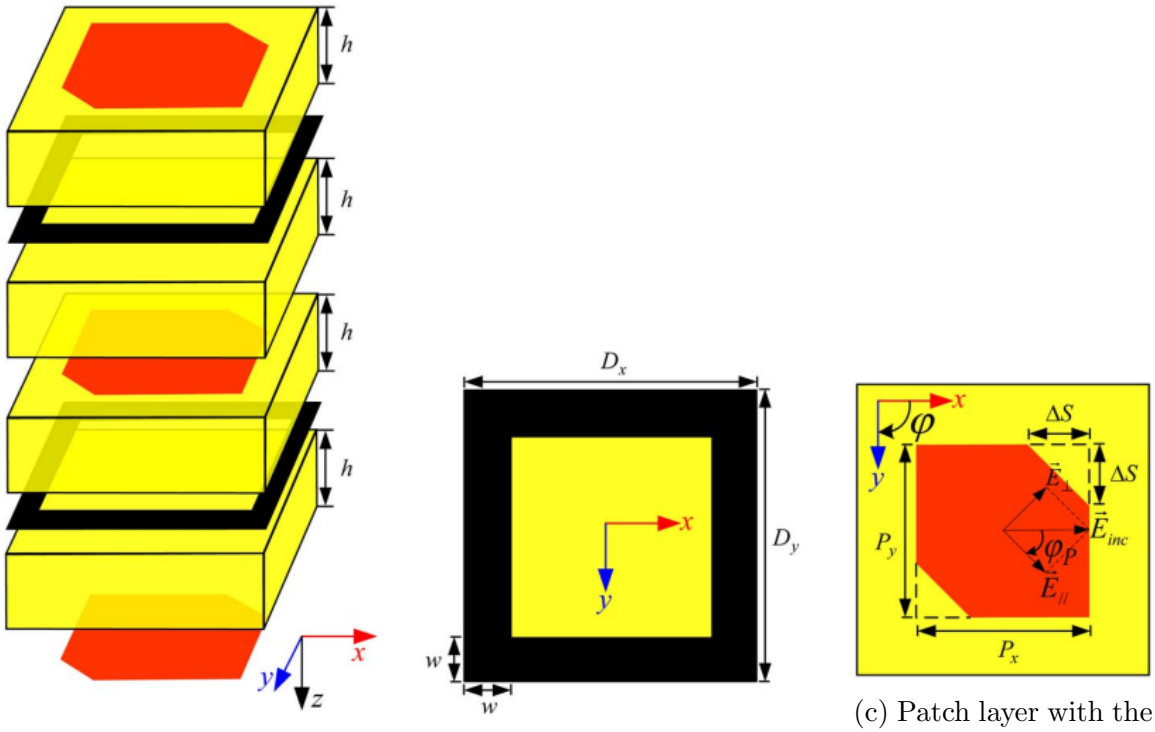

(a) Expanded and side views.

(b) Grid line layer.

(c) Patch layer with the truncated corners.

Figure 3.1: 5-layered polarization-converter FSS proposed in [147].

A broadband polarization converter is proposed in [148], with axial ratio bandwidth reaching 74% at normal incidence. The design consists of a multi-layer FSS

formed by four metallic layers as shown in Figure 3.2. Two of these layers have their element arrays composed of cross-shaped geometry, and the others use metal strips. The metal strip in the y-direction and the metal-free in the x-direction provide different transmission characteristics to the two orthogonal electric field vectors, producing a certain phase difference through each layer. The results show that the proposed FSS covers the band from 5.75 GHz to 11.2 GHz.

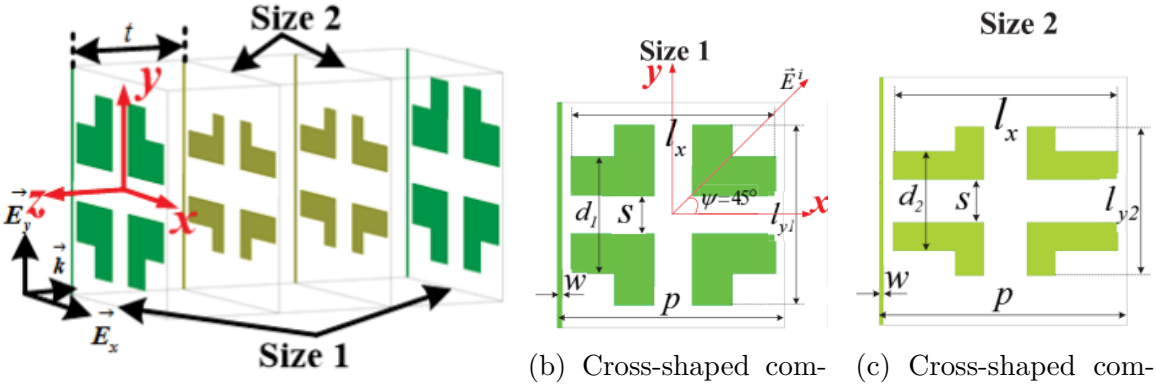

(a) Expanded and side views.

(b) Cross-shaped composite, size 1.

(c) Cross-shaped composite, size 2.

Figure 3.2: 4-layered polarization-converter FSS proposed in [148].

A 10-GHz FSS polarizer loaded with complementary split ring resonator (CSRR) for non-planar and conformal applications is presented in [149] (Figure 3.3). The structure is fabricated on liquid crystal polymer substrate material, which offers good mechanical flexibility, with double-metallic layers. The CSRR elements are aligned in the vertical direction without any displacement. A substrate integrated waveguide cavity is used to enhance the Q-factor. The results show that this structure presents minimum transmission loss for TE-polarization incidence wave of 0.75dB at the 10.24 GHz and 19.05 dB for TM-polarization incidence wave, with an extinction ratio of 18.3dB.

The motivation of this work is to investigate the design procedure of a polarization converter, to operate at 5.2 GHz for 5G applications, using a single-layer FSS based on the four-arms star geometry, including the theoretical calculation of the AR that shows a 3-dB bandwidth of 29% for the desired frequency.

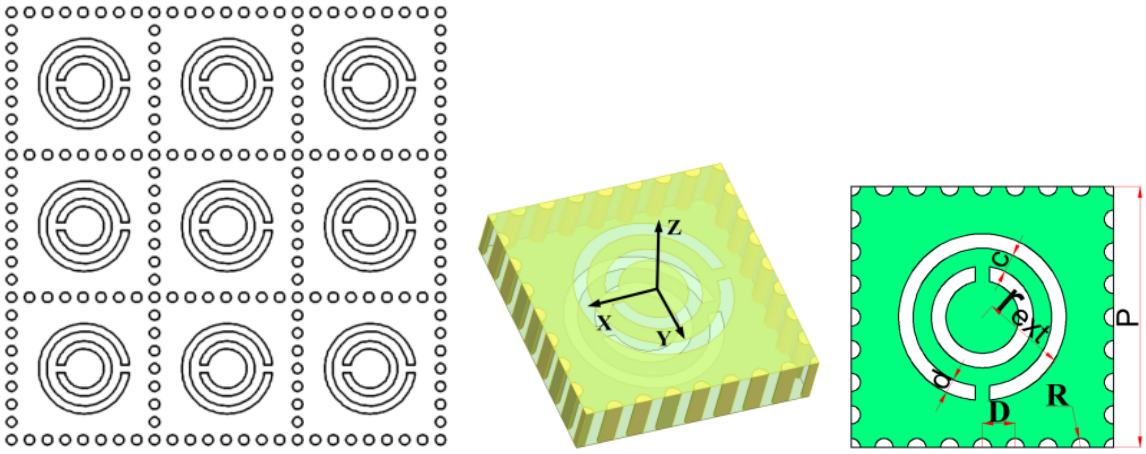

(a) Array. (b) Side view. (c) Unit cell element.

Figure 3.3: 2-layered polarization-converter FSS proposed in [149].

3.2 FSS polarization converter design

3.2.1 Topology structure

The FSS polarization converter proposed in this work is based on the four-arms star geometry with a gap, which has previously shown very interesting characteristics such as miniaturisation and switch applications [150], [151]. The following steps are performed to achieve the four-arms star geometry: the unit cell dimension is defined as p_p, and then a rectangular patch is designed as a_p, where the arms are shaped. From the edges, lines cross the rectangular patch with b_p are drawn, and the star geometry is achieved with pointed arms. A small square patch of width s_p is etched at the center to connect all four arms. Finally, the outside of the element is detached from the metallic surface, and the four-arms star unit cell is completed. Figure 3.4 illustrates the unit cell with this element, including its parameters, without the gap. In this case, the element is completely symmetric with respect to x- and y-directions.

The design process to determine the first resonance frequency for the symmetrical four-arms star FSS can be carried out using the following equations. The size of the arms defines the resonance frequency according to

$$f(\text{GHz}) = \frac{0.3}{2a_p\sqrt{\epsilon_{r_{\text{eff}}}}} \tag{3.1}$$

Reference [152] presents an interpolating formula that fits the variation of the effective permittivity

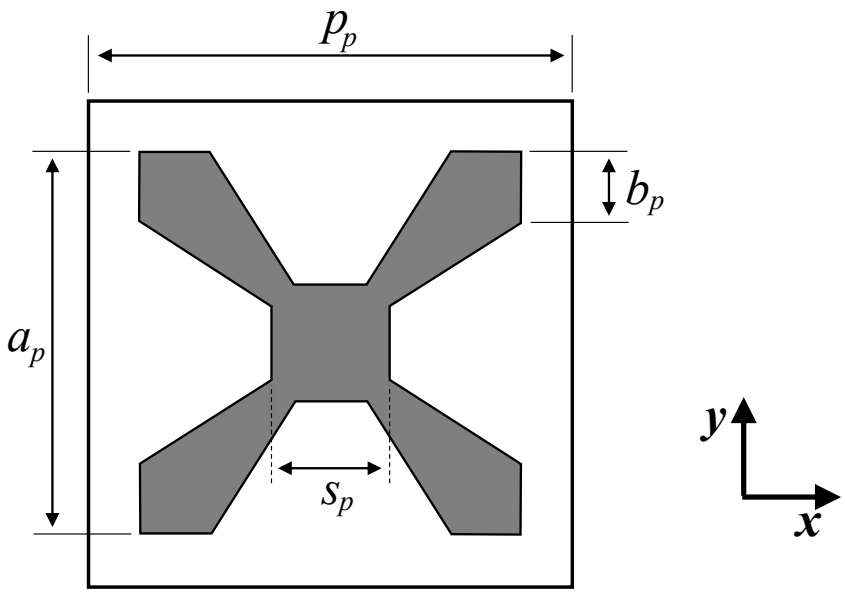

Figure 3.4: Geometry and parameters of the four-arms star FSS unit cell.

$$\epsilon_{r_{\text{eff}}} = \epsilon_r + (\epsilon_r - 1)\left[\frac{-1}{e^{\frac{10h}{p_p}M}}\right] \tag{3.2}$$

which considers the dielectric permittivity ϵ_r and thickness h of the substrate, periodicity p_p, and the exponential factor, M, of the unit cell filling, which takes into account the slope of the curve that depends on the unit cell filling. The procedure to determine the exponential factor is described in [152], and it is applied for all elements used in this dissertation. For the geometry proposed, the value of M is 1.9.

To form different polarization states, a perturbation (gap) is added to the original geometry in the vertical orientation. The unit cell of the proposed FSS with the new parameter added is illustrated in Figure 3.5. The gap g provides an asymmetric element, where the upper and lower arms are physically disconnected. The size of the gap is properly adjusted for the phase difference.

Consider that the E-field arrives at the unit cell as shown in Figure 3.5. In this scenario, the horizontal E-field sees that the arms are electrically connected for the TM polarization, and Equation (3.1) can be applied to estimate the first resonance, $f = f_{\text{TM}}$. For the TE polarization, the vertical E-field is maximum in the center of the unit cell, seeing the perturbation. In this case, the arms are physically and electronically disconnected, and the gap is seen now as an additional capacitance to the circuit, making its resonance frequency appear as [151]

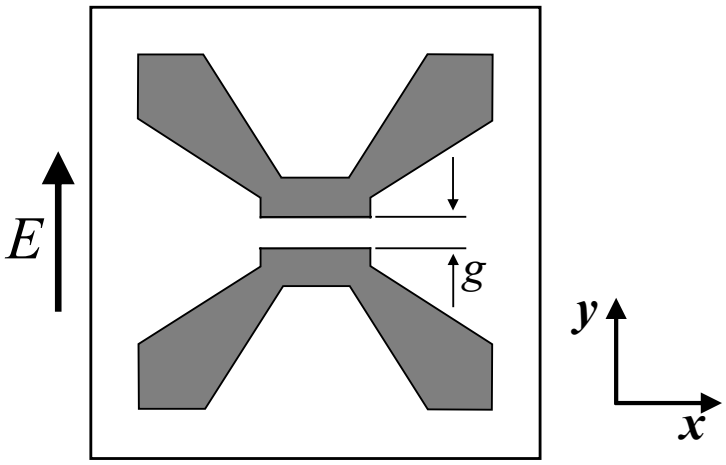

Figure 3.5: Proposed four-arms star with a gap FSS polarization converter unit cell.

$$f_{\mathrm{TE}}(\mathrm{GHz}) = 1.8 f_{\mathrm{TM}} \tag{3.3}$$

Note that the factor of 1.8 in Equation (3.3) is an approximation based on the gap of 1 mm used in this design. Other gap widths will lead to different factors.

3.2.2 Principle of operation

Linearly polarized incident wave

The condition for the outgoing circularly polarized wave is that an incident electric field, E_i, oriented at 45° with two decomposed vector components of same magnitude, i.e. $E_{i,x}$ (horizontal) and $E_{i,y}$ (vertical), experience a 90° phase difference ($\Delta\phi = 90°$) while propagating through the converter, as shown in Figure 3.6. The incident electrical field can be written as

$$E_i = E_{i,x} + E_{i,y} = E_0(\hat{e}_x + \hat{e}_y)e^{-jkz} \tag{3.4}$$

where E_0 is the magnitude of the incident electric field. $\hat{e}_x$ and $\hat{e}_y$ are the unit vectors in the x- and y-directions, respectively. k is the wavenumber in free space, and $j = \sqrt{-1}$.

The components of the transmitted wave ($E_{t,x}$, $E_{t,y}$) can be expressed by Equation (3.5).

$$\begin{pmatrix} E_{t,x} \\ E_{t,y} \end{pmatrix} = \begin{pmatrix} T_x E_{i,x} & T_{xy} E_{i,x} \\ T_y E_{i,y} & T_{yx} E_{i,y} \end{pmatrix} \begin{pmatrix} F(\theta)_{\theta=0^\circ,180^\circ} & F(\theta)_{\theta=90^\circ} \\ F(\theta)_{\theta=90^\circ} & F(\theta)_{\theta=0^\circ,180^\circ} \end{pmatrix} \tag{3.5}$$

The function $F(\theta)$ describes the distinct properties of the FSS polarization converter for vertical and horizontal component incidence:

$$F(\theta) = \begin{cases} 1, & \theta = 0^\circ, 180^\circ \\ 0, & \theta = \pm 90^\circ \end{cases} \tag{3.6}$$

If the mutual coupling between the two polarizations is considered negligible [153] (i.e., $T_{xy} = 0$ and $T_{yx} = 0$), the two orthogonal linearly polarized components can be summarized as:

$$E_{t,x} = T_x E_{i,x} \tag{3.7}$$

$$E_{t,y} = T_y E_{i,y} \tag{3.8}$$

where $T_x = |T_x| e^{j\phi_x}$ and $T_y = |T_y| e^{j\phi_y}$ are the transmission coefficients of the device for the x- and y-polarization, respectively. $|T_x|$ and $|T_y|$ are their transmission magnitudes. ϕ_x and ϕ_y are their phase shifts.

The phase difference $\Delta\phi$ is associated with the size of the gap g. It can be expressed as

$$\Delta\phi = \phi_y - \phi_x \tag{3.9}$$

To categorize the outgoing wave at the output of the converter as left-handed circular polarization (LHCP) or right-handed circular polarization (RHCP), the superposition of the TE and TM components is analyzed. If the transmission of the TM component occurs with 90° phase ahead of the TE component, the wave will be LHCP. The opposite happens when the TE component is transmitted 90° in advance of the TM component, then the wave will be RHCP.

Circularly polarized incident wave

The conversion mechanism of the proposed structure is reciprocal, which means the incident CP waves, either LHCP or RHCP, can be converted into LP waves. The following equations explain this principle. The incident electrical field of the CP

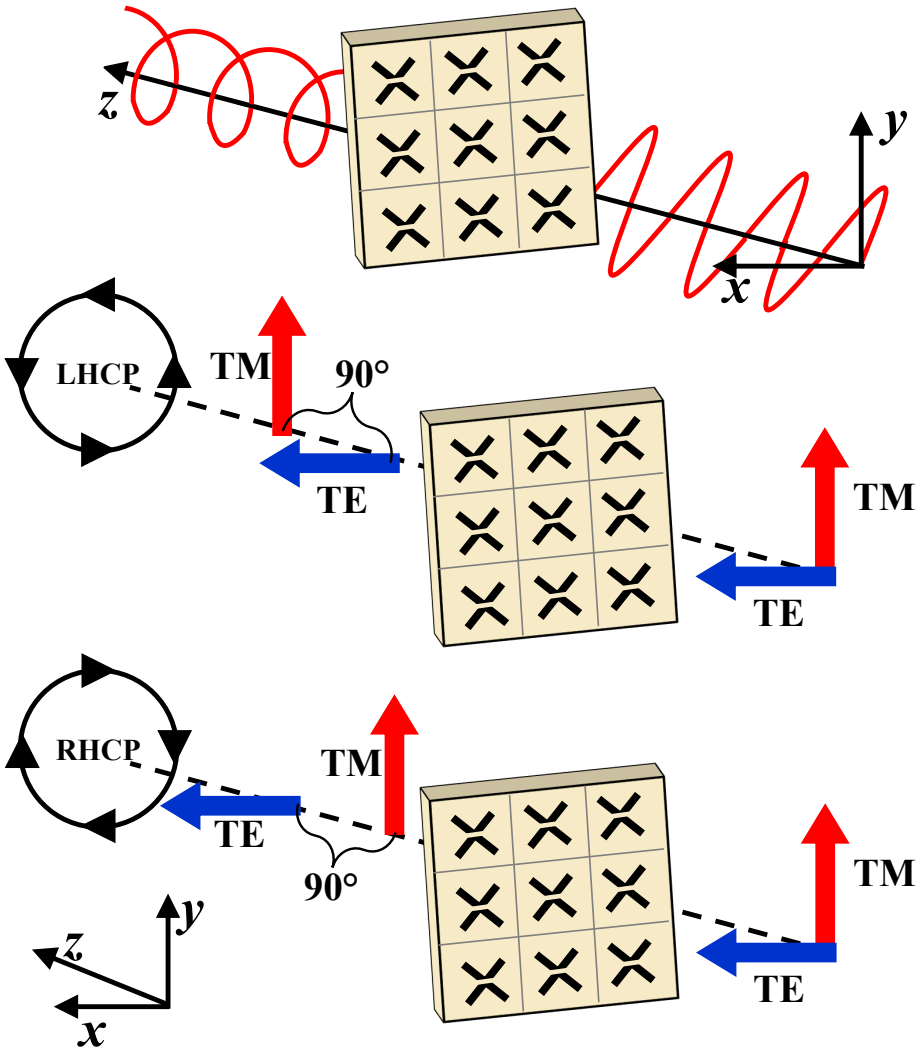

Figure 3.6: Operation principle of the linear-to-circular polarization converter.

wave, E_{iC}, can be written as

$$E_{iC} = E_{i,xC} + E_{i,yC} = E_{0C}(e^{j\phi_{xC}}\hat{e}_x + e^{j\phi_{yC}}\hat{e}_y)e^{-jkz} \tag{3.10}$$

where $E_{i,xC}$ and $E_{i,yC}$ are the horizontal and vertical E-field components of the CP incident wave, respectively. E_{0C} is the magnitude of the incident electric field. ϕ_x and ϕ_y are the phases of each E-field component. The other term in Equation (3.10) are the same as those in Equation (3.4).

The transmitted wave through the FSS converter can be expressed as

$$E_{tC} = E_{t,xC} + E_{t,yC} = T_x E_{i,xC} + T_y E_{i,yC} = E_{0C}(|T_x| e^{j(\phi_{xC}+\phi_x)} \hat{e}_x + |T_y| e^{j(\phi_{yC}+\phi_y)} \hat{e}_y) e^{-jkz} \tag{3.11}$$

where $E_{t,xC}$ and $E_{t,yC}$ are the transmitted horizontal and vertical E-field components of the CP incident waves. $T_x = |T_x| e^{j\phi_{xC}}$ and $T_y = |T_y| e^{j\phi_{yC}}$ are the transmission coefficients for the x- and y-polarization, respectively. ϕ_{xC} and ϕ_{yC} are their phase shifts.

The phase difference between two orthogonal linear components for the CP incident wave can be expressed as

$$\Delta\phi_C = \phi_{yC} + \phi_y - \phi_{xC} - \phi_x \tag{3.12}$$

The LHCP and RHCP can be converted at the output of the proposed FSS converter into LP waves. The proposed FSS polarization converter provides $\phi_y - \phi_x = 90°$ at the operating frequency. The RHCP can be converted into vertical polarization when the $\phi_{yC} - \phi_{xC} = 90°$, which gives the phase difference of the transmitted wave $\Delta\phi_C = 180°$. Similarly, the LHCP incident wave can be converted into horizontal polarization when $\Delta\phi_C = 0°$ for $\phi_{yC} - \phi_{xC} = -90°$.

3.3 Performance validation

In this section, a full-wave simulation is performed, using the commercial software package ANSYS HFSS [154], to verify the design and principle of operation of the proposed FSS polarization converter. The FSS was designed on a low-cost FR-4 fiber-glass dielectric substrate with $\epsilon_r = 4.4$, $h = 0.762$ mm and loss tangent ($\tan\delta$) of 0.025. Using the equations presented in the Section 3.2, and adjusting the size of the gap to obtain $|T_x| = |T_y|$ and $\Delta\phi = \pm 90°$, the dimensions of the structure are $p_p = 30$ mm, $a_p = 26$ mm, $b_p = s_p = 6$ mm, and $g = 1$ mm. The FSS was manufactured to validate the numerical results by experimental characterization.

The fabrication process of this and all FSS structures presented in this dissertation used the wet chemical etching technique. This process consists of first applying an etch-resistant material, to protect the area of the conductive layer where the FSS pattern will remain after etching. Then, a chemical solution is used to dissolve exposed areas of conductive layers, leaving the desired element pattern.

The prototype of the proposed FSS in this chapter was fabricated with 7 × 7 elements and overall dimensions of 21 cm × 21 cm, as shown in Figure 3.7 with an additional enlargement of the unit cell. The experimental characterizations were performed as described in Appendix A, Section A.2.2. The measurement environment for all structures designed to operate in the sub-6GHz range in this dissertation is in the antennas and microwave laboratory of the Federal Institute of Paraiba, while the FSSs in the mm-wave spectrum were measured in an anechoic chamber at the University of Victoria.

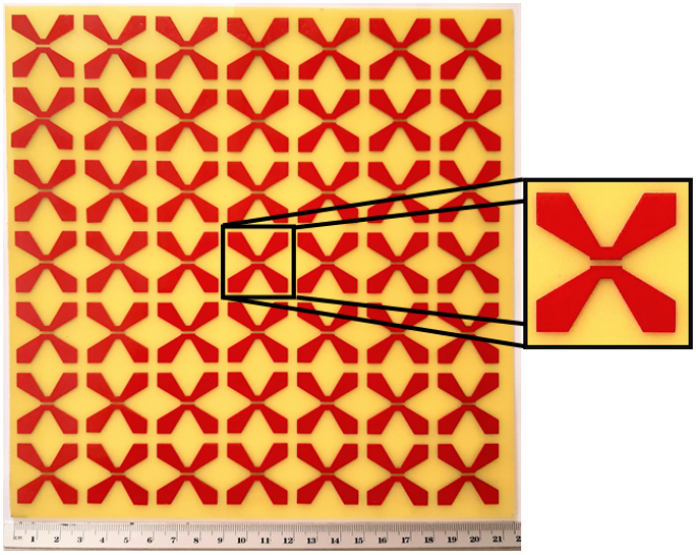

Figure 3.7: Fabricated FSS polarizer and individual cell.

3.3.1 Polarization converter results

The four-arms star geometry with a gap is polarization dependent and its results for the transmission coefficient are presented in this section. From Equation (3.1), the proposed FSS was designed for 3.8 GHz for the TM polarization and, with the additional gap in the center, the resonance frequency for the TE polarization is 6.84 GHz, according to Equation (3.3). Figure 3.8 shows the simulated transmission coefficient along with measured results, considering normal wave incidence to the FSS and FSS' rotating angle $\phi_{xy} = 0°$. The measured resonance frequencies are $f_{TM} = 3.83$ GHz and $f_{TE} = 6.97$ GHz, demonstrating a good agreement with those obtained numerically ($f_{TM} = 3.82$ GHz and $f_{TE} = 7.14$ GHz), with a maximum difference of 0.26 % and 2.38 %, respectively. To achieve circular polarization, one of the conditions is that the

magnitude of TE and TM modes must be identical at the operating frequency. Note that the magnitudes of TE and TM modes are nearly equal at 5.2 GHz with -3-dB transmission. Note that the FSS measurement results for this and following chapters of this dissertation present ripples. The results exhibiting ripples are expected due to a few factors such as the size of the FSS panel, reflections in the test environment and interference effects within the FSS structure from small deviations in the fabrication process.

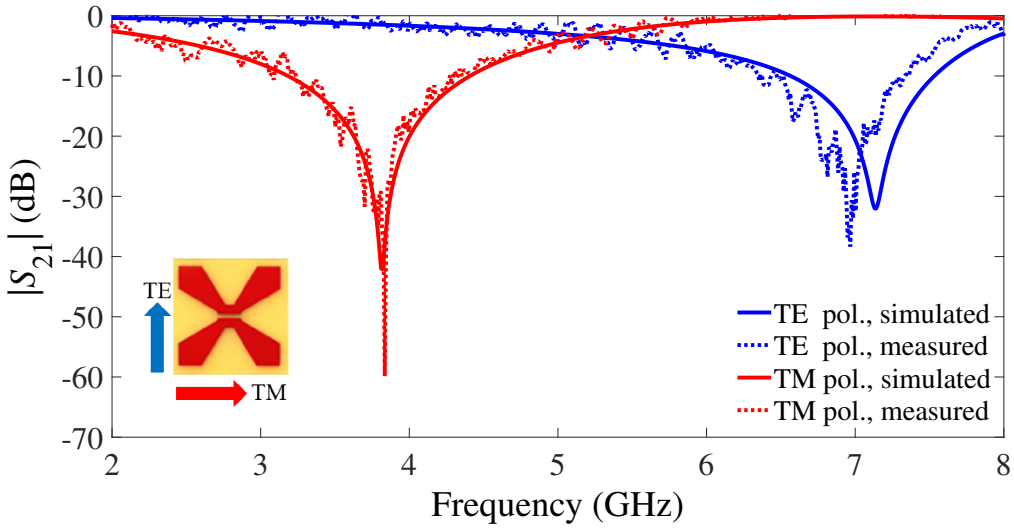

Figure 3.8: Simulated and measured results for the magnitude of the transmission coefficient of the orthogonal components of the E-field.

The gap separating the top arms of the FSS from its bottom ones produces a capacitive effect, which makes the TM mode lead the TE mode with a phase difference between them. The other condition for circular polarization to occur is that after the incoming wave passes through the converter, the phase difference between the two E-field component must be 90° (or odd multiples of it). Figure 3.9 presents the simulated and measured phase transmission coefficients of the two orthogonal field components for the proposed FSS. The results show a phase difference of nearly 90° between the TE and TM modes, indicating that circular polarization appears at 5.2 GHz.

The proposed FSS polarization converter efficiency was confirmed through simulated and measured results. For this case, the FSS is rotated by 45° as shown in Figure A.4b. The co- (vertical) and cross-polarization (horizontal) responses of the FSS are illustrated in Figure 3.10. An attenuation of 6 dB is observed at 5.2 GHz

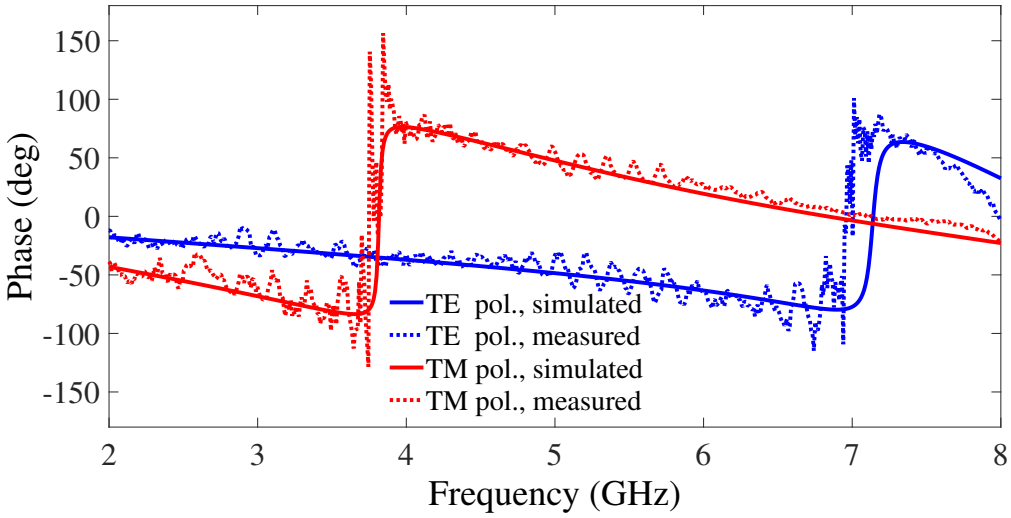

Figure 3.9: Simulated and measured results for the phases of the transmission coefficients of the orthogonal components of the E-field.

which includes the 3-dB verified in Figure 3.8. Note that the power of the incoming vertical polarization divides along the TE (+45°) and TM (-45°) polarizations. That is confirmed by nearly the same co- and cross-polarization measurements of 6-dB attenuation. The results obtained experimentally follow the curves of the numerical ones in reasonable agreement.

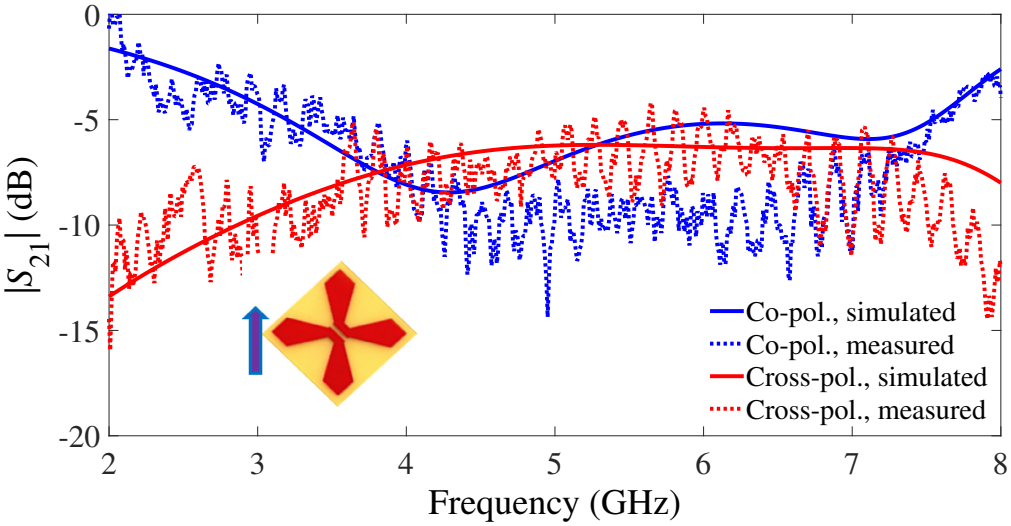

Figure 3.10: Simulated and measured results of the co- (vertical) and cross-polarized (horizontal) components.

The axial ratio (AR) can be calculated using Equation (3.13)-(3.15) [155]. The simulated and measured results of the 3-dB AR bandwidth are presented in Figure 3.11. The minimum AR occurs at 5.22 GHz (0.19 dB) and 5.21 GHz (0.02 dB) for the numerical and measured results, respectively. The bandwidth for AR $<$ 3 dB is 1.6 GHz (experimentally) and 1.56 GHz (numerically), with a maximum difference of 2.46%.

$$AR = \frac{OA}{OB} \tag{3.13}$$

where major axis (OA) of the polarization ellipse is

$$OA = \sqrt{\frac{1}{2}\left[E_x^2 + E_y^2 + \sqrt{E_x^4 + E_y^4 + 2E_x^2E_y^2\cos\left(2\Delta\phi\right)}\right]} \tag{3.14}$$

and minor axis

$$OB = \sqrt{\frac{1}{2}\left[E_x^2 + E_y^2 - \sqrt{E_x^4 + E_y^4 + 2E_x^2E_y^2\cos\left(2\Delta\phi\right)}\right]} \tag{3.15}$$

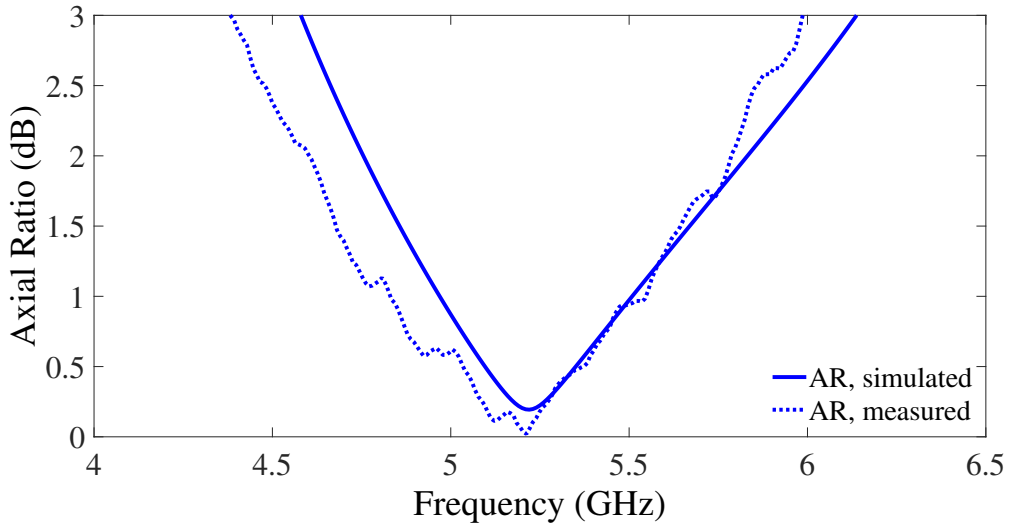

Figure 3.11: Simulated and measured axial ratio of the proposed polarizer.

3.3.2 Performance assessment

Table 3.1 compares the proposed FSS converter with previous works available in the literature in terms of number of metal layers, 3-dB AR bandwidth and electrical size.

The proposed FSS polarization converter demonstrates a good performance; when compared to other converters, it proposes a geometry that can be easily designed, it just uses a single metalized substrate, and it presents wide AR bandwidth. Both RHCP or LHCP can be achieved by rotating the direction of the FSS by 90°.

Reference	Frequency (GHz)	Number of layers	3-dB AR bandwidth	Dimensions of unit cell
[147]	10	5	15%	$0.33\lambda_0 \times 0.33\lambda_0$
[148]	9	4	74%	$0.45\lambda_0 \times 0.45\lambda_0$
[149]	10	2	–	$0.24\lambda_0 \times 0.24\lambda_0$
This work	5.2	1	29%	$0.52\lambda_0 \times 0.52\lambda_0$

Table 3.1: Comparison between the designed polarization converter and previous works.

Chapter 4

Using an Equivalent-Circuit Model to Design Ultra-Wide Band-Stop FSS for 5G mm-Wave Applications

In this chapter a system of two frequency-selective surfaces (FSSs) with an ultra-wide band-stop response for 5G millimeter-wave applications is proposed. The analyses are based on the equivalent circuit method, which predicts the transmission characteristics for a plane wave with normal and oblique incidence, and the scattering matrix technique, which provides the result of the cascaded structure. The geometries used in the single-layer FSSs are simple to design, and a series of basic equations are described in order to calculate the inductance and capacitance of conducting strips. FSSs prototypes are fabricated and measured in an anechoic chamber. The first FSS is shaped with the four-arms star geometry, which has a resonance frequency at 27.92 GHz for both measured and simulated results. The second FSS is based on the quasi-square geometry, whose resonance frequencies for the experimental and numerical results are 35.68 GHz and 35.76 GHz, respectively, for the transverse electric polarization. These two single-layer FSSs present theoretical resonance frequencies at 28 GHz (FSS #1) and 35.8 GHz (FSS #2). Cascading the two FSSs is realized by using an air gap whose effect is analyzed. A gap space in the order of about $\lambda/4$ matches with the predicted resonance frequency of the individual structures. The proposed structure demonstrates that a single Fano resonance (FR) is excited when the symmetry of the overall cascaded element is broken at an incidence of $\theta \geq 20^{\circ}$ in the TE polarization. Numerical and measured results show excellent agreement with a maximum error of

1.03%. All measured results closely follow those of simulated ones, thus validating the design approach and applications.

This chapter contains material extracted from the following publications:

D. F. Mamedes and J. Bornemann, "Using an Equivalent-Circuit Model to Design Ultra-Wide Band-Stop Frequency-Selective Surface for 5G mm-Wave Applications," in IEEE Open Journal of Antennas and Propagation, vol. 3, pp. 948-957, 2022, doi: 10.1109/OJAP.2022.3198290.

D. F. Mamedes and J. Bornemann, "Polarization-selective Fano resonance in cascaded frequency-selective surfaces," Proc. URSI Int. Symp. Electromagn. Theory, pp. 1-4, Vancouver, Canada, 2023 (invited paper).

4.1 Introduction

Single-layer FSS structures behave as a first-order filter with narrow pass-band or stop-band response [156], as explained in Chapter 2, Section 2.3.1. Although this type of FSS is easy to design and synthesize, it is very difficult to improve the bandwidth. With the new generation, wideband antennas have experienced a boost to meet their requirements, and the need for FSSs to operate over a wide range of frequencies to enhance the performance of wideband antenna systems has increased [157], [158]. In order to address this limitation, researchers have proposed the design of FSS with multiple layers as an alternative to achieve higher order filter performance, which provides a multiband or broadband response [159]. The single-layer structures are cascaded with dielectric slabs, with or without air gap in between, spacing them at approximately one quarter of the guided wavelength [160], [161].

A second-order pass-band FSS with wide out-of-band rejection from 1 to 40 GHz is presented in [162] (Figure 4.1) where an equivalent circuit model was established. The FSS provides a pass-band response operating at 10 GHz with 12% fractional bandwidth.

A new technique with a low-profile FSS with third-order band-pass responses was proposed in [159]. The structure is composed by cascading three metal layers, separated by two thin dielectric substrates (Figure 4.2). Each layer is a 2-D periodic structure with sub-wavelength unit cell size. The unit cell of this structure is composed of a combination of resonant and non-resonant elements. The structure operates with center frequency at 4 GHz and fractional bandwidth of 20%.

A three-layer FSS is described in [163] with an ultra-wideband stop-band response.

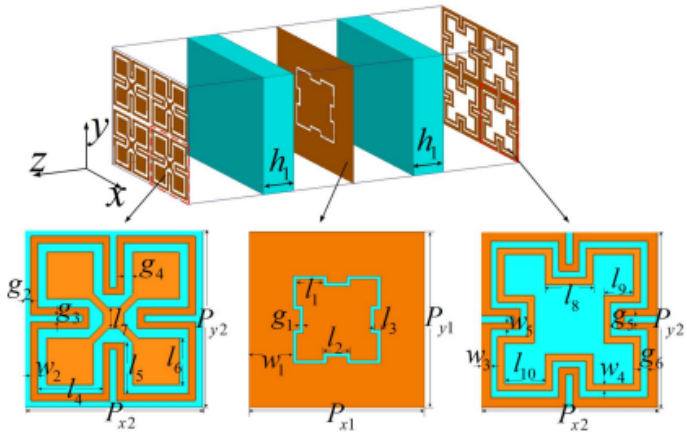

Figure 4.1: 3-D view of 3-layered pass-band FSS with wide-of-band rejection, and top view of unit cell proposed in [162].

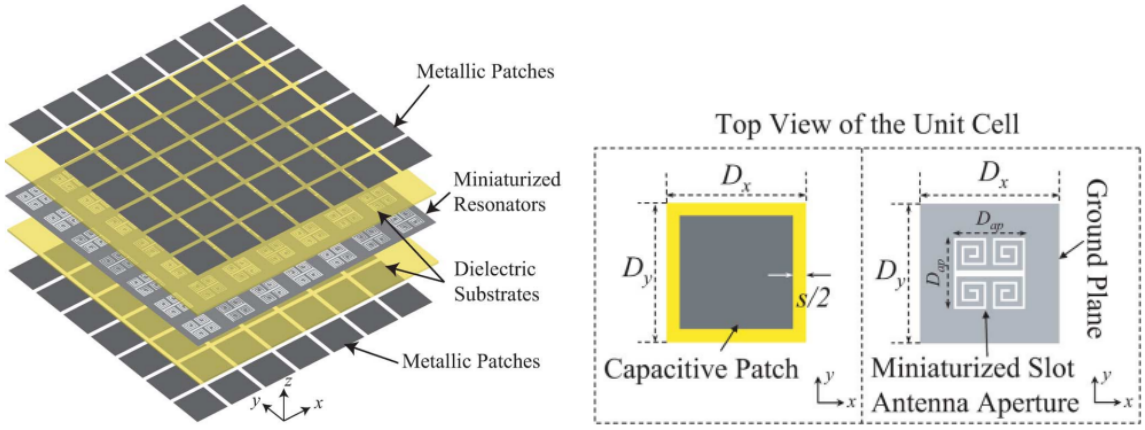

(a) Expanded and side views.

(b) Top view of the unit cell.

Figure 4.2: 3-layered third-order band-pass FSS proposed in [159].

The structure is formed by cascaded layers of rectangular patches and rectangular patches with notches printed on dielectric substrates (Figure 4.3). The results show that the prototype covers the band from 4 to 14 GHz for vertical polarization and from 5 to 15 GHz for horizontal polarization.

The equivalent circuit model (ECM) is a method that provides characteristics of transmission from the structure to a plane wave and requires less computing effort compared with field solvers. Here, capacitive and inductive components are modeled from segments of strips placed in a periodic array [115], [164]. Therefore, the process of designing a double-layer FSS with ultra-wideband rejection response is described in this chapter. The proposed FSS combines two single-layer FSSs with different geom-

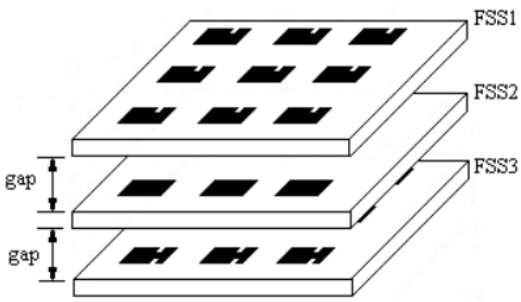

(a) Expanded and side views.

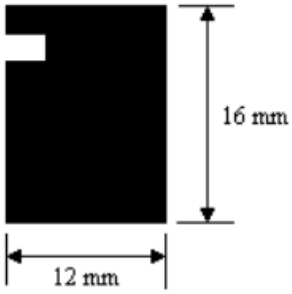

(b) Top metal layer structures.

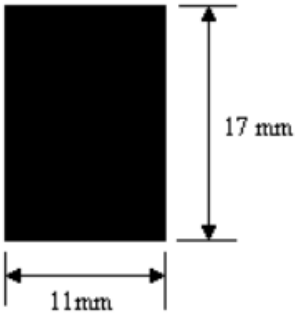

(c) Intermediate metal layer structure.

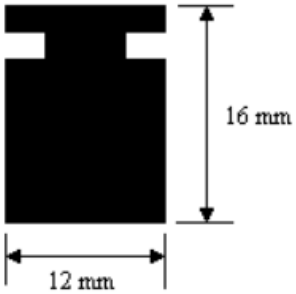

(d) Bottom metal layer structures.

Figure 4.3: 3-layered ultra-wide band FSS proposed in [163].

etry with interesting characteristics such as simple design and miniaturization, and it is analyzed and designed through ECM by simply adapting Marcuvitz's equations [40] for conductive strips. The cascaded structure covers the K (18 GHz to 26.5 GHz) and Ka band (26.5 GHz to 40 GHz), with a bandwidth of approximately 24.4 GHz, operating from 18.3 GHz to 42.7 GHz in simulated results. The proposed structure has transmission zeroes at 28 GHz and 36 GHz applicable for 5G technology, which is designed to reflect signals in the range of frequency from K to Ka band. It is important to mention that distinguished bands have been allocated in each region [165], and the proposed FSS is suitable in different bands and frequencies, while offering high bandwidth. The resonance frequencies and bandwidth can be adjusted by optimizing the dimensions of the proposed FSS. A prototype is fabricated and measured, and experimental results show excellent agreement with simulations.

4.2 Equivalent circuit model

As mentioned in Section 2.6.2, FSS design and analysis can be done by modelling its EC, which uses less computational effort compared to full-wave methods. Following

the modeling approach by Marcuvitz [40] (Figure 2.22), the EC can be determined using general formulas for the inductive reactance, X_L, and capacitive susceptibility, B_C [113]:

$$\frac{X_L}{Z_0} = F(p, w, \lambda, \theta) = \frac{p\cos\theta}{\lambda}\left\{\ln\left[\csc\left(\frac{\pi w}{2p}\right)\right] + G(p, w, \lambda, \theta)\right\} \tag{4.1}$$

$$\frac{B_C}{Y_0} = 4F(p, g, \lambda, \phi) = \frac{4p\cos\theta}{\lambda}\left\{\ln\left[\csc\left(\frac{\pi g}{2p}\right)\right] + G(p, g, \lambda, \phi)\right\} \tag{4.2}$$

where λ is the wavelength, and G is a correction factor that allows incidence of the plane waves at arbitrary angles by varying θ and ϕ.

$$G(p, w, \lambda, \theta) = \frac{0.5(1-A^2)^2\left[\left(1-\frac{A^2}{4}\right)(B_+ + B_-) + 4A^2B_+B_-\right]}{\left(1-\frac{A^2}{4}\right) + A^2\left(1+\frac{A^2}{2}-\frac{A^4}{8}\right)(B_+ + B_-) + 2A^6B_+B_-} \tag{4.3}$$

Note that when calculating the capacitive susceptibility, the function G can be solved by replacing ϕ with θ and w with g.

$$A = \sin\left(\frac{\pi w}{2p}\right) \tag{4.4}$$

$$B_\pm = \left[1 \pm \frac{2p\sin\theta}{\lambda} - \left(\frac{p\cos\theta}{\lambda}\right)^2\right]^{-\frac{1}{2}} - 1 \tag{4.5}$$

Equations (4.1) and (4.2) have limitations and must meet the following conditions $w/p \ll 1$, $p/\lambda \ll 1$, and $p(1+\sin\theta)/\lambda < 1$. They are not suitable for modelling of cross polarization [38].

The elements are printed on a dielectric substrate which modifies the capacitance of the FSS as a function of the dielectric permittivity ϵ_r, and thickness of the substrate h. For thin substrates involving higher-order Floquet modes, a closed formula based on Green's functions cannot be pursued. The effective electrical permittivity is obtained as described in Section 3.2.1, Equation 3.2, [152].

4.3 Single-layer FSS analysis and design

This section presents the design of two simple geometries with simplified formulation. The equations for their equivalent circuits are straightforwardly implemented in Matlab.

4.3.1 Four-arms star geometry

The first FSS (FSS #1) is based on the four-arms star geometry (Figure 3.4), whose design procedure was introduced in Section 3.2.1. The ECM is applied to predict the frequency response of this element by the following equations.

The normalized inductive reactance X_f and the normalized capacitive susceptance B_f of the structure based on the four-arms star geometry are defined as

$$\frac{X_{L_f}}{Z_0} = 1.5\frac{a}{p}F(p, b, \lambda, \theta) \tag{4.6}$$

$$\frac{B_{C_{g_f}}}{Y_0} = \frac{4b}{1.5p}F(p, g_{f_1}, \lambda, \phi) \tag{4.7}$$

$$\frac{B_{C_{a_{1_f}}}}{Y_0} = \frac{4(p-b)}{1.5p}F(p, g_{f_2}, \lambda, \phi) \tag{4.8}$$

$$\frac{B_{C_{a_{2_f}}}}{Y_0} = 4\frac{(p-s)}{p}F(p, g_{f_3}, \lambda, \phi) \tag{4.9}$$

The presence of dielectric support is taken into account in the ECM by including its dielectric effective permittivity value in the capacitive elements of the circuit.

$$\frac{B_{C_{1_f}}}{Y_0} = (B_{C_{a_{1_f}}} + B_{C_{g_f}})\epsilon_{r_{eff_f}} \tag{4.10}$$

$$\frac{B_{C_{2_f}}}{Y_0} = 0.25(B_{C_{a_{2_f}}} + B_{C_{g_f}})\epsilon_{r_{eff_f}} \tag{4.11}$$

The admittance of the EC of the four-arms star is given by

$$Y_f = \frac{1}{X_{L_f} - \frac{1}{B_{C_{1_f}}}} - \frac{1}{\frac{1}{B_{C_{2_f}}}} \tag{4.12}$$

The transmission coefficient is found by

$$\sigma_f = \frac{1}{1 + 0.25Y_s^2} \tag{4.13}$$

The reflection coefficient is given by

$$\Gamma_f = \sqrt{1 - \sigma_s^2} \tag{4.14}$$

Section 3.2.1 presents the equations to determine the resonance frequency for the FSS using the four-arms star geometry from initial dimensions. Based on this design procedure the FSS was designed to operate at 28 GHz and adapted to the ECM. Note that the geometry used is symmetric in the x- and y-directions, which provides practically the same response for both TE and TM polarization. The dimension of the structure are $p = p_p = 4.1$ mm, $a = a_p = 3.25$ mm, $b = b_p = 0.6$ mm, and $s = s_p = 1.0$ mm, and considering a dielectric substrate with $\epsilon_r = 2.94$, and thickness of 0.508 mm. Figure 4.4 illustrates the theoretical result, with resonance frequencies at 28 GHz (-55.01 dB) and -10-dB bandwidth of 7 GHz (from 24.5 GHz to 31.5 GHz).

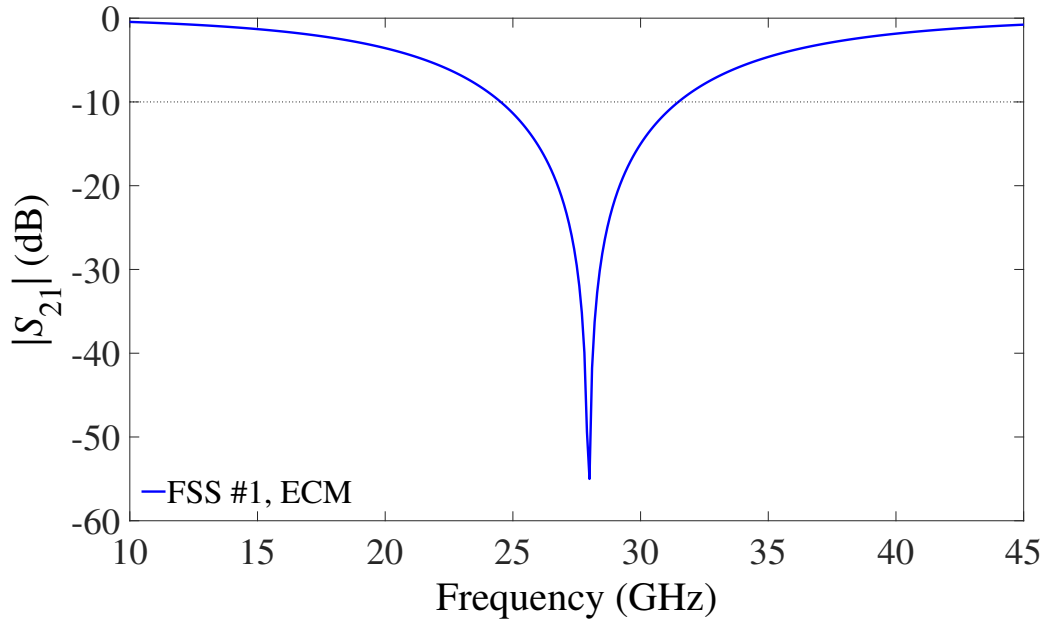

Figure 4.4: Theoretical result for FSS #1.

A comparison between the resonance frequency of FSS #1 in terms of the arms' size obtained by ECM and CST Microwave Studio is illustrated in Figure 4.5. A change in the arms' size changes the gap between copper and the unit cell, which increase the inductance and capacitance, leading to lower resonance frequencies. The

dimensions of the unit cell and square in the center are fixed with $p = 4.1$ mm and $s = 1.0$ mm. The increase in the parameters a (from 3 to 3.75 mm) and b (from 0.4 to 1.0 mm) leads to the reduction of the resonance frequency.

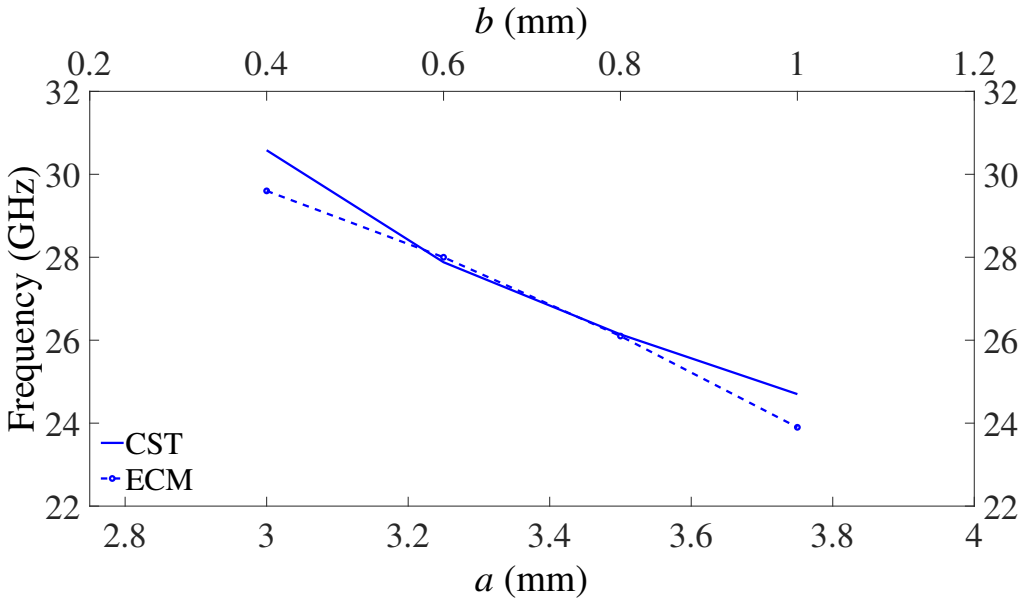

Figure 4.5: Influence of FSS #1 frequency response, with dimensions $p = 4.1$ mm and $s = 1.0$ mm, and substrate permittivity $\epsilon_r = 2.94$ and 0.508 mm in thickness.

The proposed FSS is analyzed by the ECM and CST, considering different dielectric permittivities of commercial substrates. Figure 4.6 shows the resonance frequencies versus substrate thickness. All curves follow the same profile, proving that the model can be used for any realistic substrate. The increase in the thickness translates to the reduction in resonance frequency.

4.3.2 Quasi-square geometry

The second geometry proposed is shown in Figure 4.7 (FSS #2). To design it, initially a square patch p is dimensioned. Slot sections are inserted, crossing it in the middle, both vertically and horizontally, of width g_1. In this part, the FSS behaves as a capacitor with a wideband response. The final step to achieve the geometry is to add a square slot of size g_2, in the center of the patch, and the metallic surface has a width of w. Depending on the size of this square, the FSS starts increasing its inductance and hence, its resonance frequency and bandwidth decrease.

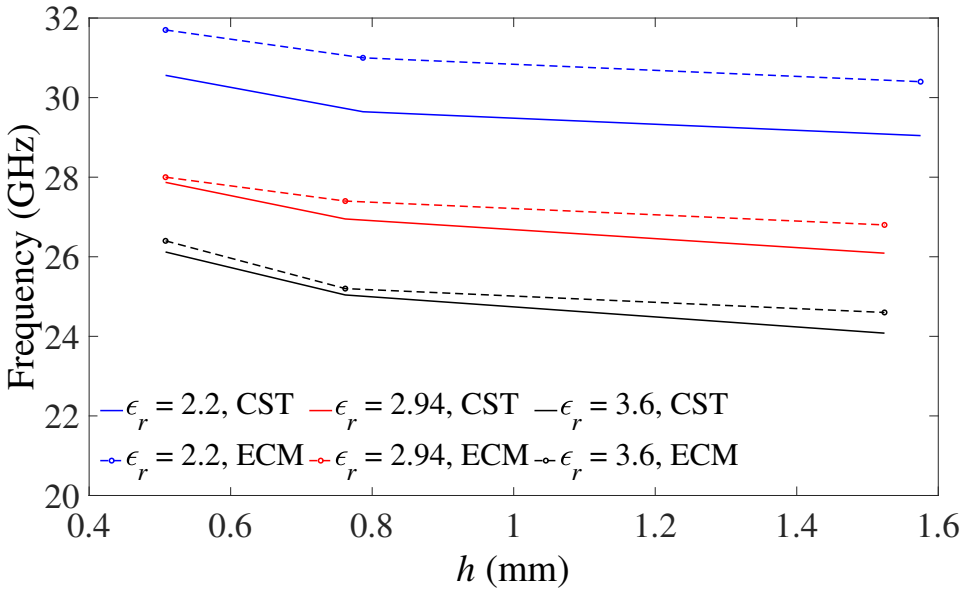

Figure 4.6: Comparison of resonance frequencies as a function of dielectric permittivity while variating the substrate thickness of FSS #1.

The inductive reactance X_s and the capacitive susceptance B_s, normalized to the intrinsic impedance of free space ($Z_0 = 1/Y_0$), of the quasi-square FSS are

$$\frac{X_{L_s}}{Z_0} = 0.5\frac{(p-w)}{p}F(p,w,\lambda,\theta) \tag{4.15}$$

$$\frac{B_{C_{sg_1}}}{Y_0} = 4\frac{w}{p}F(p,g_1,\lambda,\phi) \tag{4.16}$$

$$\frac{B_{C_{sg_2}}}{Y_0} = 4\frac{(p-w)}{p}F(p,g_2,\lambda,\phi) \tag{4.17}$$

$$\frac{B_{C_{1s}}}{Y_0} = 0.5B_{C_{sg_1}}\epsilon_{r_{eff_s}} \tag{4.18}$$

$$\frac{B_{C_{2s}}}{Y_0} = 0.25(B_{C_{sg_2}} + B_{C_{sg_1}})\epsilon_{r_{eff_s}} \tag{4.19}$$

The admittance is calculated as

$$Y_s = \frac{1}{X_{L_s} - \frac{1}{B_{C_{1s}}}} - \frac{1}{\frac{1}{B_{C_{2s}}}} \tag{4.20}$$

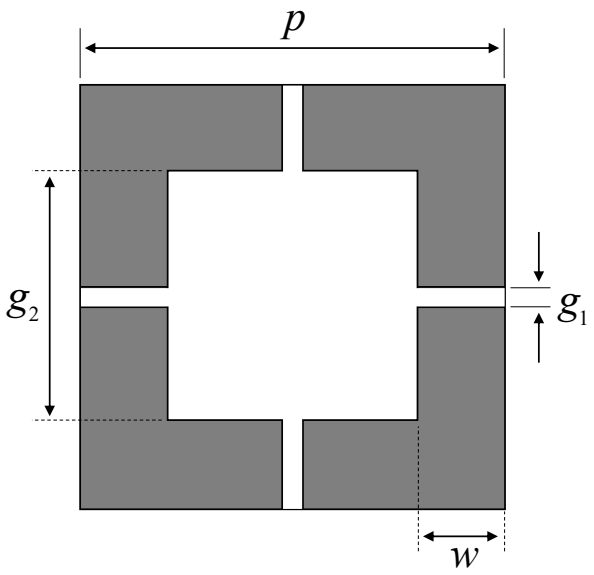

Figure 4.7: Geometry and parameters of FSS #2.

The transmission coefficient (σ_s) can be calculated from Equation (4.13) by replacing the admittance Y_f with the admittance of the second FSS (Y_s). Hence, the reflection coefficient (Γ_s) for the quasi-square FSS is found from Equation (4.14), by using the calculated value of σ_s.

This second FSS was designed for 35.8 GHz, and the properties of the dielectric substrate are the same used for FSS #1. The unit cell has the same size as that of FSS #1, $p = 4.1$ mm. The design is numerically optimized until the desired characteristics are achieved with dimensions $w = 0.85$ mm, $g_1 = 0.2$ mm and $g_2 = 2.4$ mm. For the geometry proposed, the value of M is 1.5. Figure 4.8 shows the numerical result of the transmission coefficient, with the resonance frequency at 35.8 GHz (-70.52 dB) and -10-dB bandwidth of 18.2 GHz (from 23 GHz to 41.2 GHz).

The effect in the resonance frequency as a function of the size of g_2 as analyzed by ECM is presented in Figure 4.9. The other parameters are fixed, except for w that is inversely proportional to g_2. The capacitance and inductance is proportional to an increase of g_2, thus leading to a gradual reduction of the resonance frequency.

The applicability of ECM for FSS #2 considering different dielectric permittivities of substrates is compared to a full-wave method. The dimensions of the structure are the ones used to obtain the result in Figure 4.8. Figure 4.10 shows the resonance frequencies versus substrate thickness. As expected, the results prove that the model can be used for any realistic substrate. To provide a comparison of CPU times between

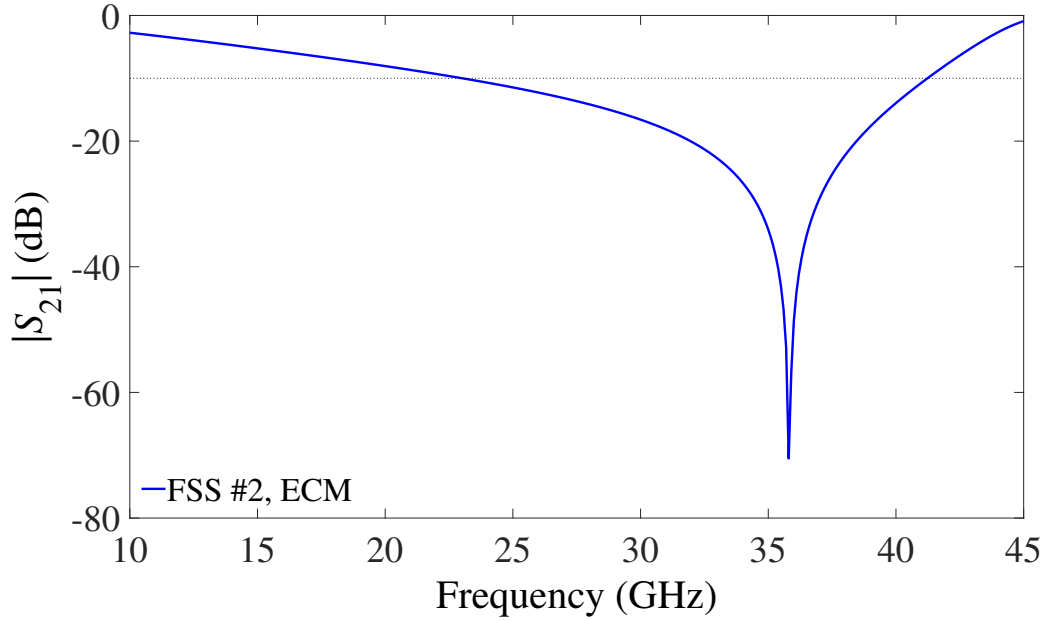

Figure 4.8: Theoretical result for FSS #2.

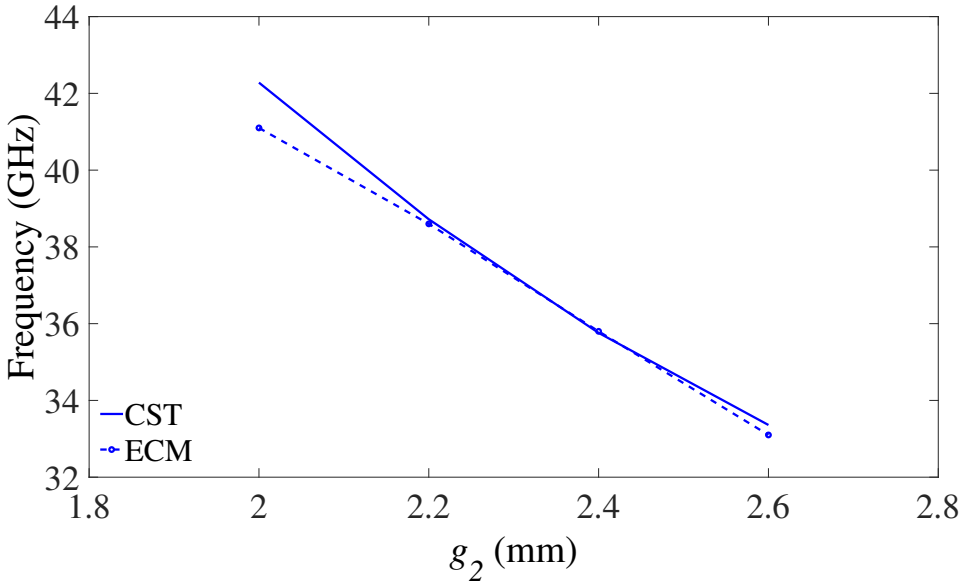

Figure 4.9: Influence of FSS #2 frequency response, with dimensions $p = 4.1$ mm and $g_1 = 0.2$ mm, and substrate permittivity $\epsilon_r = 2.94$ and 0.508 mm in thickness.

the two methods, for the example with $\epsilon_r = 3.6$ and $h = 0.762$ mm, the ECM was approximately 390 times faster than CST.

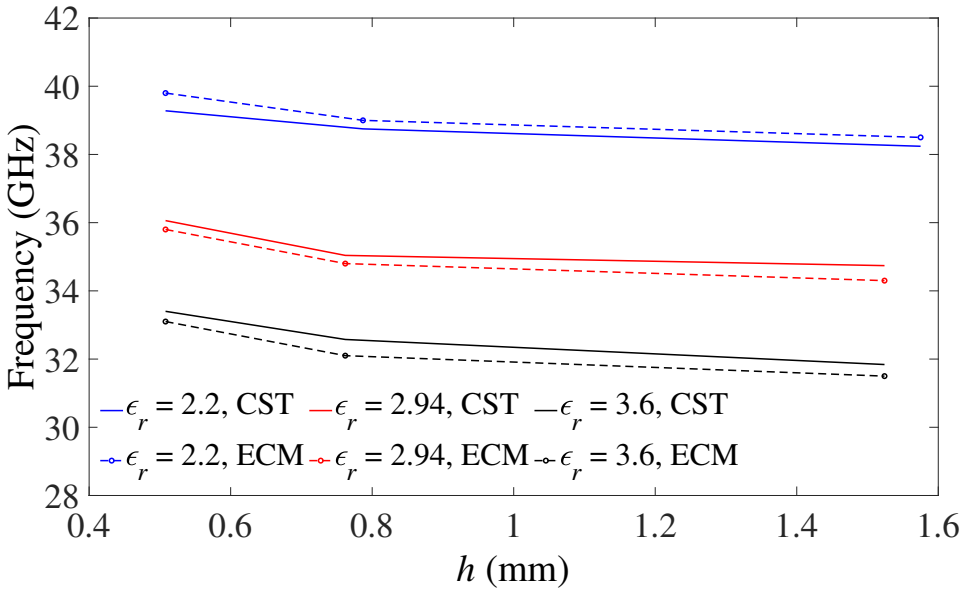

Figure 4.10: Comparison of resonance frequencies as a function of dielectric permittivity while variating the substrate thickness of FSS #2.

4.4 Cascaded FSS design

The cascading of FSSs is used to obtain an ultra-wide band-stop response by exploiting multiple resonances. Each single-layer structure provides a different transmission zero as shown in Section 4.3. In order to compute the performance of N cascaded structures separated by a distance d_{n-1} (Figure 4.11), the scattering matrix can be applied using single-mode interaction.

In this section, the two single-layer structures presented in the previous section are cascaded, and the 2×2 scattering matrix $[S]$ is determined as

$$\overline{\overline{S}}_n = \begin{bmatrix} \sigma_n \left(1 - \frac{\Gamma_n^2}{\sigma_n^2}\right) & \left(\frac{\Gamma_n}{\sigma_n}\right) e^{j2kl_n} \\ -\left(\frac{\Gamma_n}{\sigma_n}\right) e^{-j2kl_n} & \frac{1}{\sigma_n} \end{bmatrix} \tag{4.21}$$

where

$$l_n = d_1 + d_2 + \cdots + d_{n-1}, \tag{4.22}$$

$n = 1, 2, \cdots, N$

The matrix with C, D, E, F elements is given as

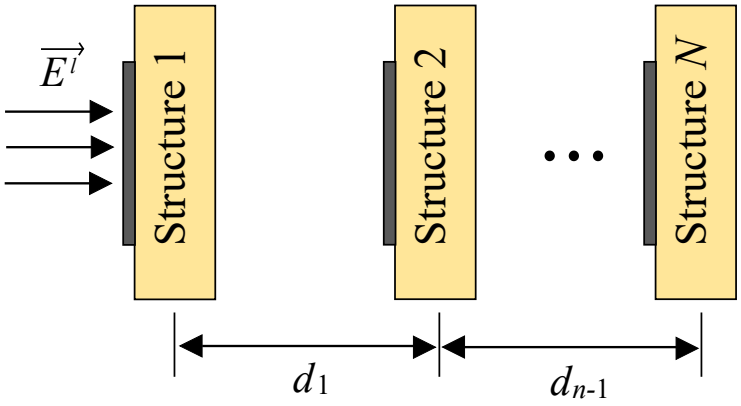

(a) Cascading N FSS structures.

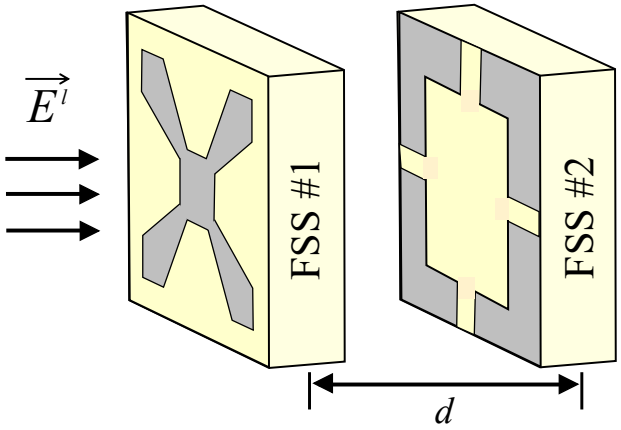

(b) 3-D view of the proposed cascaded FSS.

Figure 4.11: Cascading system of FSSs.

$$\begin{bmatrix} C & D \\ E & F \end{bmatrix} = \overline{\overline{S}}_n \overline{\overline{S}}_{n-1} \cdots \overline{\overline{S}}_3 \overline{\overline{S}}_2 \overline{\overline{S}}_1 \tag{4.23}$$

Applying the single-mode iteration, the total transmission and reflection coefficients are [28]

$$\sigma = C - \frac{DE}{F} \tag{4.24}$$

$$\Gamma = -\frac{E}{F} \tag{4.25}$$

The coupling between the two structures is determined by their spatial separation d. The influence of the coupling, considering an air gap with different spacing ($d = 1.0$

mm, 2.5 mm and 4.0 mm) is presented in Figure 4.12. In the first analysis with spacing $d = 1.0$ mm, the resonance frequencies are 27.96 GHz and 38.6 GHz, with a -10-dB bandwidth of 24.82 GHz. In the second case, $d = 2.5$ mm, the resonance frequencies are 27.96 GHz and 35.84 GHz, with 23.02 GHz of bandwidth. It can be seen in the third case ($d = 4$ mm) that the numerical result is about the same as for the individual structures, presenting two stop-bands, the first resonance frequency f_{z_1} is at 27.96 GHz with 13.8 GHz of bandwidth and the second resonance frequency f_{z_2} is at 35.76 GHz with 11.04 GHz of bandwidth. This last case also presents a resonance frequency at 31.6 GHz (-4.07 dB) with a band-pass behavior. With the increase of coupling (increasing the spacing d), the anti-parallel currents are induced in the resonators, causing the destructive interference of scattering fields. The transparency window becomes stronger for $d = 4$ mm, and this behavior is known as the Electromagnetically Induced Transparency (EIT) effect, which is a physical phenomenon that eliminates the effect of a medium in an electromagnetic radiation [166]–[168].

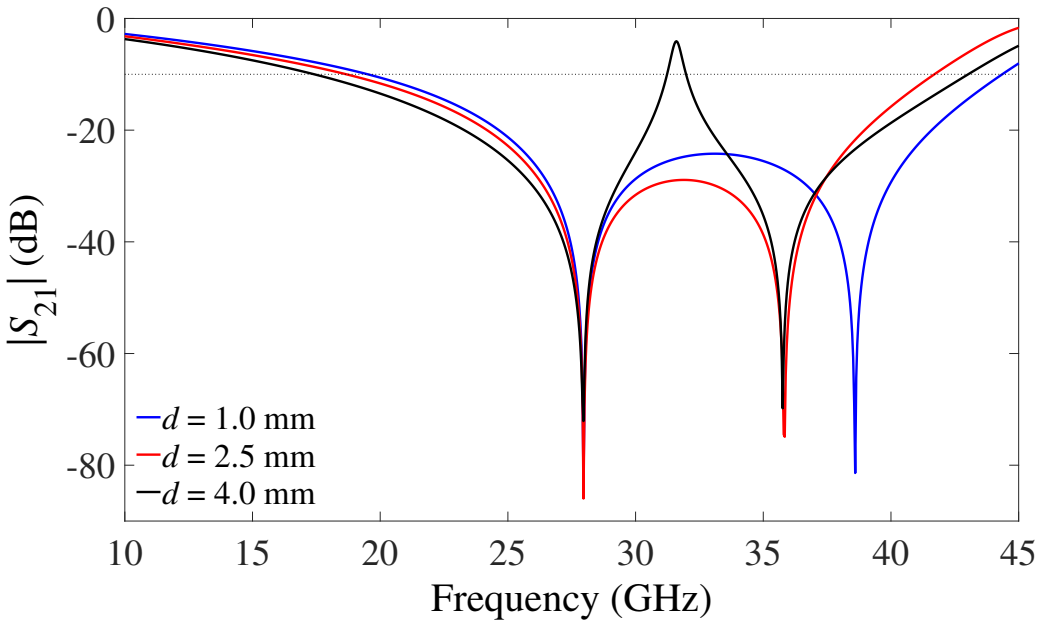

Figure 4.12: Simulated results for cascaded FSS, considering different spacing.

These results are summarized in Table 4.1, showing the difference when compared to the individual FSSs.

Figure 4.13 compares the theoretical results of the individual structure and cascaded one by applying ECM. These results indicate that the prediction in terms of frequency response of the cascaded FSS follows the ones from the single-layer FSSs,

Structure	f_{z_1} (GHz)	Diff. (%)	f_{z_2} (GHz)	Diff. (%)
FSS #1	28	—	—	—
FSS #2	—	—	35.8	—
1st Cascade (d = 1.0 mm)	27.96	0.14	38.6	7.82
2nd Cascade (d = 2.5 mm)	27.96	0.14	35.84	0.11
3rd Cascade (d = 4.0 mm)	27.96	0.14	35.76	0.11

Table 4.1: Comparison of Resonance Frequencies Between Individual and Cascaded FSSs

with larger bandwidth and multiple resonances. It can be noticed that the two transmission zeroes in the cascaded FSS are created by the resonators in each layer and the ultra-wide band-stop by the EIT effect. The cascading was done considering an air gap of d = 2.5 mm between the two FSSs as shown in Figure 4.12. The two resonance frequencies are 27.96 GHz (-85.96 dB) and 35.84 GHz (-74.91 dB) and the mutual coupling resulted in a -10-dB bandwidth of 23.02 GHz.

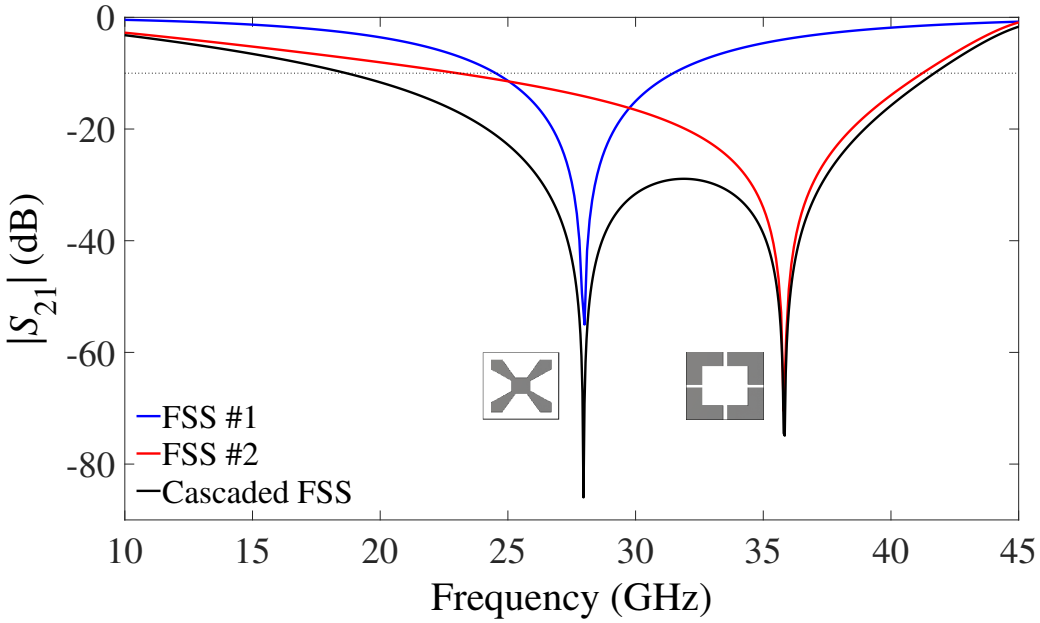

Figure 4.13: Comparative of numerical results of individual FSSs and cascaded one.

4.4.1 Fano resonance

The FSS frequency response depends on in a variety of parameters as explained in Chapter 2, Section 2.2, Figure 2.1. The type of the element (patch or aperture) and its

shape defines if the FSS has a capacitive or inductive response, i.e., the FSS presents an extended or narrow bandwidth, and suppression or promotion of grating lobes. In some designs, symmetrical-shaped elements are used to provide polarization stability. However, the symmetry of the element can be broken, exciting a Fano resonance (FR) [169], [170]. The proposed cascaded FSS in this chapter can generate an FR mode at oblique incidence in the millimeter-wave range. A parametric analysis is performed to determine the FR, and results are presented in Section 4.5.

FR is an interference effect between two resonators. The resonances of these resonators are generally classified as bright (or continuum or broad) mode and dark (or discrete or narrow) mode [171]. The Fano effect arises when the geometry is broken, then the incident wave efficiently excites the bright mode, overlapping the dark mode, which does not couple efficiently to the wave. This scattering phenomenon is identified by nonlinear distortion of the transmission coefficient with ultrahigh quality factor (Q-factor) shifted from the central frequency [172]. The FR has been intensively studied in the fields of plasmonics and metamaterials [173]. Due to its unique sensitivity and high Q-factor, FR has found applications in ultrasensitive sensors [174], lasing [175], switching [176], slow light [177], and ultracompact antennas [169].

4.5 Performance validation

The numerical characterization was done considering the excitation of the proposed structure with the electric (E) field at transverse electric (TE), transverse magnetic (TM) incidence, and circular polarization, as shown in Figure 4.14.

Two FSSs with the proposed geometries were manufactured to validate the numerical results by experiments. The prototypes were fabricated on single-layer Rogers Duroid/RT 6002 dielectric substrate with $\epsilon_r = 2.94$, thickness of 0.508 mm, and loss tangent of 0.0012, with 26 $\times$ 26 elements and overall dimensions of 10.7 cm $\times$ 10.7 cm (Figure 4.15). The measurement procedure of the proposed FSS is described in Appendix A, Section A.2.1.

4.5.1 Single-layer FSS results

Note that in both FSSs the geometries are symmetric in the x- and y-direction, i.e., the frequency response is independent of the electric field polarization, therefore the results for both polarizations are similar. The measured transmission coefficient of the

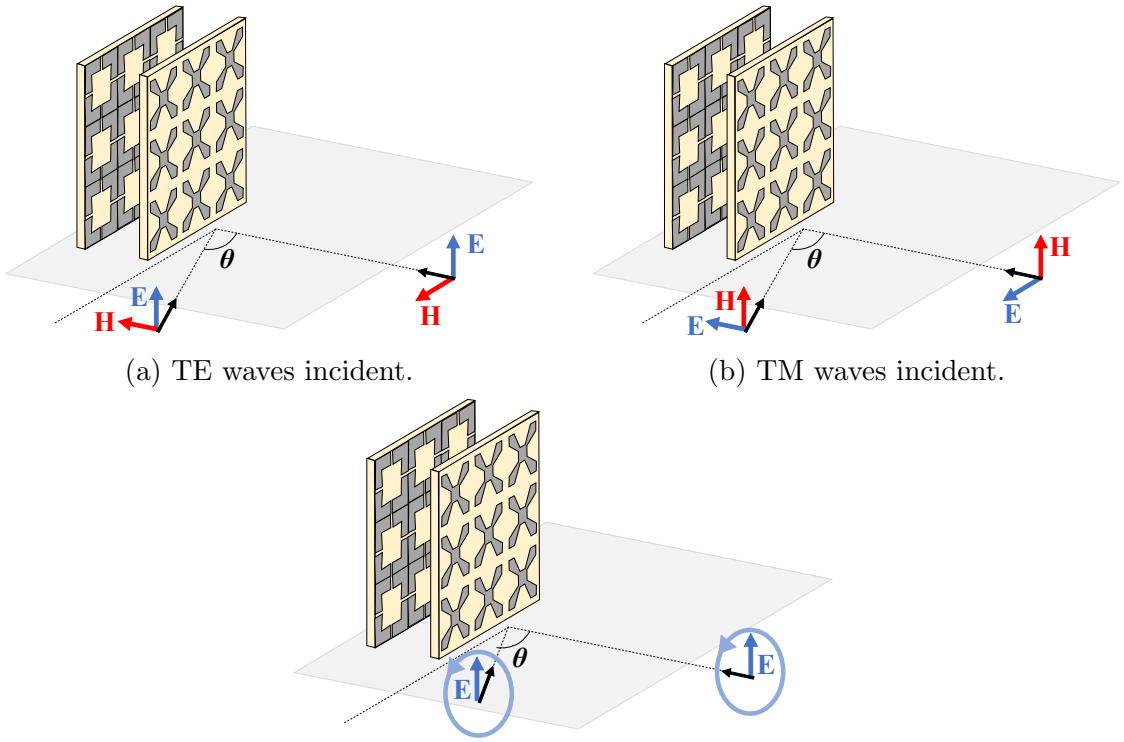

(a) TE waves incident.

(b) TM waves incident.

(c) Circular waves incident.

Figure 4.14: Polarizations of the incident wave on the cascaded FSS.

fabricated structures, considering single- and double-layers, under normal incidence along with the numerical characterizations obtained by ECM and CST are presented for TE and TM polarizations.

Figure 4.16 presents the simulated and measured transmission coefficients for the first structure. For the TE polarization, the measured resonance frequency is 27.92 GHz compared to simulated ones of 27.92 GHz from CST and 28 GHz for ECM, thus showing excellent agreement with a maximum difference of only 0.28%. The -10-dB bandwidth obtained for the measured and simulated results are 6.88 GHz (experimental), 7.08 GHz (CST) and 7 GHz (ECM). A CPU time comparison reveals that using the theoretical equations presented in Section 4.3 is at least 280 times faster than CST. In the TM polarization, the results are very similar with resonance frequencies at 27.92 GHz (CST) and 28.16 GHz (measured), with maximum difference of 0.57%, and bandwidth of 7.08 GHz and 7.02 GHz for numerical and experimental results.

The FSS #2 was designed for 35.8 GHz. Figure 4.17 shows the comparison between numerical (CST and ECM) and experimental results, with resonances at 35.76

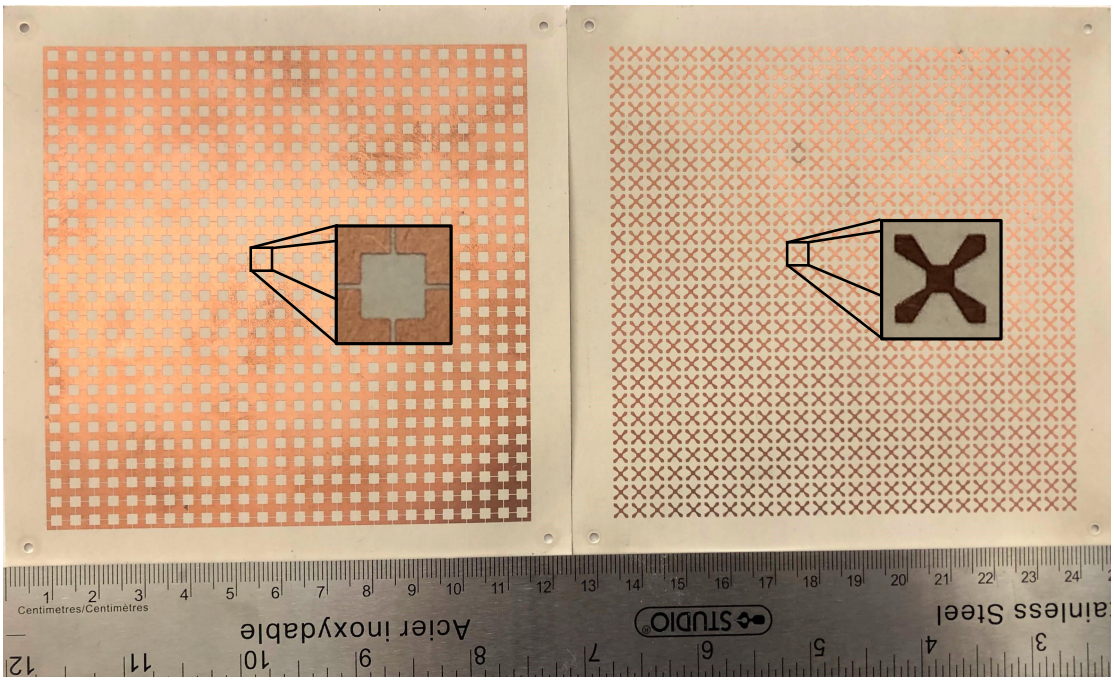

Figure 4.15: Fabricated FSSs with quasi-square (left) and four-arms star (right) geometries, and their individual cell.

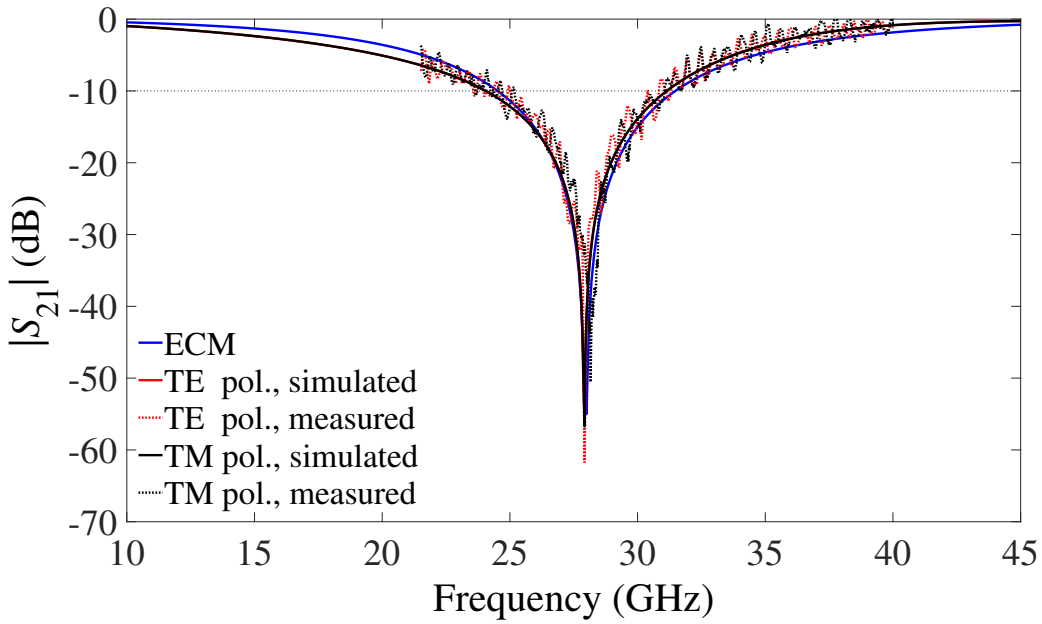

Figure 4.16: Simulated and measured results for prototype FSS #1.

GHz, 35.8 GHz and 35.68 GHz, respectively – a maximum difference of 0.33%, for the

TE polarization. The bandwidth in this polarization in the simulation was 17.68 GHz (CST) and 18.2 GHz (ECM). The measurement goes up to 40 GHz (antenna's maximum frequency), thus we were unable to measure the entire bandwidth. However, it is obvious that the measured result shows the same behavior as the simulation. A comparison of CPU times between the two methods shows that our ECM was 250 times faster than CST. In the TM polarization, the resonance frequency is 35.8 GHz (CST) and 35.56 GHz (measured), with a maximum difference of 0.67%, and -10-dB bandwidth of 17.64 GHz.

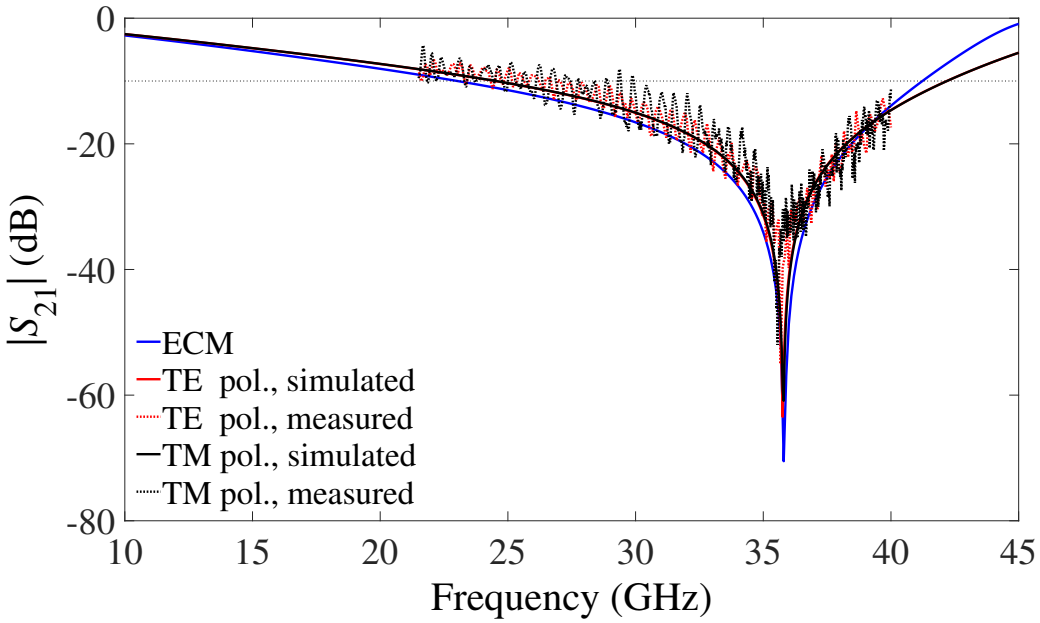

Figure 4.17: Simulated and measured results for prototype FSS #2.

4.5.2 Cascaded FSS results

After the confirmation of the results for the single-layer FSSs, the structures were assembled to then validate the proposed cascaded FSS and ECM. Figure 4.18 shows the measured transmission coefficient along with numerical results for the cascaded FSS. The air gap between the structures is 2.5 mm based on Figure 4.12, provided by using Teflon spacers, nuts and screws to complete the cascade. The measured transmission zeros in the TE polarization are 28.08 GHz (-74,73 dB) and 36 GHz (-57.19 dB), and show excellent agreement with those obtained by CST (f_{z1} =27.92 GHz and f_{z2} =36.04 GHz) and our ECM (f_{z1} =27.96 GHz and f_{z2} =35.84 GHz), with

a maximum difference of 0.28% and 0.67%, respectively. From numerical results, the cascaded FSS has a bandwidth of 24.38 GHz (CST) and 23.02 GHz (ECM), going from 18.34 to 42.72 GHz and 18.68 to 41.70 GHz, respectively. Due to limitations in the frequency range of the horn antennas used, the measured results are shown from 21.5 GHz to just 40 GHz, although it can be observed that the experimental curve closely follows the numerical one. The theoretical method also showed to be faster than CST for the cascaded FSS in order of 345 times. The characterization of the TM polarization was also performed, and due to the symmetry of the structure, the results obtained are very similar to the TE polarization. The two occurring transmission zeros are 28.02 GHz and 36.17 GHz for the measured results, and the numerical ones are 27.96 GHz and 36.04 GHz (CST), with a maximum difference of 0.14% and 1.03%, respectively. The numerical bandwidth is 24.36 GHz with a band-stop range from 18.34 GHz to 42.70 GHz.

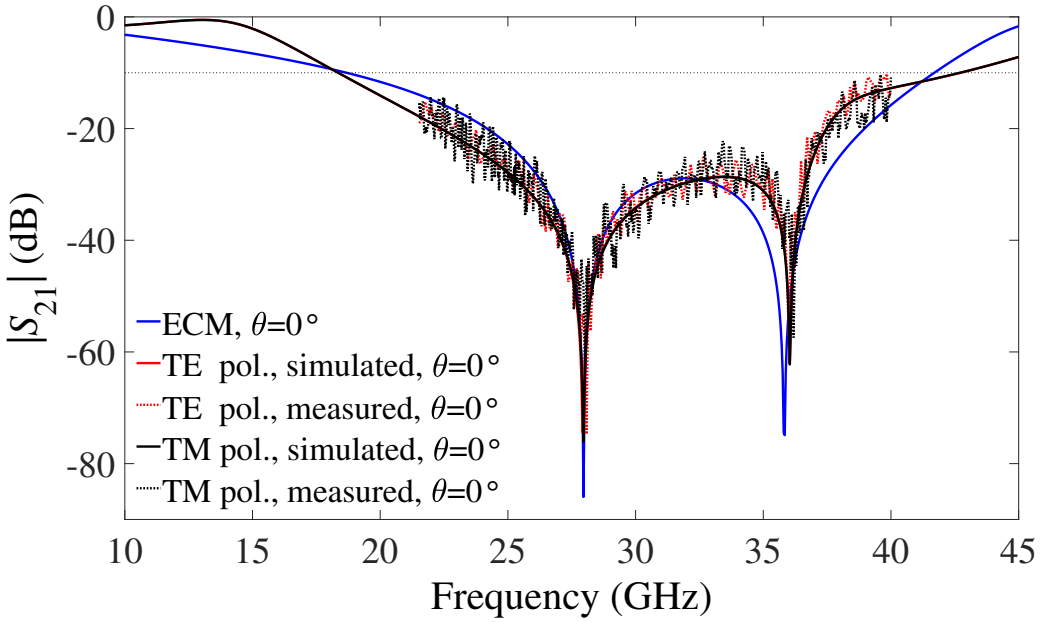

Figure 4.18: Simulated and measured results for cascaded FSS at normal incidence.

The transmission coefficients of simulated and measured results for TE and TM polarization off-normal incidence with $\theta = 15°$ is shown in Figure 4.19. The results obtained numerically show that the proposed FSS presents a wide bandwidth of approximately 22.6 GHz (ECM), and 20.5 GHz (CST – TE polarization) and 21.48 GHz (CST – TM polarization).

As mentioned above, at normal incidence ($\theta = 0°$), the E-field experiences a per-

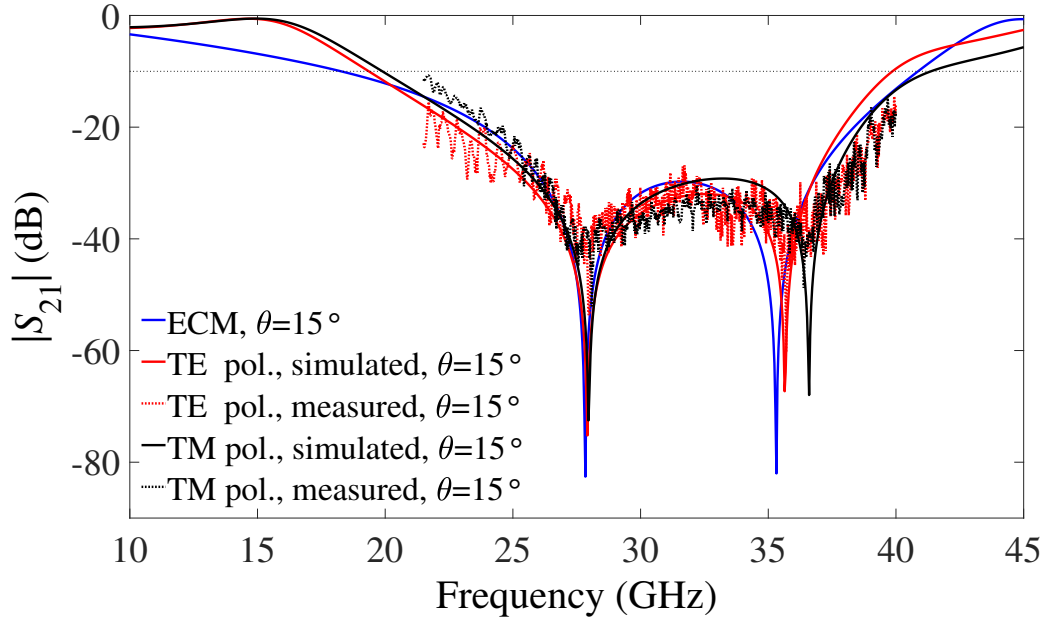

Figure 4.19: Simulated and measured results for cascaded FSS off-normal incidence.

fectly symmetrical structure in both (TE and TM) polarizations. When the wave is incident at an oblique angle ($\theta \neq 0°$), the E-field may start to probe the broken intrinsic symmetry of the proposed structure, hence its frequency response changes. In this condition for the TE polarization, a sharp asymmetric line-shaped Fano resonance is excited when $\theta \geq 20°$ (Figure 4.20), due to the interference between the two independent resonance modes, as f_{z2} moves closer to f_{z1}. Figure 4.20 shows that the profile of the FR is stable with an increase of amplitude and bandwidth while increasing the angle of incidence.

Figure 4.21 shows the measured transmission coefficient along with numerical results for the proposed cascaded FSS for TE polarization, comparing the normal ($\theta = 0°$) and oblique incidence ($\theta = 30°$). The measured and simulated results at $\theta = 30°$ for f_{z1} are 28.11 GHz and 28.28 GHz, respectively. The resonance f_{z2} changed to a lower frequency, when compared to normal incidence, and it is found to be at 35.07 GHz (measured) and 34.24 GHz (CST). For this polarization, the structure is weakly coupled to free space, which leads to the emergence of an FR at 23.3 GHz (measured) and 23.16 GHz (CST).

The comparison for the TM polarization was also performed numerically and experimentally (Figure 4.22). The transmission coefficient of simulated and measured results for off-normal incidence with $\theta = 30°$ is analyzed. It is observed that the f_{z1}

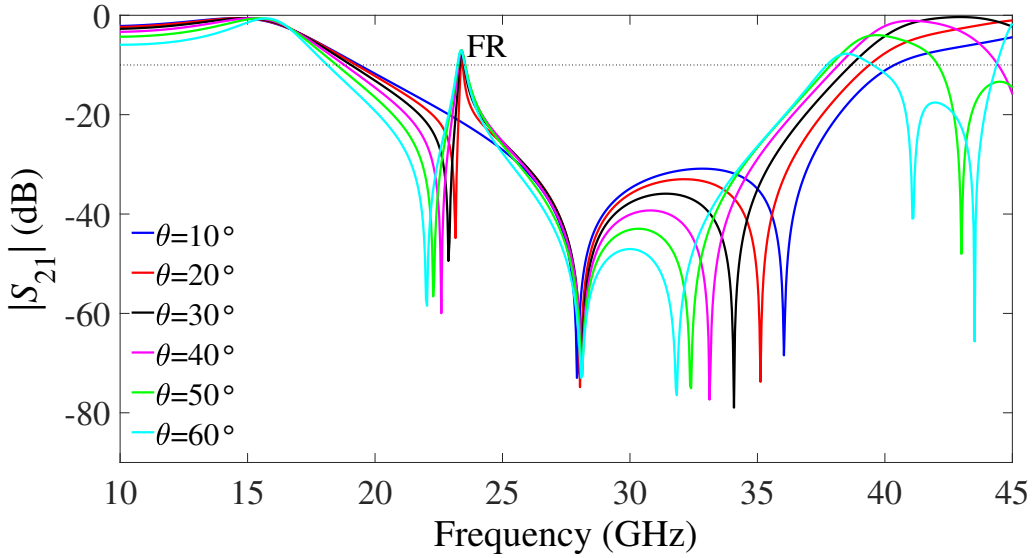

Figure 4.20: Simulated results for the TE polarization of the cascaded FSS at different incident angle.

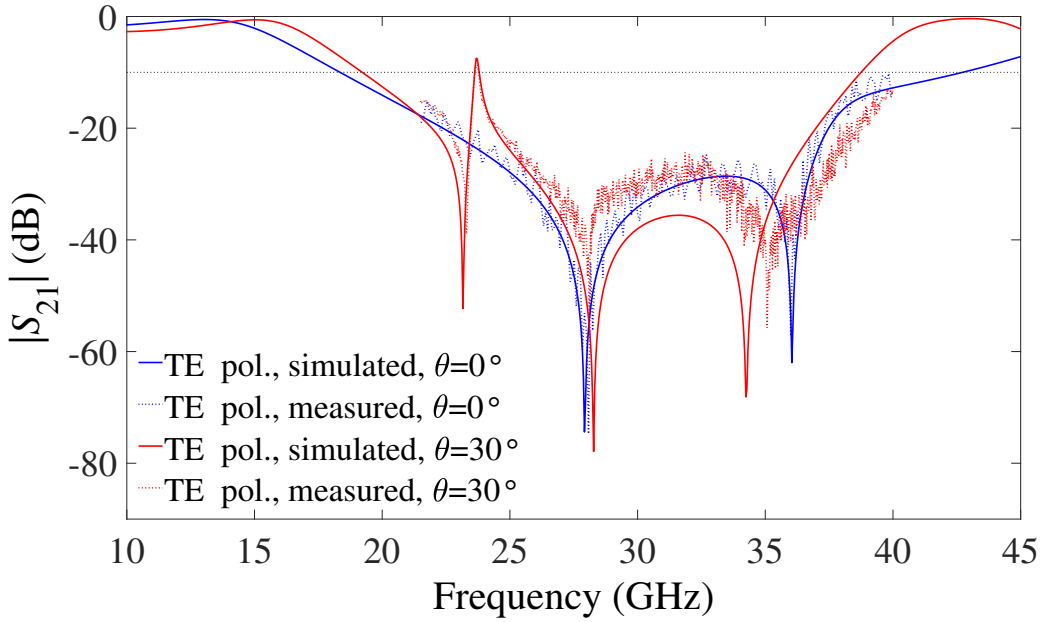

Figure 4.21: Simulated and measured results for the TE polarization of the cascaded FSS at normal and oblique incidence.

remains basically at the same frequency, but f_{z2} is moved to a higher frequency (37.08 GHz in CST and 37.13 GHz measured). This change occurs because the dimensions

of parameters w and g_1 of the FSS #2, seen by the wave with incidence at $\theta = 30°$ for TM polarization, are reduced. The resonances of the proposed structure are coupled strongly to free space, thus not generating any Fano mode. The result obtained numerically shows that the proposed FSS presents a wide bandwidth of approximately 20.56 GHz.

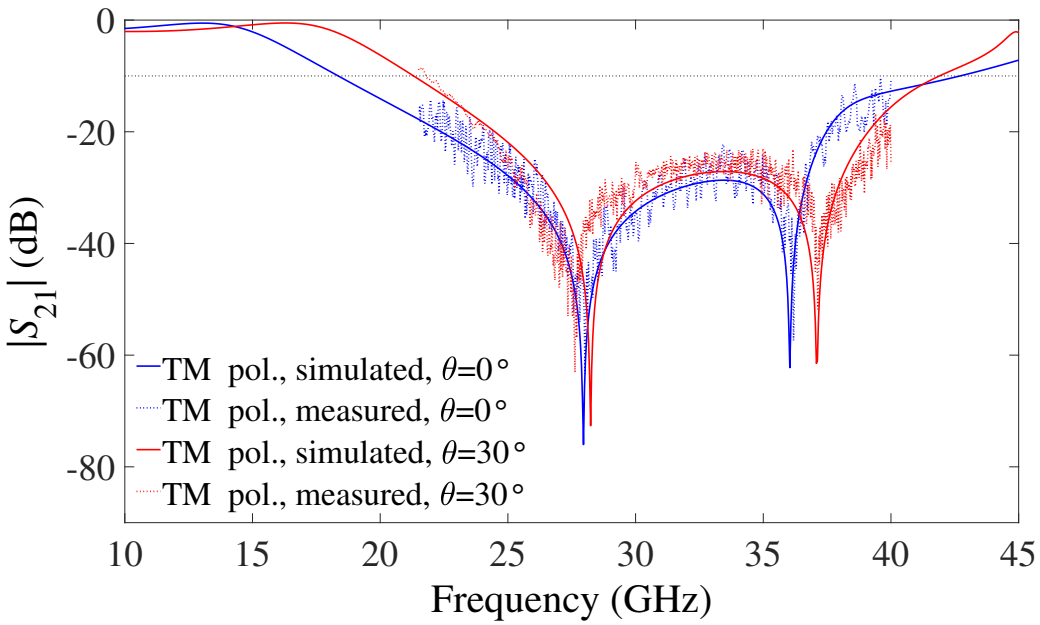

Figure 4.22: Simulated and measured results for the TM polarization of the cascaded FSS at normal and oblique incidence.

By analyzing the influence of the parameters of FSS #1 and FSS #2 considering the case when $\theta = 30°$ for TE polarization, the distortion of the transmissivity curve is found to happen when the size of the element of FSS #1 changes. This distortion is the dark mode (or FR), and the investigation of its response is presented in Figure 4.23 for different values of a. With the change of this parameters, f_{z1} is also affected since it corresponds to the resonance of the resonator FSS #1. While a increases, the FR and f_{z1} are reduced as well as the FR amplitude. These results are summarized in Table 4.2.

An incoming circular polarized wave arrives on the cascaded FSS at $\theta = 30°$ as illustrated in Figure 4.14c, and the result of the axial ratio (AR) of the transmitted wave is presented in Figure 4.24. The maximum AR is found at the Fano resonance, proving that the vertical and horizontal components are affected differently, resulting in an outgoing elliptically polarized wave.

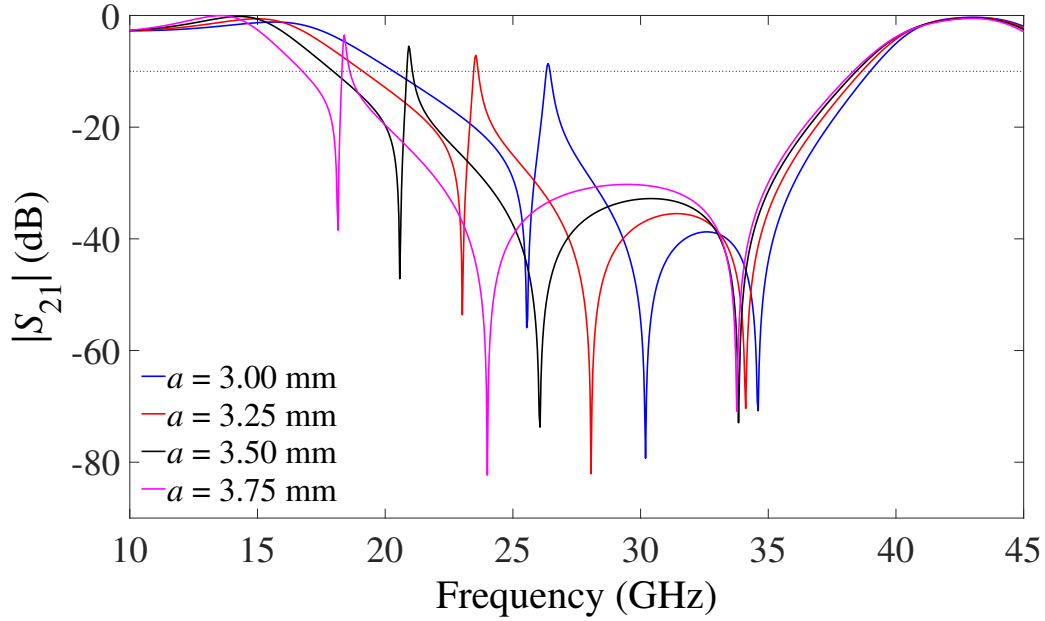

Figure 4.23: Influence of FSS #1 on the Fano resonance, with dimensions dimensions $p = 4.1$ mm, $b = 4.1$ mm and $s = 1.0$ mm, and substrate permittivity $\epsilon_r = 2.94$ and 0.508 mm thickness, at $\theta = 30°$.

a (mm)	FR (GHz)	f_{z1} (GHz)
3.00	25.54	30.19
3.25	23.16	28.28
3.50	20.57	26.06
3.75	18.15	24.00

Table 4.2: Resonance frequencies of FR and f_{z1} for different values of a.

4.5.3 Performance assessment

The transmission measurement results confirm that the proposed cascaded FSS achieves wide bandwidth in the K and Ka bands. Furthermore, the numerical and experimental results prove that the FR is sensitive to the geometric parameters of the proposed FSS and polarization of the incident field.

A detailed comparison between the proposed FSS and other previously reported ones, including their type of configuration, 10-dB fractional bandwidth, number of transmission zeros and unit cell dimensions, is shown in Table 4.3. It can be seen that besides the complexity of the structure's geometry the resonances depend mainly on the number of layers for the bandwidth response. The proposed FSS demonstrates to

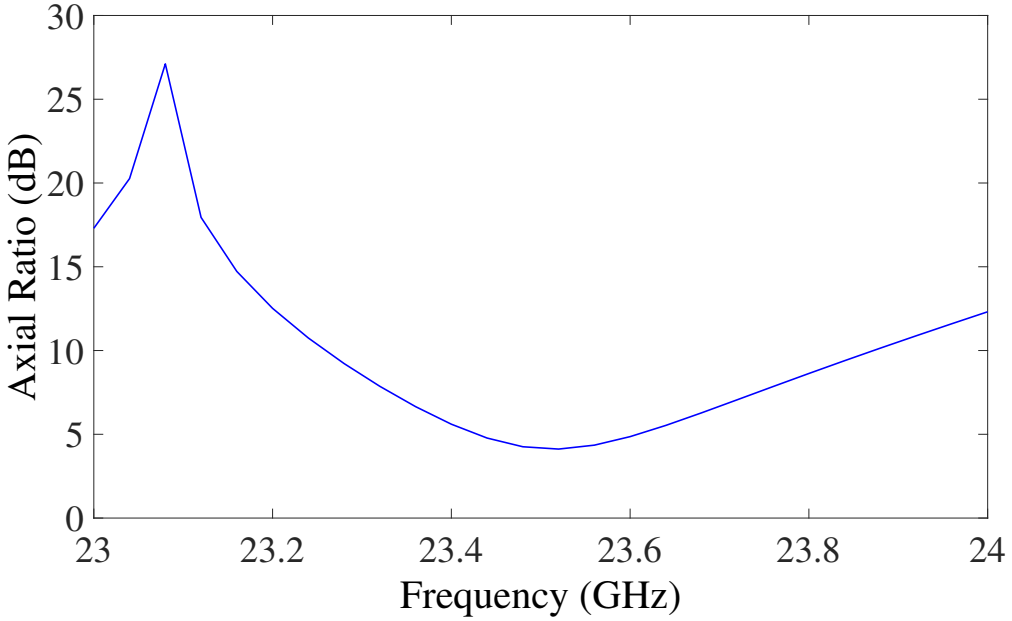

Figure 4.24: Simulated axial ratio of the proposed structure.

have wider bandwidth when compared to others, only using two layers with simple geometries.

Ref.	Configuration	10-dB bandwidth (%)	Resonances	Unit cell size
[178]	2-D single layer	47.6	1	$0.25\lambda \times 0.25\lambda$
[179]	2-D single layer	50.0	1	$0.37\lambda \times 0.74\lambda$
[180]	3-D cascaded annular ring	53.8	2	$0.48\lambda \times 0.48\lambda$
[181]	2-D double layer	54.5	2	$0.34\lambda \times 0.34\lambda$
[182]	2-D double layer	54.5	3	$0.20\lambda \times 0.20\lambda$
[183]	2-D three layers	68.4	3	$0.23\lambda \times 0.23\lambda$
This work	2-D double layer	79.8	2	$0.41\lambda \times 0.41\lambda$

Table 4.3: Comparison of proposed FSS with other reported ones.

Chapter 5

Beam-Tilting Bio-Inspired Antenna With Gain Enhancement Using FSS for 28 GHz

This chapter presents a tilted-beam antenna with gain enhancement based on a single-layer FSS operating at 28 GHz for millimeter-wave applications. The antenna is bio-inspired by the Wayfaring-tree leaf geometry with end-fire radiation, which excites the FSS panel. The chapter describes each technology used and simulated performances, and equations are discussed. The antenna's design is achieved using polar transformations by applying the superformula of Gielis. The number of elements in the FSS panel is analyzed to achieve the best antenna performance in terms of realized gain and beam-tilting.

This chapter contains material extracted from the following publication:

D. F. Mamedes and J. Bornemann, "Gain Enhancement of Bio-inspired Antenna Using FSS for 28 GHz 5G Application," SBMO/IEEE MTT-S International Microwave and Optoelectronics Conference (IMOC), Fortaleza, Brazil, 2021, pp. 1-3, doi: 10.1109/IMOC53012.2021.9624742.

5.1 Introduction

Microstrip patch antennas are attractive for 5G applications due to their characteristics of low-cost, low-profile, compactness, multi-band or broadband operation, and easy fabrication [184], [185]. These types of antennas are composed of a radiating

element etched on a dielectric substrate and a ground plane on the opposite side [186]. The performance of the antenna depends on the geometry chosen which can be a conventional patch shape (rectangular, circular, triangular, etc.) or more complex ones (e.g., fractal [29]). Bio-inspired geometries have attracted interest among microwave engineers to design new microstrip antenna geometries. This study has started due to similarities of a leaf's characteristics and antennas in terms of reception of electromagnetic waves, i.e. in the way that leaves capture sunlight and transform it into chemical energy for the plant's survival [187].

During the last decades, various methods for designing high-gain antennas as well as for steering the main beam of antennas were reported. These methods include conventional approaches such as antenna arrays and new ones such as artificial magnetic conductors [188], electromagnetic band-gap structures [189], integrated lens antennas [190] and frequency-selective surfaces [191]. Recently, the interest in using FSSs has grown due to its transmission and reflection properties.

Reference [192] presents a high-gain end-fire antenna using an array of Mu-near-zero (MNZ) unit cells (Figure 5.1). The antenna consists of rounded bow-tie radiators fed by a microstrip-to-slot transition line that acts as a balun. A 2×7 array of double-sided split-ring resonators (SRRs), that acts as MNZ media, is integrated vertically in front of the bow-tie antenna to increase the antenna gain. The number of SRR slabs defines how much the gain can be increased. When the number of SRR slabs increases from 2 to 4, the gain is increased by 2.1 dB, but if the number of layers increase from 5 to 7, the gain is improved slightly by 0.7 dB. Although this system can provide a maximum of 5-dB gain improvement, it does not allow to tilt the beam.

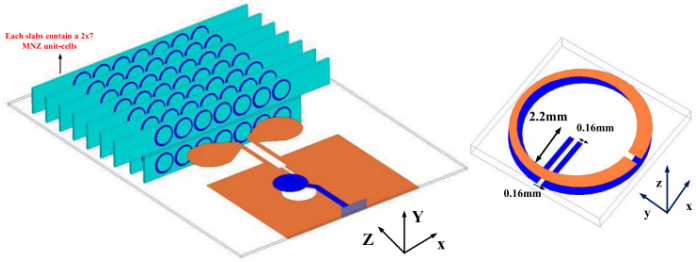

Figure 5.1: Rounded bow-tie antenna with 7 double-sided layers metamaterial and close-up view of SRR unit cell proposed in [192].

A system that tilts the main beam of an antenna while improving its gain was proposed in [193]. The planar dipole antenna is loaded with a 3×4 array of high refractive-index metamaterial unit cells (Figure 5.2) in the elevation plane to realize

beam deflection of 30°. This technique also provided a gain enhancement of 5 dB at 60 GHz.

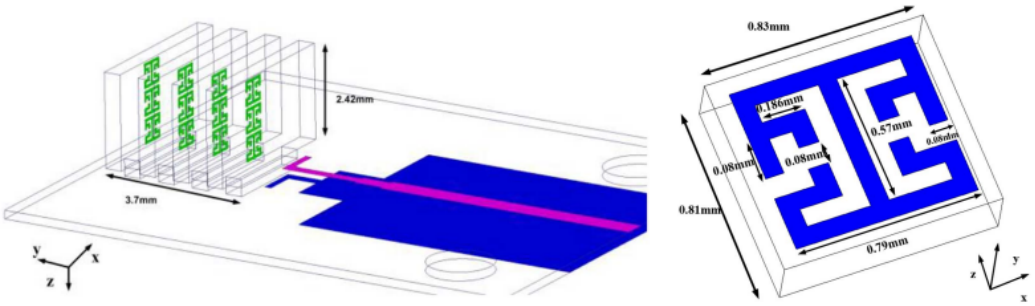

Figure 5.2: Single-dipole antenna embedded with a 3 × 4 arrays of high refractive-index metamaterial (left) and the close-up view of metamaterial unit cell (right) proposed in [193].

Reference [194] proposes a transparent artificial periodic structure (APS) adopting indium tin oxide (ITO) as conductive layer, and double-split ring elements printed on both sides are used to realize refractive index. The ITO-based APS is integrated with front end of a dipole antenna as shown in Figure 5.3. The beam-tilting angle is provided by the refractive indices and dimensions of the two media. Moreover, the structure shows a gain increase of 2.2 dB at the operating frequency.

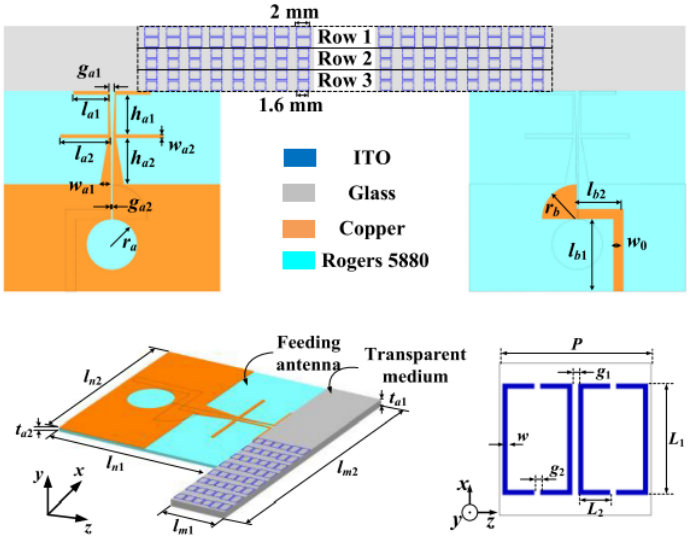

Figure 5.3: Antenna loaded with transparent medium made of artificial periodic structures and close-up view of the unit cell proposed in [194].

Multi-layer FSS structures are employed to control beam tilting and enhancement of the gain of an end-fire Vivaldi antenna operating at 28 GHz in [195]. The FSS

unit cell is designed on dual-sided printed single-layer substrate with two C-shaped resonators at the top metal layer and a slotted circular patch at the bottom side. The best antenna performance is achieved when two unequal-sized FSS layers are used and rotated to 45°, as shown in Figure 5.4, providing a maximum beam tilt angle of 38° in the H-plane and increase of gain of 3 dB.

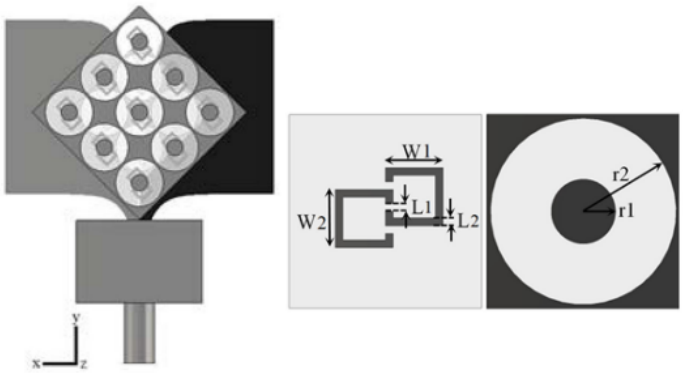

Figure 5.4: Vivaldi antenna with gain enhancement using multi-layer FSS (left), and unit cell in the bottom (middle) and top (right) of each FSS layer, proposed in [195].

This chapter presents a 28 GHz (N257 band) bow-tie antenna which is the bio-inspired version of the Wayfaring-tree leaf geometry and uses an FSS to enhance the antenna's gain. The leaf geometry is designed based on the superformula proposed by Gielis [196]. The numerical characterizations were obtained using the commercial software CST Microwave Studio. All proposed structures are designed on a Rogers Duroid/RT 6002 dielectric substrate with $\epsilon_r = 2.94$, $h = 0.508$ mm, and loss tangent of 0.0012.

5.2 Polar coordinates

Polar coordinates were initially used to study some specific curves. Bonaventura Cavalieri was the first to describe the use to find an area within a spiral, related to a parabola. Pascal also used them to calculate the length of a parabola. Isaac Newton was the first to use polar coordinates as a means of locating any point appearing in a plane. James Bernoulli showed a higher interest in this system; he wrote an expression for the radius of curvature when the equation for the curve is given in the polar form [197].

A polar coordinate system is a two-dimensional coordinate system that consists of a reference point O, called the pole, and a ray from the pole in the reference direction OA, is called a polar axis. A point P on a plane is determined by the distance from a reference point and angle from a reference direction, as shown in Figure 5.5a, $P = (r, \theta)$. If $r > 0$, the point (r, θ) is located in the same quadrant as theta; if $r < 0$, it is located in the quadrant opposite the pole, Figure 5.5b.

(a) (b)

Figure 5.5: Polar coordinates.

Polar equations express a curve in polar coordinates, and its graph is represented by an equation of $f(r, \theta) = 0$, where f is a defined and continuous function in polar coordinates that consists of all points P that have, at least, a polar representation. Figure 5.6 presents some well-known mathematical curves.

5.2.1 Superformula of Gielis

Gabriel Lamé generalized the concept of an ellipse to a super-ellipse [198]. These curves are defined according to the expressions given in Equations (5.1) and (5.2), respectively.

$$\left|\frac{x}{a}\right|^2 + \left|\frac{y}{b}\right|^2 = 1 \tag{5.1}$$

$$\left|\frac{x}{a}\right|^n + \left|\frac{y}{b}\right|^n = 1 \tag{5.2}$$

Lamé super-ellipses are given in polar coordinates r and θ by using the substitution $x = r\cos\theta$ and $y = r\sin\theta$ in Equation (5.2) and solving for $r = f(\theta)$.

$$r = \left(\left|\frac{\cos\theta}{a}\right|^n + \left|\frac{\sin\theta}{b}\right|^n\right)^{-1/n} \tag{5.3}$$

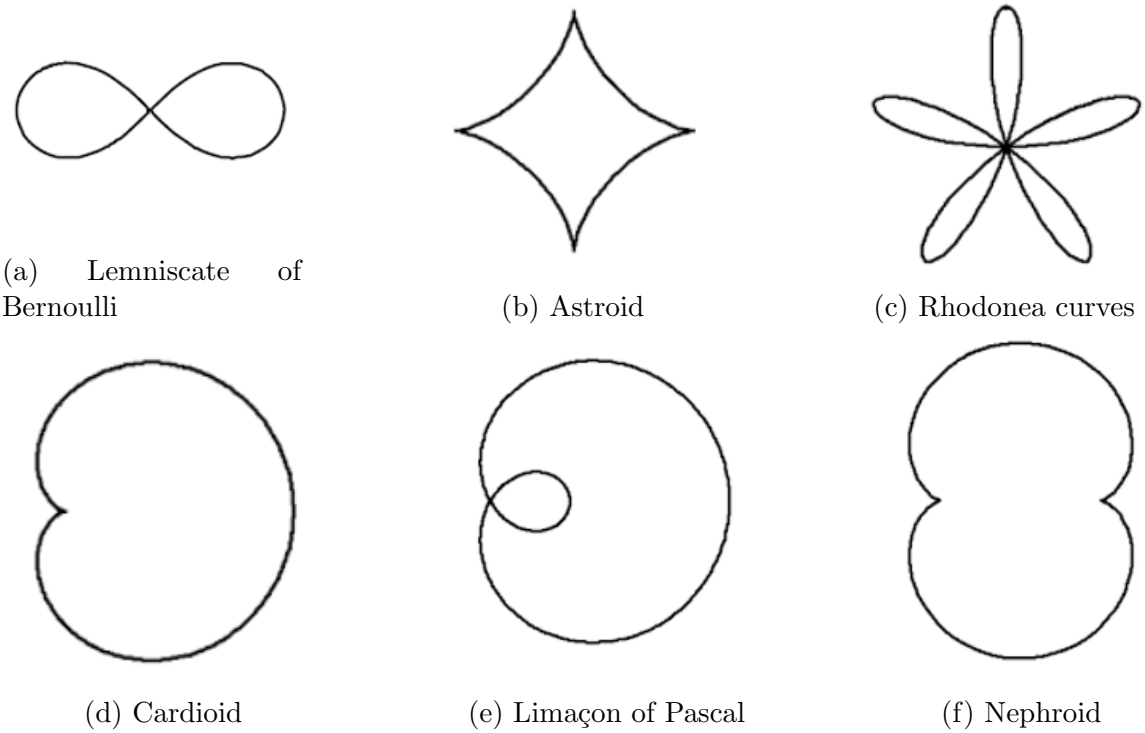

(a) Lemniscate of Bernoulli

(b) Astroid

(c) Rhodonea curves

(d) Cardioid

(e) Limaçon of Pascal

(f) Nephroid

Figure 5.6: Examples of mathematical curves.

From Equation (5.3), Gielis [196] developed a superformula that represents shapes of plants and animals. By using the superformula of Gielis (Equation (5.4)), it is possible to generate several geometries.

$$r = f(\theta) = \frac{1}{\left(\left| \frac{1}{a} \cos\left(\frac{m}{4}\theta\right) \right|^{n_2} + \left| \frac{1}{b} \sin\left(\frac{m}{4}\theta\right) \right|^{n_3} \right)^{1/n_1}} \tag{5.4}$$

The exponent n is applied to the trigonometric functions. The parameter $1/n_1$ acts as a pull or push force on the sides of the shape. For $n_2 = n_3$ and $n_{2,3} < 1$, the shape is inscribed in the base circle $n_{2,3} = 2$. For $n_{2,3} > 2$ the shape will circumscribe the circle. The coefficient $m/4$ allows more particular symmetries of rotation around O than those related to the four quadrants of the Cartesian coordinate system [196]. In Table (5.1) some examples of abstract shapes generated by the superformula are shown.

$n_2 = n_3$	$m = 1$	$m = 2$	$m = 3$	$m = 4$
0.1	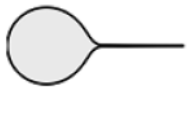		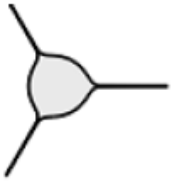	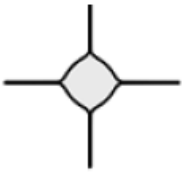
0.5	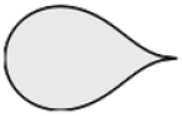		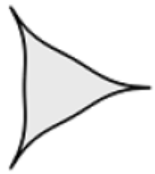	
1	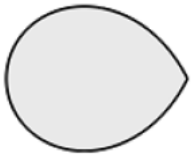		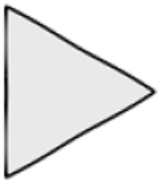	
5	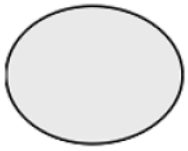			
10				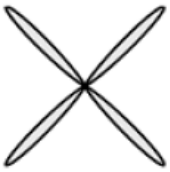

Table 5.1: Examples of various abstract shapes with $n_1 = 0.5$.

5.3 Bio-inspired antenna design and results

Antennas bio-inspired in plants use the shape of plants or part of them (leaves, stems, etc) to develop antennas. Table 5.2 presents some examples of works that are related to antennas bio-inspired in plants.

The printed antenna proposed in this work is bio-inspired by the Wayfaring-tree leaf geometry. This leaf is predominantly found in the Northeast of North America. The shape of this leaf is demonstrated in Figure 5.7, which is large, oval, slightly wrinkly-looking, with round-toothed edges.

The proposed antenna has a length of L_v and width of W_v, as shown in Figure 5.8. A Matlab code was developed for the design of the patch of the antenna, using image processing to adapt contours from the leaf according to the superformula of

Reference	Bio-inspired	Geometry
[199]	Korean striped maple leaf	
[200]	Four-leaf Clover	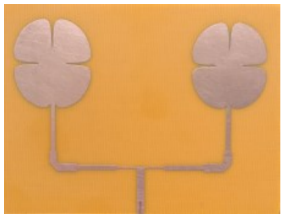
[201]	Castor leaf	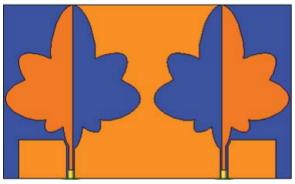
[202]	Fibonacci pattern in oak trees	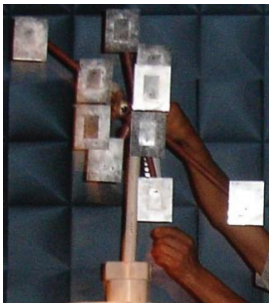

Table 5.2: Examples of bio-inspired antennas.

Figure 5.7: Wayfaring-tree (Viburnum lantana) leaf shape.

Gielis (5.4) [196]. The image obtained from the polar geometric transformations using mathematical functions is converted into a DXF (Drawing Exchange Format) file to

be imported and simulated in the commercial field solver CST Microwave Studio.

To obtain the shape shown in Figure 5.8, the parameters used are $a = 1$, $b = 1$, $m = 1$, $n_1 = 0.5$, $n_2 = 0.5$, $n_3 = 0.5$. The antenna was designed with one leaf each located on the top and bottom sides of the dielectric substrate, with a truncated ground plane of width g. It is fed through the microstrip line with width of m_x. To design it for the required frequency of operation, the initial dimensions of the bio-inspired antenna were set as those of the bow-tie antenna (Figure 5.11a) and then optimized to final dimensions. The parameters are $W_a = 6$ mm, $L_a = 5.3$ mm, $W_v = 2.14$ mm, $L_v = 1.68$ mm, $m_x = 0.58$ mm, $m_y = 2.8$ mm, and $g = 1.05$ mm, with overall size of $0.56\lambda \times 0.49\lambda \times 0.047\lambda$.

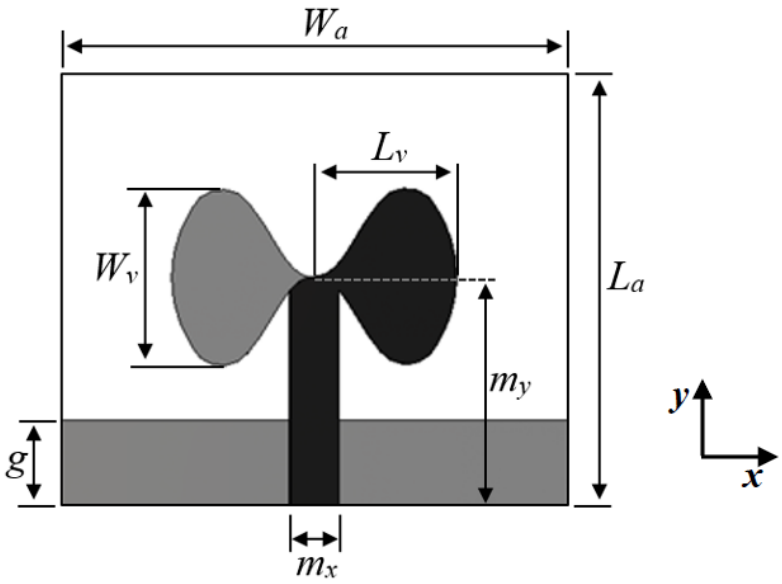

Figure 5.8: Designed antenna and its dimensions with dark and light shades indicating front and back metallization, respectively.

The frequency response for the bio-inspired antenna is presented in Figure 5.9. The result shows the resonance frequency at 27.96 GHz, with a reflection coefficient of -60.58 dB; the encircled edge provides a better current distribution, which gives a better impedance match, and a bandwidth from 25.69 to 31.32 GHz, based on -10-dB reflection, which includes the desired frequency range of the N257 band (26.5 – 29.5 GHz).

The radiation pattern in the E-plane, according to the coordinate system of Figure 5.14b, has an end-fire behavior with maximum gain, in the perpendicular direction, of 1.25 dBi at $\theta = 7°$ and 1.58 dBi at $\theta = 185°$ shown in Figure 5.10a. In Figure

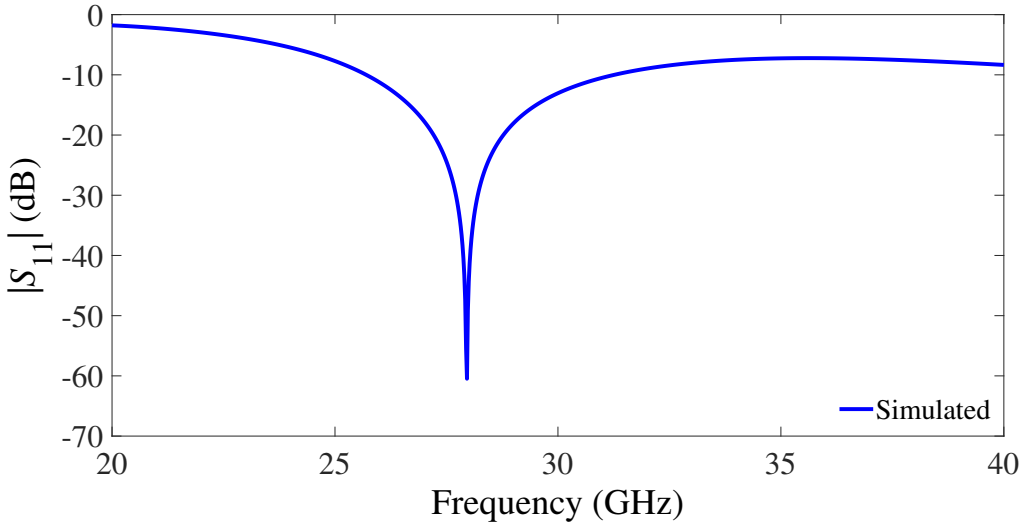

Figure 5.9: Simulated reflection spectrum of the bio-inspired antenna.

5.10b, the radiation pattern for the H-Plane is more directive, due to the antipodal structure, with a truncated ground place, being fed by the microstrip line, with a gain of 4.55 dBi at $\theta = 260°$, and Half Power Beamwidth (HPBW) of 175.3°. The overall realized gain is 4.6 dBi.

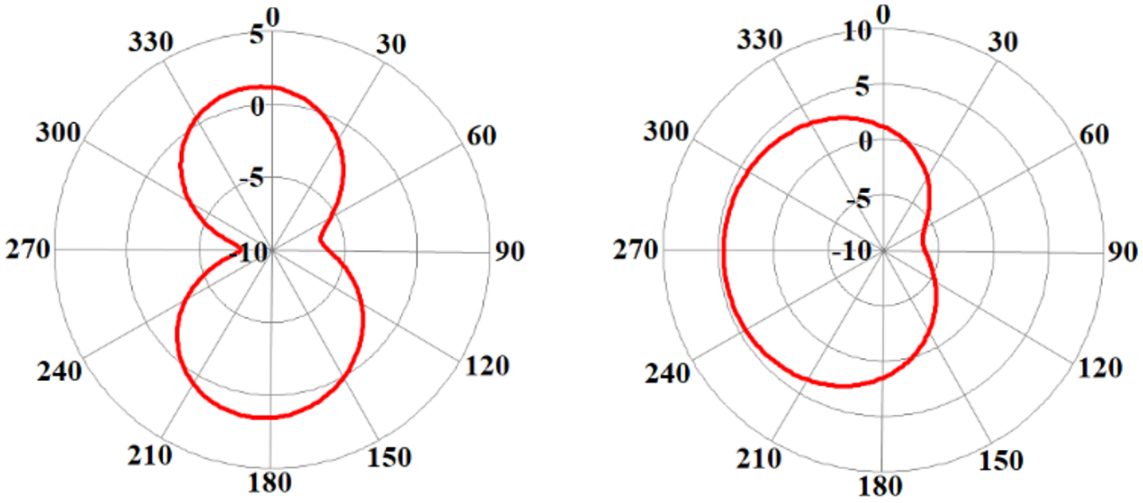

(a) E-plane.

(b) H-plane.

Figure 5.10: Simulated radiation pattern of the bio-inspired antenna; coordinate system according to Figure 5.14b.

The bio-inspired antenna used as the feeding source of the proposed system in this chapter is compared in design and performance with other planar antennas, operating

at the same frequency, found in the literature and shown in Figure 5.11. The original bow-tie antenna and its dimensions is illustrated in Figure 5.11a, which occupies a slightly higher area as the proposed bio-inspired antenna. The reflection spectrum for this antenna (Figure 5.12) shows that it has poorer impedance matching when compared to the proposed one, and about the same bandwidth from 25.55 to 31.03 GHz. The radiation pattern is similar to the one from the bio-inspired antenna, with realized gain of 4.52 dBi, which is slightly less gain.

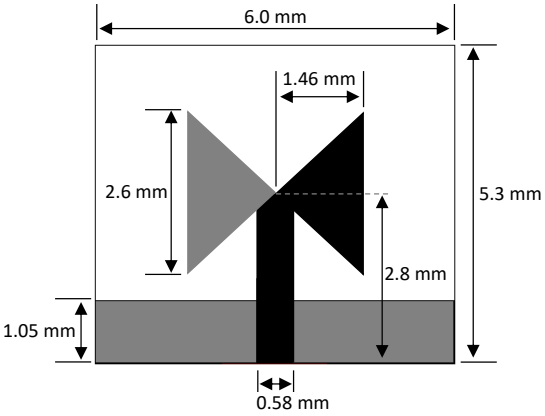

(a) Original bow-tie antenna.

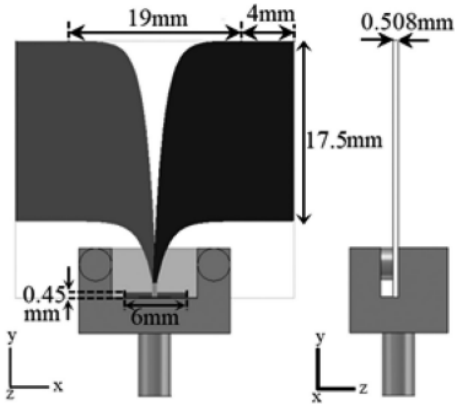

(b) Vivaldi antenna [195].

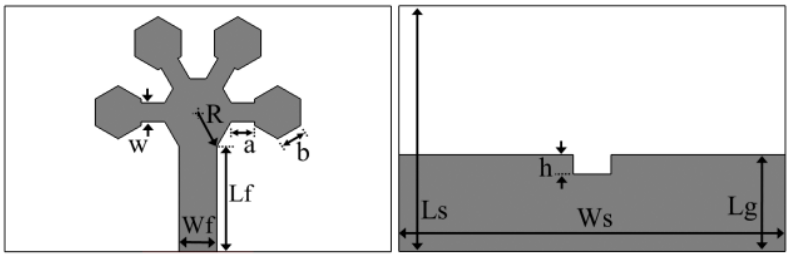

Parameter	Value (mm)
a	0.49
b	0.55
R	0.8
h	0.4
w	0.4
Ws	8
Ls	5
Wf	0.8
Lf	2.2
Lg	2

(c) Snowflake Fractal antenna [203].

Figure 5.11: Antennas designed to operate at 28 GHz.

Figure 5.11b and Figure 5.11c show a Vilvadi antenna [195] and a snowflake-fractal antenna [203], respectively, both operating at 28 GHz. The Vivaldi antenna designed in [195] has an overall size of $2.52\lambda \times 2.3\lambda \times 0.047\lambda$ and presented a realized gain of 5.5 dBi. Although the Vivaldi antenna presents a gain 0.9 dB higher when compared to the bio-inspired antenna, its width and length are approximately 50 times bigger then the proposed antenna. The snowflake-inspired fractal antenna proposed in [203] has an overall size of $0.75\lambda \times 0.47\lambda \times 0.024\lambda$ and presents a realized gain of 3.12 dBi. The bio-inspired and snowflake-inspired fractal antennas have about the same overall

dimensions, but the proposed antenna in this work presents a 1.48 dB higher gain.

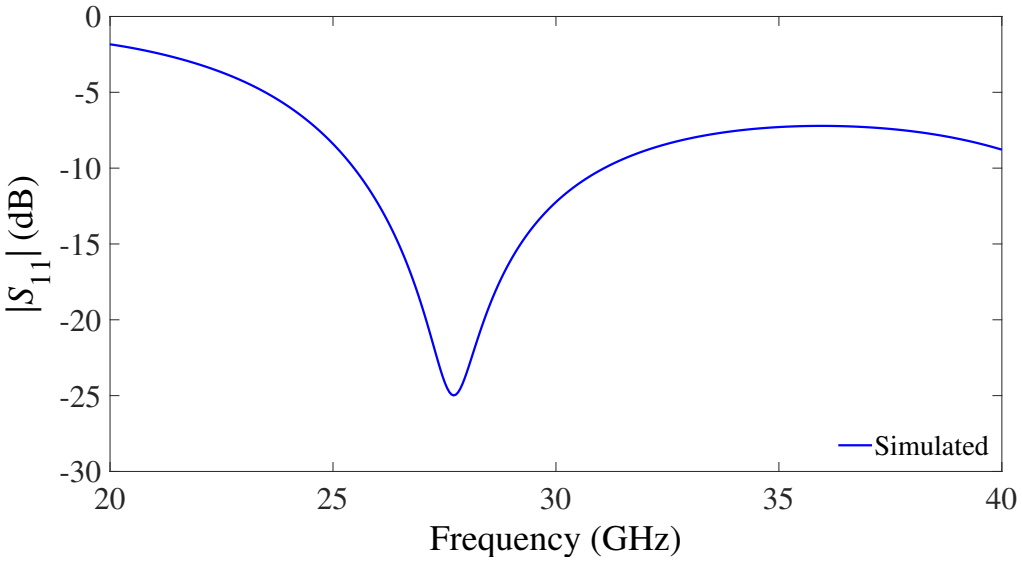

Figure 5.12: Simulated reflection spectrum of the original bow-tie antenna.

5.4 FSS design and results

The FSS design is based on the symmetrical four-arms star geometry and the schematic of the proposed FSS is the same used in Chapter 3, Section 3.2.1, Figure 3.4, which follows the same concept used for a cross-dipole element. In order to enhance the gain of the bio-inspired antenna, the FSS is designed to operate at the same frequency as the antenna. The FSS parameters dimensions are p_p = 4.1 mm, a_p = 3.25 mm, b_p = 0.6 mm, and s_p = 1.0 mm, same as in Chapter 4, Section 4.3.1. The unit cell is compactly designed at 28 GHz, being $0.38\lambda \times 0.38\lambda$, and provides 25.28% bandwidth. When compared to a cross-dipole unit cell, the four-arms star unit cell is 1.18 times smaller for operation at the same resonance frequency and the bandwidth is 1.75 wider. Figure 5.13 illustrates the numerical results for the transmission coefficient of TE and TM polarization at normal incidence, with resonance frequencies at 27.88 GHz and 27.94 GHz, respectively.

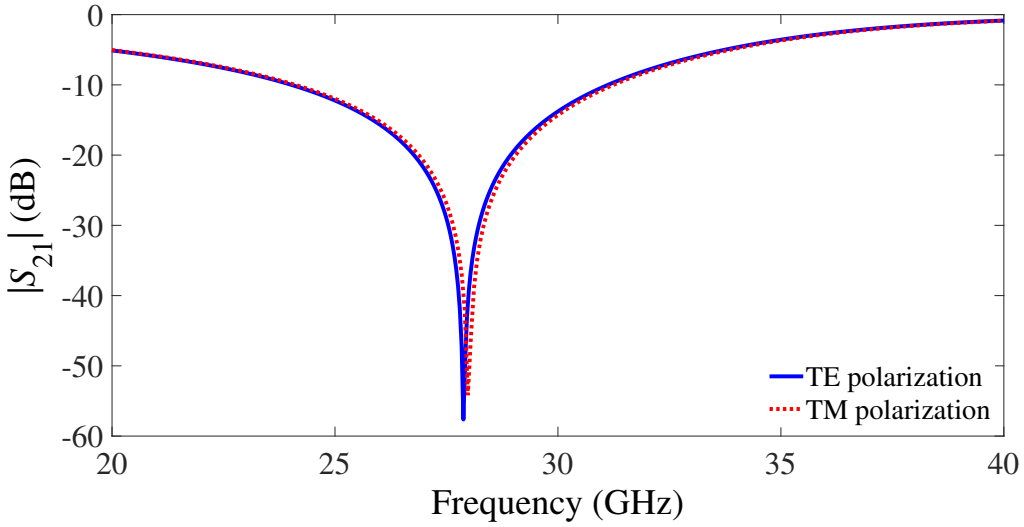

Figure 5.13: Simulated transmission spectra of the FSS.

5.5 Antenna with FSS as reflector design

The system proposed in this chapter consists of a bio-inspired antenna with an FSS implemented as reflector to enhance the antenna's gain, hence achieves better antenna performance. As seen in previous sections, the antenna and FSS are designed with the same resonance frequency, and the FSS has stopband characteristics, which allows to steer the beam. Figure 5.14 shows the schematic diagram, where the FSS is placed at a distance of $d = 2.5$ mm, which is 0.23λ at 28 GHz, behind the antenna. A parametric analysis demonstrates the influence that the number of elements in the FSS panel has on the gain and the tilt of the beam. Two cases are considered: the first one has a panel that consists of 2×2 elements and overall dimensions of 8.2 mm $\times$ 8.2 mm, and the second one has 3×3 elements and overall dimensions of 12.3 mm $\times$ 12.3 mm.

The radiation pattern of the proposed antenna system that is composed of a bio-inspired antenna and a 2×2 FSS is shown in Figure 5.15. The radiation pattern is directive in the E-plane, with maximum gain of 6.4 dBi in the perpendicular direction at $\theta = 357°$ and HPBW of 70.9°, as shown in Figure 5.15a. In the H-plane (Figure 5.15b), the radiation pattern is also more directive with gain of 7.38 dBi in the direction forward from the antenna at $\theta = 332°$, with the HPBW of 95.5° and beam tilt angle of 72°. Figure 5.15c shows the 3D radiation pattern for the bio-inspired antenna with a 2×2 FSS panel, whose vertical and horizontal radiation patterns are

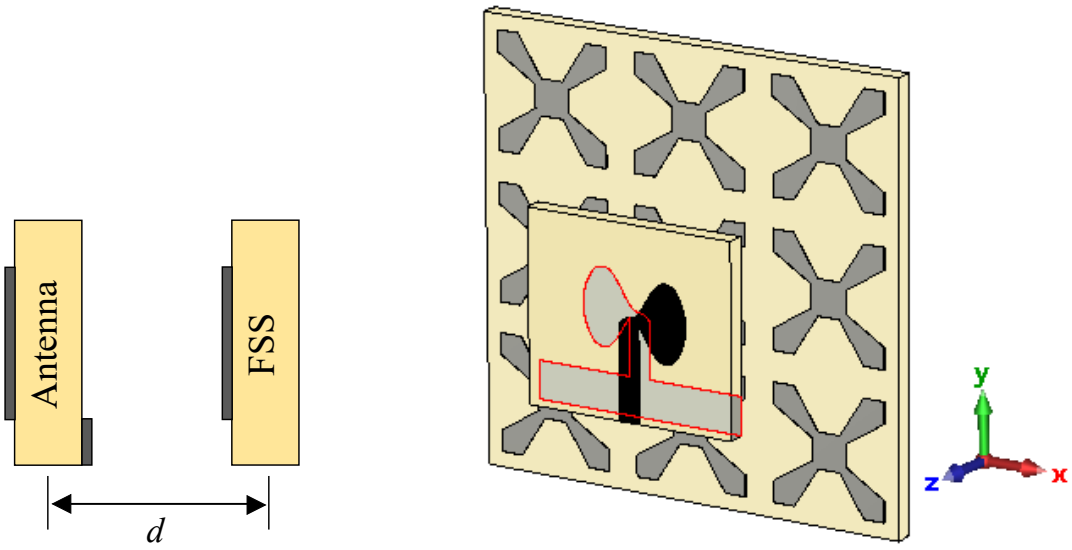

(a) Side view. (b) 3-D view.

Figure 5.14: Schematic diagram of proposed enhanced gain antenna using FSS.

illustrated in Figures 5.15a and 5.15b. From the 3D radiation pattern, the antenna gain obtained is 7.38 dBi. The FSS proves to be a viable option to enhance the gain by acting as a planar lens, and if it is a reconfigurable FSS, it can reconfigure the antenna radiation pattern.

The radiation pattern of the proposed antenna system using a 3 × 3 FSS panel is shown in Figure 5.16. As expected, the results show similar characteristics as for the one with the 2 × 2 panel. In the E-plane, the maximum gain is 7.68 dBi in the perpendicular direction at $\theta = 357°$ and HPBW of 64.1°, as shown in Figure 5.16a. In the H-plane (Figure 5.16b), the radiation pattern shows a gain of 8.68 dBi in the direction forward from the antenna at $\theta = 338°$, with the HPBW is 77.2° and beam tilt angle of 97°. Figure 5.16c shows the 3D radiation pattern for the antenna with 3 × 3 FSS, and the antenna gain obtained is 8.68 dBi.

By increasing the number of unit cells in the panel, the realized gain and tilt angle are also increased. When the FSS panel increased from 2 × 2 elements to 3 × 3 elements the gain is improved by 1.3 dB and the beam tilt angle by 25°. The panel using a four-arms star as element shape is more compact when compared to the cross-dipole, e.g., a panel of the proposed geometry with 6 × 6 occupies about the same area as one panel with 5 × 5 cross-dipole elements.

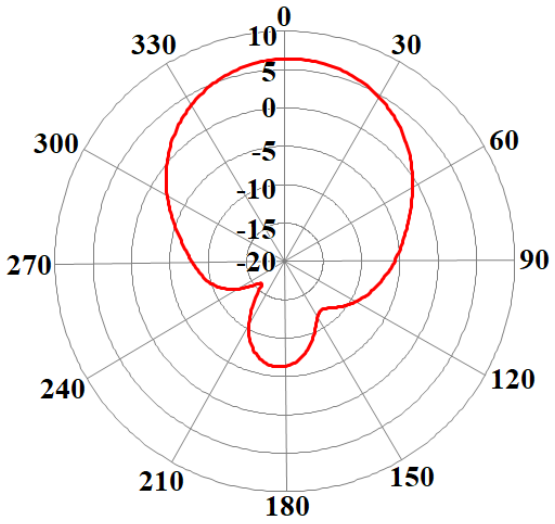

(a) E-plane.

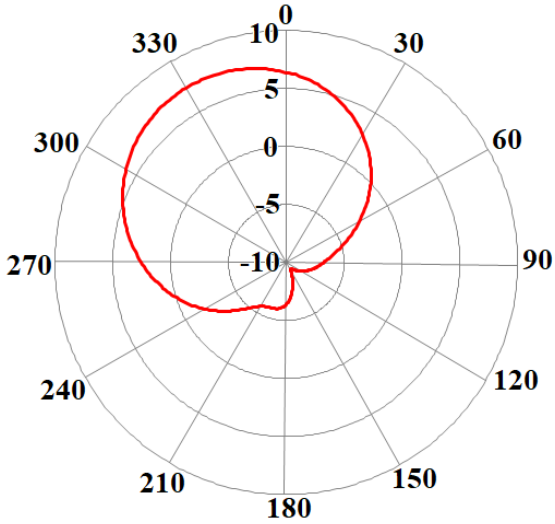

(b) H-plane.

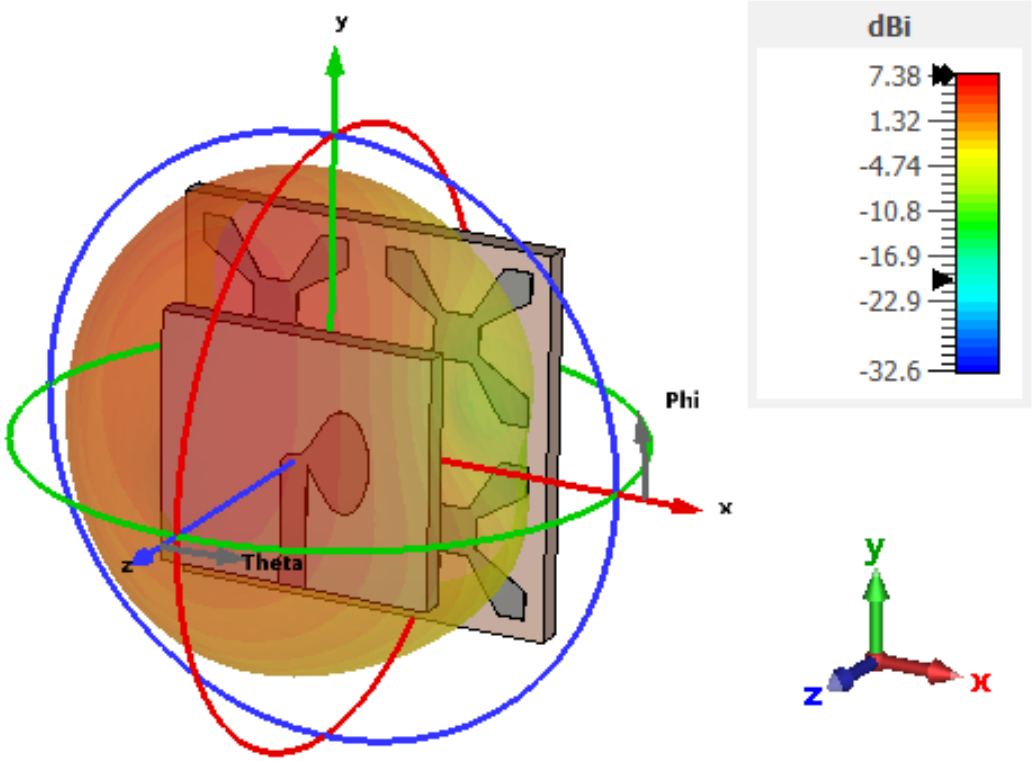

(c) 3-D view.

Figure 5.15: Simulated radiation pattern of the proposed antenna system with enhanced gain by using 2 × 2 FSS panel.

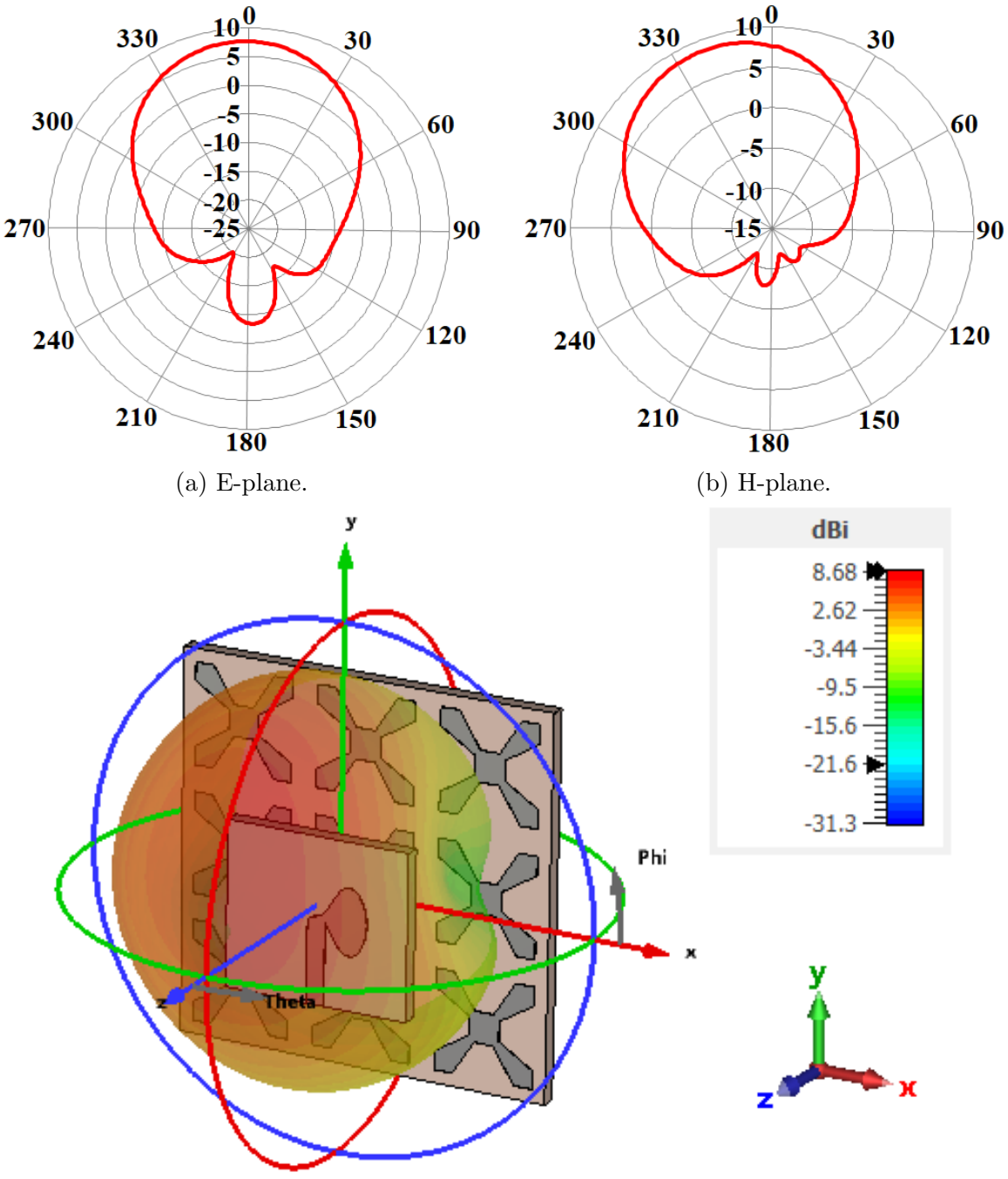

(a) E-plane.

(b) H-plane.

(c) 3-D view.

Figure 5.16: Simulated radiation pattern of the proposed antenna system with enhanced gain by using 3 × 3 FSS panel.

5.5.1 Performance assessment

The results from the proposed antenna system showed that the FSS with unit cell based on the four-arms star geometry acts as a reflector, enhancing the antenna gain,

and also has the ability to tilt the beam.

A comparison of the proposed antenna system with previously related works is summarized in Table 5.3, in terms of frequency of operation, gain enhancement, beam-tilting, and technique applied to achieve better performance. The proposed system is able to achieve high gain and high beam tilt angle. Moreover, the technique applied consists of using only an FSS as reflector, which offers less complexity to be implemented.

Ref.	Gain enhancement (dB)	Freq. (GHz)	Beam tilting (°)	Technique
[192]	5	6.5	Not available	7-double-layers vertical metamaterial
[193]	5	60	30	4-layers vertical metamaterial
[194]	2.2	9.5	17	Single-layer artificial medium
[195]	3	28	38	2-double-layer FSS
This work	4.08	28	97	Single-layer FSS

Table 5.3: Comparison of proposed antenna system with other reported ones.

Chapter 6

Dual- and Triple-Passband Coupled Complementary FSSs Based on Electromagnetically Induced Transparency Effect

In this chapter systems of closely coupled complementary FSSs with dual- and triple-passband responses are proposed. Four complementary structure configurations are presented, and depending on the configuration chosen, the structure can create two or three transmission bands in one or both polarizations of the electromagnetic waves. The designed FSSs are compact and have stable behavior at different incident angles. The complementary FSS passes signals around 2.6 GHz and 6.2 GHz, and a structural offset allows the transmission at a third frequency (4.2 GHz). To validate the proposed designs, four prototypes are fabricated and measured. Numerical and experimental characterizations are in good agreement.

This chapter contains material extracted from the following paper:

D. F. Mamedes, J. Bornemann, A. Gomes Neto and Sérgio L. M. Sales Filho, "Dual- and Triple-Passband Coupled-Complementary FSSs Based on the Four-Arms Star Geometry," accepted in IET Microwaves, Antennas & Propagation.

6.1 Introduction

The fifth generation (5G) wireless communication systems provide high speed and good quality transmission, while supporting a wide variety of data usage volumes, as discussed in Chapter 1. Modern communication systems face the existence of various kinds of interference signals and limited spectrum resources. Systems that can serve users with multiple bands at the same time, while blocking unwanted signals have become desirable. FSSs with multi-band characteristics have appeared as a solution to be incorporated in these systems to meet their stringent requirements.

When the periodic arrays of patch- and slot-type elements have identical shape, they present a complementary response, i.e., the specular reflection of EM waves for one array is equal to the transmission of EM waves of its complementary one. This arrangement follows Babinet's principle which states that the sum of the wave transmitted through a screen with an aperture and the wave transmitted through a complementary structure is equal to the wave transmitted when no screen is present [12], [204]. Note that Babinet's principle is for free- standing structures, i.e., complementary FSSs (CFSSs) are not purely Babinet's complement because of the presence of a dielectric (for mechanical purposes) between the patch and slot arrays, but the general concept still applies [205]. The two metallic layers combined in CFSSs will experience an interaction of transmission and reflection characteristics of each individual layer, due to a strong EM coupling between the layers, leading to the CFSS response.

Reference [206] proposes an angular stable dual-band FSS with anchor-shaped elements with different structural parameters along the x-axis alternately within a hexagonal wire grid mounted on a single-layer dielectric substrate (Figure 6.1). The FSS operates its two passbands in the Ku-band. Although the structure only uses one metal and one dielectric layer, the geometry is complex to design. The operating frequencies are stable under oblique incidence, but there is a deterioration of the first transmission band by about 50% at an angle of incidence of 60°, and the structure is polarization sensitive.

Reference [207] presents an antipodal F-type FSS with multi-band characteristics. The structure consists of a dielectric substrate with double metallization. The top layer is formed by four rotated F-type resonators, another set of them scaled down placed in the inner side of this layer, and a square loop surrounding all resonators. The bottom layer is formed by antipodal all F-type resonators (Figure 6.2). The structure

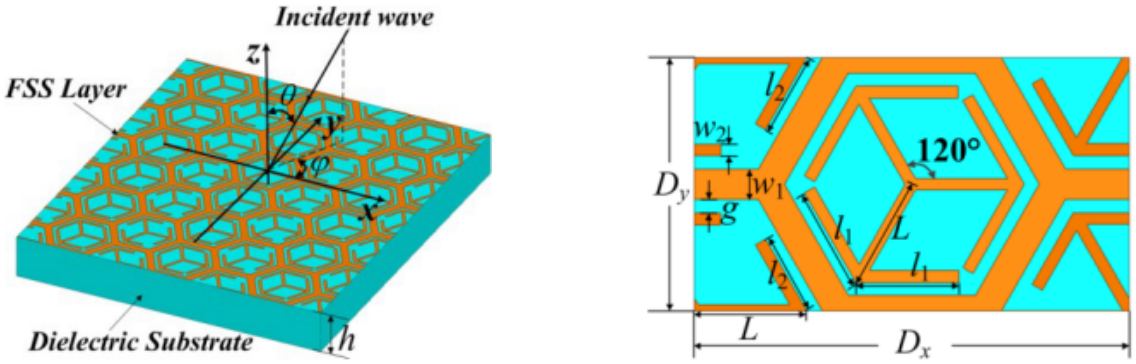

(a) 3-D view. (b) Unit cell.

Figure 6.1: 1-layered multi-band FSS proposed in [206].

operates at 2.4, 5.2 and 5.9 GHz with measured results for normal incidence ($\theta = 0°$), and stable performance for oblique incidence up to 60° for numerical results with maximum resonance frequency deviation (RFD) of 1.6%.

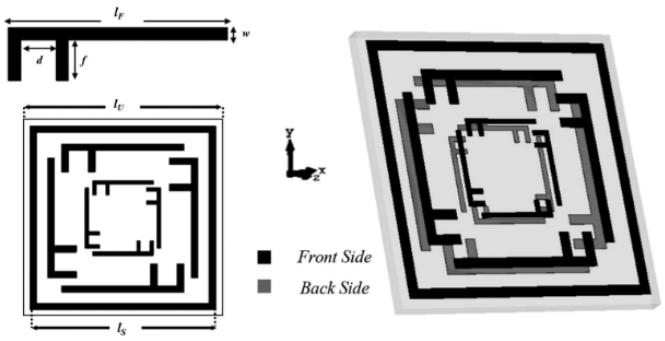

Figure 6.2: F-type element, unit cell top view, and 3-D view of 2-layered multi-band FSS proposed in [207].

A dual-band FSS, operating in the Ku-band, based on two circular patches and a circular coupling aperture, whose elements have different sizes, is presented in [208]. The structure is composed of three metallic and two dielectric layers, with unit cell dimensions of about half a wavelength, which makes the proposed FSS large and bulky (Figure 6.3). The results show low attenuation in the rejection band (approx. -18 dB) between the two passbands, and insertion loss of the two passbands are 0.22 and 0.26 dB, respectively. The -3-dB bandwidths of the lower and upper passbands are 1.14 GHz (11.81–12.95 GHz) and 1.02 GHz (16.42–17.44 GHz), respectively, at normal incidence.

A miniaturized dual-band FSS with frequencies of operation in X- and Ka-band is

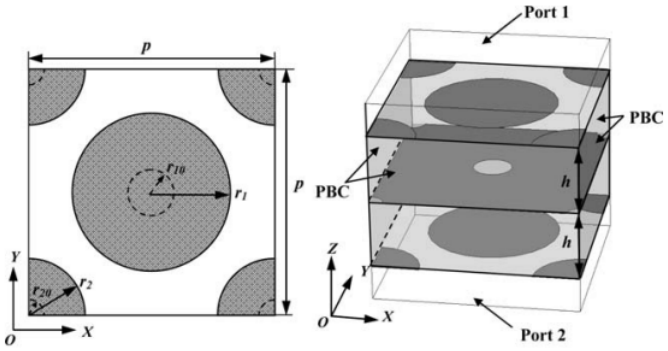

Figure 6.3: Unit cell top view and 3-D view of 3-layered multi-band FSS proposed in [208].

proposed in [209] where a cascade system of two-dimensional periodic arrays of double square loops and an array of wire grids are implemented to achieve small element size (Figure 6.4). The proposed structure is composed of three metal and two dielectric layers that act as a spatial dual-band microwave filter with large band separation. There are two transmission windows at X- and Ka-bands with center frequencies at 9.95 and 31.85 GHz, respectively. The -3-dB bandwidths of the lower and upper passbands are 3.5 ($8.1 - 11.6$ GHz) and 6.2 GHz ($28.8 - 35$ GHz), and the fractional bandwidths are 35% and 19.5%, respectively.

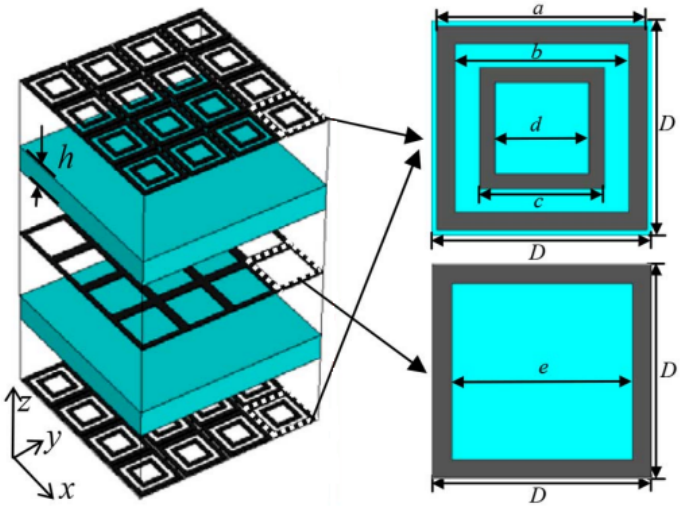

Figure 6.4: Expanded view and enlargement of the unit cells of 3-layered multi-band FSS proposed in [209].

Reference [210] proposes a multi-layered FSS with multi-band response and polarization dependence. The structure is composed of three layers of metal and two

layers of dielectric substrate. The design consists of a metal square aperture element between two identical asymmetric Jerusalem cross patches, resulting in a miniaturized structure (Figure 6.5). It presents dual-band behavior for the TE polarization with resonance frequencies at 7.28 GHz and 26.94 GHz, and single-band characteristics for the TM polarization with a resonance frequency at 11.39 GHz.

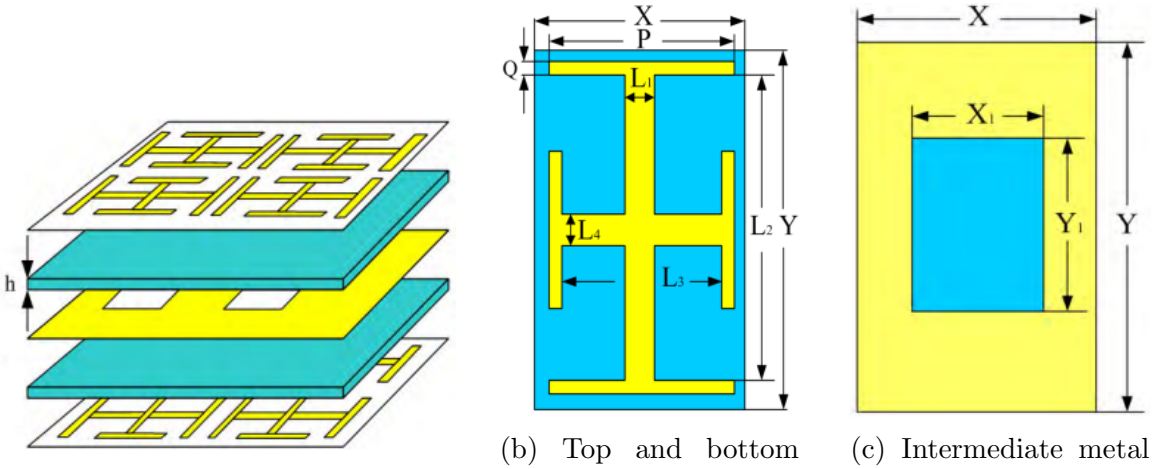

(a) Expanded and side views.

(b) Top and bottom metal layer structures.

(c) Intermediate metal layer structure.

Figure 6.5: 3-layered multi-band FSS proposed in [210].

A triple-passband highly selective FSS with miniaturization characteristics is proposed in [211]. The structure consists of a multi-layer combination of three metal layers separated by two dielectric substrates. The top and bottom layers have the same pattern which is composed of a meandered cross slot and four edge slots. The middle layer is formed by metallic square loops (Figure 6.6). The three passbands are located at 20.9 GHz, 29.9 GHz and 38.5 GHz. The out-of- band isolation between operating bands is up to 20 dB.

Reference [212] presents an FSS with triple-passband response achieved by cascading three layers of periodic arrays. The top and bottom layers are composed of gridded-double square loop elements and the middle layer is composed of double square loops (Figure 6.7). The results show a wide out-of-band rejection between the adjacent passbands provided by multiple transmission minimums. As the angle of incidence increases, the attenuation reduces by about 20 dB for an incidence of 60°.

A dual-band FSS with passband response is developed in [213]. The FSS is composed of two metal-based square patch layers at the two ends and one aperture type layer in the middle, separated by two dielectric substrates (Figure 6.8). The structure exhibits two passbands at 2.5 and 5.5 GHz. The design is polarization sensitive, and

(a) Expanded and side views.

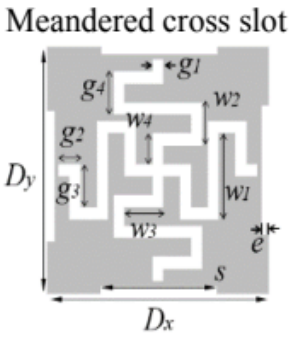

(b) Top and bottom metal layer structures.

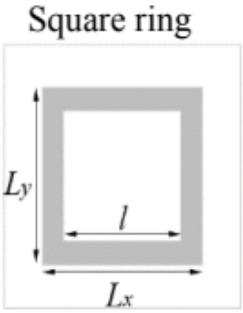

(c) Intermediate metal layer structure.

Figure 6.6: 3-layered multi-band FSS proposed in [211].

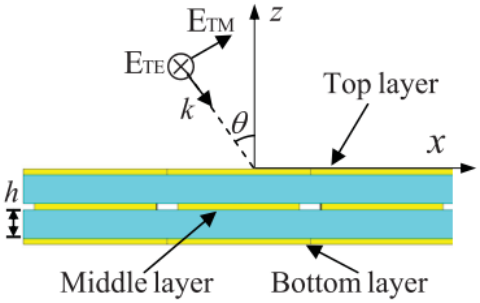

(a) Expanded and side views.

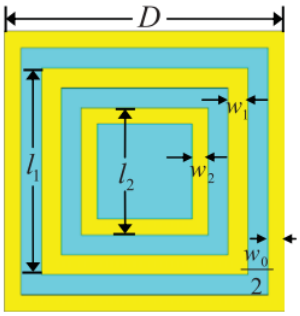

(b) Top and bottom metal layer structures.

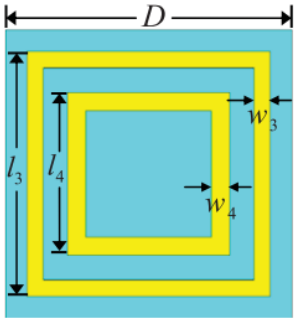

(c) Intermediate metal layer structure.

Figure 6.7: 3-layered multi-band FSS proposed in [212].

the authors only exploited the transverse electric (TE) polarization, showing it to be stable for oblique incidence up to 45°.

In this work, dual- and triple-passbands FSSs are proposed for 5G applications using complementary structures. Double- and single-metallic layered structures, supported by only a single substrate, represent closely coupled complementary FSSs inspired from Babinet's principle. The element's geometry and filtering mechanism are presented, showing that the operating frequencies can be adjusted independently. And offset-based structures are proposed as well, and they are fabricated to validate their design, where the Electromagnetically Induced Transparency (EIT) effect is applied to create an extra passband. Measurements of the transmission coefficients, including normal and oblique incidence, are presented, showing good agreement with simulated results.

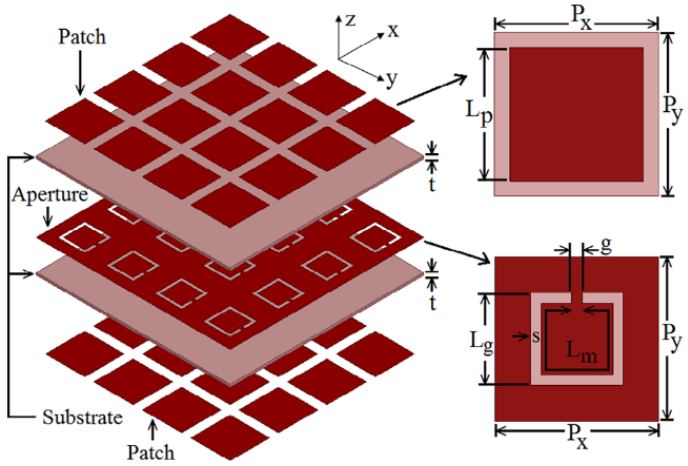

Figure 6.8: Expanded view and enlargement of the unit cells of 3-layered multi-band FSS proposed in [213].

6.2 Single-layer FSS analysis and design

This section presents the design and analysis of a unit-cell FSS based on the four-arms star geometry with a patch-type element and its complementary one, individually, on a single-layer substrate. The numerical characterizations of all structures are obtained through the commercial software package CST Microwave Studio. The dielectric substrate considered in the simulation has $\epsilon_r = 4.4$, thickness of 1.0 mm, and loss tangent of 0.025.

6.2.1 Four-arms star patch-type FSS

The first structure is the four-arms star patch-type element so that in this case, the inside of the element has metallic filling. The design procedure for this geometry was described in Chapter 3, Section 3.2.1. Figure 6.9a illustrates the unit cell with this element, including its parameters. The dimensions of the structure are $p_p = 17$ mm, $a_p = 15.4$ mm, $s_p = 2$ mm and $b_p = 1.5$ mm. The numerical characterization of the four-arms star patch-type FSS is shown in Figure 6.10 (blue curve), with resonance frequency at 5.24 GHz and characteristics as a stop-band filter.

6.2.2 Four-arms star slot-type FSS

The design procedure of the four-arms star slot type is similar to the patch one, except that in this case the inside of the element is detached from the metallic surface. Figure

6.9b shows the slot unit cell with its parameters.

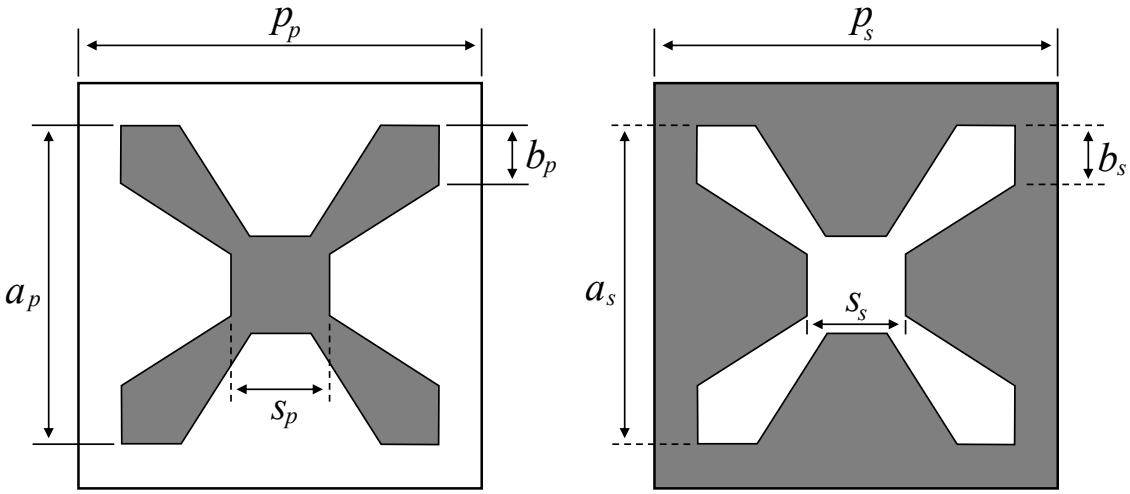

(a) Patch-type. (b) Slot-type.

Figure 6.9: Geometry and parameters of single-layer FSSs.

The design process of the four-arms star slot-type FSS follows the same concept used for a cross-dipole element [12], where the length of the arms is set to half wavelength, then the first resonance frequency can be estimated as

$$f_{\text{slot}}(\text{GHz}) = \frac{0.3}{2a_s\sqrt{\epsilon_{r_{\text{eff}}}}} \tag{6.1}$$

Note that the design considers a dielectric slab added to the array, thus the resonance frequency is shifted when compared to the free-standing structure. The frequency is shifted with the factor $\sqrt{\epsilon_{r_{\text{eff}}}}$ as shown in the above equation. Reference [152] presents an interpolating formula that fits the variation of the effective permittivity

$$\epsilon_{r_{\text{eff}}} = \epsilon_r + (\epsilon_r - 1)\left[\frac{-1}{e^{\frac{10h}{p_s}N}}\right] \tag{6.2}$$

which considers the dielectric permittivity and thickness of the substrate h, periodicity p_s, and the exponential factor, N, of the unit cell filling. For the geometry proposed, the value of N is 3.8.

In this design, the structure parameters have the same value as the patch-type one, i.e., $p_s = p_p$, $a_s = a_p$, $s_s = s_p$ and $b_s = b_p$. As expected, the frequency response of the slot FSS has a band-pass behavior with resonance frequency at 4.82 GHz (Figure 6.10, red curve), with a difference of 8% compared to the resonance frequency of the

patch-type FSS. The difference between the reflection coefficient of the patch element and the transmission coefficient of its complementary one is due to the fact that the structures are not freestanding. A dielectric substrate is used for mechanical support, and its parameters affect the frequency response of the arrays, shifting their resonance frequency as established in Equation 6.1. If the dielectric slab is removed from both structures, they will exhibit the same resonance frequency.

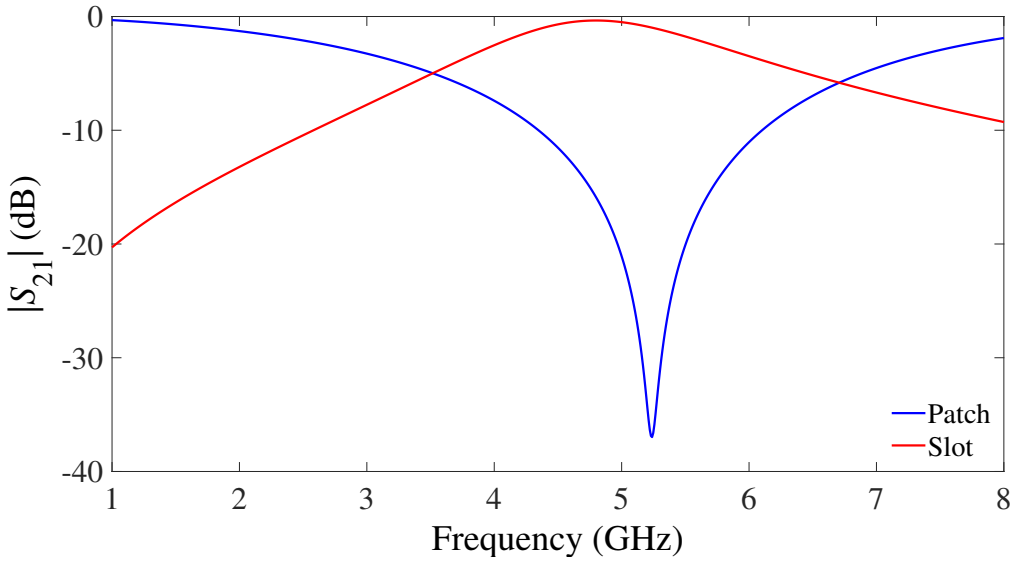

Figure 6.10: Numerical results of patch-type and slot-type elements FSSs.

6.3 Babinet's principle for electromagnetic fields

The patch and slot elements presented in the previous section are complementary structures for which Babinet's principle applies. Babinet's principle follows from the Huygens-Fresnel principle, wherein the diffraction stems from the mutual interference of the secondary wavelets originating from the wave-front, and states that the sum of the wave transmitted through a screen with an aperture and the wave transmitted through a complementary structure is equal to the wave transmitted when no screen is present [12], [204], [214]. Babinet's principle in optics does not consider polarization, it deals primarily with absorbing screens. An extension of Babinet's principle, which includes polarization, was introduced by Booker [215], [216], who considered perfectly electrically conducting screens and demonstrated that the electromagnetic fields in

the complementary screen (labeled with a $'$) that appear in Babinet's principle should be the dual fields $-B'$ and E' rather than the nominal fields E' and B'.

Considering the incident fields being labeled with i, the incident fields for the complementary case are $E'_i = -B'_i$ and $B'_i = E'_i$. Then, the fields on the side of the screen away from the sources is

$$E_{\text{away}} + B'_{\text{away}} = E^i_{\text{away}} \tag{6.3a}$$

$$B_{\text{away}} - E'_{\text{away}} = B^i_{\text{away}} \tag{6.3b}$$

Therefore, the electromagnetic version of Babinet's Principle for the fields on the same side of the screen as the sources related to the transmitted fields (labeled with a t) E_t and B_t, if the perfectly conducting screen had no apertures is given by:

$$E_{\text{same side}} - B'_{\text{same side}} = E^t_{\text{same side}} \tag{6.4a}$$

$$B_{\text{same side}} + E'_{\text{same side}} = B^t_{\text{same side}} \tag{6.4b}$$

6.3.1 Solution for dual fields

Heaviside [217] extended Maxwell's equations so that magnetic charges and currents could be included,

$$\nabla \cdot E = 4\pi\rho \tag{6.5a}$$

$$\nabla \cdot B = 4\pi\rho' \tag{6.5b}$$

$$\nabla \times E = -\frac{4\pi}{c}J' - \frac{1}{c}\frac{\partial B}{\partial t} \tag{6.5c}$$

$$\nabla \times B = \frac{4\pi}{c}J + \frac{1}{c}\frac{\partial E}{\partial t} \tag{6.5d}$$

where ρ and J are the densities of electrical charge and current, and ρ and J are the densities of hypothetical magnetic charge and current. These equations admit E and B as solutions only when electrical charges and currents are present ($\rho' = 0$ and J'

= 0). So, if only magnetic charges and currents are considered, the electromagnetic fields E' and B' obey the duality relations expressed by

$$E' = -B' \tag{6.6a}$$

$$B' = E' \tag{6.6b}$$

6.4 Complementary FSS analysis and design

This section describes the design procedure of the CFSS, which combines the structures presented in the previous section. Four complimentary configurations are derived from combinations of the patch- and slot-type FSSs.

6.4.1 CFSS configuration

The complementary structure is achieved by designing the patch and slot elements using identical geometry shape and dimensions, and these elements are spaced by a medium. Figure 6.11 illustrates the three-dimensional topology of the proposed CFSS. The medium used to separate the elements is a dielectric substrate with thickness h and dielectric constant ϵ_r. The top layer of the substrate is formed by the patch element, while the bottom layer carries the slot one. In this work, the CFSS was designed with the same dimensions used for the individual FSSs presented in Section 6.2.

CFSS working principle

The patch and slot FSSs have complementary responses as demonstrated in Section 6.2. This occurs because the patch element behaves as a series LC circuit, providing a stopband filter response, while the slot element has characteristics of a parallel LC circuit with passband filter response [12]. When these two elements are stacked, e.g., as illustrated in Figure 6.11, the frequency response presents two transmission poles separated by a transmission minimum [218]–[220].

A TE (Figure 6.12a) and TM (Figure 6.12b) polarized wave arrives at the complementary FSS at normal ($\theta = 0°$) and oblique ($\theta \neq 0°$) incidence. The simulated transmission spectra of the complementary FSS considering these incidences are plot-

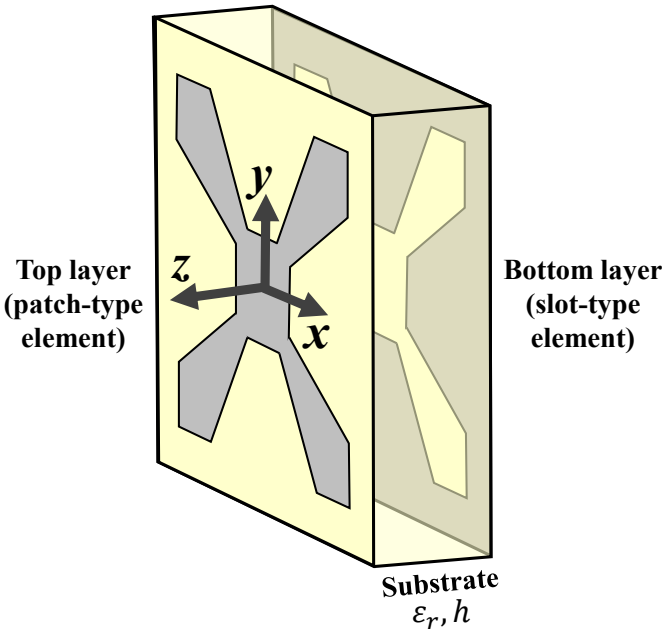

Figure 6.11: CFSS structuring.

ted in Figure 6.13. The corresponding spectrum exhibits two transmission maxima (f_{p1} and f_{p2}), as exploited above, and a transmission minimum (f_z) at normal incidence for both polarizations. When the angle of the incident wave is increased, the horizontal E-field probes a break in the symmetry of the two resonators, making the transmission minimum to become a transmission maximum (f_o). This phenomenon is known as Electromagnetically Induced Transparency (EIT) effect. The destructive interference at a particular frequency cancels the resonance effect due to the antiparallel currents of the two closely placed resonators. To further understand the physical mechanism, the surface current on each metal layer at the resonance frequencies are shown in Figure 6.14. Note that all currents are plotted with a common scale of 0 – 200 A/m.

This first proposed structure exhibits the same response at normal incidence for TE and TM polarization. Thus the surface current of this structure is plotted when the E-field of the incident wave is vertically polarized (Figure 6.14a–6.14c). The surface current of the two transmission maxima is demonstrated in Figure 6.14a and Figure 6.14b, suggesting that the passbands are formed by the edges of the arms of the slot element and the center of the patch element so that the current maxima of opposite directions appear around the corner of this spot in each element. Figure

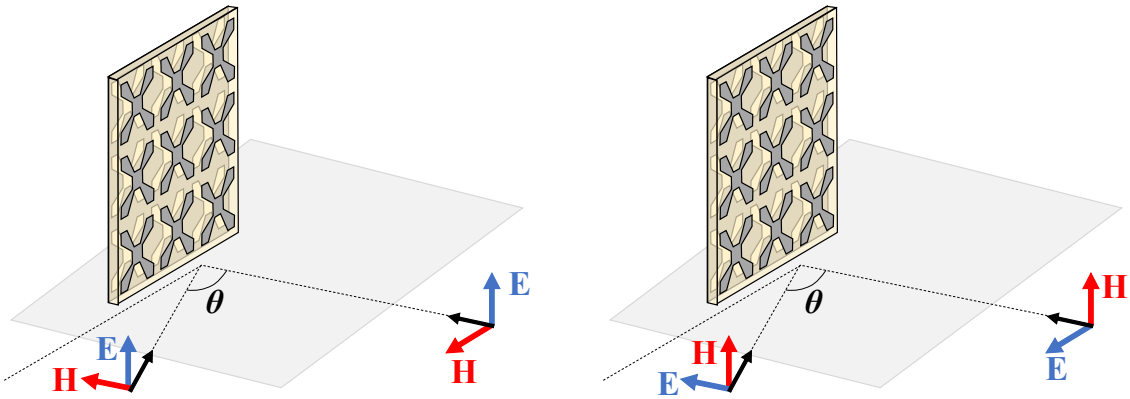

(a) TE waves incident. (b) TM waves incident.

Figure 6.12: Polarizations of the incident wave on the complementary FSS.

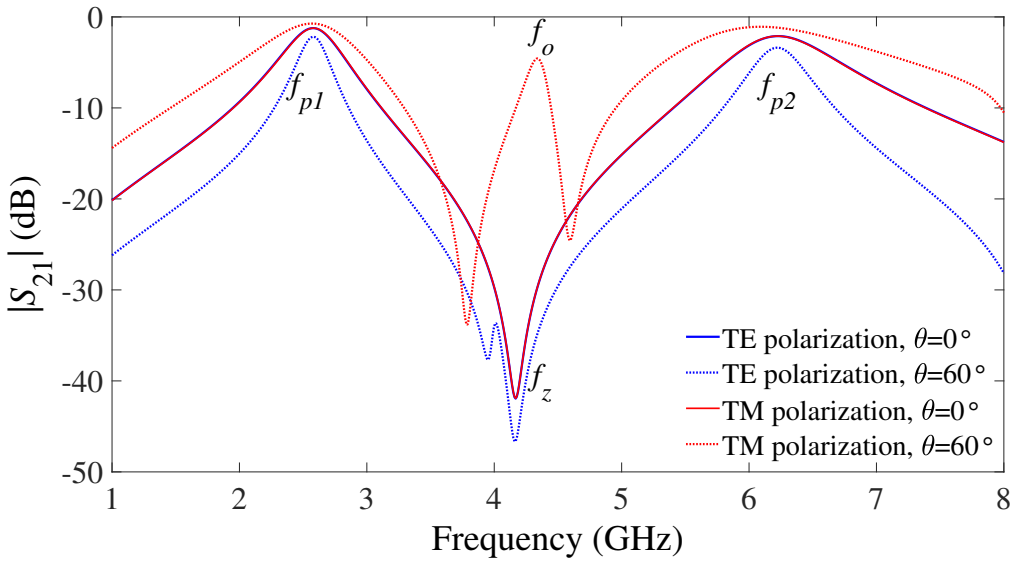

Figure 6.13: Simulated transmission spectra of proposed CFSS for TE and TM polarization at $\theta = 0°$ and $\theta = 60°$.

6.14c shows the surface current of the stopband at f_z, and there is no area with dense current distribution, which means the electromagnetic wave reflects through the FSS. As mentioned above, a transparency window is seen at oblique incidence for the TM polarization. To sort out the causes for f_o, we check the current distribution due to horizontally polarized oblique ($\theta = 60°$) incidence (Figure 6.14d). The current distribution in this scenario is similar to the ones found for f_{p1} and f_{p2} for the slot element, while in the patch element the current maximum happens on one of each

edges of the arms. This happened because in this condition the geometry symmetry is broken, leading to the excitation of the EIT effect by the coupling of the resonators modes.

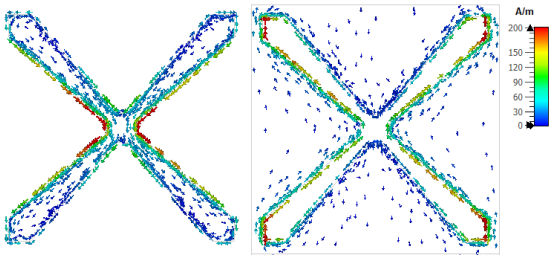

(a) Vertical polarized normal incidence at f_{p1}.

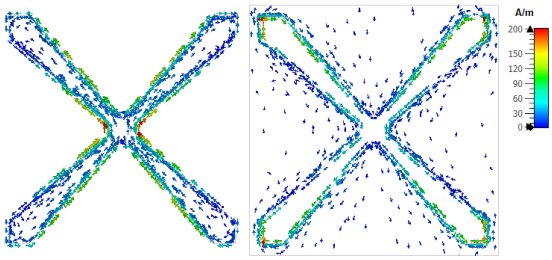

(b) Vertical polarized normal incidence at f_{p2}.

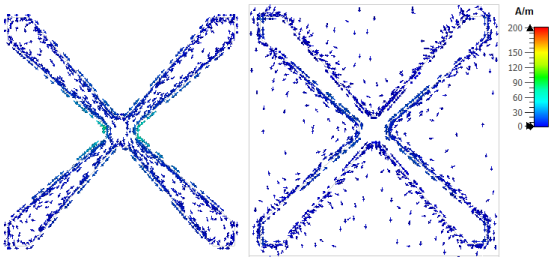

(c) Vertical polarized normal incidence at f_z.

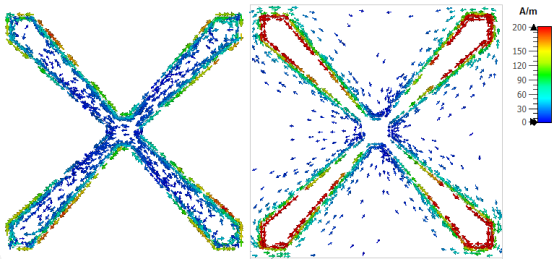

(d) Horizontal polarized oblique ($\theta = 60°$) incidence at f_o.

Figure 6.14: Surface currents on CFSS#1.

A parametric analysis served to evaluate the influence of the substrate thickness h and dielectric permittivity ϵ_r. Figure 6.15a presents the results considering $\epsilon_r = 4.4$ and varying the substrate thickness of $h = 0.25$, 0.5, 0.75, 1.00 1.50, 3.00 and 6.00 mm at normal incidence. The increase in the parameter h leads to the increase of the insertion loss at the desired frequencies. This effect is due to the degradation of coupling between the patch and slot elements. Note that the substrate thickness does not affect the resonance frequency of the first passband, only its bandwidth, because the substrate thickness is much smaller than the equivalent wavelength, but does affect the second pass-band frequency. As h increases, the second passband moves closer to the first one, until the separation of the elements causes its decoupling, making the second passband disappear completely and the FSS complementarity breaks down. The effect of the dielectric permittivity can be seen in Figure 6.15b. In this case, three substrate materials were considered, each of them has a different dielectric permittivity, with the substrate thickness set to $h = 1$ mm. The materials analyzed are Rogers RT5880 with $\epsilon_r = 2.2$ and loss tangent ($\tan\delta$) of 0.009, FR-4

fiber-glass with $\epsilon_r = 4.4$ and $\tan\delta = 0.025$, and Rogers RT6006 with $\epsilon_r = 6.45$ and $\tan\delta = 0.0027$. As ϵ_r increases, the resonance frequencies reduce as expected from Equation (6.1) and [221] and [222] for the design of the single-layer structures, which governs the CFSS response, and the bandwidth for both passbands are decreased. Although the thinner substrate and Rogers' materials offer low insertion loss, the FR-4 with $h = 1$ mm is chosen due to its low cost, commercial availability, and ease of fabrication/use.

6.4.2 Offset CFSS configuration

To evaluate the FSS complementarity, the patch and slot elements were offset from the center of the unit cell and its frequency response checked. In CFSS #2, a vertical offset of the elements is considered (Figure 6.16, left), while for CFSS #3 the elements are moved diagonally (Figure 6.16, right). Note that these structures have their elements with the same parameters dimension as in CFSS #1.

Offset CFSS working principle

The main idea of offsetting the elements is to form a transmission window at normal incidence in one or both polarizations by applying the EIT effect. When both elements of the CFSS are offset vertically (y-direction), the E-field in the TE polarization sees that the overall geometry is disturbed. In this scenario, a new transmission maximum (f_o) arises at the frequency that was initially the transmission minimum (f_z) between f_{p1} and f_{p2} from the original CFSS configuration (Figure 6.17, solid blue curve). In the TM polarization, the E-field does not see this change, thus maintaining almost the same response as in the original CFSS with normal incidence (Figure 6.17, dotted blue curve). For the CFSS with both elements offset in the diagonal orientation, a perturbation in the geometry of the unit cell is noticed by the vertical and horizontal E-field, allowing a transparency window to appear between f_{p1} and f_{p2} in both polarizations (Figure 6.17, solid and dashed red curves).

The induced surface current of the vertical and diagonal offset structures at f_o is demonstrated in Figure 6.18, considering the vertical E-field at normal incidence. The offset placement of the elements induces the anti-parallel currents, canceling the transmission minimum by inducing an EIT effect to achieve a bandpass window in the transmission spectra. Note that the current distribution for the vertical offset at normal incidence in the TE polarization, shown in Figure 6.18a, is similar to the one

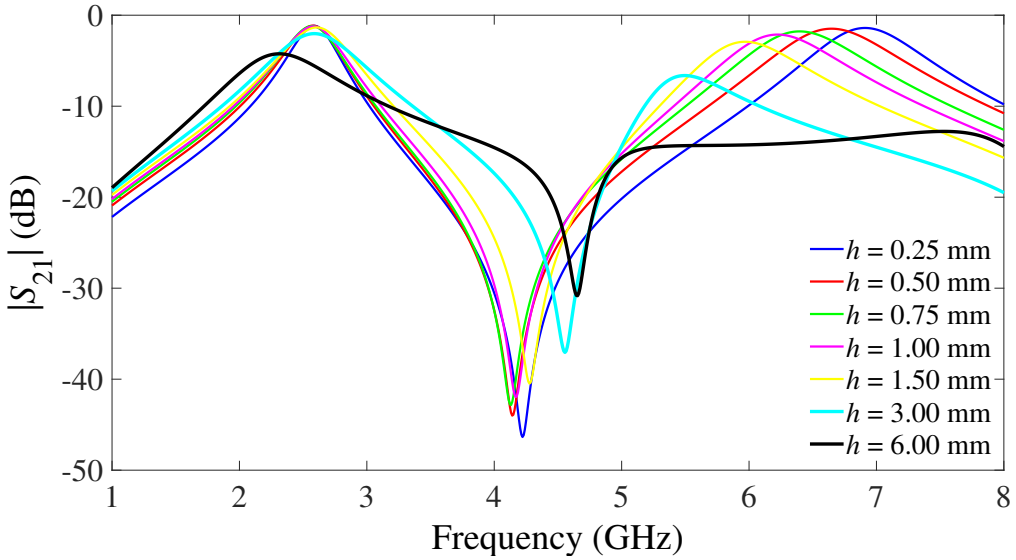

(a) Varying substrate thickness with $\epsilon_r = 4.4$.

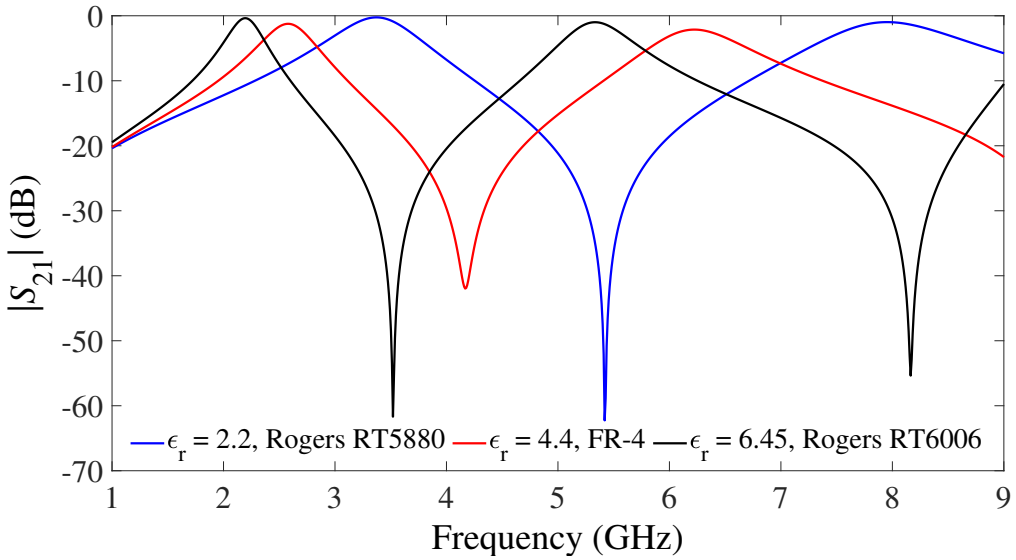

(b) Varying dielectric permittivity with $h = 1$ mm.

Figure 6.15: Comparison of frequency response of CFSS as a function substrate properties.

found in CFSS #1 with $\theta = 60°$ in the TM polarization (Figure 6.14d). Moreover, the vertical offset only offers a transmission window in one polarization, making the structure polarization dependent. When the diagonal offset is applied, a transparency window is achieved in both polarizations, making the structure polarization insensitive. As shown in Figure 6.18b, the diagonal offset also induces an EIT effect, but

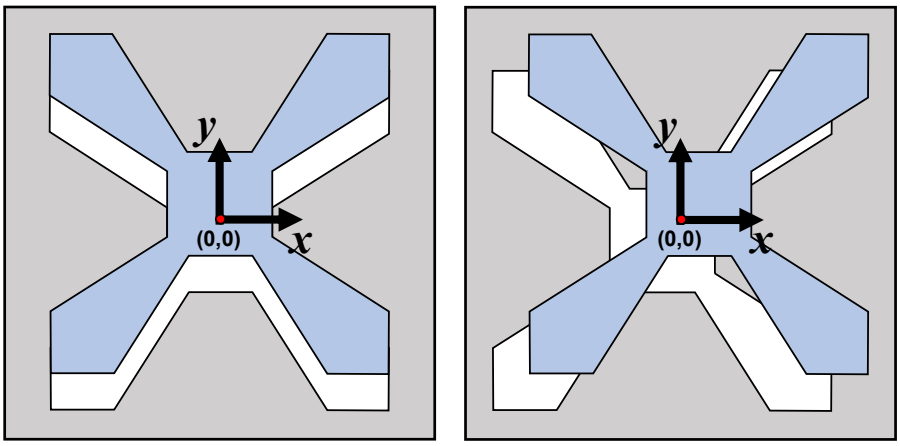

Figure 6.16: CFSS-based configurations with vertical (CFSS #2, left) and diagonal (CFSS #3, right) offset.

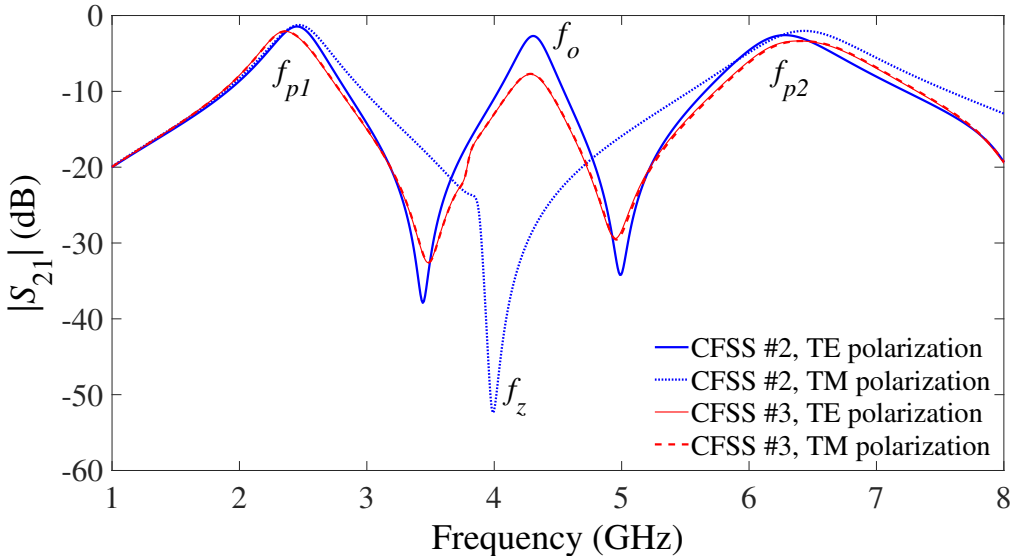

Figure 6.17: Simulated transmission spectra of CFSS #2 and CFSS #3 for TE and TM polarization at $\theta = 0°$.

the power in the f_o band is divided.

6.4.3 Single-layer quasi-CFSS configuration

In order to further evaluate the coupling between the elements, a fourth CFSS-based configuration is designed. In this configuration, the substrate only has a single-metal layer, and both patch and slot elements are etched on it. The elements are

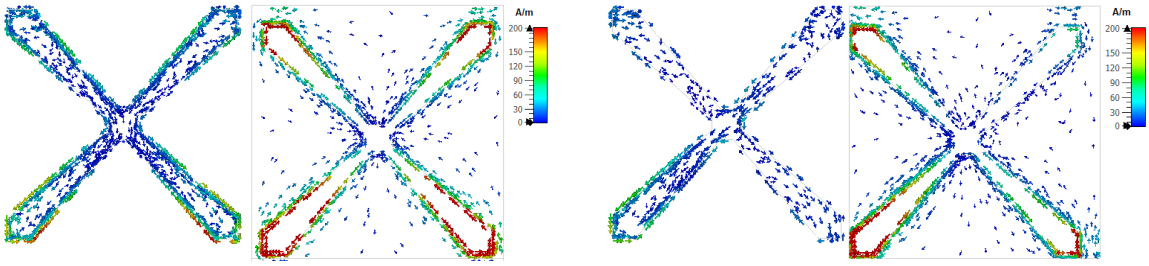

(a) CFSS#2. (b) CFSS#3.

Figure 6.18: Surface currents on offset CFSSs with vertical polarized normal incidence.

complementary in shape, but not in size. The patch element's dimension remains basically the same, but the unit cell of the slot element is adjusted to dovetail all the elements. Figure 6.19 shows the proposed single-layer complementary-based FSS (CFSS #4).

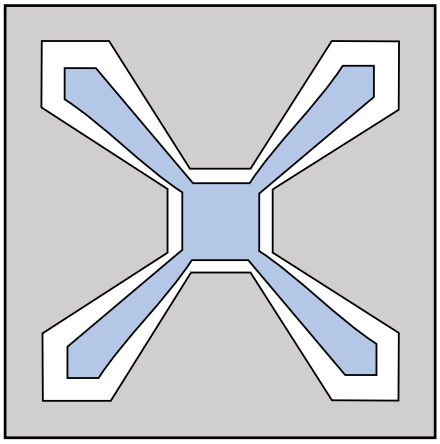

Figure 6.19: Single-layer complementary based FSS (CFSS #4).

Single-layer quasi-CFSS working principle

A parametric analysis is carried out to assess the influence of each element's size in the frequency response of the structure. Seven cases are analyzed with different values for the parameters of the elements (Table 6.1), but all cases consider the same unit cell size $p = 18$ mm, and FR-4 substrate with $h = 1$ mm.

From the results shown in Figure 6.20, it can be seen that each parameter affects differently the CFSS #4 response. The first case (Case #1) shows the effect of a_s

Table 6.1: Values of CFSS#4 parameters (mm). Dimensions according to Figure 1.

	a_p	a_s	b_p	b_s	s_p	s_s
Case #1	15.5	16	1.5	5	2	3
Case #2	14.5	17	1.5	5	2	3
Case #3	15.5	17	3	5	2	3
Case #4	15.5	17	1.5	3	2	3
Case #5	15.5	17	1.5	5	2.8	3
Case #6	15.5	17	1.5	5	2	5
Case #7	15.5	17	1.5	5	2	3

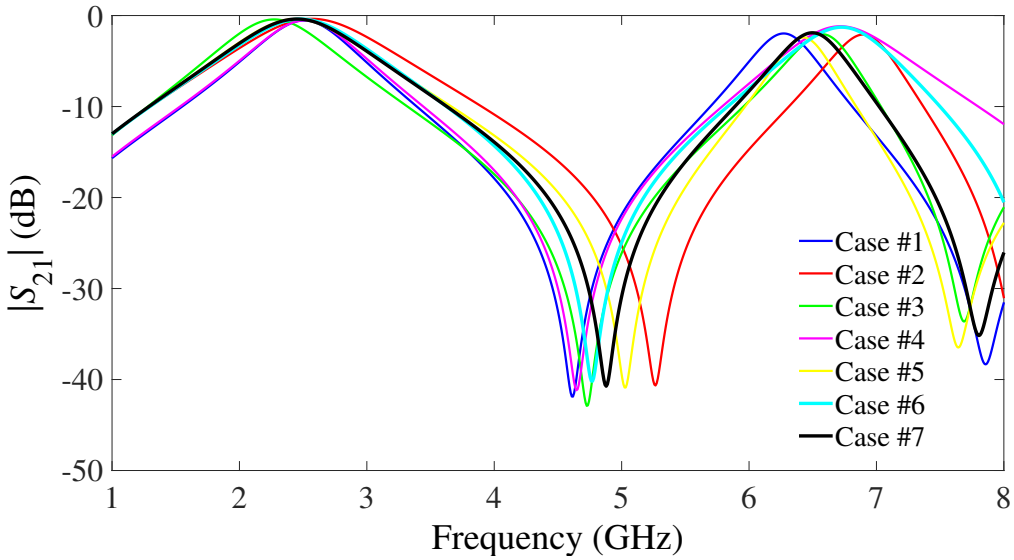

Figure 6.20: Comparison of frequency response as a function of varying CFSS #4 parameters as shown in Table 6.1 with unit cell size of 18 mm.

in the response of the structure, which moves f_{p2} and maintains its bandwidth, but it changes the bandwidth of the first passband to becoming more capacitive as a_s is increased. In Case #2 the size of the arms of the patch element (a_p) is changed, which shows a similar behavior as in Case #1 of moving f_{p2} and not altering its bandwidth, but now the first passband becomes more inductive as a_p increases. For Case #3, b_p only affects f_{p1} and its bandwidth by moving f_z while maintaining the second passband. Case #4 changes the value of b_s, hence moves f_{p2} and adjusts the transmission minimums to change the transmission bandwidth while keeping the same rejection bandwidth. If the first passband gets narrow, the second one gets wider and vice-versa. In Case #5 and Case #6 the parameters s_p and s_s are analyzed. For both cases the first transmission resonance and its bandwidth remain untouched, while

the second transmission maxima and their bandwidths change. The second passband becomes narrower if s_p is increased (more inductive) and wider if s_s is increased (more capacitive). To summarize, this analysis shows that the patch and slot elements are closely coupled and present the same characteristics as for the complementary FSS, and the bandwidths and resonance frequencies can be adjusted. The final dimensions chosen for CFSS #4 are presented in Case #7.

As to the CFSS #4, the S-parameter spectrum shown in Figure 6.20 indicate two passband and one stopband. Figure 6.21 shows the surface current at corresponding resonance frequencies. Similarly to CFSS #1, the current maxima of CFSS #4 are found at the same spots for Figure 6.21a and Figure 6.21b. Again, there is no dense current distribution for f_z (Figure 6.21c).

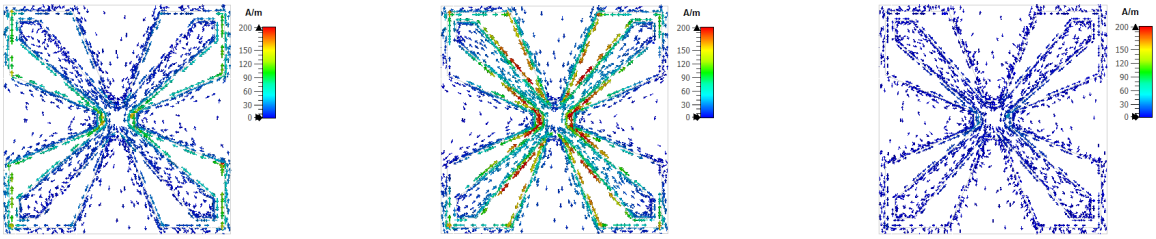

(a) f_{p1}. (b) f_{p2}. (c) f_z.

Figure 6.21: Surface currents on CFSS#4 with vertical polarized normal incidence.

6.5 Performance validation

Experimental characterizations of the four proposed CFSS-based configurations were performed to validate the numerical results. The characterizations consisted of sweeping θ in steps of 10°, but we will only exhibit the results for $\theta = 0°$, 20°, 40° and 60°, because the measured and simulated results agreed for all angles. All prototypes were manufactured on a single-layer low-cost FR-4 fiber-glass dielectric substrate with ϵ_r = 4.4, thickness of 1.0 mm, and tanδ = 0.025. Metallization are on both sides for CFSS #1, #2 and #3 designs, and single-sided for CFSS #4. The fabricated CFSSs have 11 × 11 elements and overall dimensions of 18.7 cm × 18.7 cm (CFSS #1, #2 and #3) and 19.8 cm × 19.8 cm (CFSS #4). The fabricated prototypes are presented in Figure 6.22. The top and bottom views of CFSS #1 are shown in Figure 6.22a and 6.22b, respectively, with enlargement of the unit cell of the patch and slot elements. The structures with the vertical and diagonal offsets are illustrated in Figure 6.22c

and 6.22d, respectively, only with the top view, but the overlap of the shifted elements can be clearly observed. Figure 6.22e shows the CFSS #4, which has only one metal layer.

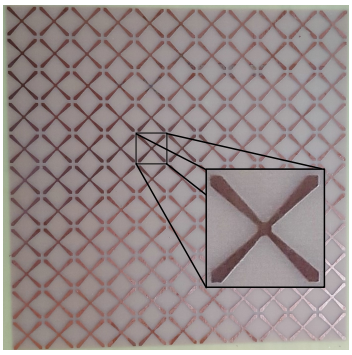

(a) CFSS#1, top view, patch elements.

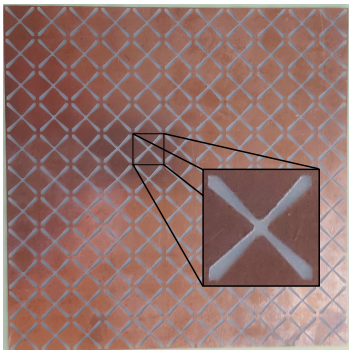

(b) CFSS#1, bottom view, slot elements.

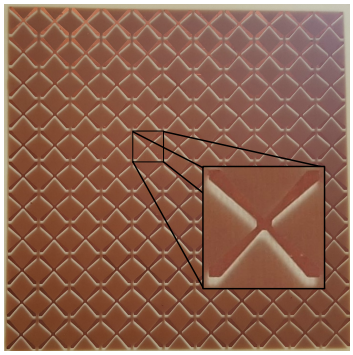

(c) CFSS#2, top view.

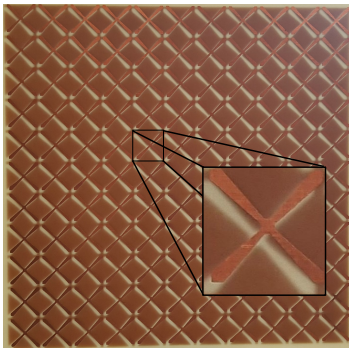

(d) CFSS#3, top view.

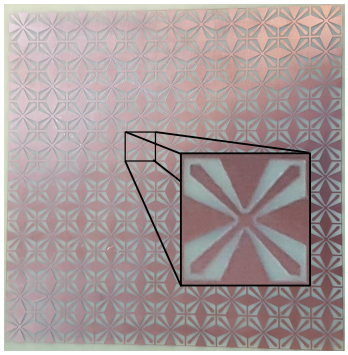

(e) CFSS#4.

Figure 6.22: Fabricated complementary structures.

Measurements were carried out with the setup described in Appendix A, Section A.2.2. The wave to the FSSs is considered to be at normal ($\theta = 0°$) and oblique ($\theta =$ up to $40°$) incidence, the latter angle limited by the absorbers around the measurement window.

6.5.1 CFSS results

The numerical and measured results for the CFSS #1 for the TE and TM polarization are presented in Figure 6.23. The behavior of the structure for normal ($\theta = 0°$) and oblique ($\theta \neq 0°$) incidence are depicted. There are two transmission maxima (f_{p1} and f_{p2}) and one transmission minimum (f_z) as predicted in the previous section for the FSS which is perfectly complemented and they are controlled by the elements'

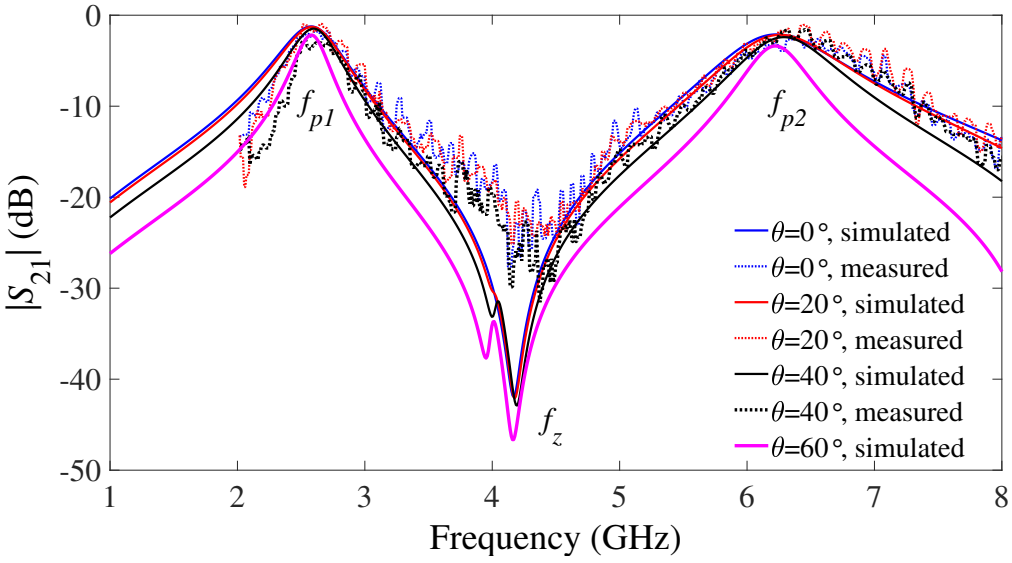

(a) TE polarization.

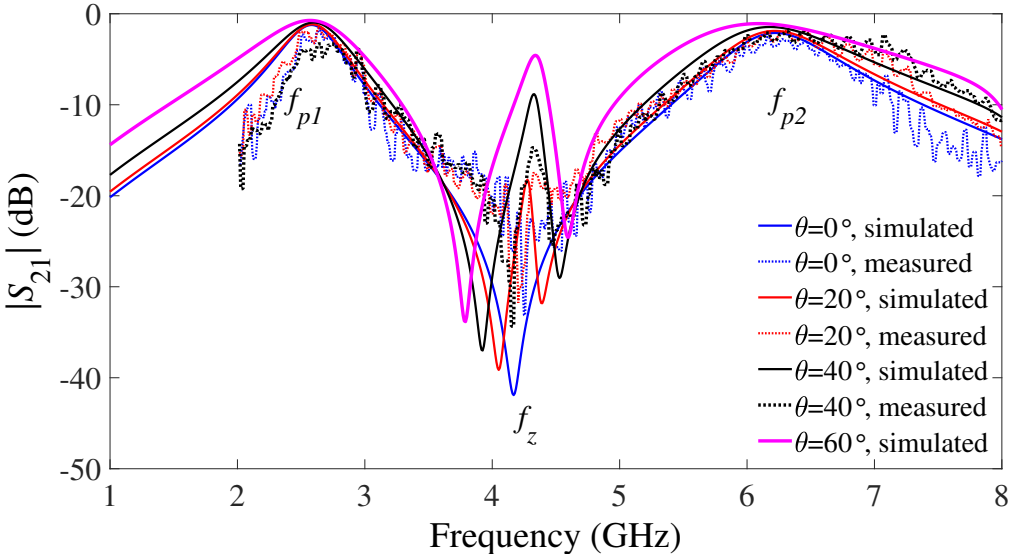

(b) TM polarization.

Figure 6.23: Simulated and measured results of CFSS#1.

dimensions. The CFSS was designed to operate at $f_{p1} = 2.6$ GHz and $f_{p2} = 6.2$ GHz. For the TE polarization (Figure 6.23a), the measured transmission maxima are 2.63 GHz and 6.37 GHz with a transmission minimum at 4.16 GHz, showing a good agreement with those obtained numerically ($f_{p1} = 2.58$ GHz, $f_{p2} = 6.26$ GHz and $f_z = 4.18$ GHz). The frequency response of the structure in this polarization is stable to the variation of incidence angle. The CFSS #1 is symmetrical, which means

the results for TM polarization are similar to the ones from TE polarization. For the TM polarization (Figure 6.23b), the simulated and measured resonance frequencies are $f_{p1} = 2.58$ GHz and 2.67 GHz, $f_{p2} = 6.22$ GHz and 6.32 GHz, and $f_z = 4.05$ GHz and 4.28 GHz, respectively. Note that in this polarization the structure is relatively stable to the normal and off-normal incidence at the transmission maxima, although a resonance arises in the transmission minimum at 4.28 GHz from simulated results. This effect occurs because the E-field starts to probe the broken intrinsic symmetry of the structure causing the destructive interference of scattered fields. The transparency window becomes stronger when θ increases, thus two transmission minimums appear. Based on this phenomenon, the offset of the elements is analyzed to understand how breaking the symmetry of complementary structures can lead to another transmission maximum.

6.5.2 Offset CFSS results

Vertical and diagonal offset were implemented to allow a transparency window between the two original transmission maxima. The simulated and measured S-parameter spectra for these structures are shown in Figure 6.24 and Figure 6.25, exhibiting a third passband obtained by the EIT effect.

Figure 6.24 shows the results of the CFSS with a vertical offset of its elements (CFSS #2). Three transmission maxima are observed in the TE polarization, two as seen in CFSS #1, and the third is due to the offset. The simulated transmission maxima are $f_{p1} = 2.45$ GHz, $f_o = 4.3$ GHz and $f_{p2} = 6.28$ GHz, and the measured ones are $f_{p1} = 2.49$ GHz, $f_o = 4.33$ GHz and $f_{p2} = 6.48$ GHz (Figure 6.24a), with a maximum difference of 1.6%, 0.69% and 3.08%, respectively. For the TM polarization (Figure 6.24b), the frequency characteristics remain similar to the ones seen for CFSS #1 with simulated and measured resonance frequencies $f_{p1} = 2.47$ GHz and 2.52 GHz, and $f_{p2} = 6.44$ GHz and 6.52 GHz, with a maximum difference of 1.98% and 1.23%, respectively. Thus, the offset in the CFSS can work as another parameter to control the frequency response by modifying the electromagnetic coupling level.

The CFSS #3 has a diagonal offset of both elements as indicated in Figure 6.16, resulting in three passbands for both TE and TM polarizations as shown in Figure 6.25a and Figure 6.25b, respectively. This configuration shows a behavior similar to that of CFSS #2, where the offset between the elements acts directly as the coupling level. The shift of the elements produces the third passband where originally there

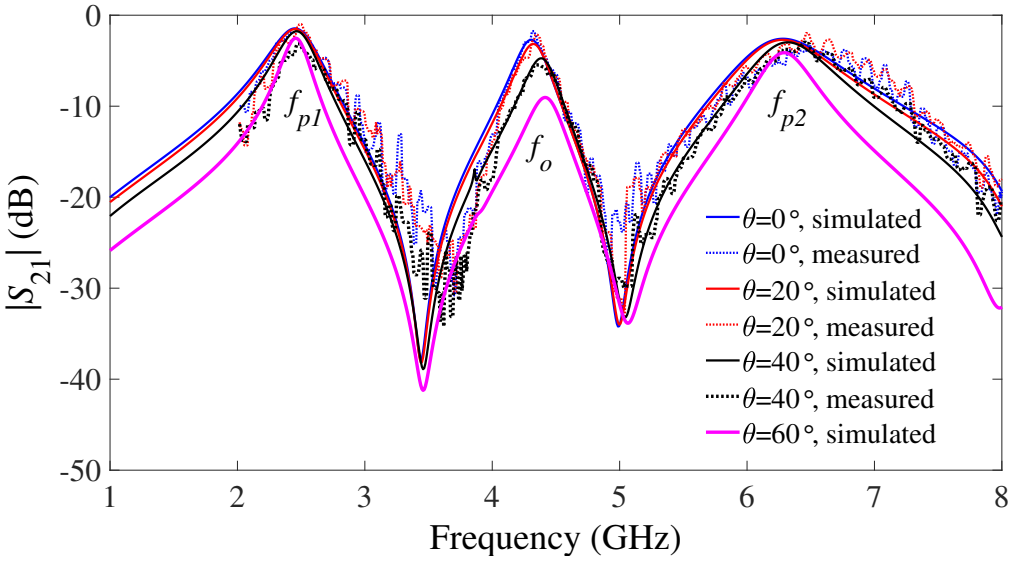

(a) TE polarization.

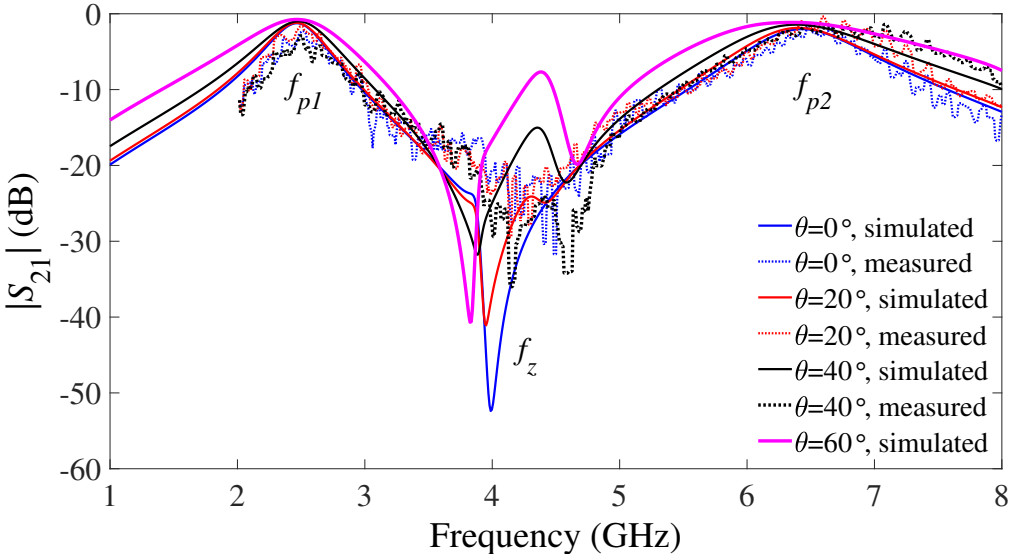

(b) TM polarization.

Figure 6.24: Simulated and measured results of CFSS#2.

was a transmission minimum. The transmission maxima in the TE polarization are $f_{p1} = 2.36$ GHz, $f_o = 4.28$ GHz and $f_{p2} = 6.39$ GHz (simulated) and $f_{p1} = 2.29$ GHz, $f_o = 4.36$ GHz and $f_{p2} = 6.66$ GHz (measured). Different from CFSS #1 and #2, this configuration presents the third passband in the TM polarization, where the resonance frequencies of the simulated and experimental characterization are $f_{p1} = 2.36$ GHz and 2.26 GHz, $f_o = 4.28$ GHz and 4.37 GHz, and $f_{p2} = 6.41$ GHz and 6.49 GHz,

respectively. Note that compared with Figure 6.15b, the higher insertion loss observed in Figure 6.25a and 6.25b is due the the fact that FR4 is a relatively lossy material with a loss tangent of only 0.025.

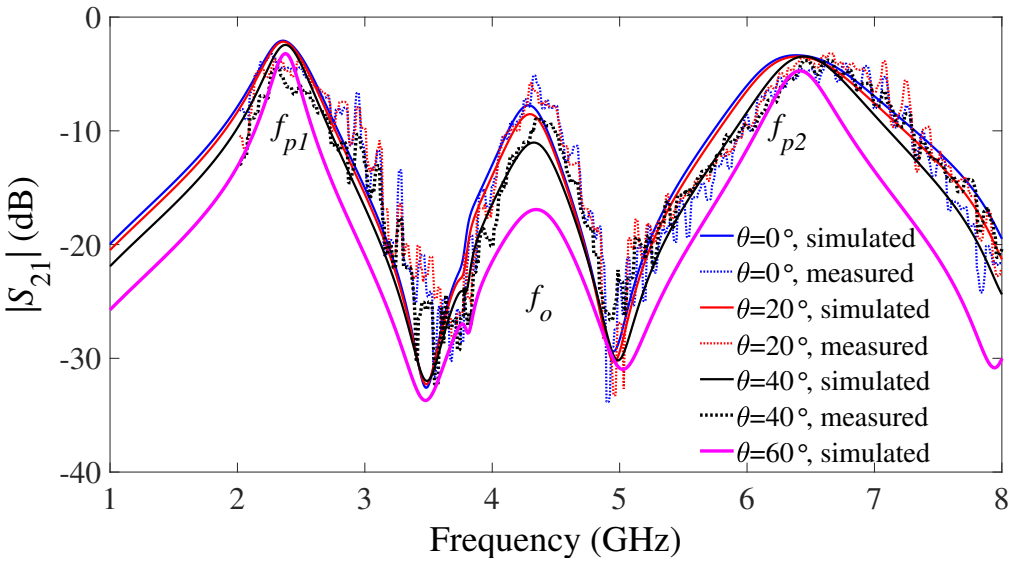

(a) TE polarization.

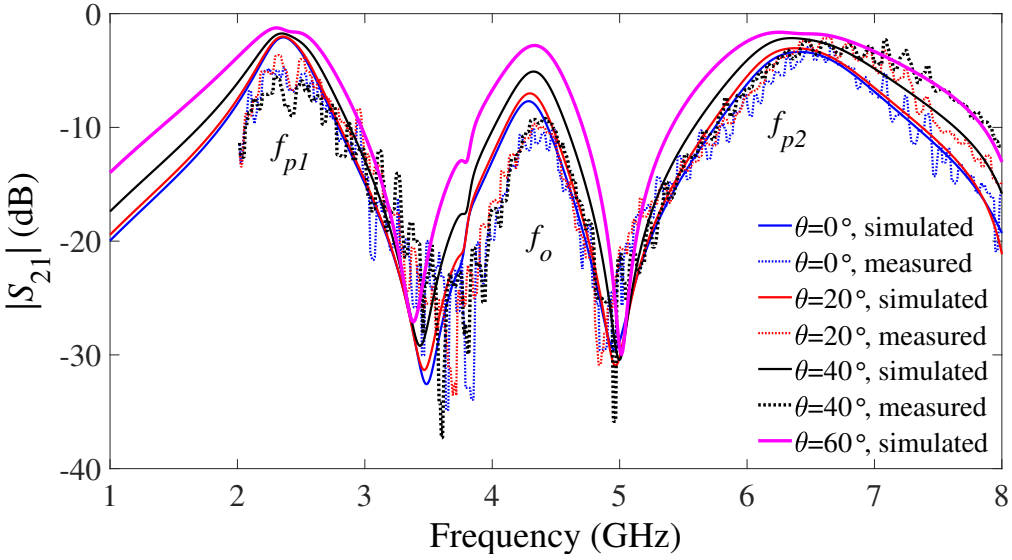

(b) TM polarization.

Figure 6.25: Simulated and measured results of CFSS#3.

6.5.3 Single-layer quasi-CFSS Results

The results of the fourth proposed complementary-based structure are shown in Figure 6.26. CFSS #4 was fabricated using the dimensions of Case #7 (Table 6.1), and its characterization also consideres normal and oblique incidence with θ up to 40°. For TE polarization, the two transmission maxima at 2.5 GHz and 6.7 GHz (numerical), and 2.66 GHz and 6.83 GHz (experimental), are the same for all incidence angles. A Fano resonance [171], [223] starts arising when $\theta = 20°$, but it does not interfere with the bandwidths. When in the TM polarization, transmission maxima are found to be basically the same as in the TE polarization due to its symmetry, with simulated and measured resonances $f_{p1} = 2.5$ GHz and 2.67 GHz, and $f_{p2} = 6.7$ GHz and 6.7 GHz, respectively. The Fano resonance is observed at $\theta = 10°$, and its amplitude increases as the oblique angle increases. Note that this structure shows a similar behavior as previous complementary FSSs, although it only uses one metal layer, and the coupling between the elements induces a Fano resonance at low oblique angles.

6.5.4 Performance assessment

Transmission measurement results confirm that a multi-band response is achieved by stacking complementary elements on double metal layer substrates or using quasi-complementary elements on a single metal layer substrate. Furthermore, if the offset of the elements is applied, a transparency window appears where initially was a transmission minimum.

The characteristics of our proposed structures are compared with previously related works in Table 6.2, which include the type of configuration, number of bands, frequencies of operation, unit cell dimensions, polarization sensitivity, angular stability and RFD. It can be observed that the proposed multi-band FSSs are more compact in terms of numbers of layers used and the size of the unit cell in order of wavelength of the lower band in free space. Depending on the configuration for the complementary structure, it can be sensitive or insensitive to the polarization of the incident wave and exhibits dual- and/or triple-bands of operations while keeping the original transmission maxima. In all configurations, the proposed CFSSs showed good angular stability for oblique incidence up to 60° with maximum RFD of 0.35% from $\theta = 0°$ to 60° (for the original CFSS). Note that the compactness and design simplicity of the proposed structures present an inherent advantage when applied in the mm-wave frequency range.

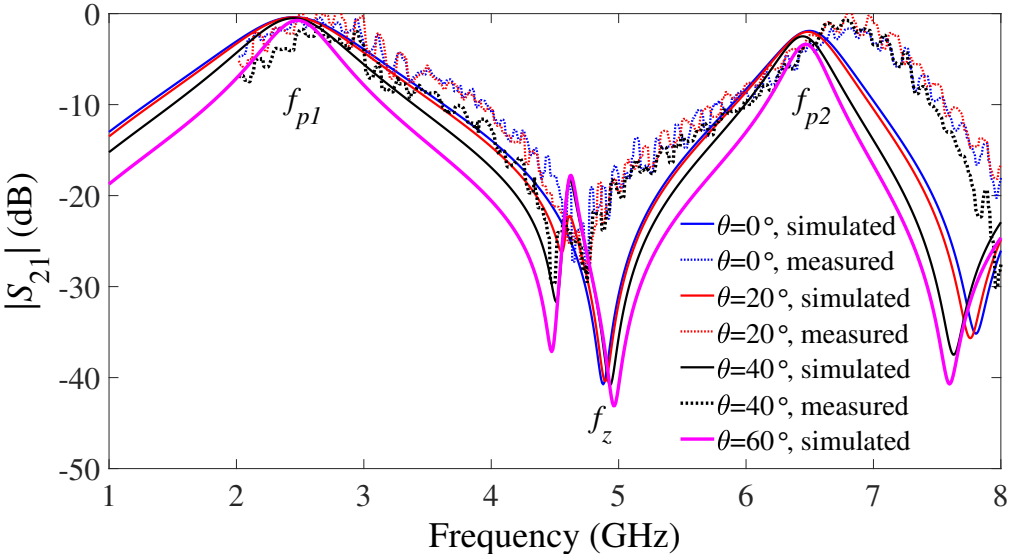

(a) TE polarization.

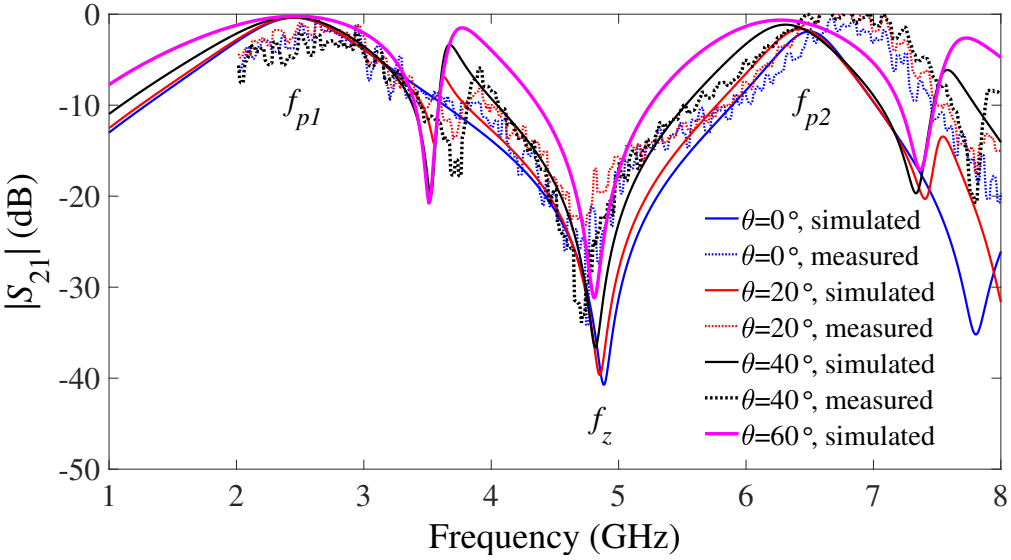

(b) TM polarization.

Figure 6.26: Simulated and measured results of CFSS#4.

Table 6.2: Comparison of proposed multi-band FSS with other reported ones.

Ref.	Configuration	Frequencies (GHz)	No. of bands	Unit cell size
[206]	1-metal and 1-dielectric	11.13 and 13.29	2	$0.27\lambda \times 0.27\lambda$
[207]	2-metal and 1-dielectric	2.4, 5.2 and 5.9	3	$0.20\lambda \times 0.20\lambda$
[209]	3-metal and 2-dielectric	9.95 and 31.85	2	$0.10\lambda \times 0.10\lambda$
[210]	3-metal and 2-dielectric	7.28 and 26.94, and 11.39	2 and 1	$0.08\lambda \times 0.24\lambda$
[211]	3-metal and 2-dielectric	20.9 and 29.9 and 38.5	3	$0.15\lambda \times 0.15\lambda$
[212]	3-metal and 2-dielectric	7.7, 12.8 and 18.9	3	$0.13\lambda \times 0.13\lambda$
[213]	3-metal and 2-dielectric	2.5 and 5.5	2	$0.10\lambda \times 0.10\lambda$
This work	2-metal and 1-dielectric	2.6, 4.2 and 6.2	2 and/or 3	$0.14\lambda \times 0.14\lambda$
Ref.	Polarization insensitive	Angular stability ($\theta_{\max}$)	RFD (%)	
[206]	No	60°	0.50	
[207]	Yes	60°	1.60	
[209]	Yes	60°	NA	
[210]	No	60°	NA	
[211]	Yes	60°	1.00	
[212]	Yes	60°	NA	
[213]	No	45°	NA	
This work	Dual	60°	0.35	

NA, RFD value is not available.

Chapter 7

FSS With Reconfigurable Response

This chapter describes a system of complementary FSSs that offers a reconfigurable frequency response. The proposed structure is developed based on Babinet's principle. The elements of the FSSs are formed by the four-arms star geometry. Initially, the slot element is designed along with its complementary one, and analyses of the individual structure are performed similarly as in Chapter 6. Then, the patch element is modified by adding a switching point to insert the active component and bias lines for feeding. The final configuration of the proposed structure consists of stacking these two elements on a single-layer substrate. Passive structures are used to demonstrate the potential reconfiguring features. Then, the active component, a PIN diode, is inserted to electrically reconfigure the frequency response of the proposed structure. Three states of the diode are analyzed as off-state, on-state and threshold-state. By biasing the diode with reverse voltage, the structure shows single-passband response, while with the forward voltage applied, it shows dual-passband response. When the threshold voltage is applied, the FSS presents a very interesting behavior where no specific passband appears. Moreover, by switching off/on states, the structure achieves switchable reflection and transmission characteristics.

This chapter contains material extracted from the following paper:

D. F. Mamedes, J. Bornemann, A. Gomes Neto and Sérgio L. M. Sales Filho, "Frequency-Selective Surface With Reconfigurable Response Based on Duality Theorem," submitted to IEEE Transactions on Antennas and Propagation.

7.1 Introduction

In principle, FSSs are passive structures, which means that their electromagnetic characteristics remain unchanged after fabrication [224]. To achieve adaptive performance features, reconfigurable FSSs (RFSSs) have been introduced as an alternative to satisfy modern wireless communications systems requirements. The RFSS enables changes in its frequency response of the reflection and transmission spectra after fabrication. As discussed in Chapter 2, Section 2.4, there are two main approaches to reconfigure FSSs: electrical and mechanical methods. In the following few paragraphs, a few published works on reconfigurable FSSs are described to highlight the complexity of their designs as opposed to the simplified structure presented in this chapter.

An FSS absorber with switchable stop-band frequency and with point-to-point biasing control system is presented in [68] (Figure 7.1). The structure consists of two dielectric substrates separated by an air spacer. The top of the upper substrate is composed of two split rings, with three resistors and one PIN diode employed in the outer ring, and two resistors in the inner ring. The lower substrate has two metal layers, one being the ground plane and the other carrying the biasing circuit. Thin metal posts (vias) are used to connect the bias lines from the bottom substrate to the elements in the top substrate. The state of the PIN diode in each unit cell is controlled by a single-chip microcomputer. Each chip can drive 16 PIN diodes individually and 16 chips were needed to control the panel. The results demonstrate that fast switching function from 5.2 to 8.6 GHz with the absorption depth below 10 dB.

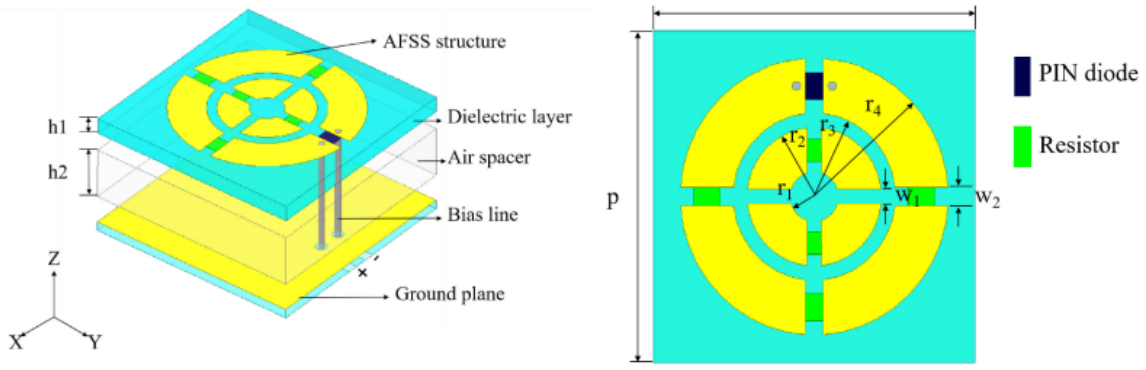

Figure 7.1: Reconfigurable multi-layer FSS using a PIN diode proposed in [68].

A dual-band multi-layer FSS with reconfigurable response is presented in [70]

(Figure 7.2). The structure is formed by three metal layers and two dielectric substrates. The unit cell in the top layer is composed of four rectangular patches and four PIN diodes, one for each patch, and the bottom layer has its unit cell arranged as a rotational symmetry of the one in the top. Two bias networks are used, being designed separately for each layer. Meander line structures are inserted into the bias line connecting adjacent patches. The unit cell of the metal layer, sandwiched between the upper and lower dielectric substrates, has coupling slots, and it is used as DC ground by the biasing network. Vias are used to connect the middle layer with the top and bottom ones. This structure offers independent control of its two passbands by switching the state of the PIN diodes, where the structure can exhibit the passbands or attenuate them with approximately 10-dB isolation, i.e., no passband, and stable response for incidence up to 40°.

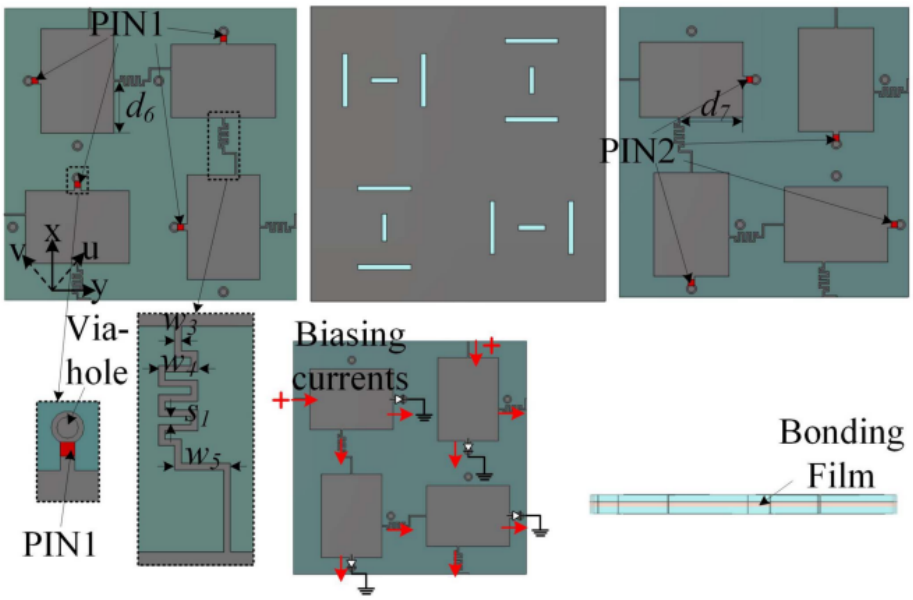

Figure 7.2: Reconfigurable multi-layer FSS using eight PIN diodes proposed in [70].

Reference [73] presents an RFSS with its passband tuned by varactors from 2.94 GHz to 5.66 GHz by reducing the capacitance from 0.8 pF to 0.1 pF (Figure 7.3). The capacitance offered to the element is achieved by reverse biasing the diodes from 4 V to 18 V. The unit cell is composed of a cross-loop slot element with four varactor diodes back-to-back, forming the top layer of the substrate. The DC bias network lies on the bottom layer of the substrate. A via is placed in the center of the cell to connect the top and bottom layers. The bias network affects the transmission coefficient of the RFSS, and because of that they use cross strip lines for biasing. In

addition, four lumped resistors are used in the bias lines to mitigate the singularity excited by the bias network.

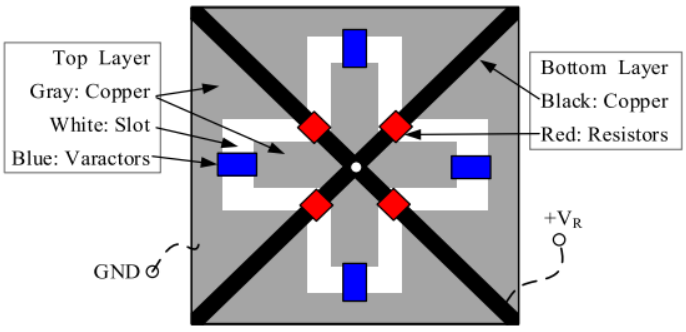

Figure 7.3: Reconfigurable multi-layer FSS using four varactor diodes proposed in [73].

A varactor tunable dual-band FSS is proposed in [225] (Figure 7.4), where its passbands can be tuned independent of each other. The structure is composed of two metallic layers printed on both sides of the substrate, where the top side has two cross strips with different dimensions encircled with high pass grids, whereas the bottom side includes the bias network. The cross strips and grids are loaded with twelve varactor diodes, positioned in a manner to achieve two independent tunable passbands. The bias network is designed with AC-blocks to provide tuning capability without any desired effect on the FSS operation. The bias network is composed of two independent DC networks, one to control the low-pass varactors and the other one to the high-pass varactors. Vias are used to connect the bias lines from the bottom layer to the elements in the top layer. This structure can operate from 2.28 GHz to 4.66 GHz and from 5.44 GHz to 11.3 GHz by proper tuning of the varactors located in the large and small cross strips with good results for oblique incidence up to 60°.

A reconfigurable FSS based on origami patterns by morphing its unit cell shape is proposed in [64] (Figure 7.5). The original unit cell is formed by a standard square loop element that is conform to the Miura-Ori pattern. By folding/unfolding the FSS unit cell, i.e. vertex angle equal to 45°/90°, the structure response switches between dual stopband to single stopband, respectively, with stable results for incidence up to 45°.

Reference [67] presents a mechanically RFSS inspired by the shutter mechanism of the Venetian blind (Figure 7.6). The structure is formed by an array of cross dumbbell elements on a single-layer substrate. This structure offers a single stopband frequency

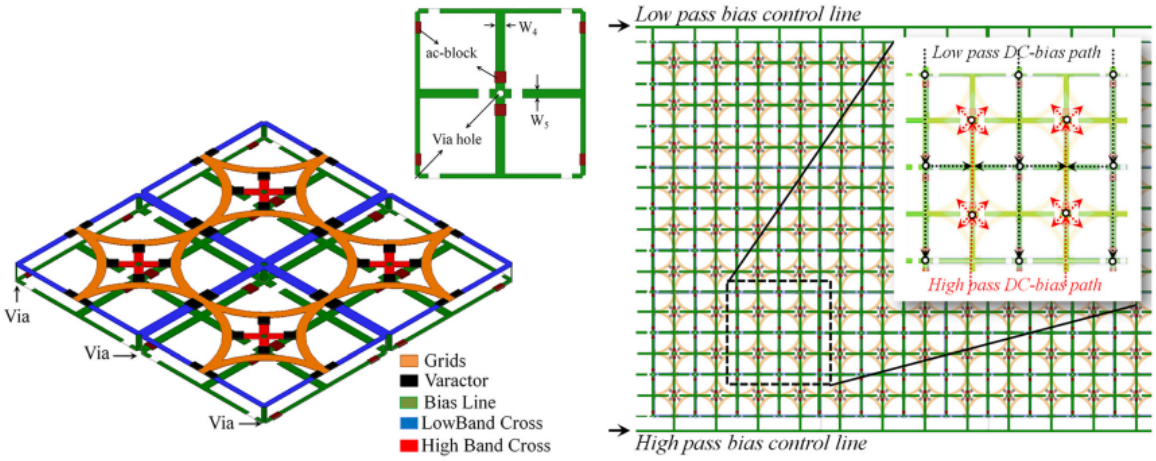

Figure 7.4: Reconfigurable multi-layer FSS using twelve varactor diodes proposed in [225].

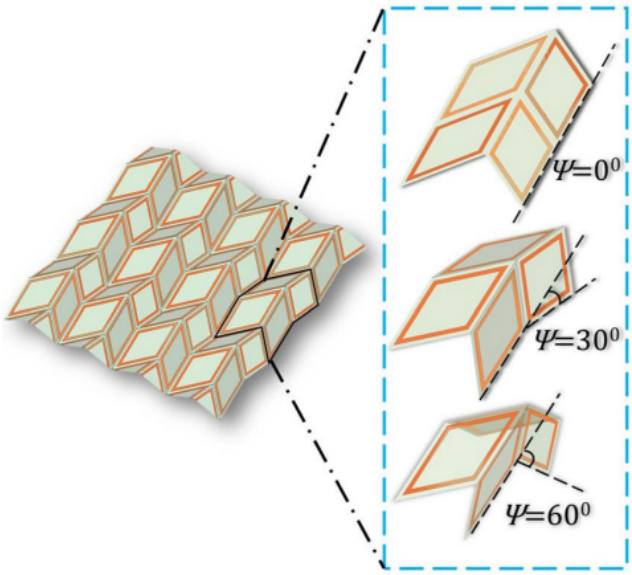

Figure 7.5: Reconfigurable FSS using folding mechanism proposed in [64].

that can be tuned by motor-driven rotation of the horizontal grid orientation at maximum angle of 60°. This structure operates at 3.2, 4.75, and 5.2 GHz, when it has 60°, 30°, and 0° rotation, respectively.

In this chapter, a much simpler FSS with reconfigurable properties is proposed. The structure consists of two metal layers, supported by only a single substrate, and the elements in these layers are designed based on the duality theorem. A single PIN diode is used as active component in each unit cell. The unit cells are connected by the bias lines to form the bias network within the array, where the PIN diodes

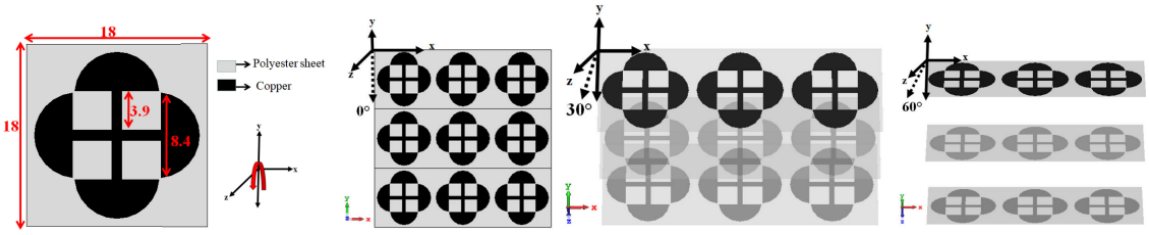

Figure 7.6: Reconfigurable FSS using rotating blinds mechanism proposed in [67].

in each row are in parallel. Three states of the PIN diode are evaluated; they are forward biased, reverse biased and when the threshold voltage is applied. By loading the diodes' state, the proposed structure can reconfigure its frequency response to present single- (3.75 GHz), dual- (2.0 GHz and 6.9 GHz) or no-passband operations. Another feature that this structure can provide is the ability, at approximately 3.75 GHz, to switch into either a passband or a stopband frequency. The proposed RFSS has elements that are simple to design, with a single-slab configuration, a simple control mechanism, and angular stability.

7.2 Single-layer FSS analysis and design

This section presents the design and analysis of a unit-cell FSS based on the four-arms star geometry with a slot-type element and its complementary one (patch type), individually, on single-layer substrate. The patch-type element is modified by inserting a gap in the center of the unit cell (to act as a switching point) to provide reconfiguration functionality. Initially, the single-metallic layer structure is analyzed considering the passive configuration, i.e., the ideal structure. Then, a PIN diode is used as an active component to reconfigure the FSS transmission characteristic. The numerical characterizations of all structures are obtained through the commercial software package CST Microwave Studio. The dielectric substrate considered in the simulation has $\epsilon_r = 4.4$, thickness of 1.0 mm, and loss tangent of 0.025.

7.2.1 Four-arms star slot-type FSS

The first structure is the slot type, in this case the outside of the element has metallic filling, which provides transmission of the incident EM waves at the desired frequency. The design procedure is the same as in Chapter 6, Section 6.2.2, where Figure 6.9b illustrates the unit cell with this element, including its parameters. The dimensions

are $p_s = 16$ mm, $a_s = 15$ mm, $b_s = 3$ mm and $s_s = 3$ mm. The frequency response of this structure is shown in Figure 7.7 (blue curve), with resonance frequency at 4.8 GHz. Note that this structure is symmetric, leading to the same frequency response for the TE and TM polarizations at normal incidence.

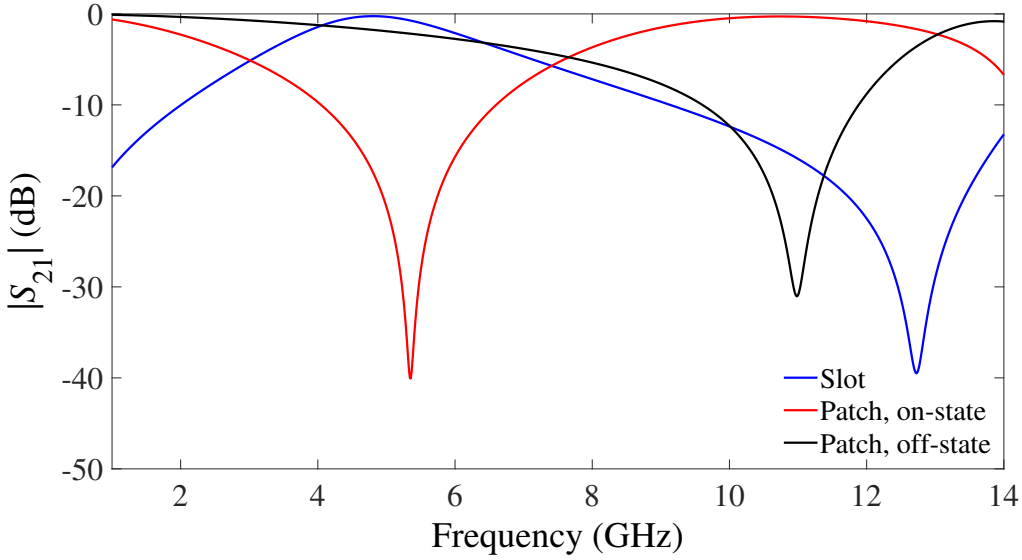

(a) TE polarization.

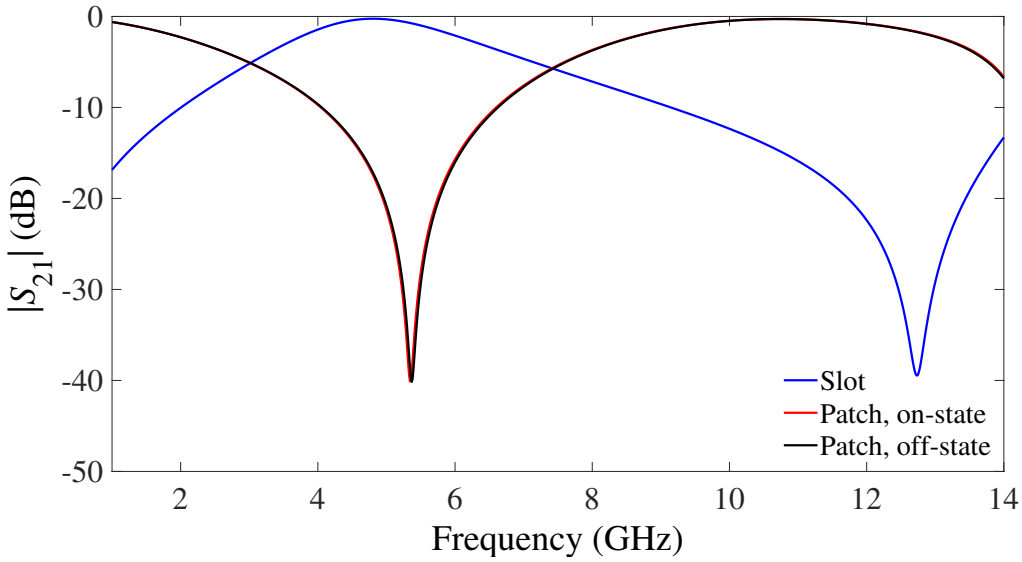

(b) TM polarization.

Figure 7.7: Numerical results of slot-type and patch-type, in the on- and off-state without bias lines, ideal elements FSSs.

7.2.2 Four-arms star patch-type FSS

The design procedure of the symmetrical four-arms star patch type is similar to the slot one, except that in this case the outside of the element is detached from the metallic surface. The patch-type structure is designed as the complement of the slot one, i.e., they have the same dimensions ($p_p = p_s$, $a_p = a_s$, b_p b_s and $s_p = s_s$). This structure behaves as a stop-band filter with resonance frequency at 5.35 GHz (Figure 7.7, red curve). Although the duality theorem states that the designs of complementary elements provide opposite passband and stopband in the same frequency, from Figure 7.7 we can see that the resonance frequency for the symmetric slot and patch elements are not the same with a difference of 10%. As expected for the symmetrical structure, the TE and TM polarizations present the same characteristics.

To form different reconfiguration states, a gap g is added to the original geometry as a switching point. The unit cell of the patch-type FSS with the new parameter added is illustrated in Figure 7.8a. The gap provides an asymmetric element, where the upper and lower arms are physically disconnected. As explained in Chapter 3, Section 3.2.1, if we consider that the E-field arrives at the unit cell as shown in Figure 7.8a, the arms are electrically connected for the TM polarization and electronically disconnected for the TE polarization, leading to different transmission coefficients for each polarization. The asymmetry of the element is provided by the gap of $g = 0.8$ mm, characterized as patch-type in the off-state. The gap width is designed based on the available diode size. Figure 7.7 shows the results of the asymmetric geometry. As predicted, the resonance frequency is moved in the TE polarization to 10.98 GHz (black curve), while for the TM polarization it is untouched, presenting the same response as for the symmetric element.

Analyses of the proposed structure in the ideal state conditions are performed to estimate the frequency response of the practical FSS. The first ideal case consists of the unit cell with all the arms connected by a strip line with width w_s (Figure 7.8a), providing a similar characteristic as a forward biased PIN diode. In the second condition, the upper and lower arms are physically separated by the gap g, acting as if the PIN diode was not biased. The connection of the arms can be restored by the width w_s with different sizes. To achieve the perfect complementary (or symmetric) structure, w_s must be equal to s_p, which is the patch-type in the on-state.

As mentioned above, the ideal structures emulate the characteristic of the practical one. In order to more accurate predict the frequency response of the practical

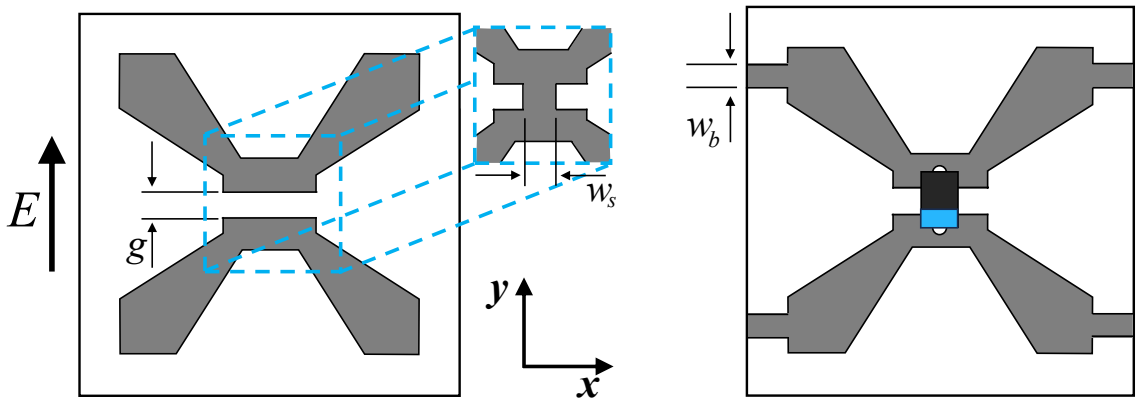

(a) Ideal asymmetric patch-type.

(b) Practical patch-type with bias lines and diode.

Figure 7.8: Geometry and parameters of single-layer RFSSs.

patch-type FSS when in on-state, an evaluation of the strip line's size is performed, considering $w_s = 0.1$ mm, 1.0 mm and 3.0 mm. The electrical model of the PIN diode when forward biased is an inductor in series with a resistor. The conducting strip provides an inductance characteristic to the FSS when the E-field is parallel to it. As w_s decreases, the transmission zero is moved to a lower frequency, getting closer to the actual response if a PIN diode was used. Figure 7.9a presents the simulated results for this analysis. The resonance frequencies for $w_s = 0.1$ mm, 1.0 mm and 3.0 mm are 4.42 GHz (blue curve), 4.9 GHz (red curve) and 5.35 GHz (black curve), respectively, for TE polarization. When the E-field is perpendicular to the FSS, it is practically null in the middle of the unit cell, which makes it not being affected by the different w_s sizes, with resonance frequency at 5.34 GHz for all cases (Figure 7.9b). Due to limitation in the manufacture process, the width chosen for w_s for the ideal on-state condition is set to 1.0 mm.

The passive model provides a good understanding of the reconfigurability of the element, but in practice the electronic model uses an active component (e.g. PIN diode). The biasing circuit is another key element in the design of the RFSS, and it is difficult to incorporate the active component along with the FSS' element. It is found in the literature that the feeding plane can be performed using an extra layer [226], and vias can be used to connect the element's layer to the biasing network [227]. Furthermore, some of these biasing systems have the diodes connected in series [228], [229], requiring high voltage level power supplies. In this work, the entire diode bias network is placed in the same plane as the FSS' element by adding bias lines

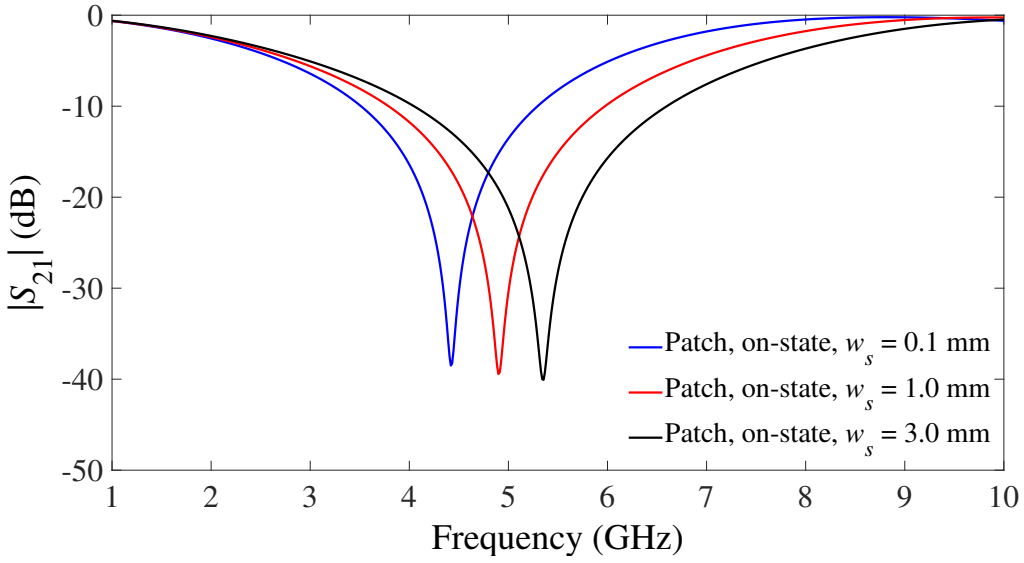

(a) TE polarization.

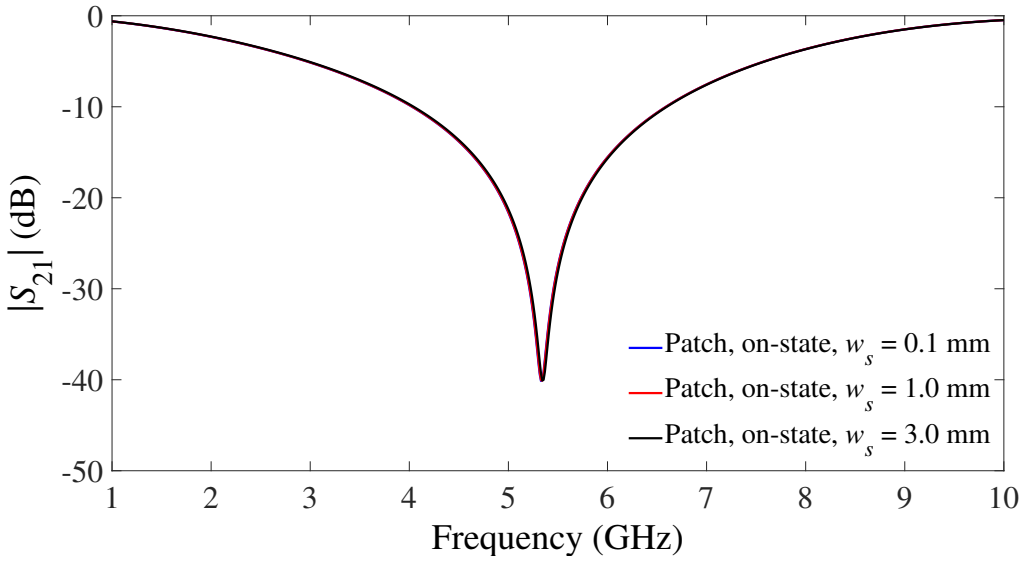

(b) TM polarization.

Figure 7.9: Numerical results of patch-type in the on-state, without bias lines, ideal elements FSSs as a function of strip size w_s.

horizontally with width w_b in the edges of each arm as shown in Figure 7.8b. The size of w_b almost has no effect on the frequency response of the FSS in both states for the TE polarization, where the resonance frequency is determined by the size of the arms (Figure 7.10a). However, in the TM polarization, the FSS frequency response changes completely, showing to be dependent on w_b, creating a transmission

maximum that gradually inclines and then declines steeply to the transmission zero that is up-shifted (Figure 7.10b). By incorporating a PIN diode with the bias lines into the unit cell, the four-arms star patch-type is split, which shifts the resonance frequency in one polarization, because the structure becomes polarization dependent, due to its asymmetry in the x- and y-directions. Switching the PIN diode on or off changes the effective inductance and capacitance of the element.

The ideal and practical structures with the patch-type element in its final configuration were characterized numerically and the computed magnitude of transmission coefficients is shown in Figure 7.11. The bias lines have $w_b = 1$ mm. The Skyworks SMP1340-079LF PIN diode was selected, and touchstone files were used in the simulation for the on- and off-state. When in the on-state, all arms are connected and the resonance frequencies for the ideal and practical structures are 4.99 GHz and 4.79 GHz (Figure 7.11a), respectively, for the TE polarization, with maximum difference of 4%. It can be seen in Figure 7.11a that by loading the off-state, the stopband of the ideal with reference to practical FSSs is up-shifted significantly due to the added capacitance between the gap in the center of the unit cell. The off-state FSS resonates at 10.85 GHz and 8.36 GHz for the ideal and practical cases, respectively. When the PIN diode is reversed biased, its circuit comprises of a capacitor with a large shunt resistor. Reference [230] suggests that the PIN diode in this condition (at V = 0 V) offers a capacitance of 0.24 pF. Note that the resonance difference of the ideal and practical FSS is associated with the fact that the gap g does not emulate the same capacitance as the PIN diode. Figure 7.11b shows the results in the TM polarization; it is observed that the bias lines affect the transmission responses due to its inductance when compared to those in Figure 7.9b. As explained above, for the TM polarization, the on/off state present the same resonance frequency at 10.9 GHz, because the E-field is null in the diode area.

7.3 Reconfigurable complementary FSS design

This section describes the design procedure of a complementary-based FSS with reconfigurability features based on Babinet's principle for electromagnetic fields [204], [214]–[216]. The reconfigurable complementary FSS (RCFSS) proposed in this dissertation combines the slot-type element and asymmetric patch-type element with bias lines, both topologies presented in previous section. The combination of the CFSS arrays based on the four-arms star geometry will result in a dual-passband FSS.

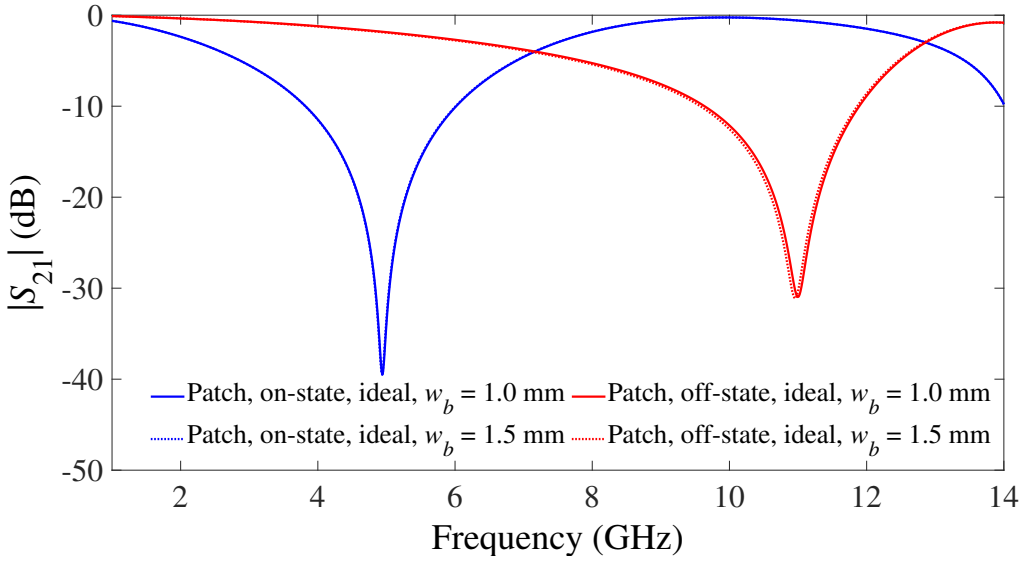

(a) TE polarization.

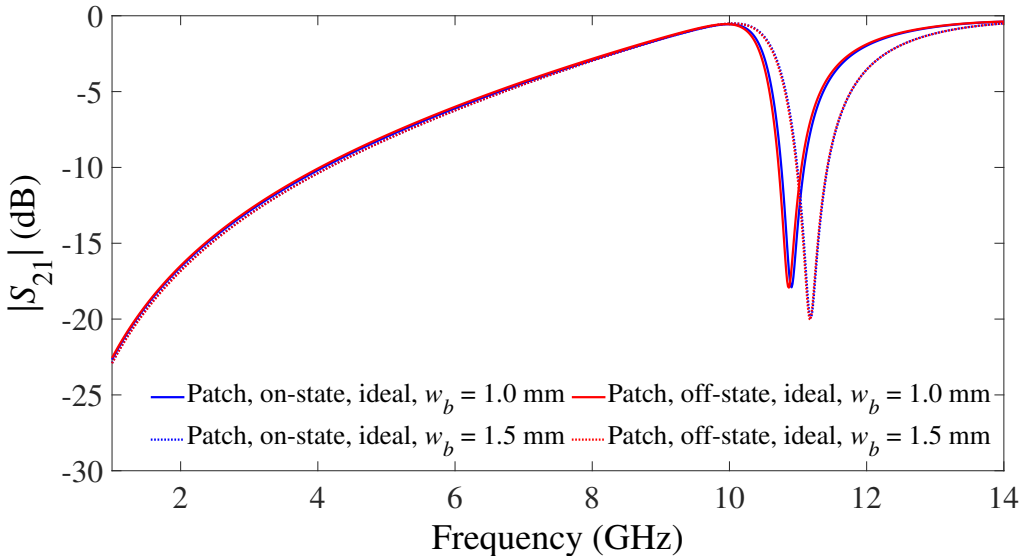

(b) TM polarization.

Figure 7.10: Numerical results of patch-type in the on- and off-state ideal elements FSSs as a function of bias lines size w_b.

The complementary structure is achieved by designing the patch and slot elements using identical geometry shape and dimensions, and these elements are spaced by a medium. We do not truly follow this approach because the shape of the patch element is disturbed by the gap inserted in the center of the unit cell and bias lines in the edges of the arms. Figure 7.12 illustrates the three-dimensional topology of the proposed

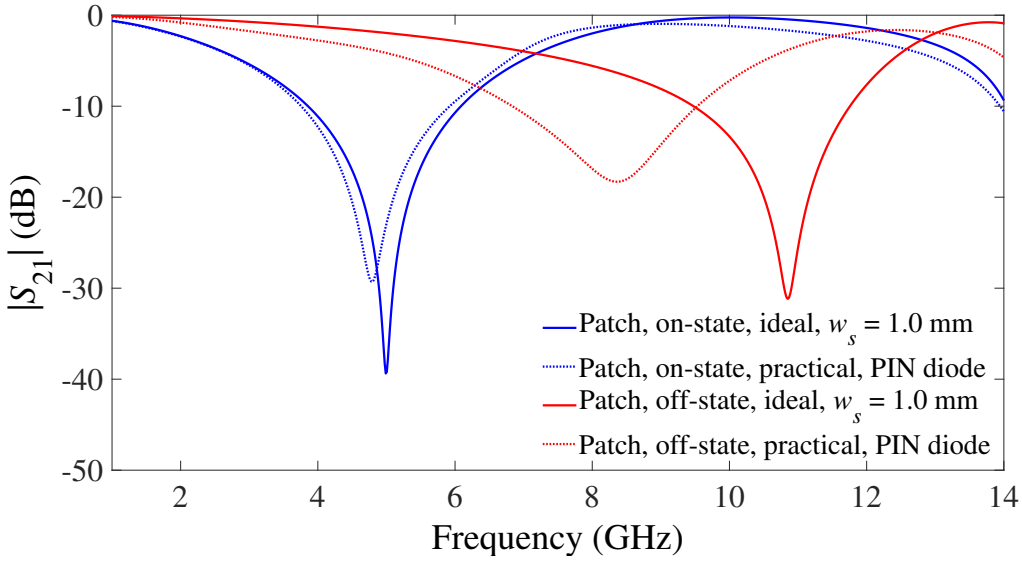

(a) TE polarization.

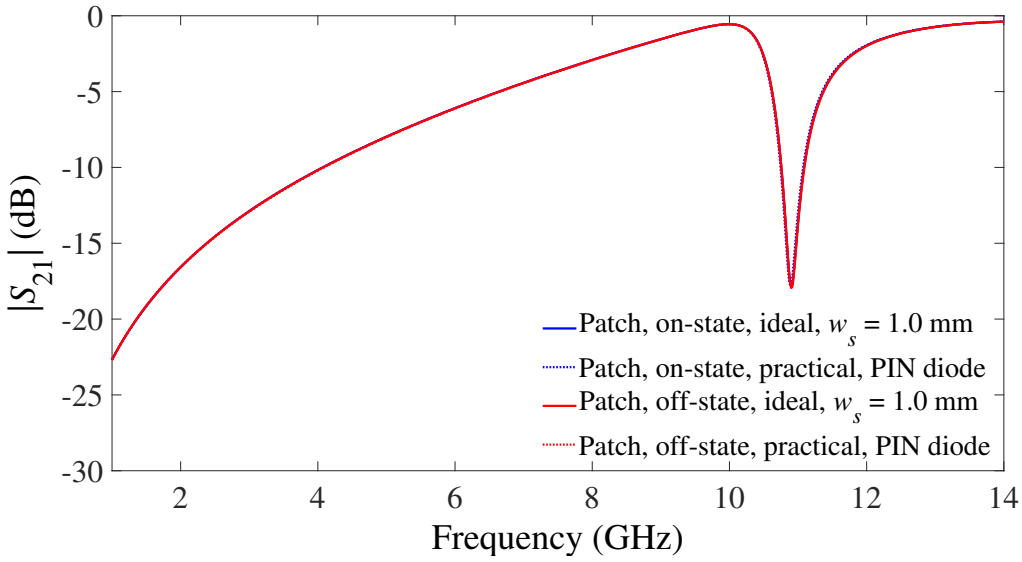

(b) TM polarization.

Figure 7.11: Comparison of frequency response of the ideal and practical patch-type elements FSSs with bias lines in the on- and off-state.

RCFSS. The medium used to separate the elements is a dielectric substrate with thickness h and dielectric constant ϵ_r. The top layer of the substrate is formed by the patch element, while the bottom layer carries the slot one. In this work, the RCFSS was designed with the same dimensions used for the individual FSSs presented in Section 7.2.

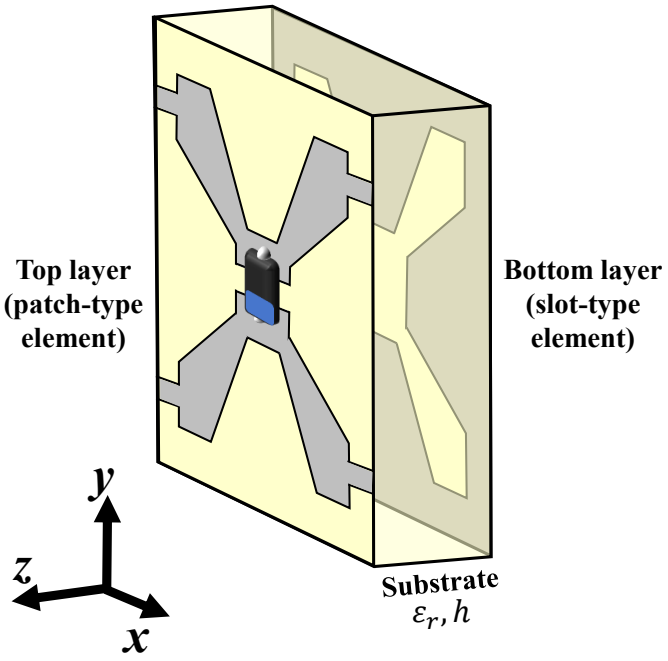

Figure 7.12: RCFSS structuring.

7.4 Performance validation

Experimental characterizations of the proposed reconfigurable CFSS-based configuration were performed to validate the numerical results. All prototypes were manufactured on a single-layer low-cost FR-4 fiber-glass dielectric substrate and metallization are on both sides, with $\epsilon_r = 4.4$, thickness of 1.0 mm, and $\tan\delta = 0.025$. Three FSSs were fabricated to examine the scattering properties, being two passive CFSSs and one RCFSS. The fabricated prototypes are presented in Figure 7.13 with the close-up view of the unit cells. The fabricated CFSSs have 12 $\times$ 12 elements and overall dimensions of 19.2 cm $\times$ 19.2 cm. Figure 7.13a shows the array formed by slot elements found in the bottom layer of all structures. Figure 7.13b and Figure 7.13c show the top view of the passive CFSS in the on- and off-states, respectively. The diode-mounted RCFSS is shown in Figure 7.13d with a total of 144 soldered diodes. The surface-mountable Skyworks SMP1340-079LF PIN diodes in plastic package, with parasitic inductance of 0.7 nH, are used. The package length and width are 1.1 mm and 0.7 mm, respectively. When forward biased, these diodes offer low resistance with typical value of 0.85 Ω at 10 mA and 0.85 V. When reverse biased, they can reach a capacitance as low as 0.21 pF at 5 V [230].

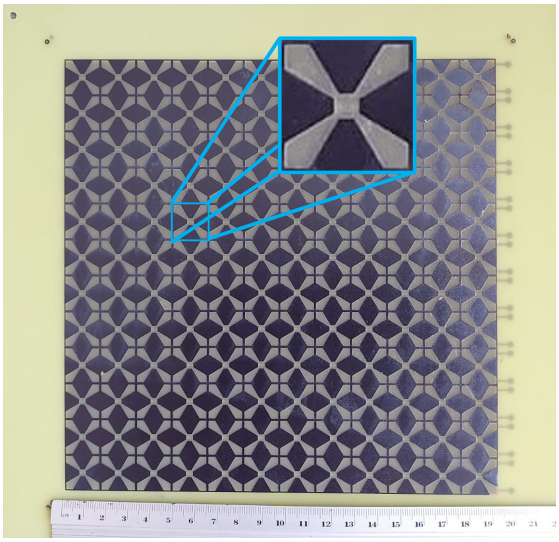

(a) Slot elements present in all structures (bottom view).

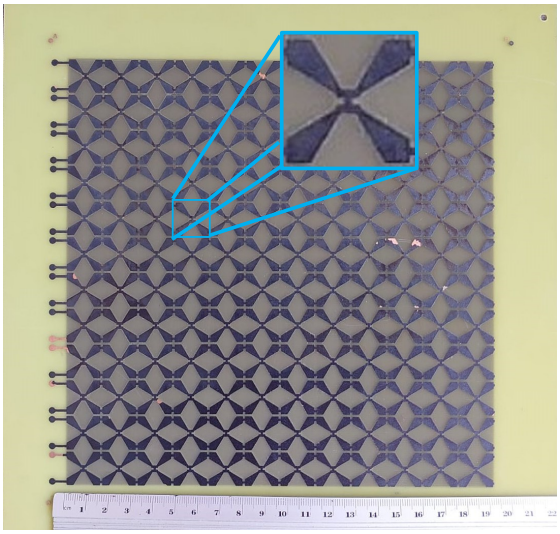

(b) Ideal CFSS on-state (top view).

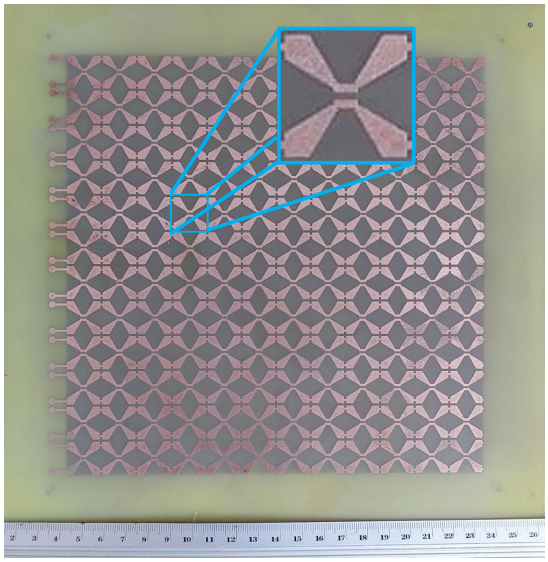

(c) Ideal CFSS off-state (top view).

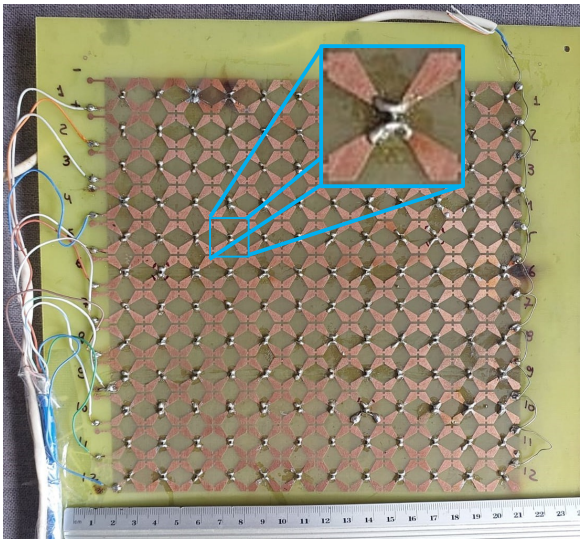

(d) RCFSS with diodes (top view).

Figure 7.13: Fabricated reconfigurable complementary structures.

The bias lines connect the diodes in parallel, allowing each FSS row to be independently controlled, while applying low voltage levels. A resistor of 230 Ω is added in series to each FSS' row to limit the current flowing through the diodes, as illustrated in Figure 7.14. The biasing circuitry is formed by using single-core wires as shown in Figure 7.13d, connected to auxiliary strip lines of 8 mm. The biasing network indicates that there are 12 diodes connected in parallel per row, and a total of 12

rows.

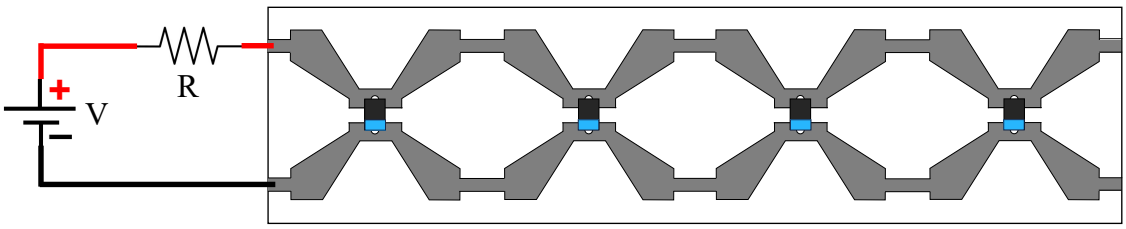

Figure 7.14: Biasing schematic per RFSS' row.

The experimental characterizations were performed using the measurement setup described in Appendix A, Section A.2.2. The measured transmission coefficients shown in Figures 7.15 – 7.19 are computed by subtracting the transmission spectra of each polarization without the devices under test. The incidence of the wave to the FSSs is considered to be at normal ($\theta = 0°$) and oblique (θ = up to 50°). The characterizations were performed sweeping θ in steps of 10°, but we will only exhibit the results for $\theta = 0°$, 20° and 50°, because the measured and simulated results agreed for all angles.

7.4.1 Passive CFSS results

When the elements of the proposed FSS are assembled in quasi-complement of one another, i.e., the patch element is in on-state, a dual-band response is expected due to their coupling. The numerical and measured results of the transmission coefficient for the ideal CFSS when it is in the on-state are presented in Figure 7.15. The ideal CFSS in the on-state has a strip line of $w_s = 1.0$ mm to emulate the forward-biased PIN diode. The numerical characterization shows two transmission maxima (f_{p1} and f_{p2}) at 2.29 GHz and 6.48 GHz, and a transmission zero (f_z) at 3.97 GHz for the TE polarization at normal incidence (Figure 7.15a). The experimental characterization confirms the result from the simulation with $f_{p1} = 2.14$ GHz, $f_{p2} = 6.53$ GHz and f_z 3.83 GHz. It is observed that for oblique incidence, the first transmission maximum and transmission zero remain almost the same, but the second transmission maximum down-shifts as θ increases. As explained in Section 7.2.2, the bias lines create a transmission maximum at a higher frequency for the patch element in the TM polarization. When this element is combined with the slot one, two transmission maxima appear to be closely spaced as illustrated in Figure 7.15b. The first transmission maximum is found at 5.68 GHz (simulated) and 5.84 GHz (measured), while the second

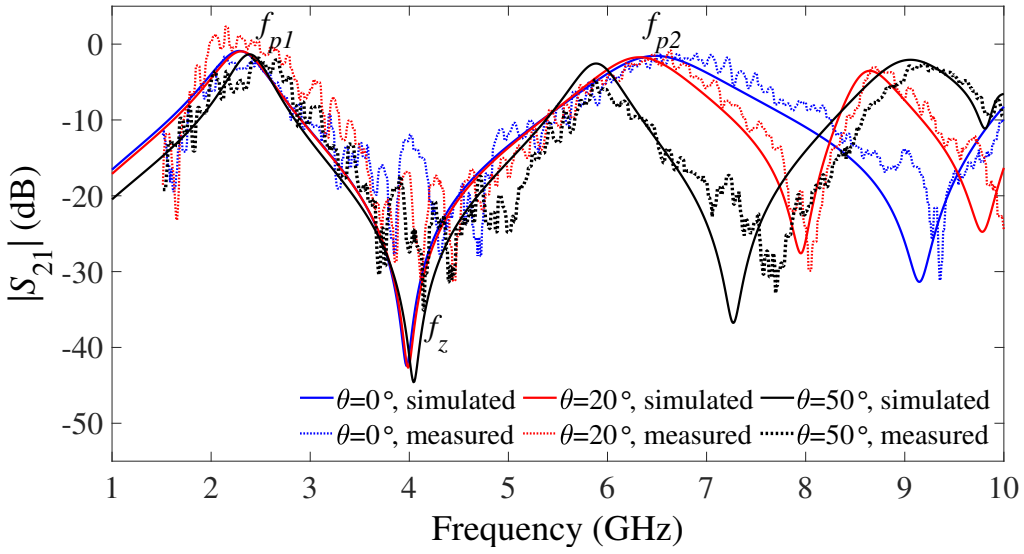

(a) TE polarization.

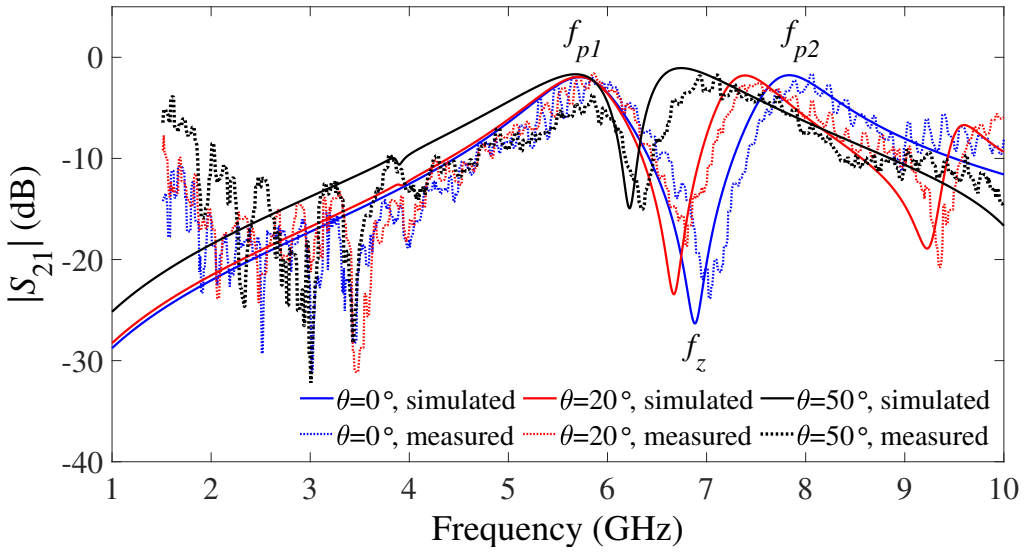

(b) TM polarization.

Figure 7.15: Simulated and measured results of ideal RCFSS in the on-state.

transmission maximum is at 7.81 GHz (simulated) and 8.06 GHz (measured), with a transmission zero between them at 6.89 GHz (simulated) and 7.02 GHz (measured) at normal incidence, with frequency separation ratio of 1.37. For oblique incidence, the first transmission maximum remains the same, while the transmission zero and second transmission maximum move closer to the first one when θ increases, with frequency separation ratio of 1.19 for $\theta = 50°$.

The ideal case for the CFSS when the patch element is in the off-state was analyzed numerically and experimentally, and its transmission spectra is shown in Figure 7.16. In this condition, the gap g emulates the reverse-biased PIN diode, and the capacitance offered by the gap shifts the resonance frequency of the patch element, as shown in Section 7.2.2, for the TE polarization. The elements are decoupled for this state and only one passband is seen for this frequency range, which correspond to the response characteristic provided by the slot element. At $\theta = 0°$, the simulated and measured transmission maximum (f_p) is at 4.31 GHz and 3.62 GHz, respectively (Figure 7.16a). The angular incidence was analyzed, and the results show that the structure is stable up to $\theta = 50°$. The numerical and measured results for the TM polarization over different incident angles are presented in Figure 7.16b, and they show to be basically the same as the ones obtained in the TM polarization for the on-state. This behavior is expected because the E-field is almost null at the center of the unit cell.

7.4.2 RCFSS results

The passive CFSSs provide an understanding of the response the proposed structure can offer. The next step in the design is to insert the PIN diode to characterize the real response. Different levels of voltage were applied across the shunt diodes, from 0.0 V to 2.0 V with steps of 0.2 V, and the frequency response of the proposed structure was observed. The PIN diodes allow current flows from 0.8 V on. We display the results of three cases when the PIN diodes are biased with 2.0 V (forward region, Figure 7.17), 0.6 V (threshold region, Figure 7.18) and 0.0 V (reverse region, Figure 7.19).

As predicted from the passive CFSS in the on-state, the practical RCFSS presents similar results for both polarizations. When the PIN diodes are forward biased with V = 2.0 V, the elements are coupled and two transmission maxima are observed at f_{p1} = 2.28 GHz and f_{p2} = 6.53 GHz from the simulated results, and f_{p1} = 2.03 GHz and f_{p2} = 6.9 GHz from the measured results for the TE polarization at normal incidence (Figure 7.17a). The transmission zero is found at 3.86 GHz and 3.64 GHz from the numerical and measured results, respectively. The maximum difference between the simulated and measured results for the first transmission maximum, the transmission zero and the second transmission maximum are 10.96%, 5.69% and 5.66%, respectively. Note that the results agree with the ones predicted by the on-state passive

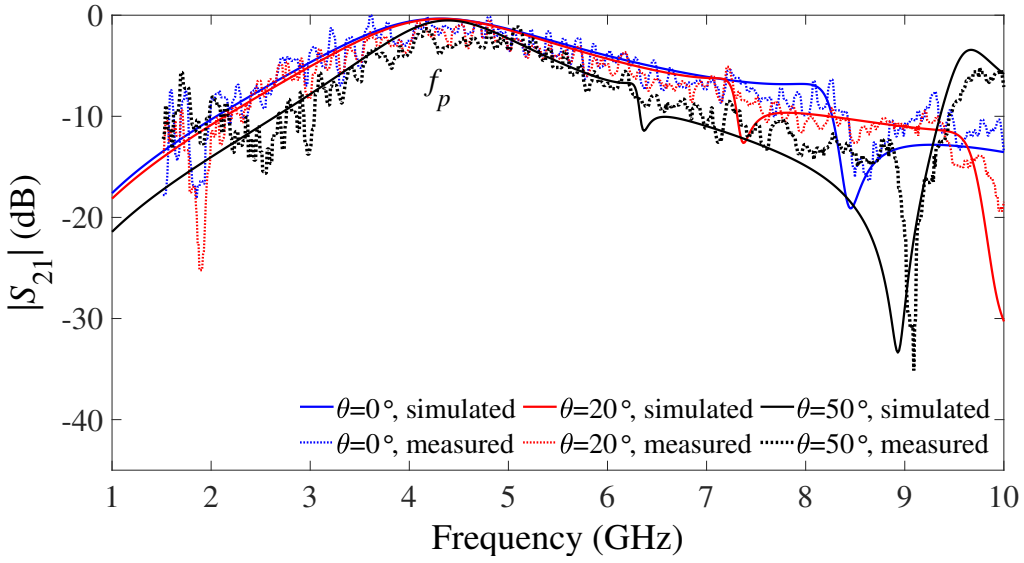

(a) TE polarization.

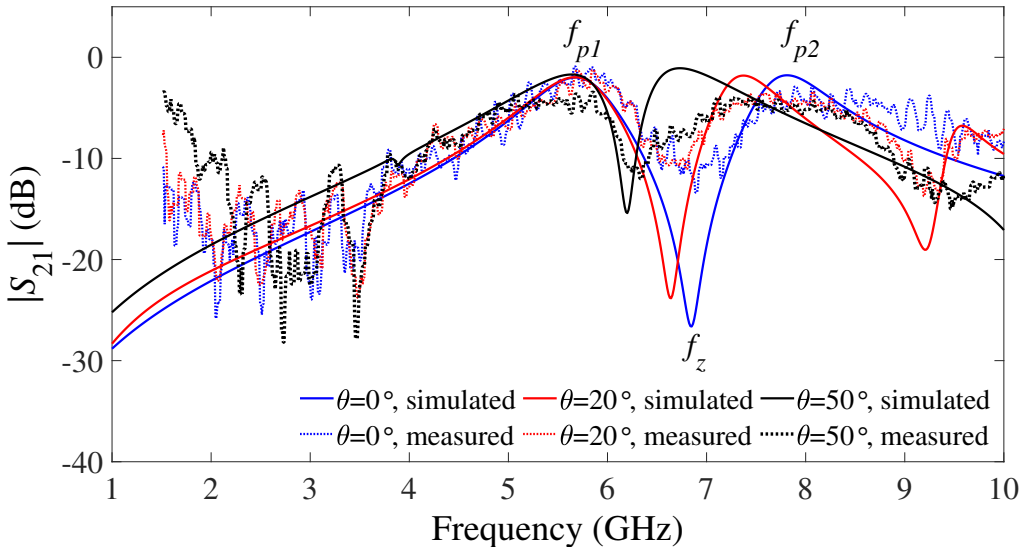

(b) TM polarization.

Figure 7.16: Simulated and measured results of ideal RCFSS in the off-state.

CFSS for all incidence angles, and, again, it is observed that as θ increases, the second transmission maximum reduces while the first transmission maximum and transmission zero remain the same. Figure 7.17b shows the results for the TM polarization, and two transmission maxima at 5.7 GHz and 7.83 GHz with a transmission zero at 6.87 GHz are observed numerically. The experimental characterization obtained these resonance frequencies at $f_{p1} = 5.92$ GHz, $f_{p2} = 8.57$ GHz and $f_z = 6.99$ GHz.

Again, the results from the on-state RCFSS follow the ones obtained by the on-state passive CFSS, including the results by varying θ.

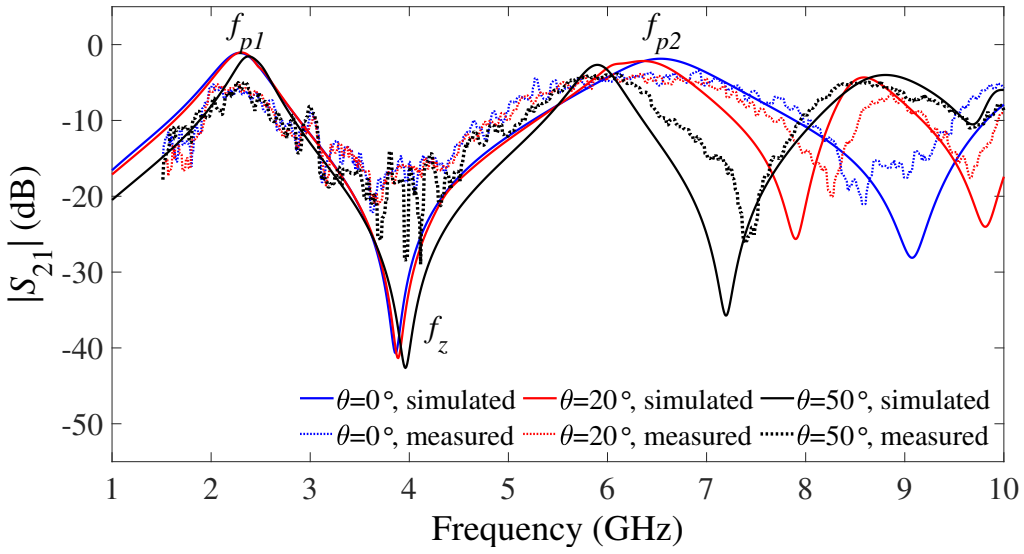

(a) TE polarization.

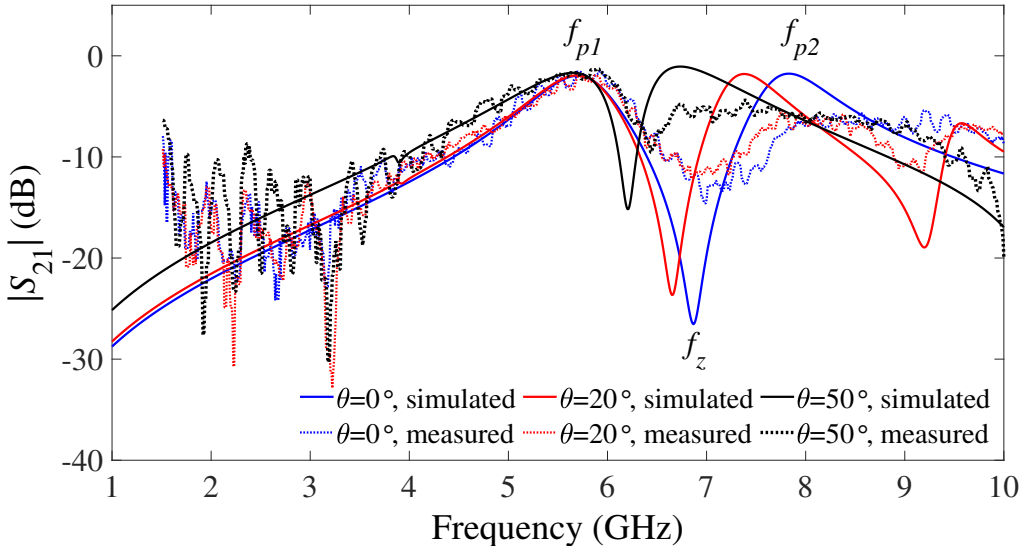

(b) TM polarization.

Figure 7.17: Simulated and measured results of practical RCFSS in the on-state, biasing diodes with V = 2.0 V.

The transmission spectra of the proposed structure when the PIN diodes are biased with the threshold voltage, V = 0.6 V, is shown in Figure 7.18. In this condition, the equivalent circuit of the PIN diode consists of a capacitor with a shunt

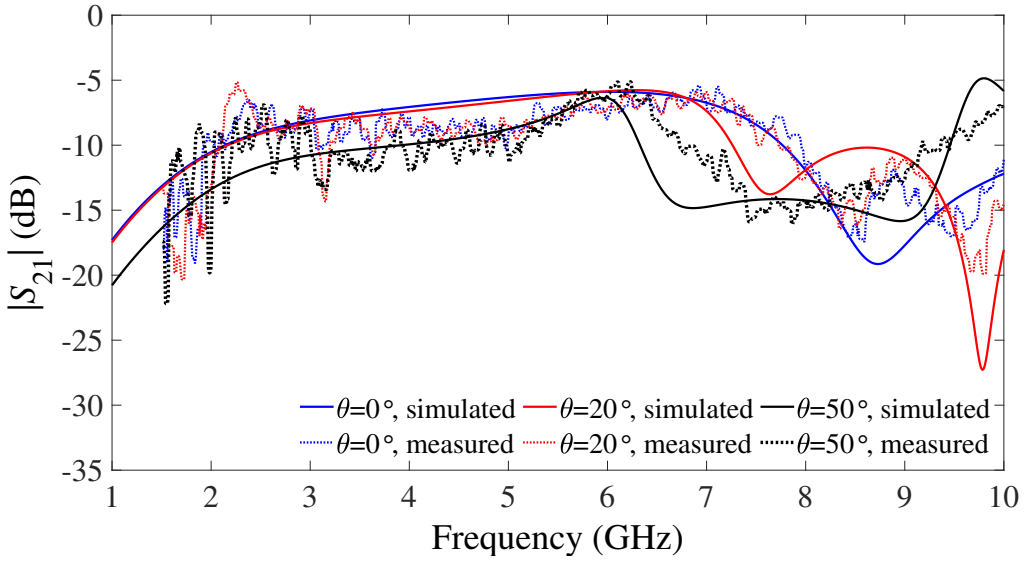

(a) TE polarization.

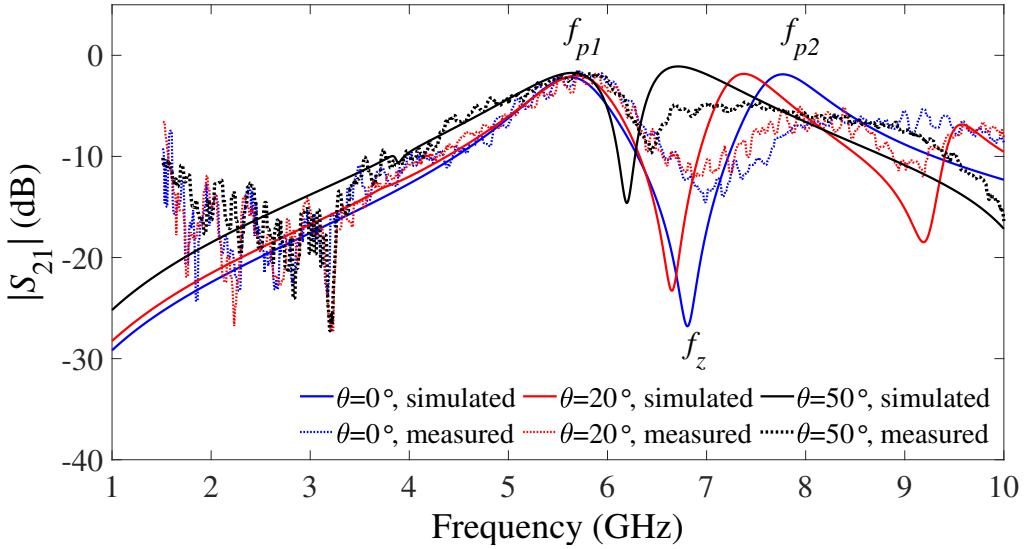

(b) TM polarization.

Figure 7.18: Simulated and measured results of practical RCFSS with diodes in the threshold region, biased with V = 0.6 V.

resistor. The resistance of this resistor is not low enough to let the currents flow freely. The results show that no obvious passband is available with an average of -7-dB (simulated) and -8-dB (measured) attenuation over the frequency range from 2 GHz to 8 GHz for the TE polarization, as shown in Figure 7.18a. As mentioned above, in the TM polarization the biased PIN diode has no effect on the frequency

response of the structure, thus the two transmission maxima with a transmission zero are seen as illustrated in Figure 7.18b. The simulated and measured results agree for both polarizations.

Figure 7.19 illustrates the transmission spectra of the RCFSS when the PIN diodes are reverse biased, V = 0.0 V, which show to have similar response to the ones for the off-state passive CFSS. For the TE polarization, one transmission maximum is observed at 3.89 GHz (simulated) and 3.75 GHz (measured) at $\theta = 0°$ (Figure 7.19a) with maximum difference of 3.6%. The structure shows to be stable at different angles of incidence with maximum resonance frequency deviation of 0.26% and 5.33% for the numerical and experimental results, respectively, from $\theta = 0°$ to 50°. Figure 7.19b shows the simulated and measured transmission coefficients in the TM polarization, which present the same response as the ones from the previous biasing conditions.

7.4.3 Performance assessment

The elements of the proposed RCFSS were designed based on Babinet's principle, and the results presented in Sections 7.4.1 and 7.4.2 confirm that the PIN diode can be used to reconfigure the proposed structure's frequency response, achieving a switchable reflection and transmission of approximately 2.3 GHz (-10-dB bandwidth) for TE polarization, with -40.7 dB and -22 dB of isolation between on/off states at off-state resonance frequency. Considering the on-state for the passive and active structures, dual-passband characteristic is obtained. When the PIN diode switches to the off-state in the practical case and the ideal structure considers a gap g, a single-passband response is observed. Additionally, the transition between on/off states was evaluated by biasing the PIN diodes with threshold voltage, which demonstrates the very interesting response that no transmission maximum or transmission zero was presented, with the signal attenuated in the entire band.

A comparison of our proposed structure with previously related works is shown in Table 7.1, in terms of types of configuration, tuning method applied, reconfigurable properties, biasing network, frequencies and number of bands of operation, unit cell dimensions, angular stability, and other requirements. Our proposed structure shows to be more compact in terms of number of layers and unit cell size in order of wavelength of the lower band in free space. The structure is geometrically simple to design, using fewer active devices and it has a very simple biasing network. It can operate with single-, dual- or no-passband, depending on the diode's state. Moreover, it can

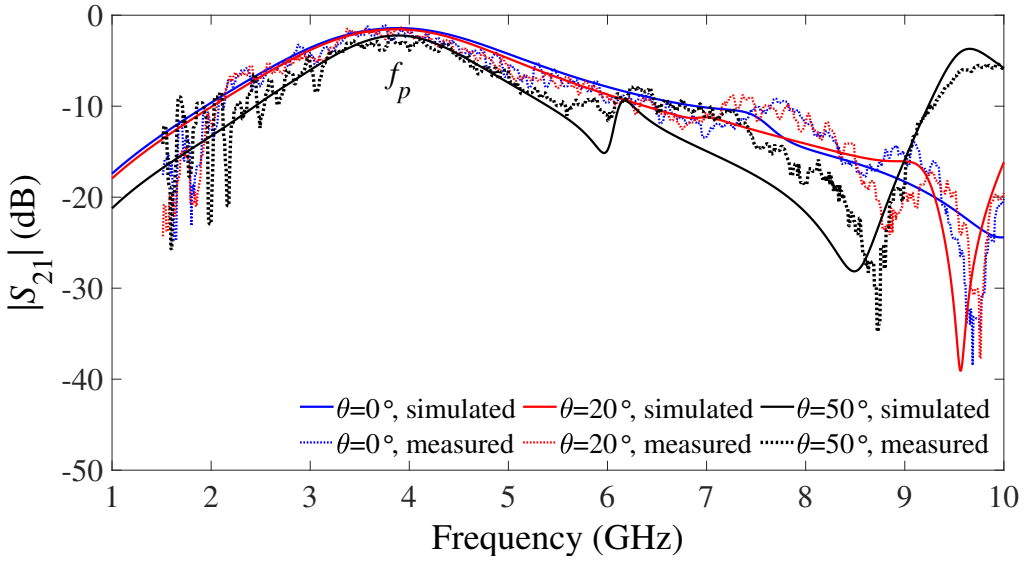

(a) TE polarization.

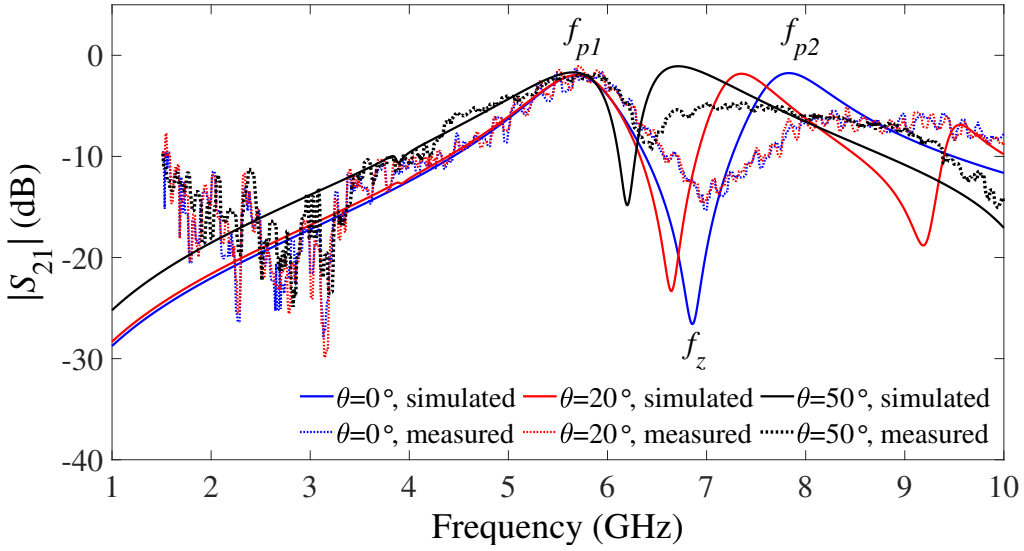

(b) TM polarization.

Figure 7.19: Simulated and measured results of practical RCFSS in the off-state, biasing diodes with V = 0.0 V.

reconfigure its response into passband or stopband within the same frequency band.

Ref.	Configuration	Unit cell size	Reconfigurable properties
[68]	3-metal and 2-dielectric	$0.31\lambda \times 0.31\lambda$	Switchable stop-band frequency
[70]	3-metal and 2-dielectric	$0.66\lambda \times 0.66\lambda$	Switchable pass/no-pass band
[73]	2-metal and 1-dielectric	$0.12\lambda \times 0.12\lambda$	Tunable pass-band frequency
[64]	1-metal and 1-dielectric	$0.67\lambda \times 0.67\lambda$	Switchable single to dual stopband
[67]	1-metal and 1-dielectric	$0.19\lambda \times 0.16\lambda$	Tunable stop-band frequency
[225]	2-metal and 1-dielectric	$0.05\lambda \times 0.05\lambda$	Independently tunable pass-band frequency
This work	2-metal and 1-dielectric	$0.11\lambda \times 0.11\lambda$	Switchable pass/stop/no-pass band
Ref.	Tuning method	Angular stability	Biasing network
[68]	1-PIN-diode loaded	30°	Point-to-point feeding
[70]	8-PIN-diodes loaded	40°	Two bias networks within array and extra ground layer
[73]	4-varactors loaded	Not available	Bias network within array and extra ground layer with lumped devices
[64]	Folding	45°	Not designed
[67]	Rotating blinds	60°	Not designed
[225]	12-varactors loaded	60°	Two bias networks and lumped devices in extra layer
This work	1-PIN-diode loaded	50°	Parallel feeding
Ref.	Number of bands	Freq. (GHz)	Power and other requirements
[68]	Single	5.2 and 8.6	Requires single-chip microcomputer
[70]	Single, dual and none	3.03 and 4.33	Requires DC power supplies, voltage not reported
[73]	Single	2.94–5.66	Requires 18-V DC voltage
[64]	Single and Dual	2 and 2.8	Require driving apparatus
[67]	Single	3.2–5.5	Require driving apparatus
[225]	Dual	2.28–4.66 and 5.44–11.3	Requires DC power supplies, voltage not reported
This work	Single, dual and none	3.75 or 2.03 and 6.9	Requires 2-V DC voltage

Table 7.1: Comparison of proposed reconfigurable CFSS with other reported ones.

Chapter 8

High-Gain Reconfigurable Antenna Systems

High-gain reconfigurable antenna systems that use PIN-diode-switched FSSs are presented in this chapter. The first configuration is a reconfigurable corner reflector antenna, which uses FSSs as reflectors with aperture angles of 45° and 90°. Its pattern characteristics are altered by on-off state biasing of the PIN diodes. From the analysis of the FSSs' influence on this system, a reconfigurable sectoral antenna is developed for 5G applications, operating at 3.5 GHz. Six cases of diode configurations are considered, confirming the design approach of the circuit for steering the beam and enhancing the gain.

This chapter contains material extracted from the following publications:

D. F. Mamedes, A. G. Neto and J. Bornemann, "Reconfigurable corner reflector using PIN-diode-switched frequency selective surfaces," IEEE International Symposium on Antennas and Propagation and North American Radio Science Meeting, Montreal, Canada, 2020, pp. 127-128, doi: 10.1109/IEEECONF35879.2020.9329791.

D. F. Mamedes and J. Bornemann, "High-gain reconfigurable antenna system using PIN-diode-switched frequency selective surfaces for 3.5 GHz 5G application," SBMO/IEEE MTT-S International Microwave and Optoelectronics Conference (IMOC), Fortaleza, Brazil, 2021, pp. 1-3, doi: 10.1109/IMOC53012.2021.9624918.

D. F. Mamedes, J. Bornemann and A. G. Neto, "Single- and dual-band FSS with switchable characteristics," accepted in IEEE International Symposium on Antennas and Propagation and USNC-URSI Radio Science Meeting (AP-S/URSI), Florence, Italy, 2024.

8.1 Introduction

Beam-switching/steering antennas have been receiving special attention in modern communication systems as discussed in Chapter 1, as an alternative solution to complex and expensive antenna array systems [231]. Pattern reconfigurable antennas have shown to improve the antenna performance by applying new reconfiguring techniques such as introducing parasitic elements in stacked [232] or planar [233] configurations, exciting different working modes of a single antenna [234], reconfiguring the electrical structure of the antenna [235], etc. FSSs have been engineered to achieve antenna beam switching/steering by their reconfigurability features using various tuning technologies such as, e.g., some presented in Chapter 7.

Reference [236] presents a beam-steering partially reflective surface (PRS) antenna, which consists of a probe-fed square patch antenna acting as the radiator and a reconfigurable PRS structure. Figure 8.1 shows the PRS unit cell and the biasing schematic. Each unit cell uses two PIN diodes. It is shown that the beam can be tilted ±22° in the azimuth direction in the frequency range from 5.44 to 5.66 GHz with maximum gain of 10 dBi.

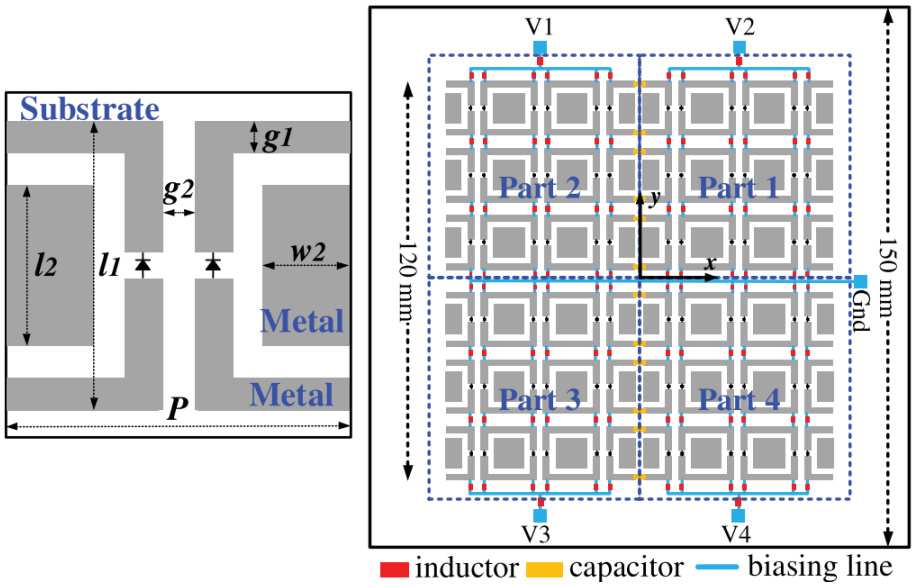

Figure 8.1: Reconfigurable PRS proposed in [236].

A PRS antenna with a simple network and using one PIN diode is presented in

[237] as shown in Figure 8.2. The structure can achieve a ±18° electronic beam steering with respect to the broadside direction for operation at 5.5 GHz with maximum gain of 11 dBi.

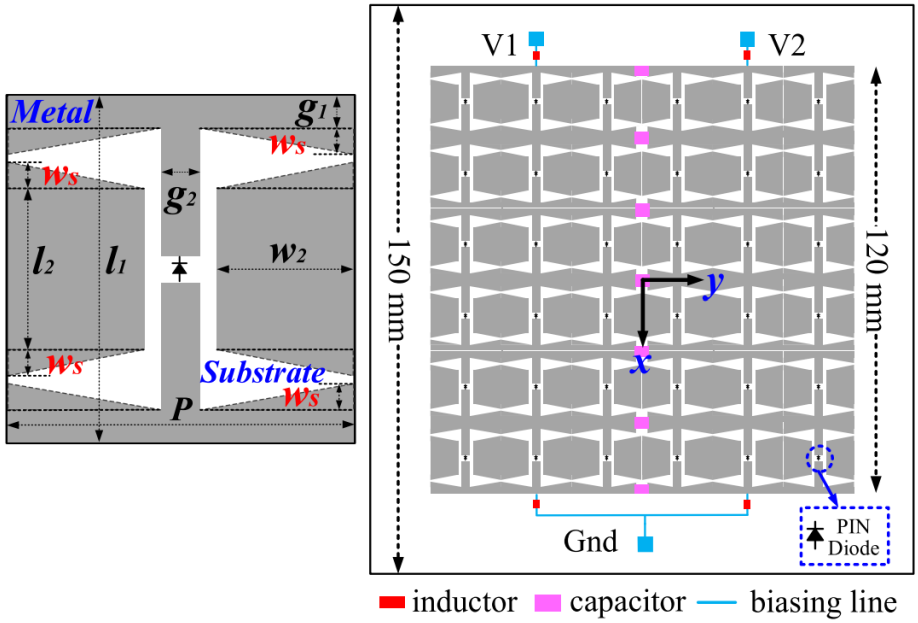

Figure 8.2: Reconfigurable PRS proposed in [237].

Reference [238] developed a beamwidth control of omnidirectional antennas using passive convex FSS and FSS-based corner reflectors. Figure 8.3 shows the proposed system and the unit cell of both FSSs, which is based on the meander geometry. The structure presents a maximum gain of 8.3 dBi at 5.8 GHz and 6.8 dBi at 3.5 GHz, leading to beam diversity, but without beam tilting.

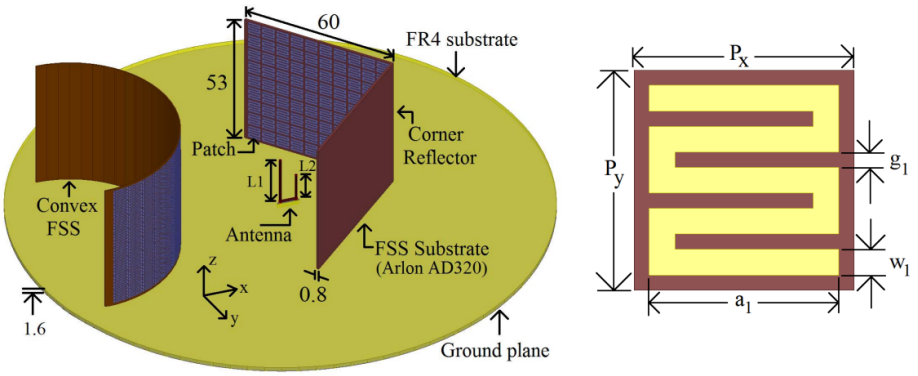

Figure 8.3: System of monopole antenna with convex FSS and FSS-based corner reflectors proposed in [238].

Two reconfigurable corner reflector antenna designs for point-to-point 2.4 GHz applications were investigated in [239]. FSSs are used as corner reflectors as shown in Figure 8.4. The first design uses an FSS with conductor loop elements connected by six PIN diodes, which allows to shift the beam in 1°, 3°, and 5°, with gain of 9.3 dB. The second design uses segment strips with three PIN diodes per unit cell, offering 3° and 5° beam-shifting with the main lobe gain of 9.5 dB.

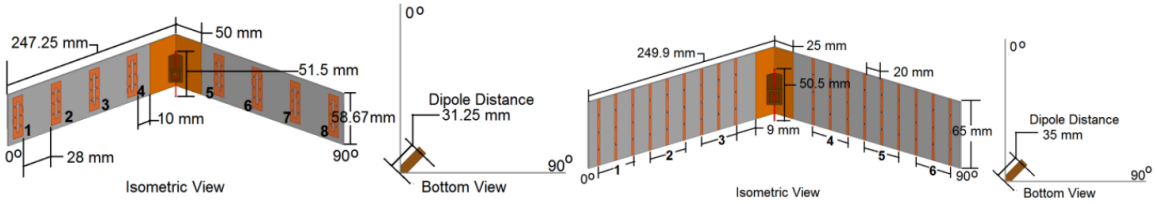

(a) FSS reflector with loop elements.

(b) FSS reflector with strip elements.

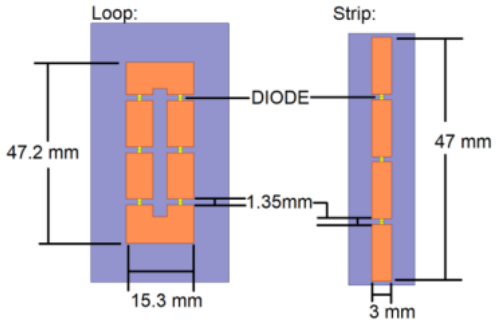

(c) Unit cells.

Figure 8.4: Reconfigurable corner reflector antenna systems proposed in [239].

An electronically reconfigurable FSS-inspired transmit array is proposed in [226]. The structure is composed of five stacked layers of 5×5 unit-cells loaded with varactor diodes combined with a feeding network (Figure 8.5). This structure provides beam steering up to 28° in the azimuth and 26° in the elevation plane at 5.2 GHz.

Reference [240] presents a beam-switching antenna that uses an FSS-based reconfigurable reflector. The reconfigurable reflector antenna consists of multiple FSS panels arranged as a parabolic reflector (Figure 8.6). Mechanical and electrical switching are involved to offer beam scanning of 360° by rotating the panels with certain angles and switching the PIN diodes on and off. This hybrid approach demonstrated an 11.25-dBi gain at 2.45 GHz.

A beam-switching antenna using an active cylindrical slot frequency selective surface is presented [241]. The antenna system is composed of an omnidirectional monopole antenna and the FSS that uses one PIN diode as active device (Figure 8.7).

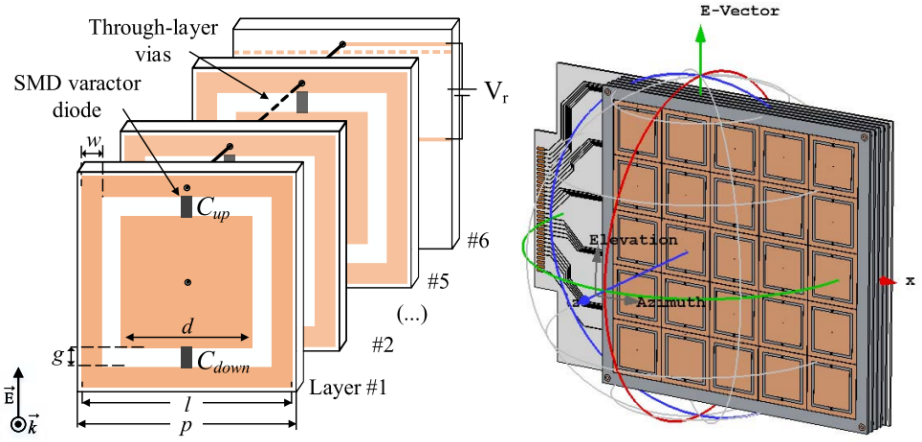

Figure 8.5: Reconfigurable FSS-inspired transmit array proposed in [226].

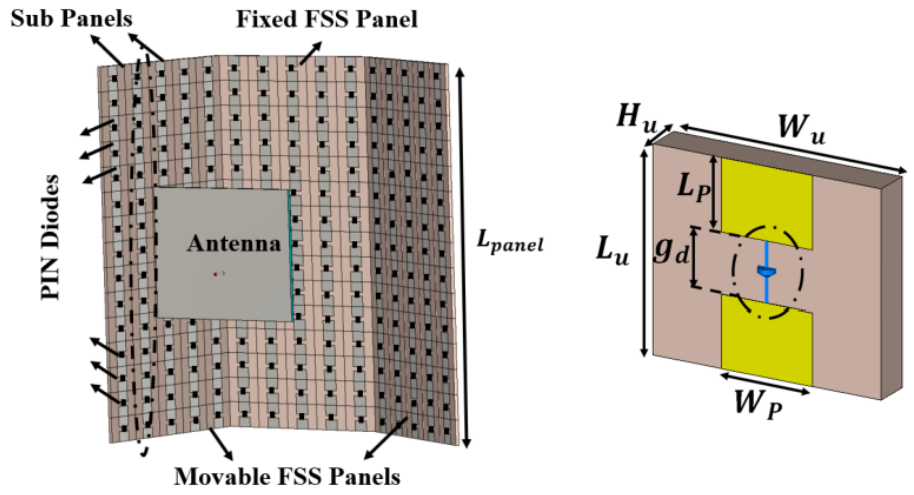

Figure 8.6: Reconfigurable beam-switching antenna system proposed in [240].

The FSS has two layers, being the top one where the slop element is presented, and the bottom layer carries the biasing circuitry and PIN diode. This system covers the entire azimuth plane by steering the beam when determined columns of diodes are set off or on. The H-plane gain was 8.7 dB at 2.45 GHz in the most commonly used narrow-beam mode.

Reference [242] presents a beam-switching antenna with coverage in the azimuth plane. The system consists of an omnidirectional dipole and a phase adjustable active FSS with 18 columns as shown in Figure 8.8. To steer the pattern of the dipole, each FSS structure is embedded with two varactors with an orderly bias voltage under the guidance of the phased compensation method. The results show that the gain is 13.3

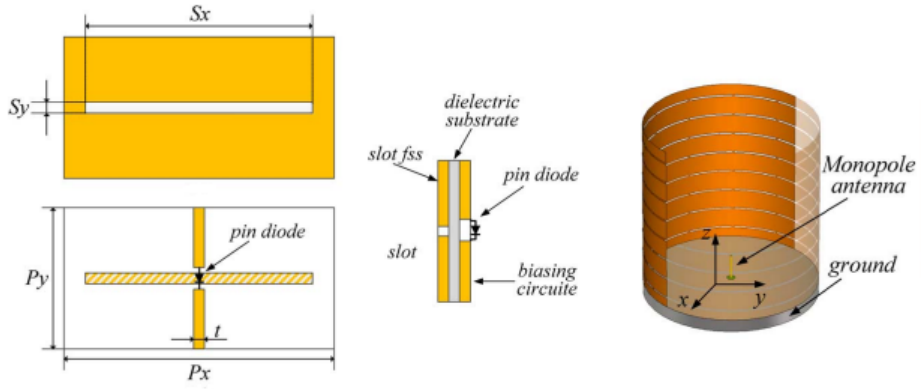

Figure 8.7: Reconfigurable beam-steering antenna system proposed in [241].

dBi at 2.45 GHz, the side-lobe level in the H-plane is 9.8 dBi, and the side-lobe level in the E-plane is 14.3 dBi.

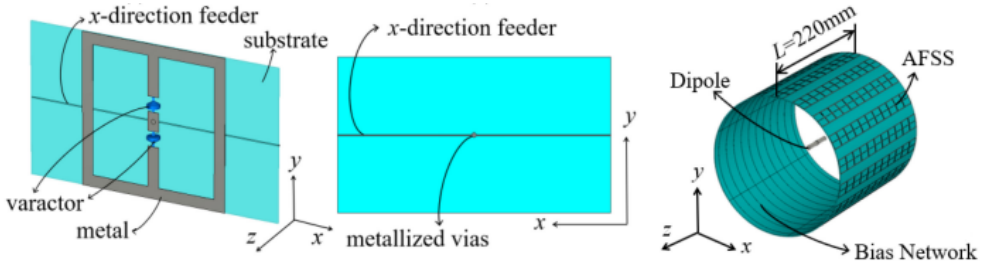

Figure 8.8: Reconfigurable beam-steering antenna system proposed in [242].

In this chapter, two electronic beam-steering antenna systems are proposed by employing reconfigurable FSSs. The radiation pattern of an omnidirectional source is controlled and shaped for better coverage in both works. The first system consists of a reconfigurable corner antenna that alters the beam direction in the azimuth plane and enhances the gain. The second system consists of a reconfigurable sectoral antenna that offers beam sweeping in the azimuth plane and beam scanning in the elevation plane, with variable gain. The proposed systems are featured with power consumption as only a single PIN diode is used per unit cell. The independent control of the FSS rows offer three FSS transmission responses that are exploited in the antenna system designs.

8.2 Dipole antenna design

The half-wave dipole antenna is one of the most used and simple antennas, which consists of two aligned metallic segments. The length of its conductive elements is approximately half a wavelength ($L \approx \lambda/2$) in free space at the frequency of operation [231], Figure 8.9.

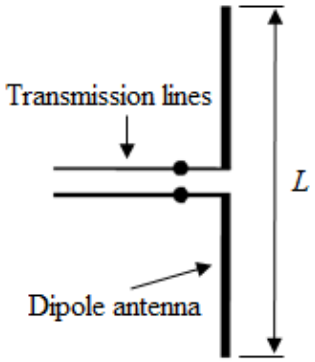

Figure 8.9: Parameter of half-wave dipole antenna.

The radiation resistance of a half-wavelength dipole is 73 Ω, which is very near to the 50-Ω impedance of the transmission line. Initially, the dipole is designed considering 100% of $\lambda/2$ and then it is optimized to match its impedance with the transmission line at the desired frequency. The dipole antenna has a length of 35 mm when designed to operate at 3.5 GHz (Figure 8.10) and 30 mm for resonance frequency at 4 GHz (Figure 8.13). The dipole antenna operating at 4 GHz was built using a Huber-Suhner model EZ141TP semi-rigid cable [243], with SMA connectors at its end. This cable is formed by a centre wire conductor with steel material of diameter equal to 0.92 mm, a PTFE dielectric of diameter equal to 2.99 mm, and a copper outer conductor covered by a tube of 3.58-mm diameter. The cable is split in half to build the poles. One of the poles is formed by the centre wire conductor and for the construction of the other pole, a part of the wire is removed and soldered to the external conductor. The fabricated dipole antenna is shown in Figure 8.12.

The half-wave dipole was chosen because it has a well-defined and symmetric radiation diagram in relation to the azimuth and elevation planes [244], as can be seen in Figure 8.11. The radiation pattern of the dipole antenna in the E-plane has an end-fire behavior with gain of 2.04 dBi at $\theta = 90°$ and 270° shown in Figure 8.11a, and HPBW of 80.9°, for 3.5 GHz. In Figure 8.11b, the radiation pattern for the H-Plane is omnidirectional with a gain of 2.04 dBi.

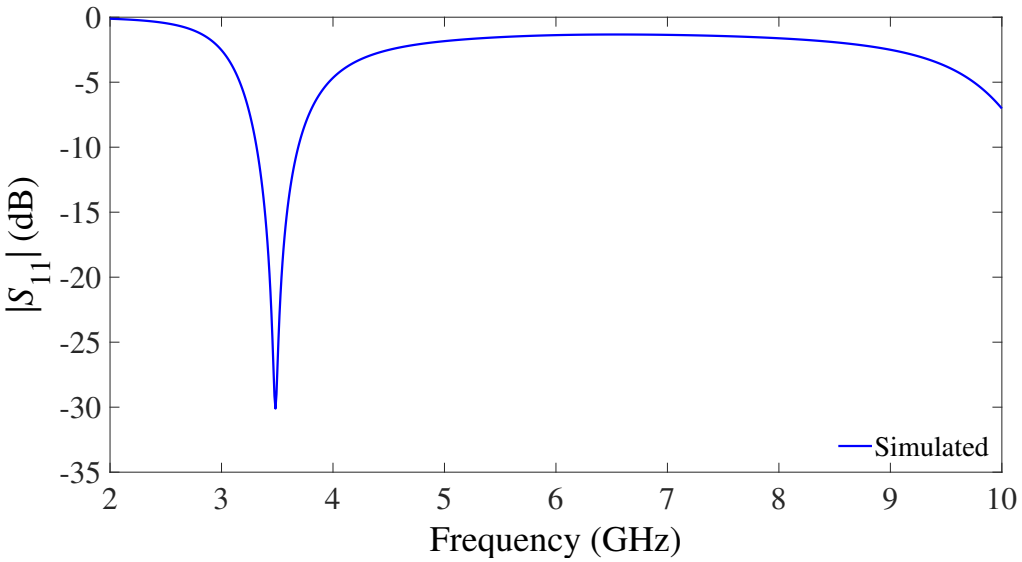

Figure 8.10: Simulated reflection spectrum of 3.5-GHz dipole antenna.

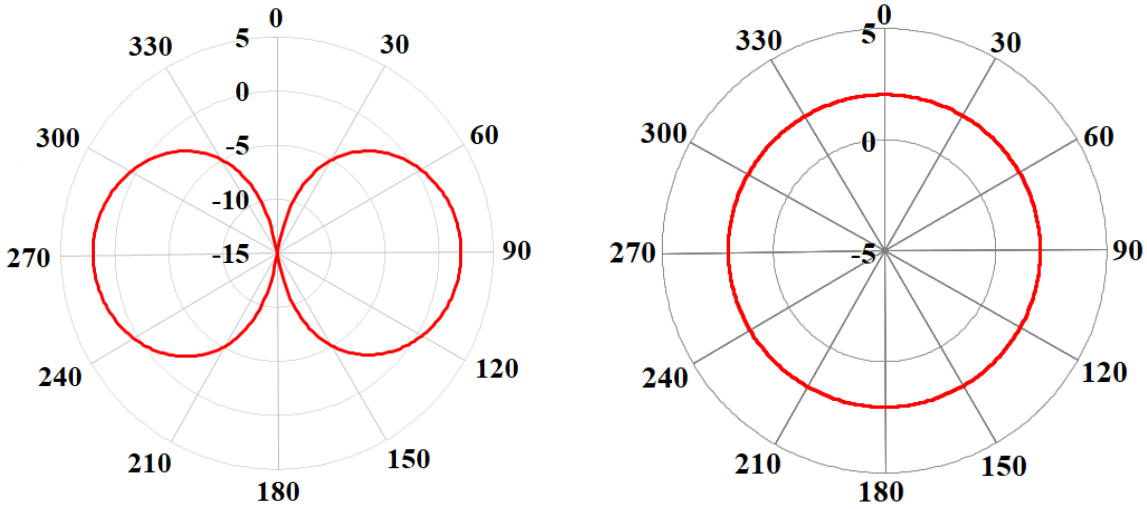

(a) E-plane. (b) H-plane.

Figure 8.11: Simulated radiation pattern of ideal half-wave dipole.

Figure 8.13 illustrates the reflection spectra of the dipole antenna designed at 4 GHz, showing a good agreement between simulation and measurement. The radiation pattern of the 4-GHz dipole antenna is the same as for the 3.5-GHz one, with about 2 dB of gain. Figure 8.14 shows the simulated and measured radiation pattern of this antenna in the H-plane. Note that the asymmetries are caused by the feeding cable.

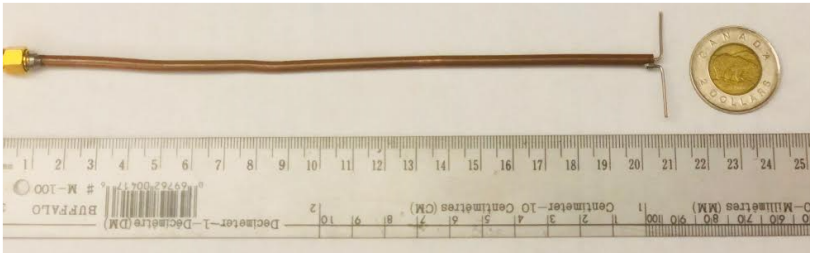

Figure 8.12: Fabricated dipole antenna.

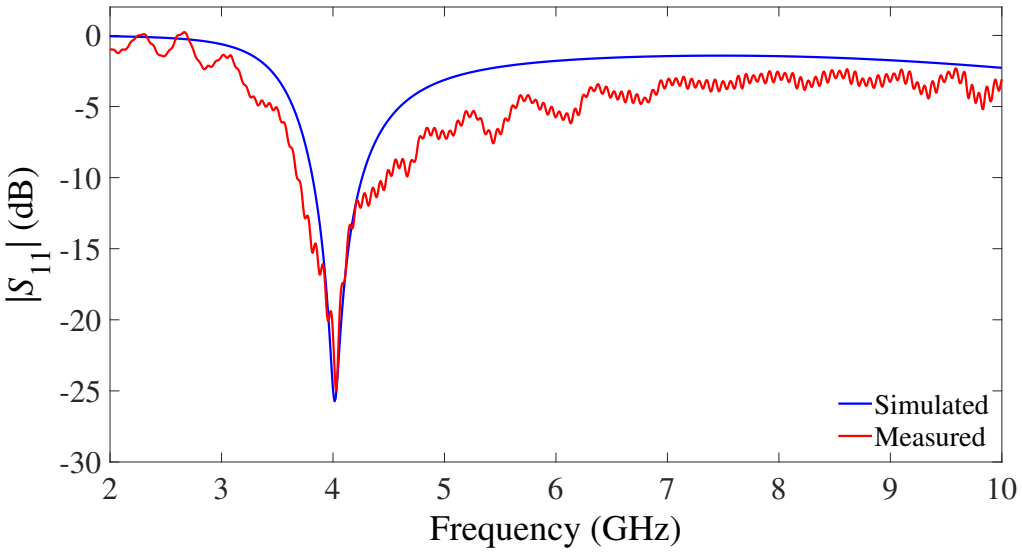

Figure 8.13: Simulated and measured reflection spectrum of 4-GHz dipole antenna.

8.3 PIN-diode-switched FSS design

The key element to realizing the beam-switching antenna is the FSS unit cell. The design of the FSS with reconfigurable transmission response is described in this section. The reconfigurable FSS based on the four-arms star geometry is used in this work, following the design procedure described in Chapter 7, Section 7.2.2, Figure 7.8, which consists of the four-arms star with a gap separating the upper and lower arms and bias lines added to all arms in the horizontal direction to apply voltage to the PIN diodes. The diode is inserted in the center of the unit cell, which can electronically connect and disconnect the arms. This structure is a good candidate due to its design simplicity as shown in the previous chapters, and its reconfigurability can be achieved by using only one PIN diode per unit cell. On- and off-states of the PIN diodes are considered.

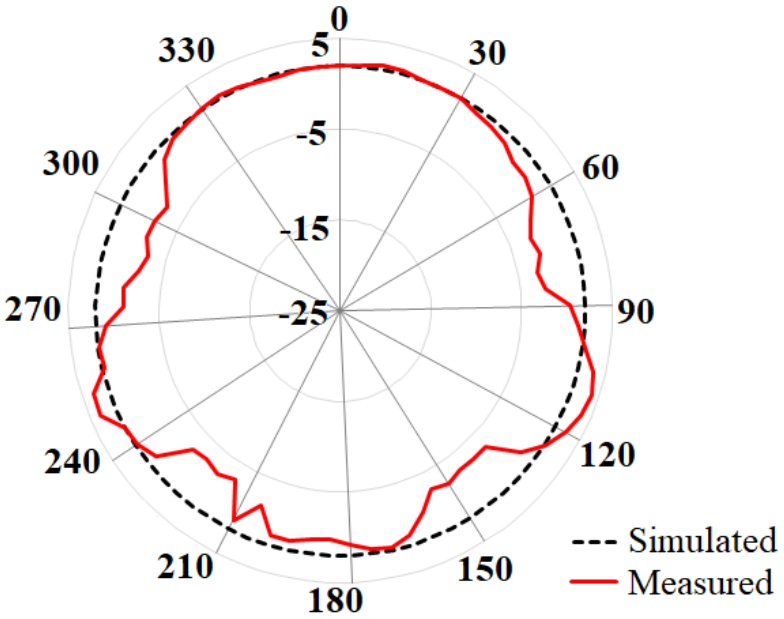

Figure 8.14: Simulated and measured results of dipole antenna radiation pattern in the H-plane.

All simulations were performed in CST Microwave Studio. The RFSSs were designed, using single-layer Rogers Duroid/RT 6002 and FR-4 dielectric substrates for 3.5 GHz (RFSS#1) and 4 GHz (RFSS#2) in their on-state, respectively. Based on the design procedure for the four-arms star geometry presented in previous chapters, the dimensions for these operating frequencies are listed in Table 8.1. The surface-mountable Infineon BAR 64-03 PIN diodes in SOD323 package, with parasitic inductance of 1.8 nH, are used. The package length and width are 1.7 mm and 1.25 mm, respectively. When forward biased, these diodes offer low resistance with typical value of 1.35 Ω at 100 mA and 0.95 V. When reverse biased, they can reach low capacitance as 0.2 pF at 0 V [245]. The biasing network is the same as in Chapter 7, Section 7.4, Figure 7.14, which allows the control of each FSS' row independently. Using a biasing voltage, the PIN diodes are switched to off- and on-states, hence the geometry's effective length and its respective resonance frequency change. Figure 8.15 shows the fabricated RFSS operating at 4 GHz with 8 × 8 elements and the enlargement of its unit cell, where the PIN diode is soldered in the switching point.

The simulated results of RFSS#1 are shown in Figure 8.16. Figure 8.16a illustrates the transmission spectra results of TE polarization for the on- and off-states with resonance frequencies at 3.47 GHz and 5.9 GHz, respectively. The resonance frequency in the off-state is approximately twice when compared to that of the on-

Freq. (GHz)	a_p (mm)	b_p (mm)	g (mm)	p_p (mm)	s_p (mm)	w_b (mm)	h (mm)	ϵ_r	tanδ
3.5	22	3	1	30	3	1	0.508	2.94	0.0012
4.0	12	2	1	22.5	3	1	1	4.4	0.025

Table 8.1: Values of RFSS parameters.

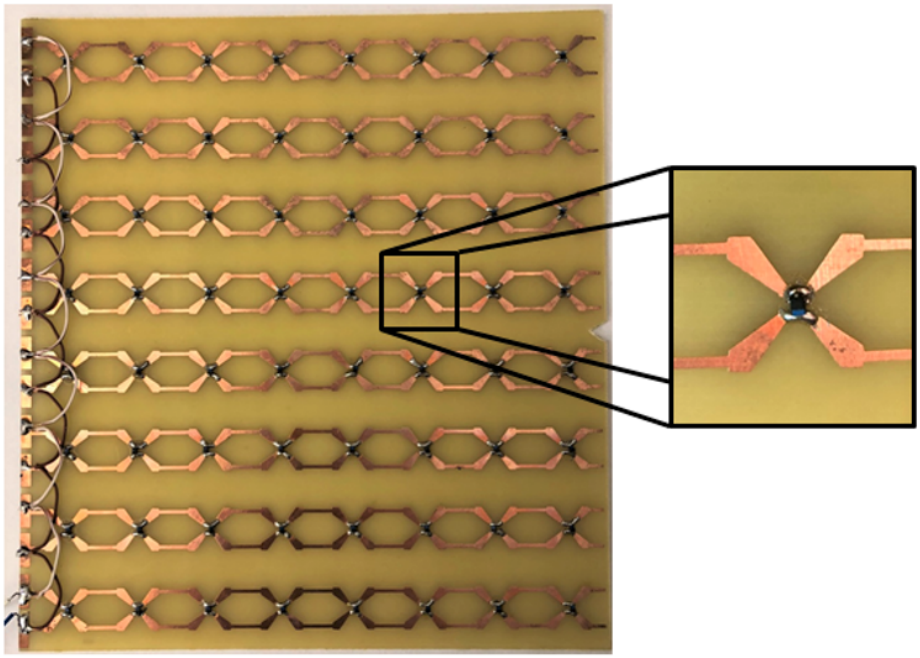

Figure 8.15: Fabricated RFSS#2.

state due to the fact that the geometry in that state is composed of two separate parts. Figure 8.16b presents the results of TM polarization for the on- and off-state; in this case the resonance frequencies for both states remain practically the same at 6.71 GHz and 6.72 GHz, respectively. These responses are expected as described in Chapter 7, Section 7.2.2.

RFSS#2 was characterized numerically and experimentally, and the results of its transmission spectra are shown in Figure 8.17 and Figure 8.18. The measurements were performed as described in Appendix A, Section A.2.2. Three state configurations to bias the FSS rows are considered and they are described in Table 8.2. Note that the diodes in each row are connected in parallel, i.e., the voltage across the diodes is the same applied in that row. Furthermore, by controlling the states of row#1 and row#2, the RFSS can be easily switched between state-11 (on-state), state-10 (intermediate state), and state-00 (off-state).

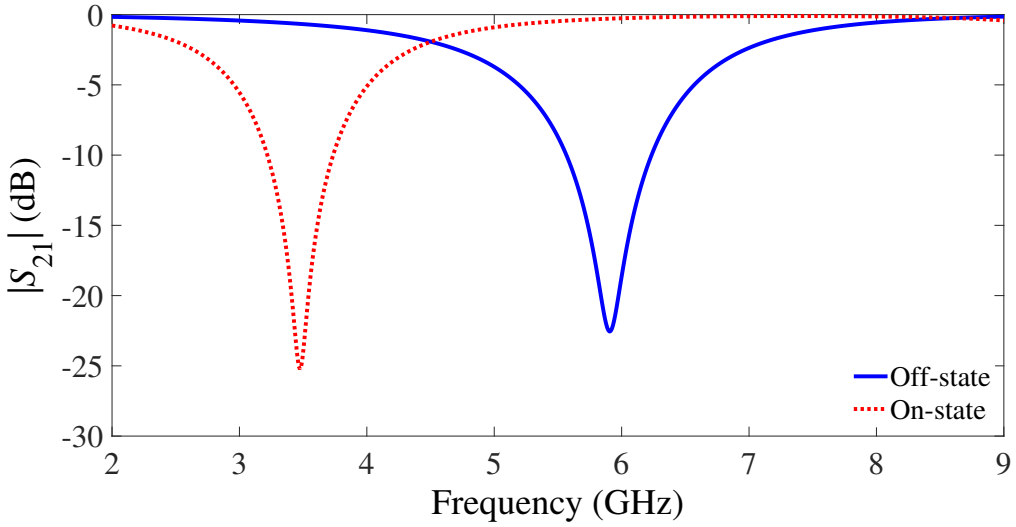

(a) TE polarization.

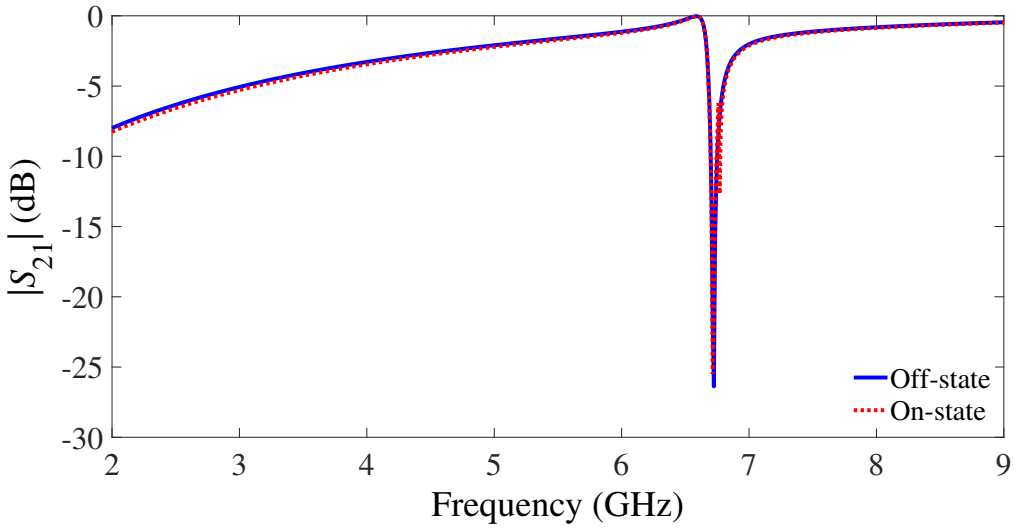

(b) TM polarization.

Figure 8.16: Simulated frequency response of RFSS#1 in the on- and off-state.

For vertical (y) polarization, numerical and measured results are presented in Figure 8.17a for the off- and on-states. In the on-state, the PIN diodes in all FSS rows are forward biased, presenting resonance frequencies at 4.06 GHz and 4.1 GHz for the simulated and measured results, respectively, with minor differences observed. When the PIN diodes in all rows are in the off-state, i.e., they are reverse biased, the RFSS' resonance frequency switches to 6.96 GHz (simulated) and 6.73 GHz (measured). Figure 8.17b presents the results of horizontal (x) polarization for the off- and on-

state; in this case the resonance frequencies for both states are approximately the same: 8.78 GHz (numerical) and 8.47 GHz (experimental). This is due to the fact that the electric field in this polarization is perpendicular to the PIN-diode leads, thus the switching operation is of hardly any effect.

	State-11	State-10	State-00
Row#1	ON	ON	OFF
Row#2	ON	OFF	OFF

Table 8.2: Switching state of the FSS rows.

The state-10 is a state where half of the rows in the FSS panel have their PIN diodes forward biased, while the other half is reserve biased. In this state, the FSS frequency response is a combination of the one for the on-state FSS and off-state FSS. Figure 8.18a shows that in the TE polarization, the FSS presents two resonance frequencies, one at 4.12 GHz and 4.15 GHz, and another at 6.84 GHz and 6.44 GHz, for the simulated and measured results, respectively, which are the transmission nulls originated from the on- and off-state FSSs. Figure 8.18b illustrates the frequency response in the TM polarization, which is the same as in Figure 8.17b.

8.4 Reconfigurable corner antenna

The first system proposed in this chapter consists of a 4-GHz dipole antenna with FSS panels acting as corner reflector to reconfigure its radiation pattern while increasing its gain. The applicability of FSSs as reconfigurable corner reflectors is demonstrated in this section.

8.4.1 Electric field of the antenna with FSS-based corner reflector

The corner reflector consists of two-plane conductive plates joined so as to form a corner of aperture angle α [17]. Half-wavelength dipoles are commonly used as feed element for corner reflectors, which are placed parallel to the vertex a distance s away. The plates have finite dimensions with width l and height h, forming the aperture angle with size of the aperture D_α [231], as illustrated in Figure 8.19.

The distance between the feed element and the reflector influences the distribution of the field around this assembly, hence affects the antenna's maximum gain.

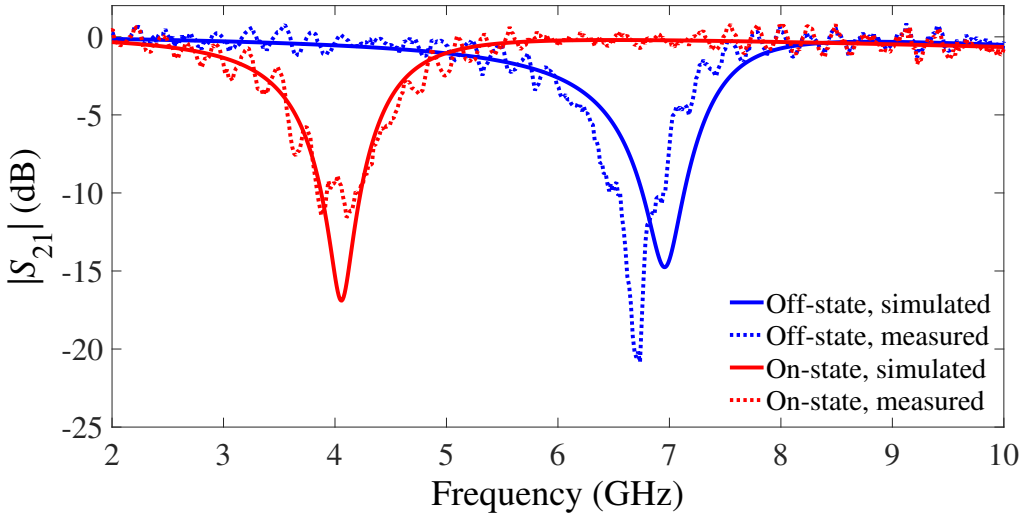

(a) TE polarization.

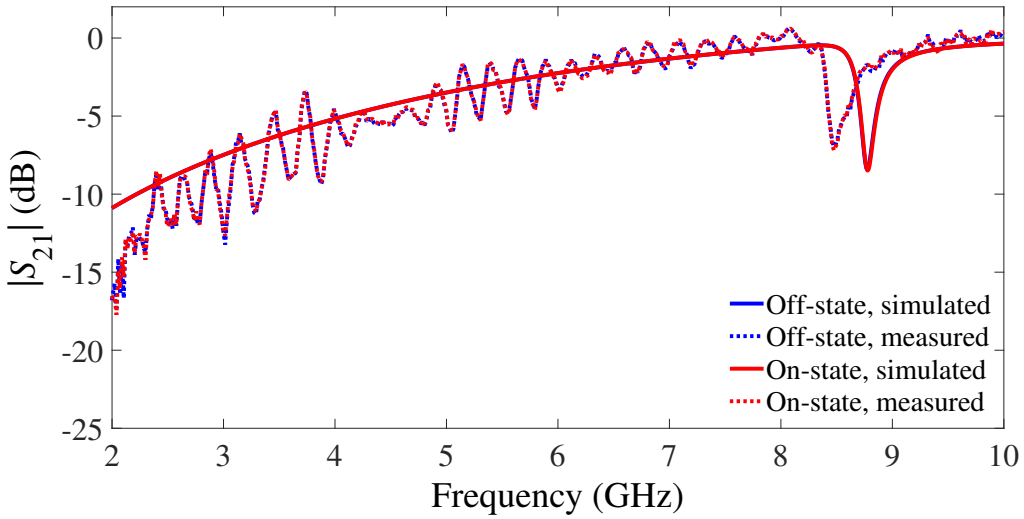

(b) TM polarization.

Figure 8.17: Simulated and measured frequency response of RFSS#2 in the on- and off-state.

Therefore, to obtain an optimized design, it is necessary to verify the behavior of the assembly as a function of this dipole-plate spacing [246].

The electrical size of the aperture is typically designed with values between one and two wavelengths ($\lambda < D_\alpha < 2\lambda$). The antenna far field can be determined by image theory. If the two plates of the reflector are electrically large, they can be approximated by infinite plates. The aperture angle and the polarization of the feed

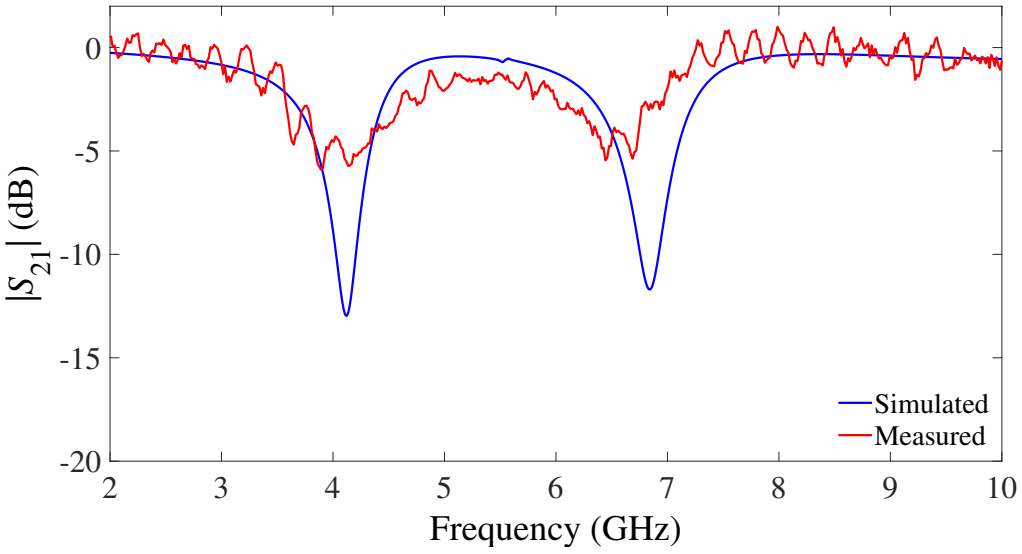

(a) TE polarization.

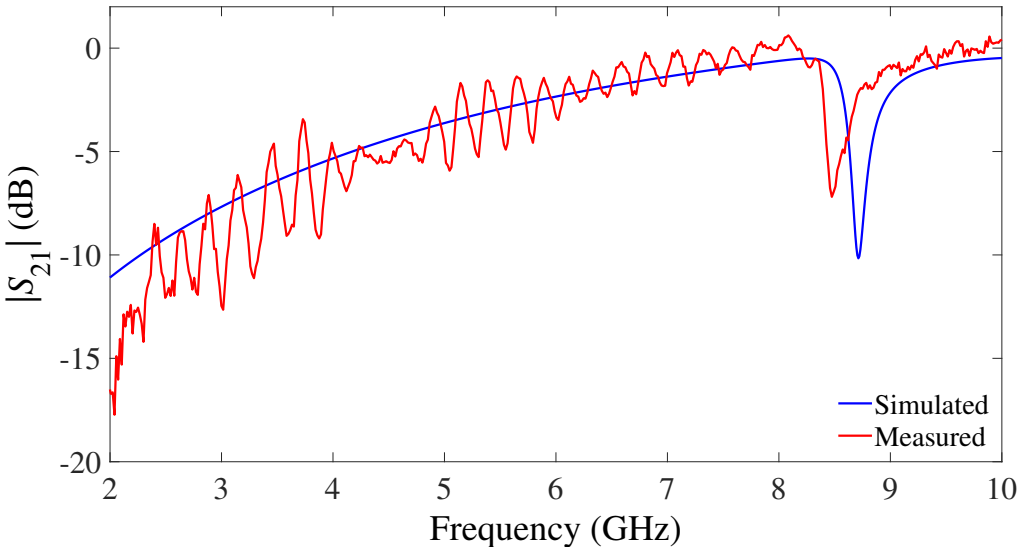

(b) TM polarization.

Figure 8.18: Simulated and measured frequency response of RFSS#2 in the state-10.

element control the number of images, their polarity, and position (Figure 8.20a). Assuming that the feed element is placed parallel to the vertex and the aperture angle of the corner reflector is 90°, the procedure to find the number, location, and polarity of the images (Figure 8.20) is as follows: the image #2 represents the image of the feed element to plate #1. Similarly, image #4 represents the image of the feed to plate #2. An additional image (#3) is required so the image #2 satisfies the

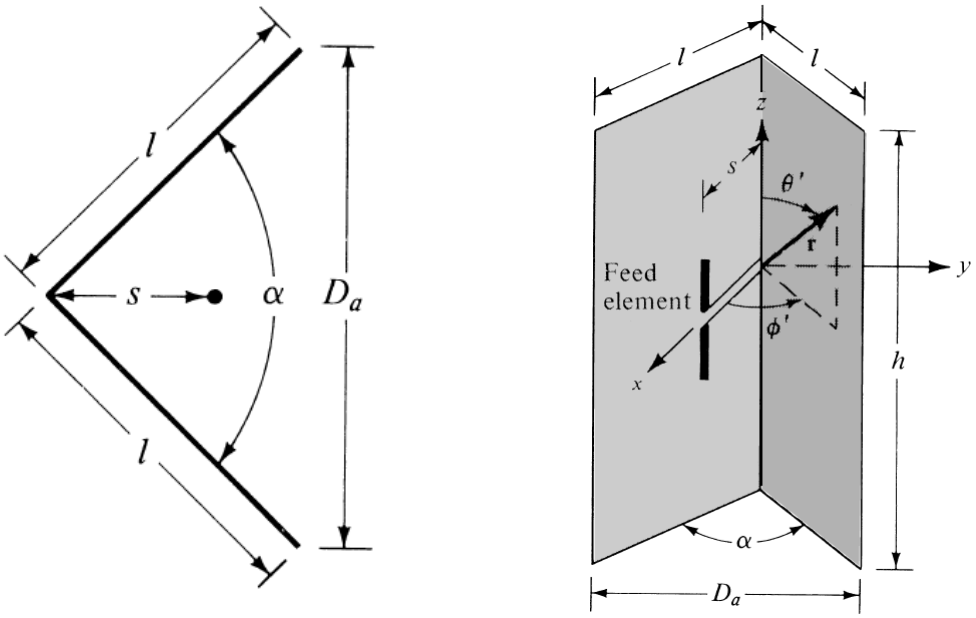

(a) Top view. (b) Perspective view.

Figure 8.19: Corner reflector and its parameters [231].

electric field boundary condition on plate #2. The image #3 also allows image #4 to satisfy the electric field boundary condition on plate #1. Summing the contributions from the feed element (E_1) and its images (E_2, E_3 and E_4), the total E-field of the system at the observation point P can be calculated as

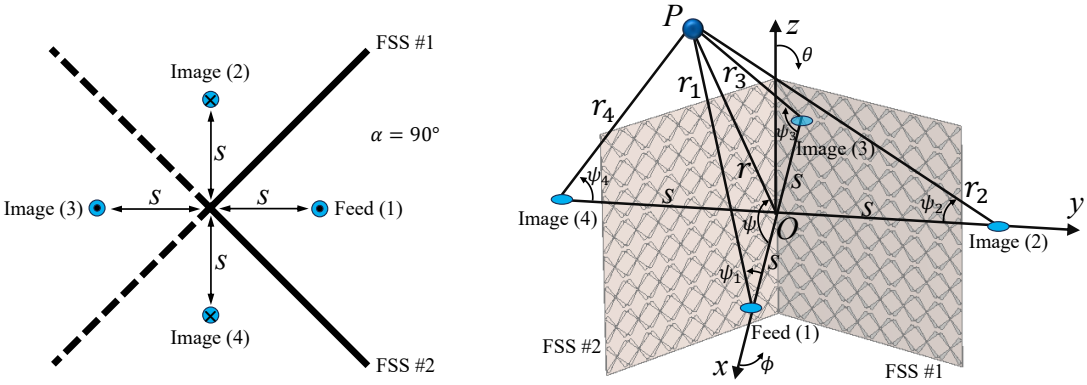

(a) Top view. (b) 3-D view.

Figure 8.20: FSS-based corner reflector and its images.

$$E(r,\theta,\phi) = E_1(r_1,\theta,\phi) + E_2(r_2,\theta,\phi) + E_3(r_+,\theta,\phi) + E_4(r_4,\theta,\phi) \tag{8.1}$$

The normalized E-field in the far field zone for each n image is written as

$$E(r_n, \theta, \phi) = f(\theta, \phi)\frac{e^{-jkr_n}}{r_n} \tag{8.2}$$

where $k = 2\pi/\lambda$ is the propagation constant. The total electric field on the conducting surface of the FSS, for the incident field E_i and the reflected field E_r, must be equal to zero [16]:

$$E_i + E_r = 0 \tag{8.3}$$

Applying the above condition on the feed element changes the polarities of the E-fields corresponding to images #2 and #4. Thus, the total scalar field at P in the far field zone is

$$E(r, \theta, \phi) = f(\theta, \phi)\frac{e^{-jkr_1}}{r1} - f(\theta, \phi)\frac{e^{-jkr_2}}{r2} + f(\theta, \phi)\frac{e^{-jkr_3}}{r3} - f(\theta, \phi)\frac{e^{-jkr_4}}{r4} \tag{8.4}$$

As shown in Figure 8.20b, the radial spacing between the origin O and the observation point is r. Any n image in the far-zone is $r_n = r$ for magnitude and $r_n = r–d\cos\psi_n$ for phase. The total E-field can be rewritten as

$$E(r, \theta, \phi) = [e^{+jks\cos\psi_1} - e^{+jks\cos\psi_2} + e^{+jks\cos\psi_3} - e^{+jks\cos\psi_4}]f(\theta, \phi)\frac{e^{-jkr}}{r} \tag{8.5}$$

where

$$\cos\psi_1 = \hat{a}_x \cdot \hat{a}_r = \sin\theta\cos\phi \tag{8.6a}$$

$$\cos\psi_2 = \hat{a}_y \cdot \hat{a}_r = \sin\theta\sin\phi \tag{8.6b}$$

$$\cos\psi_3 = -\hat{a}_x \cdot \hat{a}_r = -\sin\theta\cos\phi \tag{8.6c}$$

$$\cos\psi_4 = -\hat{a}_y \cdot \hat{a}_r = \sin\theta\sin\phi \tag{8.6d}$$

since $\hat{a}_r = \hat{a}_x\sin\theta\cos\phi + \hat{a}_y\sin\theta\sin\phi + \hat{a}_z\cos\theta$, Equation (8.5) is rewritten as

$$E(r,\theta,\phi) = 2[\cos(ks\sin\theta\cos\phi) - \cos(ks\sin\theta\sin\phi)]f(\theta,\phi)\frac{e^{-jkr}}{r} \tag{8.7}$$

The field of an isolated element in free-space is

$$E_0 = f(\theta,\phi)\frac{e^{-jkr}}{r} \tag{8.8}$$

Then, for $\alpha = 90°$, Equation (8.7) can be rewritten as

$$\frac{E}{E_0} = 2[\cos(ks\sin\theta\cos\phi) - \cos(ks\sin\theta\sin\phi)] \tag{8.9}$$

Similarly, the array factor and total E-fields are derived for aperture angles of $180°/n$, where for $\alpha = 45°$ is

$$\frac{E}{E_0} = 2\Bigg[\cos\left(ks\sin\theta\cos\phi\right) + \cos\left(ks\sin\theta\sin\phi\right) - 2\cos\left(\frac{ks\sin\theta\cos\phi}{\sqrt{2}}\right)\cos\left(\frac{ks\sin\theta\sin\phi}{\sqrt{2}}\right)\Bigg] \tag{8.10}$$

Equations (8.9) and (8.10) show that the use of FSSs as reflector increases the gain of any antenna with omnidirectional radiation pattern in a specific direction. It is also observed that the gain varies with spacing s and multiple lobes start appearing for larger spacings, that will happen for $\alpha = 90°$ when $s > 0.7\lambda$ and $\alpha = 45°$ when $s > 1.2\lambda$ [231].

8.4.2 Configuration

A dipole antenna with corner reflector, in principle, uses metallic plates to form the reflector, which can enhance its gain in a specific direction by reducing its radiation in other directions. Although metallic reflectors improve the gain and front-to-back ratio, their performance is optimal over a relatively small frequency band [247]. In this section, an FSS is designed to act as a reflector, i.e., provides reflectivity of the signal as the metallic plates. FSSs are frequency-dependent reflectors, which have the advantage of multiple frequency bands. Two FSS panels are used to form the corner reflector when it shows the same resonance frequency (4 GHz) as the feed element. The main feature of this system is because the FSS is reconfigurable, it allows to

reconfigure the antenna's radiation pattern. The configuration of the proposed system follows the process described in Section 8.4.1, where the distance between the dipole antenna and the vertex of the corner reflector depends on the aperture angle, being 75 mm for $\alpha = 45°$ and 60 mm for $\alpha = 90°$. The reconfigurable corner reflector antenna was manufactured using two RFSSs to reconfigure its radiation pattern; Figure 8.21 shows its configuration with the aperture angle of 45° of FSS panels.

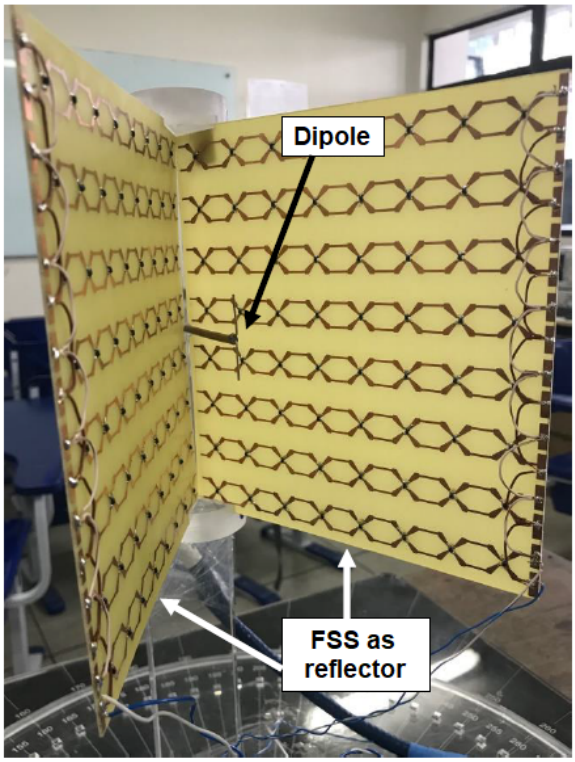

Figure 8.21: Fabricated reconfigurable corner reflector antenna.

8.4.3 Results

Figure 8.22 shows the results of numerical and experimental characterization of the system, when using the RFSSs in the on-state as reflector, with aperture angle of 45° in the azimuth plane. It is observed in this case that the RFSS behaves as a reflector, rendering the radiation pattern directive at $\theta = 0°$, with a gain of 9.16 dB in the experimental results. Simulated and measured results agree reasonably well considering the fact that all diodes have been hand soldered into the FSSs. The same applies for the following results.

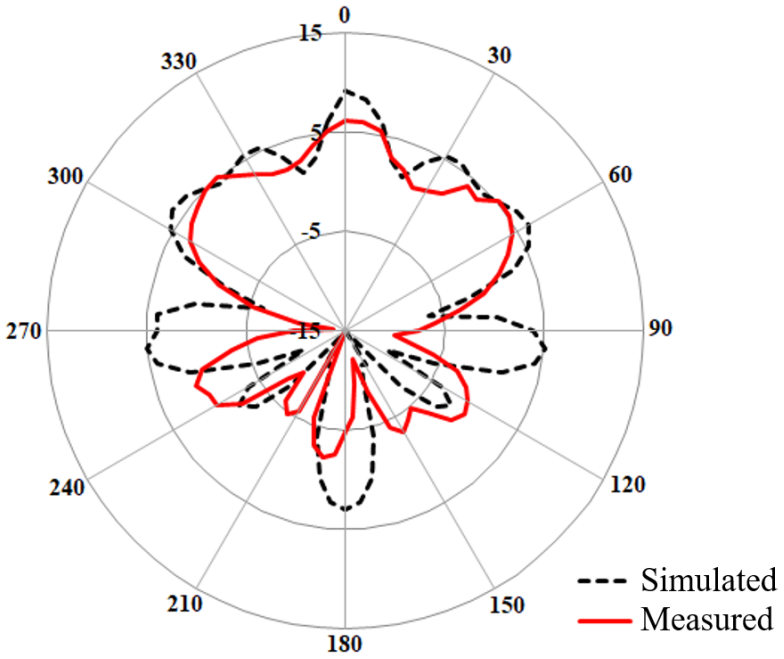

Figure 8.22: Simulated and measured results of non-normalized radiation pattern of antenna using RFSSs as $\alpha = 45°$ reflector with their diodes in the on-state.

Figure 8.23 shows the respective results when the RFSSs are used in the off-state. In this case, the RFSSs behave as directors. Due to the fact that the total phase of the FSS corner reflector system is different, the simulated and measured gains at $\theta = 0°$ decrease to -11.73 dB and -5.86 dB, respectively, and the main beams point towards angles of $\approx \pm 60°$ with maximum measured gain of 6.35 dB.

The simulated results for the reconfigurable corner reflector antenna with aperture angle of 90° in the azimuth plane is shown in Figures 8.24 and 8.25 for the diodes in the on- and off-state, respectively. It can be seen that results for this aperture angle are similar to the ones when $\alpha = 45°$ with maximum gain of 10.5 dBi and 5.95 dBi for the diodes in the on- and off-state, respectively.

8.4.4 Performance assessment

Radiation-pattern measurement results confirm that the proposed corner reflector antenna achieves reconfigurable reponse by switching the diodes' on/off states with gain difference at $\theta = 0°$ greater than 20 dB. Moreover, simulated results show that the proposed system has similar behavior for different aperture angles.

The characteristics of the proposed structure are compared with other beam-

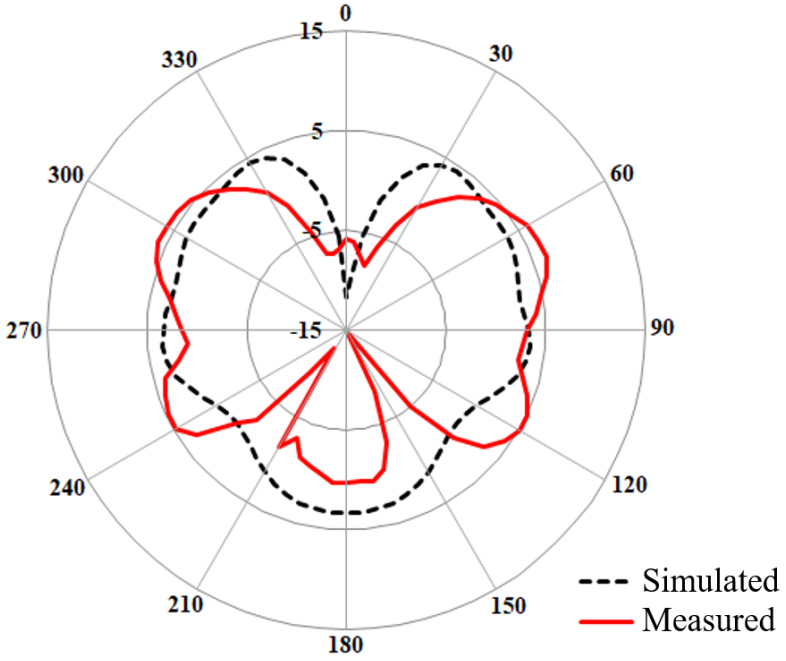

Figure 8.23: Simulated and measured results of non-normalized radiation pattern of antenna using RFSSs as $\alpha = 45°$ reflector with their diodes in the off-state.

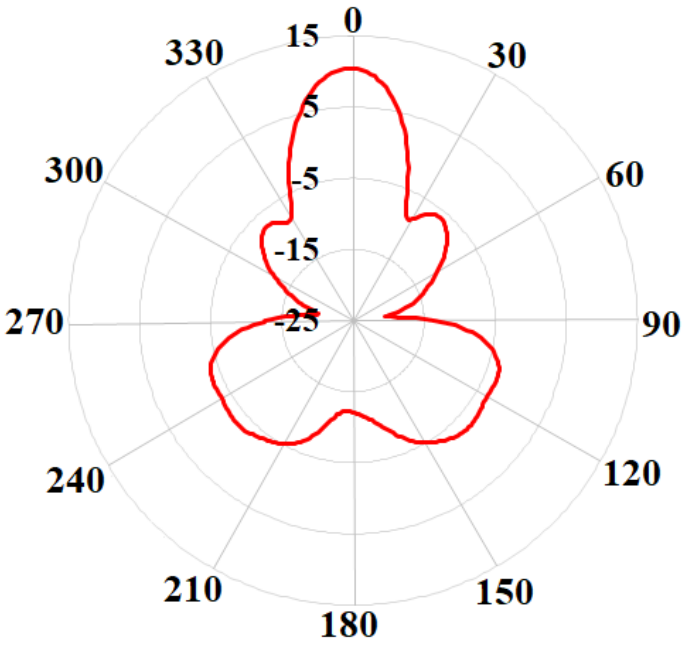

Figure 8.24: Simulated result of radiation pattern of antenna using RFSSs as $\alpha = 90°$ reflector with their diodes in the on-state.

switching/steering antenna systems, previously published, in Table 8.3, which include

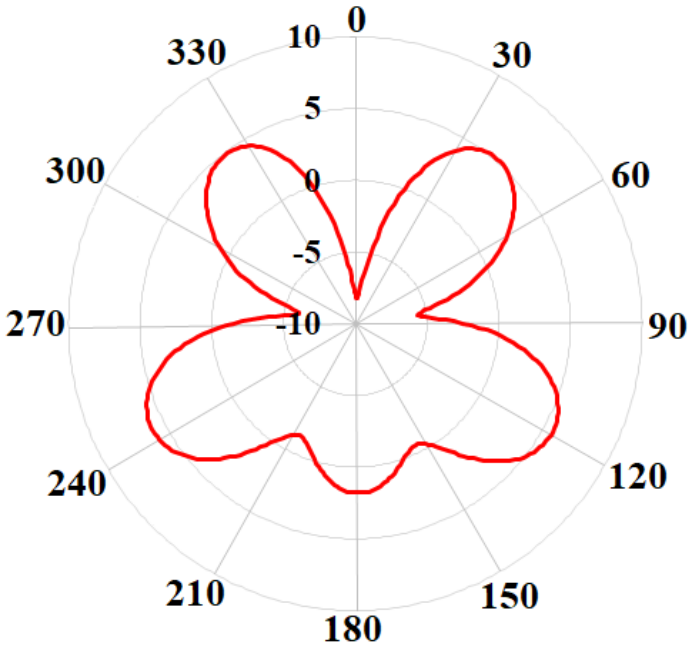

Figure 8.25: Simulated result of radiation pattern of antenna using RFSSs as $\alpha = 90°$ reflector with their diodes in the off-state.

the tuning method used, maximum gain obtained, maximum beam-steering/switching angle, and frequency of operation. The proposed corner antenna only uses one active component per unit cell to reconfigure its radiation pattern, achieving gain enhancement and directivity at desired resonance frequency, as well as wider beam switching range.

8.5 Reconfigurable sectoral antenna

The development of the reconfigurable corner antenna presented in Section 8.4 led to the design of a reconfigurable sectoral antenna, which will be demonstrated in this section. This work focuses on reconfiguring the antenna's radiation pattern in different directions in the azimuth and elevation planes for below-6GHz applications. Six different cases of antenna reconfigurability are analyzed.

8.5.1 Configuration

The proposed 3-D electronic beam-switching antenna system is designed to operate at 3.5 GHz. The reconfigurable sectoral antenna consists of four FSS panels with

Ref.	Tuning method	Maximum gain (dBi)	Beam-steering/ switching range	Frequency (GHz)
[236]	2-PIN-diodes loaded	10	±22°	5.5
[237]	1-PIN-diode loaded	11	±18°	5.5
[238]	Not available	6.8 and 8.3	Not available	3.5 and 5.8
[239]	6/3-PIN-diodes loaded	9.5	±5°	2.4
[226]	2-varactor-diodes loaded	Not reported	28°	5.2
This work	1-PIN-diode loaded	9.16	±60°	4.0

Table 8.3: Comparison of proposed reconfigurable corner antenna with other reported reconfigurable systems.

arrays of 4 × 4 elements placed with an angle of 45° in relation to the centered point, where the feed element is located (Figure 8.26a). In this work, the dipole was chosen as excitation source for the same reasons mentioned in Section 8.4. RFSS#1 is used as steerable element to control the radiation characteristics of the proposed antenna, whose resonance frequency in the on-state is the same as that of the dipole. The distance from the dipole to the centers of the RFSSs is 60 mm. Figure 8.26b shows a schematic diagram and the 3-D view of the proposed sectoral antenna.

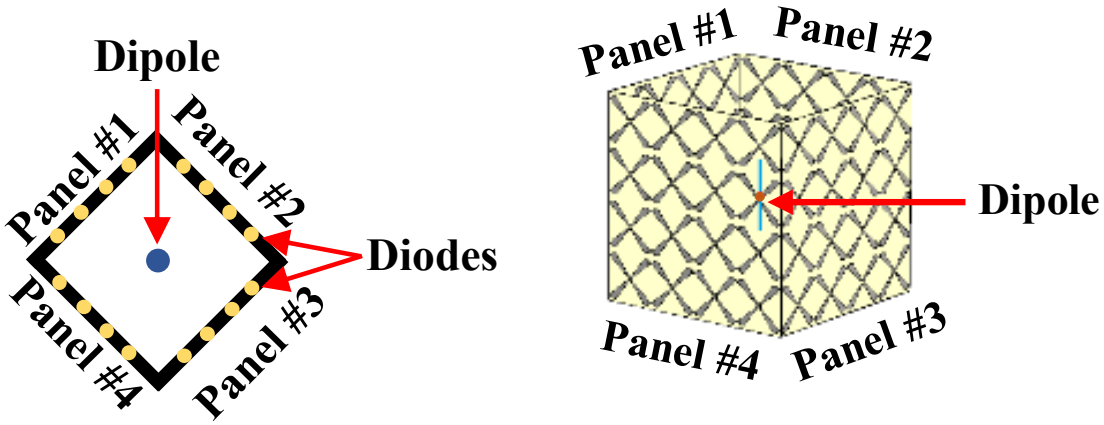

(a) Schematic diagram. (b) 3-D view.

Figure 8.26: Proposed reconfigurable sectoral antenna.

Four cases of operation are considered, where all the PIN-diodes in certain panels are in off- or on-states, as shown in Figure 8.27a. When the diodes are in the off-

state, the FSS has a high transmission coefficient at the desired frequency, allowing the incident electromagnetic (EM) waves to pass. In the on-state, the FSS has a high reflection coefficient, reflecting the incoming EM wave. Hence, this mechanism converts the omnidirectional radiation pattern of the dipole into a directive one. By switching the states, the beam can be reoriented in the azimuth plane, and its gain is enhanced. Additionally, the control of the FSS rows allows beam tilting in the elevation plane. Two cases are considered for beam tilting as shown in Figures 8.27b and 8.27c.

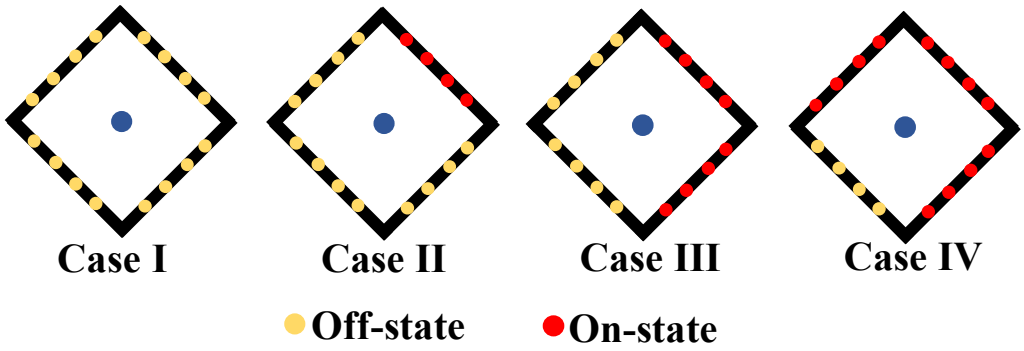

(a) Cases for switching in the azimuth plane.

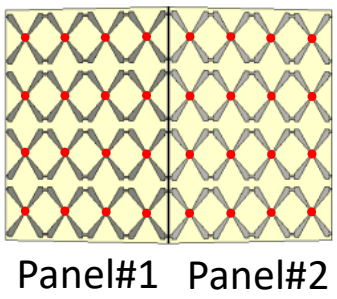

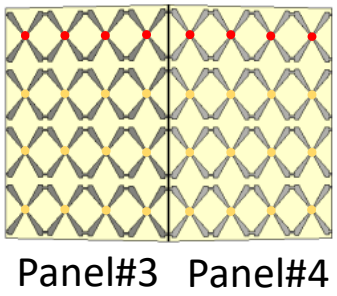

(b) Configuration for tilting in the elevation plane for Case III.

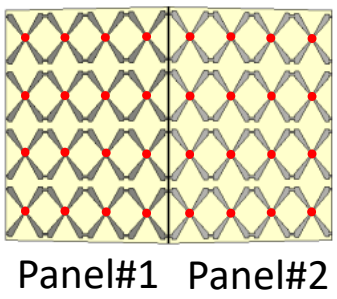

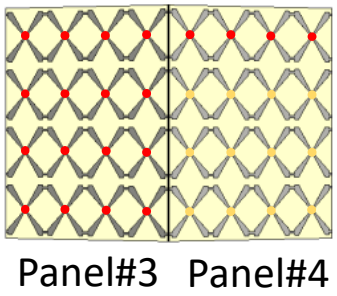

(c) Configuration for tilting in the elevation plane for Case IV.

Figure 8.27: Diodes configuration.

8.5.2 Results

Figure 8.28 shows the radiation pattern for the first case (Case I), when all diodes are in the off-state. In this case, the FSSs let the incident EM wave pass due to the fact that their resonance frequency is different from that of the dipole and the total phase of the FSS system is identical. Therefore, it can be observed that the radiation pattern follows an omnidirectional behavior, with a gain of 1.8 dBi.

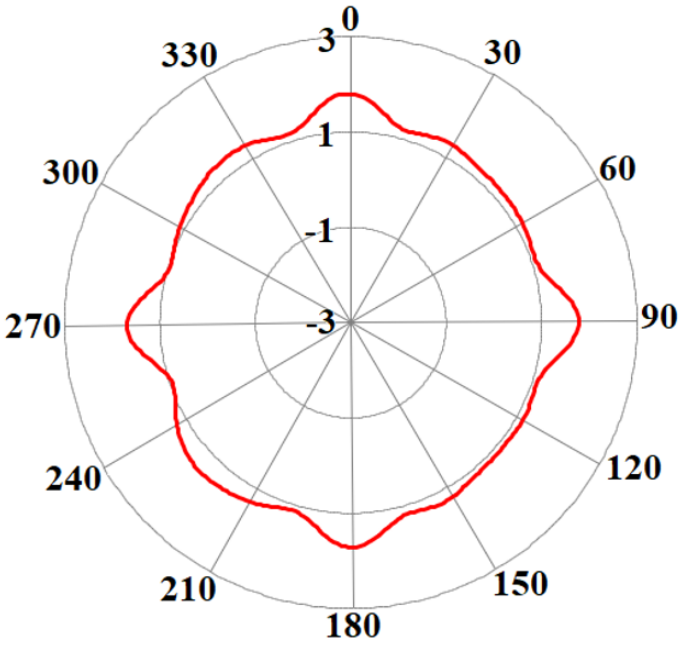

Figure 8.28: Radiation pattern of the proposed antenna for Case I in the H-plane.

In the second case (Case II), shown in Figure 8.29, one FSS panel is switched so that its diodes are in the on-state, thus reflecting the EM wave and steering the beam in the opposite direction. This makes the radiation pattern more directive when compared with the dipole, with maximum gain of 7.46 dBi at $\theta = 225°$ and a Half Power Beamwidth (HPBW) of 66.6°.

Two FSSs have their diodes in the on-state in the third case (Case III), where the beam is steered away from them. The maximum gain of around 7.7 dBi is obtained at $\theta = 210°$ and 330°, the gain at $\theta = 270°$ is 4.47 dBi. It can be seen that in this case (Figure 8.30), the radiation pattern of the antenna system is also directive. When compared to the previous case, it has a gain improvement towards the side directions.

In the last configuration (Case IV), panels #1, #2 and #3 (Figure 8.31) have their diodes in on-states, blocking the EM wave in their direction, which directs the

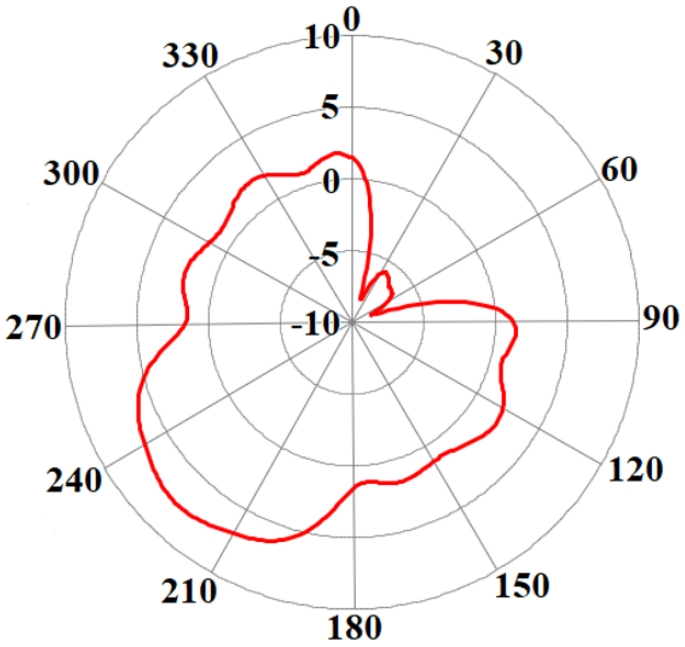

Figure 8.29: Radiation pattern of the proposed antenna for Case II in the H-plane.

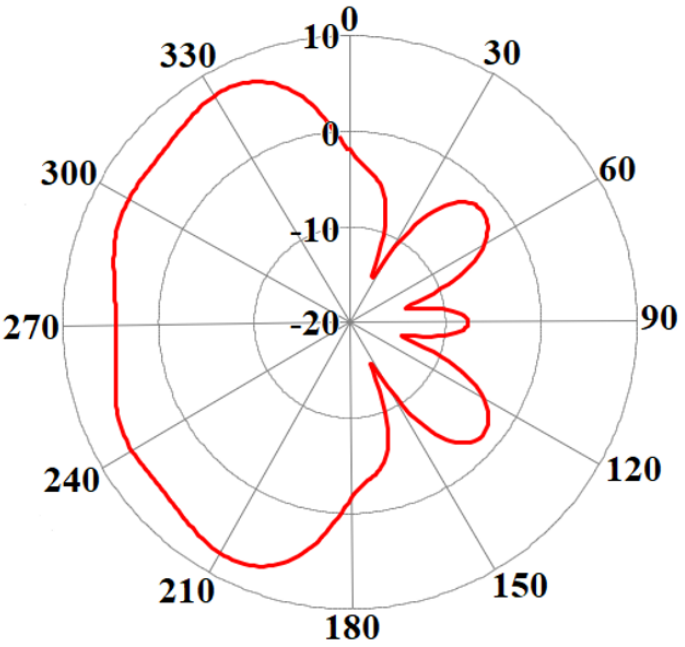

Figure 8.30: Radiation pattern of the proposed antenna for Case III in the H-plane.

beam toward panel #4. The gain is enhanced to 10.2 dBi at $\theta = 225°$ with a HPBW of 38.2°.

Obviously, the beams of Cases II, III and IV investigated here can be rotated by

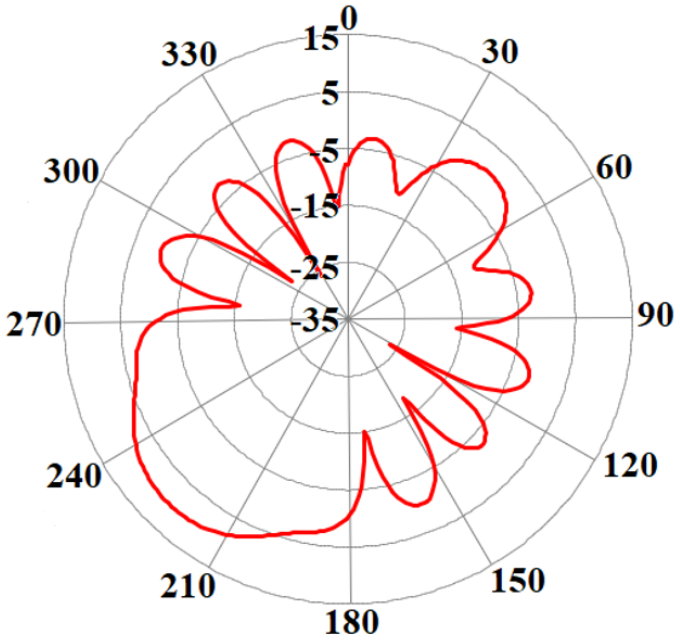

Figure 8.31: Radiation pattern of the proposed antenna for Case IV in the H-plane.

90°, 180° or 270° in the azimuth plane if the respective other FSS's are switched to their on-states. This makes the proposed antenna configuration a viable option for 5G beam switching applications.

The FSS rows in each panel can be controlled independently, which is a feature that allows the beam to be steerable in the elevation plane by switching the diodes in the row on and off, where the RFSS presents transmission response of State-10. The results in the elevation plane for Case III and when the first FSS rows in panel #3 and #4 (Figure 8.27b) are in the on-state is presented in Figure 8.32, showing that the beam is steered by 22°. Similarly, for the Case IV the beam can be steered in the elevation plane by switching the diode in the first FSS' row in panel #4 (Figure 8.27c) to their on-state as shown in Figure 8.33 by 16°.

8.5.3 Performance assessment

A comparison of the proposed reconfigurable sectoral antenna system with other related published work is summarized in Table 8.4, in terms of tuning method applied, maximum gain obtained, beam-steering range in the azimuth and elevation planes, and frequency of operation. The proposed beam-switching antenna uses only a single PIN diode per unit cell, offering full coverage in the azimuth plane by switching the

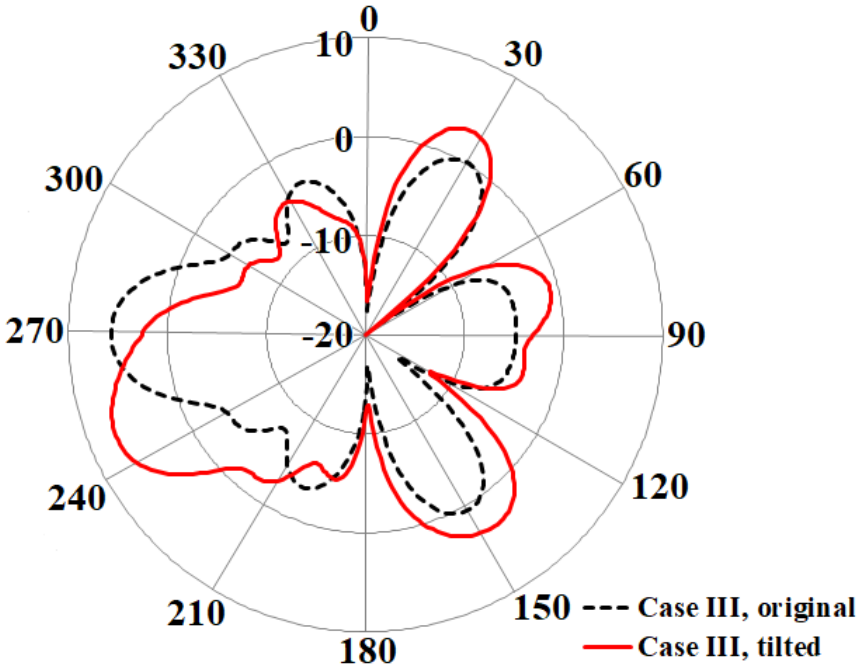

Figure 8.32: Radiation pattern of the proposed antenna for original and tilted Case III in the E-plane.

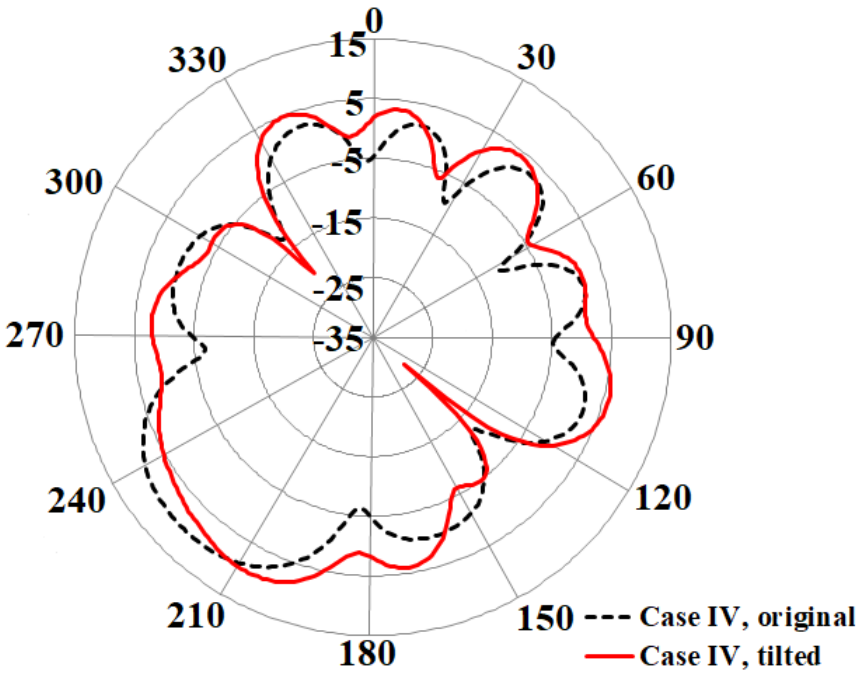

Figure 8.33: Radiation pattern of the proposed antenna for original and tilted Case IV in the E-plane.

diodes of each panel on and off, and by controlling the diode states of each FSS' row is possible to steer the beam in the elevation plane. Another advantage of using this mechanism is the variable gain available.

Ref.	Tuning method	Maximum gain (dBi)	Azimuth plane	Elevation plane	Frequency (GHz)
[240]	1-PIN-diode loaded and rotating panels	11.25	360°	Not available	2.45
[241]	1-PIN-diode loaded	8.7	360°	Not available	2.45
[242]	2-varactor-diodes loaded	13.3	360°	Not available	2.45
This work	1-PIN-diode loaded	10.2	360°	±22°	3.5

Table 8.4: Comparison of proposed reconfigurable sectoral antenna with other reported ones.

Chapter 9

Conclusions and Future Work

Modern communication systems put forward more and new requirements, and FSS' characteristics have attracted the attention of researchers to meet these demands. The designs in this dissertation were presented in both stopband and passband variants, allowing selective reflection and transmission of EM waves at specific frequencies, and providing compact and lightweight solutions for applications in the sub-6GHz and mm-wave spectra. Therefore, the structures proposed in this research can also enhance the performance of communication systems by minimizing interference and improving signal quality. A study on the geometries and functionalities was carried out, and formulas were provided to design these structures so that other researchers can adapt the design to be used for their purposes.

9.1 LP-to-CP polarization converter

A linear-to-circular polarization converter is proposed, operating at 5.2 GHz for below-6GHz applications. It is demonstrated that a single-layer FSS based on the four-arms star geometry can be used as the polarizing element. The analyzes of the FSS polarizer are performed using ANSYS tools and experimental verifications. The gap splitting the four-arms geometry in two pairs introduces a capacitive effect to the circuit. The added capacitance provides a phase difference of 90° between the TE and TM modes. The results show that the TE mode lags the TM mode, which makes the outgoing wave from the polarizer to be LHCP. The design approach, including expressions for a first and fast design of the four-arms star geometry, is described and validated with the numerical and experimental results.

9.2 Ultra-wide band-stop FSS designed by ECM

An ultra-wide band-stop double-layer FSS is proposed, operating at K (18 GHz to 26.5 GHz) and Ka band (26.5 GHz to 40 GHz), with resonance frequencies compatible to 5G mm-wave applications. It is demonstrated that combining FSSs with simple geometries can obtain a wideband response. A simple modeling of the resonance frequency behavior of the FSSs were proposed and validated, both through computer simulations and measurement of prototypes. The procedure used for computing the inductance and capacitance of the FSSs is described by modeling segments of strips by basic equations. The analyses of the single-layer structures and cascaded ones are also performed by full-wave simulations using CST. The air gap spacing parameter is analyzed, the gap with the distance of about $\lambda/4$, considering the center frequency at 30 GHz, shows to have a better match to the resonance frequencies of the individual FSS, with less discrepancy as shown in Table 4.1. The air gap between the structures also allows to control the bandwidth. Numerical and measured results show excellent agreement, with a maximum difference of 1.03%. Although it was not possible to measure the entire bandwidth of FSS #2 and the cascaded structure due to limitation in the frequency range of the horn antennas used, it can be seen that the experimental curves in both cases closely follow the ones obtained from the simulations. In all investigated cases, the theoretical method was several hundred times faster than CST, just establishing itself as an excellent option for a first and fast analysis of single-layer and cascaded FSSs.

9.3 Beam-tilting and gain enhancement antenna system

A new beam-tilting and gain enhancement system designed using a single-layer FSS for mm-wave applications, in the 5G N257 band, is detailed. A bio-inspired bow-tie antenna fed by microstrip lines with end-fire radiation is used to excite the FSS. Different sizes of the FSS panel are employed to achieve the best antenna performance in terms of beam tilting and gain. Numerical results show an increase in the gain of 6.43 dB in the E-plane and 4.14 dB in the H-plane. It was also observed that the radiation pattern for both planes became more directive. The beam was steered to a forward direction in relation to the antenna plane, with a maximum beam tilt of 97°,

with an overall gain of 8.68 dBi which presents a gain enhancement of 4.08 dB. The antenna system is compact, making it a good candidate for 5G networks.

9.4 Multi-passband CFSS based on EIT-effect

Dual- and triple-passband responses are achieved by closely coupled-complementary based FSSs. The proposed CFSSs consist of a stacked periodic array of four-arms star geometry patch-type elements and its complementary one on a single dielectric substrate. Parametric analyses and offsets were used to evaluate the coupling between these elements, and how the break of symmetry can generate a transmission window between the original transmission maxima. CFSS #1 and CFSS #4 have their elements centered within the unit cell, which can create two transmission maxima (f_p) and a transmission zero between them. Using CFSS #1 as reference, the operating frequencies are around $f_{p1} = 2.6$ GHz, $f_z = 4.2$ GHz (that can become a transmission maxima), and $f_{p2} = 6.2$ GHz. Vertical (CFSS #2) and diagonal (CFSS #3) offsets were implemented that created a third f_p, where the original was a transmission zero, by inducing an EIT effect. CFSS #2 presented three f_p in the TE polarization and two f_p in the TM polarization, showing to be polarization dependent. CFSS #3 showed three f_p in both polarizations, and the third one appeared again at the previous transmission zero frequency. CFSS #1, #3 and #4 presented polarization-insensitive performance. All structures were fabricated and characterized; the experimental results closely follow the ones obtained from the simulations. The designed structures showed stable behavior for different incident angles for both TE and TM polarizations. In comparison to related published works, this design approach exhibits dual and/or triple-bands of operation with the capability of being polarization insensitive or sensitive, and results in a compact single-substrate-layer configuration.

9.5 CFSS with reconfigurable response

A novel reconfigurable complementary-inspired FSS with single-, dual- and no-passband response is presented. The proposed structure consists of a single dielectric substrate with double metallization layers, supporting the array elements of slot type and its complementary one (patch) with immersed biasing network. Analyses of the single-metal layer were performed to evaluate the response of each element as well as the

influence of adding bias lines and switching points to the patch FSS. The final configuration of the proposed structure is developed based on the duality theorem. Passive FSSs were designed to evaluate the reconfigurability of the structure, i.e., considering the ideal cases of the off- and on-state of the PIN diodes. Then, the practical FSS was designed, including the PIN diode parameters. By changing the bias state of the diode, the FSS can be configured into single-passband for reserve biasing, dual-passband for forward biasing and no-passband when in the threshold region. Another favorable feature is that the structure has complementary reflection and transmission response at approximately 3.8 GHz with good isolation when switching the off/on states. The ideal and practical structures were fabricated and characterized numerically and experimentally, showing good agreement between the results. The designed structure showed to have simple configuration and control mechanism, exhibiting single or multi-band responses, and is stable at oblique incidence.

9.6 High-gain reconfigurable antenna systems

Two beam-switching/steering systems are developed using a dipole antenna with PIN-diode-switched FSSs. The electric field of the system in the far field zone is theoretically investigated, and its enhancement is estimated. The first type of system analyzed was a reconfigurable corner antenna. Active PIN-diode-switched FSSs are used as reflector, placed with an angle of 45° and 90°, and they proved to be a viable option to reconfigure the antenna radiation pattern. When the PIN diode is switched to the on-state, the antenna has its maximum gain at $\theta = 0°$ and nulls in sideward directions. In the off-state, a null at $\theta = 0°$ is presented with maxima towards other directions. It is observed that the measured gain difference at $\theta = 0°$ is 20.89 dB when off- and on-state switching occurs.

The second reconfigurable antenna designed was a sectoral one. Six cases of diode configurations are considered, showing that when the diodes are in on-states, the FSSs reflect the EM wave and consequently steer the beam in the azimuth and elevation planes. The antenna can be used as an omnidirectional radiator when the diodes in all FSS panels are in the off-state, while in the other cases the results show that the gain can be increased and tuned. The proposed antenna represents a good and easy option to be used for applications where the control of beam directions is needed.

9.7 Future work

The proposed structures in this dissertation were able to demonstrate good results in the sub-6GHz and mm-wave range. The following future work is recommended to enhance the development and research interests on these systems:

- Improve the polarization conversion by optimizing the FSS for a wider axial ratio bandwidth. It is also desired to reduce the attenuation between the co- and cross-polarization in the optimization and by using a dielectric substrate with less loss. Moreover, consolidate the benefits of the model developed in this work in the mm-wave range.

- The wideband cascaded FSS is sensitive to the angle of incidence of the EM wave, hence generating a Fano resonance. Further investigation could be performed to explore this response to be obtained at normal incidence for sensing applications or for fast roll-off responses.

- The antipodal bio-inspired bow-tie antenna can be improved by applying some optimization techniques for achieving better impedance match. The system with the FSS at the bottom of the antenna was able to improve the antenna's performance, but an investigation of the effects of rotating the FSS panel in the tilting angle could be explored.

- For further improvements in the multi-band FSSs, a study of the EIT-effect in a similar unit-cell geometry could be performed. The selectivity of the FSS can be improved by controlling the passband and stopband frequencies and bandwidths. The proposed FSSs can be used as a diplexer to separate signals at different frequency bands.

- It was demonstrated that adding lines into the geometry to bias the PIN diodes changes the response of the FSS. Explore other reconfiguration mechanisms with emerging technologies such as MEMS, ferroelectric and plasma materials might be an avenue to tackle this issue.

- This dissertation proposes beam scanning of antennas in the azimuth and elevation plane. Proposing a system able to scan the radiation pattern with a fine scan angle is an interesting work. The FSSs were designed as planar devices, building them into a conformal configuration could be exploited. Furthermore,

the antenna systems with the FSS panels with the PIN diodes in the threshold region could be further explored.

Appendix A

Measurement Procedure

In this appendix, the measurement procedures used in this dissertation to measure FSS transmission spectra and antenna radiation pattern are described, including the calibration process adopted.

A.1 Short-open-load-through calibration

A vector network analyzer (VNA) is an accurate measurement tool that tests the electrical performance of high-frequency components in the radio frequency (RF), microwave, and millimeter-wave frequency bands. A VNA is a stimulus response test system, composed of an RF source and multiple measurement receivers [248]. It is specifically designed to measure the forward and reverse reflection and transmission responses of RF components. The network analyzer hardware is optimized, producing a sweep of measurements that should be faster than using a single source and single receiver. Through calibration, it is possible to perform vector error correction, providing high level of accuracy for measuring RF components.

Error correction is the process of characterizing systematic errors by measuring known electrical calibration standards. Once these errors are quantified, their effects can be mathematically removed from subsequent measurements. As any test system is affected by more than one cause of measurement error, the calibration process has to measure enough standards to classify the magnitude and phase of the various errors.

This Appendix describes the calibration process carried out to remove losses from the cables and connectors used in the experimental characterization of prototypes in

this dissertation. The electrical standards used during the calibration process were passive mechanical devices, in which the calibration used was SOLT standards, which has this name because it is composed of Short, Open, Load and Through standards. Figure A.1 shows the standards used, composed of, from the left to the right, a thru, a short, an open and two 50-Ω loads, respectively, found in commercial calibration kits for the desired frequency range.

Figure A.1: SOLT standards.

The SOLT calibration process consists of five steps, as shown below and illustrated in Figure A.2.

- All cables and connectors that will be used by the antennas through ports 1 and 2 must be connected to the VNA.
- Both ports 1 and 2 are connected to 50-Ω loads and then measurement is performed.
- An open standard is connected to Port 1 and a short is connected to Port 2 to perform the measurement.
- A short standard is connected to Port 1 and an open standard is connected to Port 2 to perform the measurement.
- Thru measurement between ports 1 and 2 is performed.

Finally, the VNA makes the error estimates so that they are removed in the next measurements.

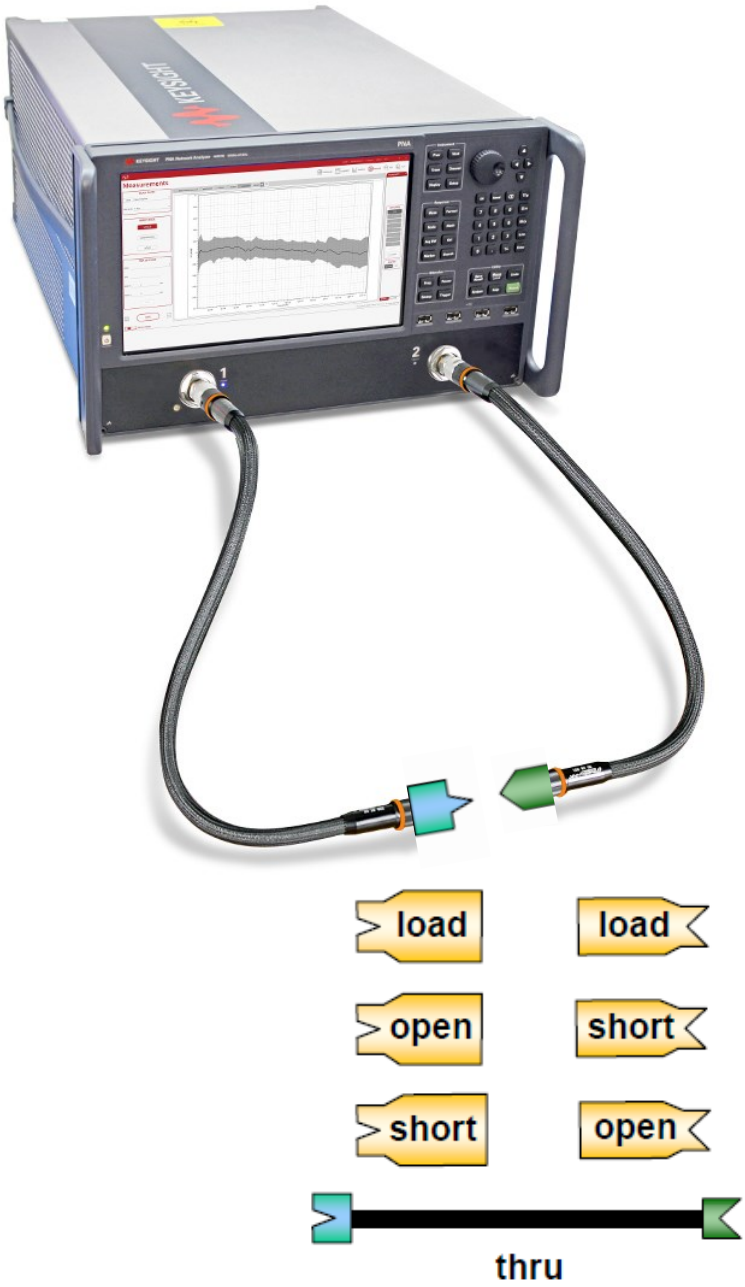

Figure A.2: SOLT calibration process [248].

A.2 Transmission spectra measurement procedure

In this dissertation, the experimental characterizations of the proposed structures' responses were carried out in two different environments, one being in an anechoic

chamber (Figure A.3) and the other using a measurement window (Figure A.4); these method are described in Section 2.7.

A.2.1 Measurement setup in anechoic chamber for FSSs in mm-wave range

Figure A.3 shows the measurement setup in the anechoic chamber to acquire the transmission coefficient response of the FSSs designed to operate in the mm-wave range. Two horn antennas were used, one acting as a transmitter (T_x) model LB-28-25-C-KF (frequency range from 26.5 to 40 GHz, and linearly polarized) [249] and the other one as a receiver (R_x) model LB-180400H-KF (frequency range from 18 to 40 GHz, and linearly polarized) [250], connected to an Anritsu 37397C two-port vector network analyzer (frequency range from 40 MHz to 65 GHz) [251]. The two horn antennas were placed facing each other at a fixed position, with a distance that ensures that the transmitter and receiver antennas are in the far-field regions. The prototype is placed in the stand between the transmitting (T_x) and receiving (R_x) antennas. The incidence of the wave to the FSSs is considered to be at normal ($\theta = 0°$) or oblique ($\theta \neq 0°$). The calibration procedure to test the manufactured structures consisted of two steps. The first one is to calibrate the cables using short-open-load-through terminations as explained in Section A.1. Secondly, the T_x and R_x antennas are aligned, and its transmission coefficient is measured, as the reference of transmissivity. Then, the results of the FSSs under test are normalized to the reference.

A.2.2 Measurement setup using measurement window for FSSs in sub-6GHz range

Measurements of transmission coefficient of FSSs in the sub-6GHz range were performed in the second environment, which uses a measurement window as shown in Figure A.4. The setup consists of an Agilent E5071C ENA two-port vector network analyzer (frequency range from 300 kHz to 20 GHz) [252], two SAS-571 double ridge horn antennas (frequency range from 700 MHz to 18 GHz, and linearly polarized) [253] and a measurement window with pyramidal radiation-absorbent material surrounding it. Similarly, as the procedure described in Section A.2.1, the antennas were spaced far enough to ensure they are in the far-field regions. The prototype

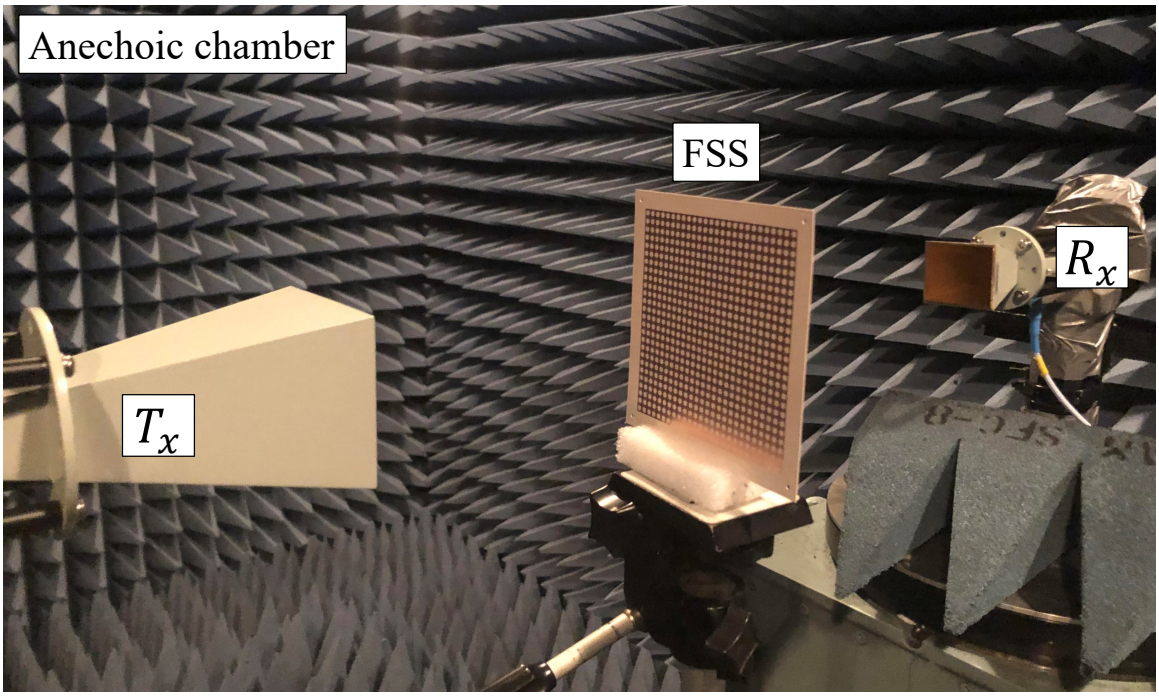

Figure A.3: FSS measurement setup in the anechoic chamber.

is placed in the center of the measurement window. Normal and oblique incidence were considered. And calibrations were performed. For measurements of co- and cross-polarization a rotating angle of the device under test is considered as $\phi_{xy} = 0°$ (Figure A.4a) and $\phi_{xy} = 45°$ (Figure A.4b), respectively.

When the device under test is an active FSS, a DC power supply is required to bias the active components. An Agilent E3631A DC power supply (triple output: 0 – ±25 V, 0 – 1A; 0 – 6 V, 0 – 5A; 80 W) [254] is added to the setup for biasing.

A.3 Radiation pattern measurement setup

In this section, the experimental characterization of antenna radiation pattern is described. The single-axis rotational pattern was the pattern-measurement technique used in this dissertation. The pattern-test setup is shown in Figure A.5. The antenna under test (AUT) is placed on a rotational positioner, and a horn antenna model ETS-Lindgren 3164-05 (frequency range from 2 to 18 GHz, linearly polarized) [255], used as transmitter, is placed level with the AUT a fixed distance away. The AUT is rotated about the azimuth, 360°, with angle steps of 5°, and the response between the antennas, S_{21}, is measured as a function of angle.

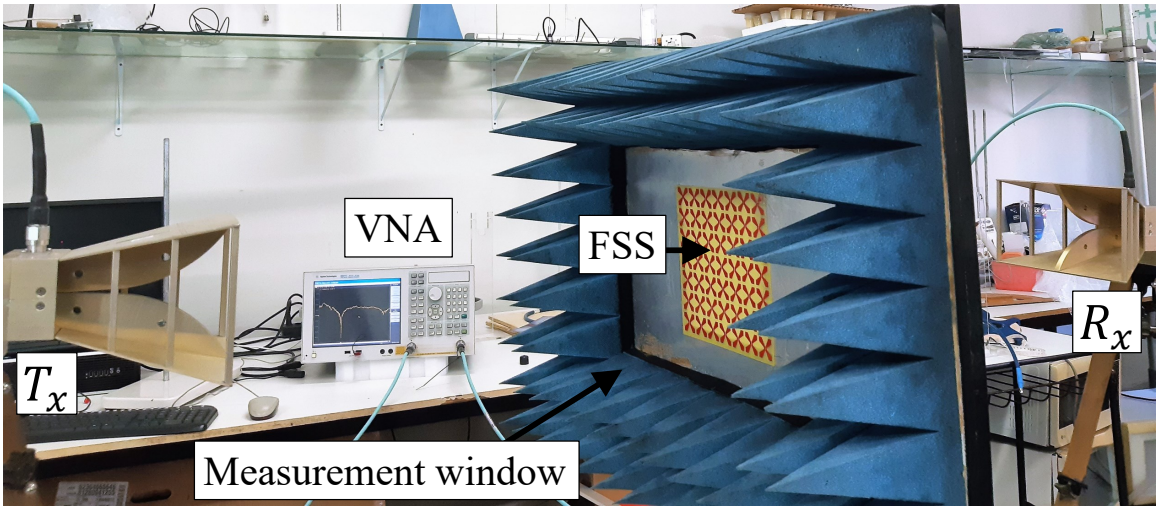

(a) Co-polarization, FSS rotated by $\phi_r = 0°$.

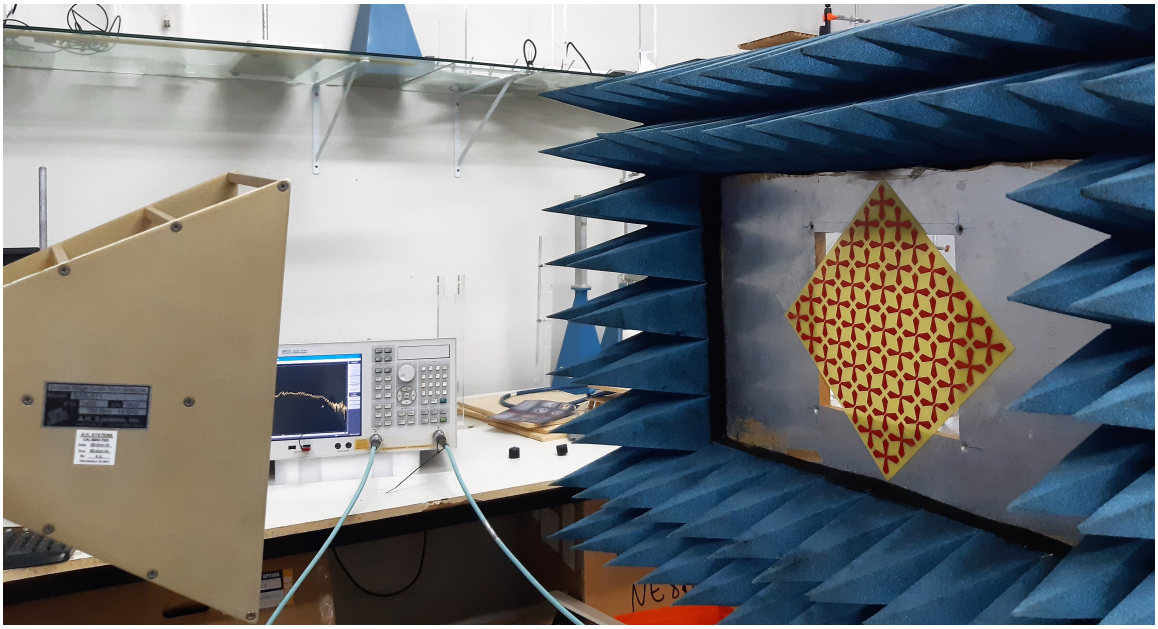

(b) Cross-polarization, FSS rotated by $\phi_r = 45°$.

Figure A.4: Measurement setup.

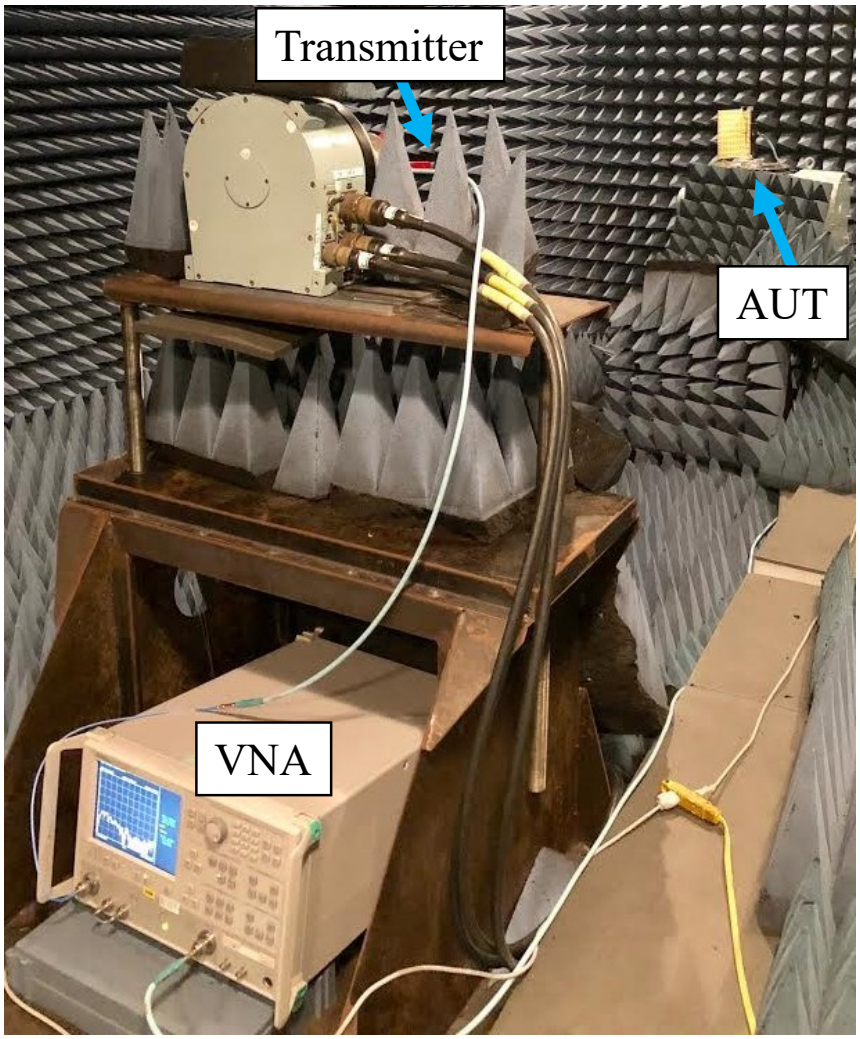

Figure A.5: Radiation pattern measurement setup.

References

[1] J. Liu, K. Au, A. Maaref, *et al.*, "Initial access, mobility, and user-centric multi-beam operation in 5G new radio," *IEEE Communications Magazine*, vol. 56, no. 3, pp. 35–41, 2018. DOI: 10.1109/MCOM.2018.1700827.

[2] T. S. Rappaport, S. Sun, R. Mayzus, *et al.*, "Millimeter wave mobile communications for 5G cellular: It will work!" *IEEE Access*, vol. 1, pp. 335–349, 2013. DOI: 10.1109/ACCESS.2013.2260813.

[3] A. Osseiran, F. Boccardi, V. Braun, *et al.*, "Scenarios for 5G mobile and wireless communications: The vision of the METIS project," *IEEE Communications Magazine*, vol. 52, no. 5, pp. 26–35, 2014. DOI: 10.1109/MCOM.2014.6815890.

[4] T.-K. Wu, "Improved broadband bandpass FSS filters for 5G applications," in *IEEE International Symposium on Antennas and Propagation USNC/URSI National Radio Science Meeting*, Boston, USA, 2018, pp. 2033–2034. DOI: 10.1109/APUSNCURSINRSM.2018.8609110.

[5] N. Ojaroudiparchin, M. Shen, S. Zhang, and G. F. Pedersen, "A switchable 3-D-coverage-phased array antenna package for 5G mobile terminals," *IEEE Antennas and Wireless Propagation Letters*, vol. 15, pp. 1747–1750, 2016. DOI: 10.1109/LAWP.2016.2532607.

[6] P. Lu, M. Steeg, K. Kolpatzeck, *et al.*, "Photonic assisted beam steering for millimeter-wave and THz antennas," in *IEEE Conference on Antenna Measurements Applications (CAMA)*, Västerås, Sweden, 2018, pp. 1–4. DOI: 10.1109/CAMA.2018.8530567.

[7] J. Mendoza, M. Karabacak, H. Arslan, and G. Mumcu, "A spatially adaptive antenna array for mm-wave wireless channel control with microfluidics based

reconfiguration," *IEEE Access*, vol. 8, pp. 182 898–182 907, 2020. DOI: 10.1109/ACCESS.2020.3028795.

[8] R. Bonjour, M. Singleton, S. A. Gebrewold, *et al.*, "Ultra-fast millimeter wave beam steering," *IEEE Journal of Quantum Electronics*, vol. 52, no. 1, pp. 1–8, 2016. DOI: 10.1109/JQE.2015.2509242.

[9] M. Akbari, S. Gupta, M. Farahani, A. Sebak, and T. Denidni, "Analytic study on CP enhancement of millimeter wave DR and patch subarray antennas," *International Journal of RF and Microwave Computer-Aided Engineering*, vol. 27, no. 1, e21053, 2017. DOI: 10.1002/mmce.21053.

[10] A. Kesavan, R. Karimian, and T. A. Denidni, "A novel wideband frequency selective surface for millimeter-wave applications," *IEEE Antennas and Wireless Propagation Letters*, vol. 15, pp. 1711–1714, 2016. DOI: 10.1109/LAWP.2016.2528221.

[11] S.-Y. Wang, J.-D. Bi, W. Liu, W. Geyi, and S. Gao, "Polarization-insensitive cross-polarization converter," *IEEE Transactions on Antennas and Propagation*, vol. 69, no. 8, pp. 4670–4680, 2021. DOI: 10.1109/TAP.2021.3060087.

[12] B. A. Munk, *Frequency selective surfaces: theory and design*. John Wiley & Sons, 2005.

[13] J. C. Vardaxoglou, *Frequency selective surfaces: analysis and design*. Research Studies Press, 1997.

[14] G. Marconi and C. S. Franklin, *Reflector for use in wireless telegraphy and telephony*. US Patent 1,301,473, Apr. 1919.

[15] C.-C. Chen, "Scattering by a two-dimensional periodic array of conducting plates," *IEEE Transactions on Antennas and Propagation*, vol. 18, no. 5, pp. 660–665, 1970. DOI: 10.1109/TAP.1970.1139760.

[16] R. Mittra, C. Chan, and T. Cwik, "Techniques for analyzing frequency selective surfaces-a review," *Proceedings of the IEEE*, vol. 76, no. 12, pp. 1593–1615, 1988. DOI: 10.1109/5.16352.

[17] T.-K. Wu, "Frequency selective surfaces," *Encyclopedia RF Microw Eng.*, 1995.

[18] S. Celozzi, R. Araneo, P. Burghignoli, and G. Lovat, *Electromagnetic shielding: theory and applications*. John Wiley & Sons, 2023.

[19] J. McSpadden, T. Yoo, and K. Chang, "Theoretical and experimental investigation of a rectenna element for microwave power transmission," *IEEE Transactions on Microwave Theory and Techniques*, vol. 40, no. 12, pp. 2359–2366, 1992. DOI: 10.1109/22.179902.

[20] K. Falconer, *Fractal geometry: mathematical foundations and applications*. John Wiley & Sons, 2004.

[21] H. Silva, C. Silva, M. R. T. de Oliveira, *et al.*, "Multiband FSS with fractal characteristic based on Jerusalem cross geometry," *Journal of Microwaves, Optoelectronics and Electromagnetic Applications*, vol. 16, pp. 932–941, 2017. DOI: 10.1590/2179-10742017v16i4984.

[22] E. A. Parker and A. El Sheikh, "Convoluted array elements and reduced size unit cells for frequency-selective surfaces," in *IEE Proceedings H-Microwaves, Antennas and Propagation*, IET, vol. 138, 1991, pp. 19–22.
DOI: 10.1049/ip-h-2.1991.0004.

[23] J. Romeu and Y. Rahmat-Samii, "Fractal FSS: A novel dual-band frequency selective surface," *IEEE Transactions on Antennas and Propagation*, vol. 48, no. 7, pp. 1097–1105, 2000. DOI: 10.1109/8.876329.

[24] J. Gianvittorio, J. Romeu, S. Blanch, and Y. Rahmat-Samii, "Self-similar prefractal frequency selective surfaces for multiband and dual-polarized applications," *IEEE Transactions on Antennas and Propagation*, vol. 51, no. 11, pp. 3088–3096, 2003. DOI: 10.1109/TAP.2003.818791.

[25] J. I. A. Trindade, P. H. da F. Silva, A. L. P. S. Campos, and A. G. D'Assuncao, "Analysis of stop-band frequency selective surfaces with Dürer's pentagon prefractals patch elements," *IEEE Transactions on Magnetics*, vol. 47, no. 5, pp. 1518–1521, 2011. DOI: 10.1109/TMAG.2010.2091112.

[26] M. R. d. Silva, C. d. L. Nobrega, P. H. d. F. Silva, and A. G. D'Assunção, "Optimal design of frequency selective surfaces with fractal motifs," *IET Microwaves, Antennas & Propagation*, vol. 8, no. 9, pp. 627–631, 2014.
DOI: 10.1049/iet-map.2013.0462.

[27] C. de Lucena Nóbrega, M. R. da Silva, W. C. de Araújo, P. H. da Fonseca Silva, and A. G. D'Assunção, "Analysis of frequency selective surfaces with T-shaped pre-fractals patch elements," in *SBMO/IEEE MTT-S International*

Microwave and Optoelectronics Conference, Natal, Brazil, 2011, pp. 694–696. DOI: 10.1109/IMOC.2011.6169410.

[28] B. Sanz-Izquierdo, E. A. Parker, J.-B. Robertson, and J. C. Batchelor, "Singly and dual polarized convoluted frequency selective structures," *IEEE Transactions on Antennas and Propagation*, vol. 58, no. 3, pp. 690–696, 2010. DOI: 10.1109/TAP.2009.2039321.

[29] G. Luciani, D. F. Mamedes, A. G. Neto, and J. Bornemann, "H-shaped fractal antennas for dual-band applications," in *SBMO/IEEE MTT-S International Microwave and Optoelectronics Conference (IMOC)*, Aguas de Lindoia, Brazil, 2017, pp. 1–4. DOI: 10.1109/IMOC.2017.8121042.

[30] P. Callaghan, E. A. Parker, and R. J. Langley, "Influence of supporting dielectric layers on the transmission properties of frequency selective surfaces," in *IEE Proceedings H-Microwaves, Antennas and Propagation*, vol. 138, 1991, pp. 448–454. DOI: 10.1049/ip-h-2.1991.0075.

[31] R. Luebbers and B. Munk, "Some effects of dielectric loading on periodic slot arrays," *IEEE Transactions on Antennas and Propagation*, vol. 26, no. 4, pp. 536–542, 1978. DOI: 10.1109/TAP.1978.1141887.

[32] A. K. Rashid, B. Li, and Z. Shen, "An overview of three-dimensional frequency-selective structures," *IEEE Antennas and Propagation Magazine*, vol. 56, no. 3, pp. 43–67, 2014. DOI: 10.1109/MAP.2014.6867682.

[33] S. Hamdy and E. A. Parker, "Influence of lattice geometry on transmission of electromagnetic waves through arrays of crossed dipoles," in *IEE Proceedings H-Microwaves, Optics and Antennas*, vol. 129, 1982, p. 7. DOI: 10.1049/ip-h-1.1982.0002.

[34] S. M. A. Hamdy and E. A. Parker, "Current distribution on the elements of a square loop frequency selective surface," *Electronics Letters*, vol. 18, no. 14, pp. 624–626, 1982. DOI: 10.1049/el:19820427.

[35] S. B. Savia and E. A. Parker, "Equivalent circuit model for superdense linear dipole FSS," *IEE Proceedings-Microwaves, Antennas and Propagation*, vol. 150, no. 1, pp. 37–42, 2003. DOI: 10.1049/ip-map:20030107.

[36] T. Larsen, "A survey of the theory of wire grids," *IRE Transactions on Microwave Theory and Techniques*, vol. 10, no. 3, pp. 191–201, 1962. DOI: 10.1109/TMTT.1962.1125490.

[37] Z. L. Wang, K. Hashimoto, N. Shinohara, and H. Matsumoto, "Frequency-selective surface for microwave power transmission," *IEEE Transactions on Microwave Theory and Techniques*, vol. 47, no. 10, pp. 2039–2042, 1999. DOI: 10.1109/22.795083.

[38] R. Langley and A. Drinkwater, "Improved empirical model for the Jerusalem cross," in *IEE Proceedings H (Microwaves, Optics and Antennas)*, vol. 129, 1982, pp. 1–6. DOI: 10.1049/ip-h-1.1982.0001.

[39] C. K. Lee and R. Langley, "Equivalent-circuit models for frequency-selective surfaces at oblique angles of incidence," in *IEE Proceedings H (Microwaves, Antennas and Propagation)*, IET, vol. 132, 1985, pp. 395–399. DOI: 10.1049/ip-h-2.1985.0070.

[40] N. Marcuvitz, *Waveguide handbook*, 21. IET, 1951.

[41] G. H. Sung, K. W. Sowerby, M. J. Neve, and A. G. Williamson, "A frequency-selective wall for interference reduction in wireless indoor environments," *IEEE Antennas and Propagation Magazine*, vol. 48, no. 5, pp. 29–37, 2006. DOI: 10.1109/MAP.2006.277152.

[42] S. Suhaimi, S. Azemi, and S. Jack, "Structural health monitoring system using 3D frequency selective surface," in *IEEE Asia-Pacific Conference on Applied Electromagnetics (APACE)*, Langkawi, Malaysia, 2016, pp. 145–149. DOI: 10.1109/APACE.2016.7915872.

[43] R. Dickie, R. Cahill, V. Fusco, H. S. Gamble, and N. Mitchell, "THz frequency selective surface filters for earth observation remote sensing instruments," *IEEE Transactions on Terahertz Science and Technology*, vol. 1, no. 2, pp. 450–461, 2011. DOI: 10.1109/TTHZ.2011.2129470.

[44] M. Qu, Y. Feng, J. Su, and S. M. A. Shah, "Design of a single-layer frequency selective surface for 5G shielding," *IEEE Microwave and Wireless Components Letters*, vol. 31, no. 3, pp. 249–252, 2021. DOI: 10.1109/LMWC.2021.3053286.

[45] D. Montofre, A. Khudchenko, F. P. Mena, R. Hesper, and A. M. Baryshev, "Single-layer dichroic filters for multifrequency receivers at THz frequencies," *IEEE Transactions on Terahertz Science and Technology*, vol. 10, no. 6, pp. 690–697, 2020. DOI: 10.1109/TTHZ.2020.3025692.

[46] P. Chomtong, N. Somjit, P. Krachodnok, C. Mahatthanajatuphat, S. Tawatchai, and P. Akkaraekthalin, "A miniaturized multiband FSS director using double layer with ICPW technique structure for wireless communication systems," *IEEE Access*, vol. 11, pp. 81 527–81 544, 2023.
DOI: 10.1109/ACCESS.2023.3300651.

[47] B. Li and Z. Shen, "Synthesis of quasi-elliptic bandpass frequency-selective surface using cascaded loop arrays," *IEEE Transactions on Antennas and Propagation*, vol. 61, no. 6, pp. 3053–3059, 2013.
DOI: 10.1109/TAP.2013.2250237.

[48] Z. Yao, S. Xiao, Y. Li, and B.-Z. Wang, "On the design of wideband absorber based on multilayer and multiresonant FSS array," *IEEE Antennas and Wireless Propagation Letters*, vol. 20, no. 3, pp. 284–288, 2021.
DOI: 10.1109/LAWP.2020.3046010.

[49] S. A. Nauroze and M. M. Tentzeris, "A thermally actuated fully inkjet-printed origami-inspired multilayer frequency selective surface with continuous-range tunability using polyester-based substrates," *IEEE Transactions on Microwave Theory and Techniques*, vol. 67, no. 12, pp. 4944–4954, 2019.
DOI: 10.1109/TMTT.2019.2946074.

[50] S.-S. Cho, S.-H. Yoon, and I.-P. Hong, "Design of three-dimensional frequency selective structure with replaceable unit structures using a 3-D printing technique," *IEEE Antennas and Wireless Propagation Letters*, vol. 17, no. 11, pp. 2041–2045, 2018. DOI: 10.1109/LAWP.2018.2871175.

[51] I. Lee and I. Hong, "3D frequency selective surface for stable angle of incidence," *Electronics Letters*, vol. 50, no. 6, pp. 423–424, 2014.
DOI: 10.1049/el.2014.0053.

[52] S. N. Azemi, K. Ghorbani, and W. Rowe, "3D frequency selective surfaces," *Progress In Electromagnetics Research C*, vol. 29, pp. 191–203, 2012.
DOI: 10.2528/PIERC12033006.

[53] D. Z. Zhu, M. D. Gregory, P. L. Werner, and D. H. Werner, "Fabrication and characterization of multiband polarization independent 3-D-printed frequency selective structures with ultrawide fields of view," *IEEE Transactions on Antennas and Propagation*, vol. 66, no. 11, pp. 6096–6105, 2018.
DOI: 10.1109/TAP.2018.2866507.

[54] S. N. Azemi, T. Baum, K. Ghorbani, and W. S. Rowe, "3D-tapered resonators for FSSs with incident angle independence," *IET Microwaves, Antennas & Propagation*, vol. 11, no. 15, pp. 2228–2234, 2017.
DOI: 10.1049/iet-map.2016.0954.

[55] V. K. Kanth and S. Raghavan, "3D frequency selective surfaces based on substrate integrated waveguide technology," in *IEEE MTT-S International Microwave and RF Conference (IMaRC)*, Kolkata, India, 2018, pp. 1–4.
DOI: 10.1109/IMaRC.2018.8877264.

[56] D. Li, T. Li, and E. Li, "Implementation of ultra-miniaturised frequency-selective structures based on 2.5 D convoluted segments," *Electronics Letters*, vol. 54, no. 8, pp. 476–478, 2018. DOI: 10.1049/el.2017.4415.

[57] H. Li, F. Costa, J. Fang, *et al.*, "2.5-D miniaturized multifunctional active frequency-selective surface," *IEEE Transactions on Antennas and Propagation*, vol. 67, no. 7, pp. 4659–4667, 2019. DOI: 10.1109/TAP.2019.2911271.

[58] Y.-M. Yu, C.-N. Chiu, Y.-P. Chiou, and T.-L. Wu, "A novel 2.5-dimensional ultraminiaturized-element frequency selective surface," *IEEE Transactions on Antennas and Propagation*, vol. 62, no. 7, pp. 3657–3663, 2014.
DOI: 10.1109/TAP.2014.2321153.

[59] C.-W. Lin, C.-K. Shen, and T.-L. Wu, "Ultracompact via-based absorptive frequency-selective surface for 5-GHz Wi-Fi with passbands and high-performance stability," *IEEE Transactions on Components, Packaging and Manufacturing Technology*, vol. 8, no. 1, pp. 41–49, 2018.
DOI: 10.1109/TCPMT.2017.2759221.

[60] T. Hussain, Q. Cao, J. K. Kayani, and I. Majid, "Miniaturization of frequency selective surfaces using 2.5-D knitted structures: Design and synthesis," *IEEE Transactions on Antennas and Propagation*, vol. 65, no. 5, pp. 2405–2412, 2017. DOI: 10.1109/TAP.2017.2673809.

[61] M. W. Niaz, Y. Yin, S. Zheng, L. Zhao, and J. Chen, "Design and analysis of an ultraminiaturized FSS using 2.5-D convoluted square spirals," *IEEE Transactions on Antennas and Propagation*, vol. 68, no. 4, pp. 2919–2925, 2020. DOI: 10.1109/TAP.2019.2951525.

[62] P. Wang and W. Jiang, "Miniaturised bandstop frequency selective surface based on multilayer 2.5-dimensional structure," in *International Symposium on Antennas and Propagation (ISAP)*, Xian, China, 2019, pp. 1–3.

[63] S. N. Azemi, K. Ghorbani, and W. S. T. Rowe, "A reconfigurable FSS using a spring resonator element," *IEEE Antennas and Wireless Propagation Letters*, vol. 12, pp. 781–784, 2013. DOI: 10.1109/LAWP.2013.2270950.

[64] A. Biswas, C. L. Zekios, and S. V. Georgakopoulos, "Transforming single-band static fss to dual-band dynamic FSS using origami," *Scientific Reports*, vol. 10, no. 1, p. 13 884, 2020. DOI: 10.1038/s41598-020-70434-y.

[65] S. A. Nauroze, L. Novelino, M. M. Tentzeris, and G. H. Paulino, "Inkjet-printed "4D" tunable spatial filters using on-demand foldable surfaces," in *IEEE MTT-S International Microwave Symposium (IMS)*, Honololu, USA, 2017, pp. 1575–1578. DOI: 10.1109/MWSYM.2017.8058932.

[66] D. Ferreira, I. Cuiñas, R. F. S. Caldeirinha, and T. R. Fernandes, "3-D mechanically tunable square slot FSS," *IEEE Transactions on Antennas and Propagation*, vol. 65, no. 1, pp. 242–250, 2017. DOI: 10.1109/TAP.2016.2631131.

[67] S. A. B, E. F. Sundarsingh, and V. S. Ramalingam, "Mechanically reconfigurable frequency selective surface for RF shielding in indoor wireless environment," *IEEE Transactions on Electromagnetic Compatibility*, vol. 62, no. 6, pp. 2643–2646, 2020. DOI: 10.1109/TEMC.2020.2983899.

[68] H. Yuan, H. Li, X. Fang, Y. Wang, and Q. Cao, "Active frequency selective surface absorber with point-to-point biasing control system," *IEEE Antennas and Wireless Propagation Letters*, vol. 20, no. 8, pp. 1429–1432, 2021. DOI: 10.1109/LAWP.2021.3085424.

[69] C. Zhao, C.-F. Wang, and S. Aditya, "Power-dependent frequency-selective surface: Concept, design, and experiment," *IEEE Transactions on Antennas and Propagation*, vol. 67, no. 5, pp. 3215–3220, 2019. DOI: 10.1109/TAP.2019.2900408.

[70] B. Jiang, H. Hu, J. Tian, S. Lei, M. Chen, and B. Chen, "A polarization-insensitive dual-band FSS with high selectivity and independently switchable characteristics," *IEEE Antennas and Wireless Propagation Letters*, vol. 22, no. 1, pp. 14–18, 2023. DOI: 10.1109/LAWP.2022.3199565.

[71] M. Guo, Y. Zheng, Q. Chen, *et al.*, "Analysis and design of a high-transmittance performance for varactor-tunable frequency-selective surface," *IEEE Transactions on Antennas and Propagation*, vol. 69, no. 8, pp. 4623–4632, 2021. DOI: 10.1109/TAP.2020.3045517.

[72] S. Ghosh and K. V. Srivastava, "Broadband polarization-insensitive tunable frequency selective surface for wideband shielding," *IEEE Transactions on Electromagnetic Compatibility*, vol. 60, no. 1, pp. 166–172, 2018. DOI: 10.1109/TEMC.2017.2706359.

[73] Q. Guo, Z. Li, J. Su, J. Song, and L. Y. Yang, "Active frequency selective surface with wide reconfigurable passband," *IEEE Access*, vol. 7, pp. 38 348–38 355, 2019. DOI: 10.1109/ACCESS.2019.2906219.

[74] F. Deng, X. Xi, J. Li, and F. Ding, "A method of designing a field-controlled active frequency selective surface," *IEEE Antennas and Wireless Propagation Letters*, vol. 14, pp. 630–633, 2015. DOI: 10.1109/LAWP.2014.2375376.

[75] C. Gu, B. S. Izquierdo, S. Gao, *et al.*, "Dual-band electronically beam-switched antenna using slot active frequency selective surface," *IEEE Transactions on Antennas and Propagation*, vol. 65, no. 3, pp. 1393–1398, 2017. DOI: 10.1109/TAP.2016.2647578.

[76] G. I. Kiani, K. L. Ford, L. G. Olsson, K. P. Esselle, and C. J. Panagamuwa, "Switchable frequency selective surface for reconfigurable electromagnetic architecture of buildings," *IEEE Transactions on Antennas and Propagation*, vol. 58, no. 2, pp. 581–584, 2010. DOI: 10.1109/TAP.2009.2037772.

[77] T. Tian, X. Huang, K. Cheng, *et al.*, "Flexible and reconfigurable frequency selective surface with wide angular stability fabricated with additive manufacturing procedure," *IEEE Antennas and Wireless Propagation Letters*, vol. 19, no. 12, pp. 2428–2432, 2020. DOI: 10.1109/LAWP.2020.3034944.

[78] A. Kesavan, M. Mantash, J. Zaid, and T. A. Denidni, "A dual-plane beam-sweeping millimeter-wave antenna using reconfigurable frequency selective surfaces," *IEEE Antennas and Wireless Propagation Letters*, vol. 17, no. 10, pp. 1832–1836, 2018. DOI: 10.1109/LAWP.2018.2867331.

[79] R. Sivasamy and M. Kanagasabai, "Novel reconfigurable 3-D frequency selective surface," *IEEE Transactions on Components, Packaging and Manufacturing Technology*, vol. 7, no. 10, pp. 1678–1682, 2017.
DOI: 10.1109/TCPMT.2017.2688367.

[80] K. Fuchi, J. Tang, B. Crowgey, A. R. Diaz, E. J. Rothwell, and R. O. Ouedraogo, "Origami tunable frequency selective surfaces," *IEEE Antennas and Wireless Propagation Letters*, vol. 11, pp. 473–475, 2012.
DOI: 10.1109/LAWP.2012.2196489.

[81] Y. Rahmat-Samii and A. Tulintseff, "Diffraction analysis of frequency selective reflector antennas," *IEEE Transactions on Antennas and Propagation*, vol. 41, no. 4, pp. 476–487, 1993. DOI: 10.1109/8.220980.

[82] M. Pasian, M. Bozzi, and L. Perregrini, "Accurate modeling of dichroic mirrors in beam-waveguide antennas," *IEEE Transactions on Antennas and Propagation*, vol. 61, no. 4, pp. 1931–1938, 2013. DOI: 10.1109/TAP.2012.2231928.

[83] Y.-L. Su, C.-C. Jian, Y.-L. Lee, C.-H. Li, and T. Lohrey, "Dichroic sub-reflector for wide band techniques for single offset antenna," in *48th European Microwave Conference (EuMC)*, Madrid, Spain, 2018, pp. 268–271.
DOI: 10.23919/EuMC.2018.8541429.

[84] J. A. Vásquez-Peralvo, J.-M. Fernández-González, P. Valtr, and J. M. Rigelsford, "Inductive frequency selective surface: An application for dichroic subreflectors," *IEEE Access*, vol. 8, pp. 22 721–22 732, 2020.
DOI: 10.1109/ACCESS.2020.2970271.

[85] B. Gao, S. Huang, Z. Ren, Y. Chen, and X. Wang, "Design and verification of an integrated free-standing thick-screen FSS radome," *IEEE Antennas and Wireless Propagation Letters*, vol. 17, no. 9, pp. 1630–1634, 2018.
DOI: 10.1109/LAWP.2018.2859232.

[86] N. Liu, X. Sheng, C. Zhang, and D. Guo, "Design of frequency selective surface structure with high angular stability for radome application," *IEEE Antennas and Wireless Propagation Letters*, vol. 17, no. 1, pp. 138–141, 2018.
DOI: 10.1109/LAWP.2017.2778078.

[87] N. Liu, X. Sheng, C. Zhang, and D. Guo, "Design and synthesis of band-pass frequency selective surface with wideband rejection and fast roll-off characteristics for radome applications," *IEEE Transactions on Antennas and Propagation*, vol. 68, no. 4, pp. 2975–2983, 2020. DOI: 10.1109/TAP.2019.2955665.

[88] S. Narayan, G. Gulati, B. Sangeetha, and R. U. Nair, "Novel metamaterial-element-based FSS for airborne radome applications," *IEEE Transactions on Antennas and Propagation*, vol. 66, no. 9, pp. 4695–4707, 2018. DOI: 10.1109/TAP.2018.2851365.

[89] C. Jin, Q. Lv, B. Zhang, *et al.*, "Ultra-wide-angle bandpass frequency selective surface," *IEEE Transactions on Antennas and Propagation*, vol. 69, no. 9, pp. 5673–5681, 2021. DOI: 10.1109/TAP.2021.3061144.

[90] D. Sievenpiper, L. Zhang, R. Broas, N. Alexopolous, and E. Yablonovitch, "High-impedance electromagnetic surfaces with a forbidden frequency band," *IEEE Transactions on Microwave Theory and Techniques*, vol. 47, no. 11, pp. 2059–2074, 1999. DOI: 10.1109/22.798001.

[91] R. Broas, D. Sievenpiper, and E. Yablonovitch, "A high-impedance ground plane applied to a cellphone handset geometry," *IEEE Transactions on Microwave Theory and Techniques*, vol. 49, no. 7, pp. 1262–1265, 2001. DOI: 10.1109/22.932245.

[92] G. I. Kiani, L. G. Olsson, A. Karlsson, K. P. Esselle, and M. Nilsson, "Cross-dipole bandpass frequency selective surface for energy-saving glass used in buildings," *IEEE Transactions on Antennas and Propagation*, vol. 59, no. 2, pp. 520–525, 2011. DOI: 10.1109/TAP.2010.2096382.

[93] M. Gustafsson, A. Karlsson, A. Rebelo, and B. Widenberg, "Design of frequency selective windows for improved indoor outdoor communication," *IEEE Transactions on Antennas and Propagation*, vol. 54, no. 6, pp. 1897–1900, 2006. DOI: 10.1109/TAP.2006.875926.

[94] A. A. Dewani, S. G. O'Keefe, D. V. Thiel, and A. Galehdar, "Window RF shielding film using printed FSS," *IEEE Transactions on Antennas and Propagation*, vol. 66, no. 2, pp. 790–796, 2018. DOI: 10.1109/TAP.2017.2780893.

[95] H. Chen, H. Chen, X. Xiu, Q. Xue, and W. Che, "Transparent FSS on glass window for signal selection of 5G millimeter wave communication," *IEEE Antennas and Wireless Propagation Letters*, pp. 1–1, 2021. DOI: 10.1109/LAWP.2021.3110053.

[96] A. Y. I. Ashyap, Z. Zainal Abidin, S. H. Dahlan, *et al.*, "Highly efficient wearable CPW antenna enabled by EBG-FSS structure for medical body area network applications," *IEEE Access*, vol. 6, pp. 77 529–77 541, 2018. DOI: 10.1109/ACCESS.2018.2883379.

[97] J. Lorenzo, A. Lázaro, R. Villarino, and D. Girbau, "Modulated frequency selective surfaces for wearable RFID and sensor applications," *IEEE Transactions on Antennas and Propagation*, vol. 64, no. 10, pp. 4447–4456, 2016. DOI: 10.1109/TAP.2016.2596798.

[98] A. Tennant, W. Hurley, and T. Dias, "Experimental knitted, textile frequency selective surfaces," *Electronics letters*, vol. 48, no. 22, pp. 1386–1388, 2012. DOI: 10.1049/el.2012.3005.

[99] A. Chauraya, R. Seager, W. Whittow, S. Zhang, and Y. Vardaxoglou, "Embroidered frequency selective surfaces on textiles for wearable applications," in *Loughborough Antennas Propagation Conference (LAPC)*, Loughborough, UK, 2013, pp. 388–391. DOI: 10.1109/LAPC.2013.6711926.

[100] R. Seager, A. Chauraya, J. Bowman, M. Broughton, R. Philpott, and N. Nimkulrat, "Fabric based frequency selective surfaces using weaving and screen printing," *Electronics Letters*, vol. 49, no. 24, pp. 1507–1509, 2013. DOI: 10.1049/el.2013.2314.

[101] M. Ghebrebrhan, F. Aranda, G. Walsh, *et al.*, "Textile frequency selective surface," *IEEE Microwave and Wireless Components Letters*, vol. 27, no. 11, pp. 989–991, 2017. DOI: 10.1109/LMWC.2017.2750031.

[102] R. McPhedran and D. Maystre, "On the theory and solar application of inductive grids," *Applied physics*, vol. 14, no. 1, pp. 1–20, 1977.

[103] S. A. Nauroze, X. He, and M. M. Tentzeris, "Fully additively manufactured tunable active frequency selective surfaces with integrated on-package solar cells for smart packaging applications," in *IEEE 69th Electronic Components and Technology Conference (ECTC)*, Las Vegas, USA, 2019, pp. 119–125. DOI: 10.1109/ECTC.2019.00026.

[104] A. Wexler, "Solution of waveguide discontinuities by modal analysis," *IEEE Transactions on Microwave Theory and Techniques*, vol. 15, no. 9, pp. 508–517, 1967. DOI: 10.1109/TMTT.1967.1126521.

[105] P. Masterman and P. Clarricoats, "Computer field-matching solution of waveguide transverse discontinuities," in *Proceedings of the Institution of Electrical Engineers*, vol. 118, 1971, pp. 51–63. DOI: 10.1049/piee.1971.0007.

[106] B. Widenberg, "A general mode matching technique applied to bandpass radomes," 2001.

[107] A. Monorchio, P. Grassi, and G. Manara, "A hybrid mode-matching finite-elements approach to the analysis of thick dichroic screens with arbitrarily shaped apertures," *IEEE Antennas and Wireless Propagation Letters*, vol. 1, pp. 120–123, 2002. DOI: 10.1109/LAWP.2002.806045.

[108] S. Narayan, K. Prasad, R. U. Nair, and R. M. Jha, "A novel EM analysis of cascaded thick FSS using mode-matching generalized scattering matrix technique," in *IEEE Applied Electromagnetics Conference (AEMC)*, Kolkata, India, 2011, pp. 1–4. DOI: 10.1109/AEMC.2011.6256848.

[109] G. MacFarlane, "Surface impedance of an infinite parallel-wire grid at oblique angles of incidence," *Journal of the Institution of Electrical Engineers-Part IIIA: Radiolocation*, vol. 93, no. 10, pp. 1523–1527, 1946. DOI: 10.1049/ji-3a-1.1946.0256.

[110] C.-C. Chen, "Transmission of microwave through perforated flat plates of finite thickness," *IEEE Transactions on Microwave Theory and Techniques*, vol. 21, no. 1, pp. 1–6, 1973. DOI: 10.1109/TMTT.1973.1127906.

[111] R. Ulrich, K. Renk, and L. Genzel, "Tunable submillimeter interferometers of the Fabry-Perot type," *IEEE Transactions on Microwave Theory and Techniques*, vol. 11, no. 5, pp. 363–371, 1963. DOI: 10.1109/TMTT.1963.1125676.

[112] S.-W. Lee, G. Zarrillo, and C.-L. Law, "Simple formulas for transmission through periodic metal grids or plates," *IEEE Transactions on Antennas and Propagation*, vol. 30, no. 5, pp. 904–909, 1982. DOI: 10.1109/TAP.1982.1142923.

[113] R. J. Langley and E. A. Parker, "Equivalent circuit model for arrays of square loops," *Electronics Letters*, vol. 18, no. 7, pp. 294–296, 1982. DOI: 10.1049/el:19820201.

[114] R. J. Langley and E. A. Parker, "Double-square frequency-selective surfaces and their equivalent circuit," *Electronics Letters*, vol. 19, no. 17, pp. 675–677, 1983. DOI: 10.1049/el:19830460.

[115] V. Krushna Kanth and S. Raghavan, "Equivalent circuit analysis of complementary FSS for selective EM shielding," in *15th International Conference on ElectroMagnetic Interference Compatibility (INCEMIC)*, Bengaluru, India, 2018, pp. 1–4. DOI: 10.1109/INCEMIC.2018.8704634.

[116] Y. Xu and S. Zhang, "An ultra wideband FSS operating at Ka band," in *IEEE International Conference on Computational Electromagnetics (ICCEM)*, Shanghai, China, 2019, pp. 1–3. DOI: 10.1109/COMPEM.2019.8778845.

[117] Y. Ma, W. Wu, Y. Yuan, X. Zhang, and N. Yuan, "A convoluted structure for miniaturized dual-bandstop frequency selective surface," *IEEE Antennas and Wireless Propagation Letters*, vol. 18, no. 2, pp. 328–332, 2019. DOI: 10.1109/LAWP.2018.2890008.

[118] M. I. Hossain, N. Nguyen-Trong, K. H. Sayidmarie, and A. M. Abbosh, "Equivalent circuit design method for wideband nonmagnetic absorbers at low microwave frequencies," *IEEE Transactions on Antennas and Propagation*, vol. 68, no. 12, pp. 8215–8220, 2020. DOI: 10.1109/TAP.2020.2983756.

[119] T. Itoh, *Numerical techniques for microwave and millimeter-wave passive structures*. Wiley, 1989.

[120] S. Skokic and Z. Sipus, "Moment method analysis of a spherical FSS in free space," in *18th International Conference on Applied Electromagnetics and Communications*, Dubrovnik, Croatia, 2005, pp. 1–4. DOI: 10.1109/ICECOM.2005.205025.

[121] X. Wang and D. H. Werner, "Improved model-based parameter estimation approach for accelerated periodic method of moments solutions with application to the analysis of convoluted frequency selected surfaces and metamaterials," *IEEE Transactions on Antennas and Propagation*, vol. 58, no. 1, pp. 122–131, 2010. DOI: 10.1109/TAP.2009.2036196.

[122] R. Courant *et al.*, "Variational methods for the solution of problems of equilibrium and vibrations," *Lecture notes in pure and applied mathematics*, pp. 1–1, 1994.

[123] P. Silvester, "Finite element solution of homogeneous waveguide problems," *Alta Frequenza*, vol. 38, no. 1, pp. 313–317, 1969.

[124] B. R. Archambeault, O. M. Ramahi, and C. Brench, *EMI/EMC computational modeling handbook*. Springer Science & Business Media, 2012, vol. 630.

[125] E. Lucas and T. Fontana, "A 3-D hybrid finite element/boundary element method for the unified radiation and scattering analysis of general infinite periodic arrays," *IEEE Transactions on Antennas and Propagation*, vol. 43, no. 2, pp. 145–153, 1995. DOI: 10.1109/8.366376.

[126] T. Eibert, J. Volakis, D. Wilton, and D. Jackson, "Hybrid FE/BI modeling of 3-D doubly periodic structures utilizing triangular prismatic elements and an MPIE formulation accelerated by the Ewald transformation," *IEEE Transactions on Antennas and Propagation*, vol. 47, no. 5, pp. 843–850, 1999. DOI: 10.1109/8.774139.

[127] K. Yee, "Numerical solution of initial boundary value problems involving Maxwell's equations in isotropic media," *IEEE Transactions on Antennas and Propagation*, vol. 14, no. 3, pp. 302–307, 1966. DOI: 10.1109/TAP.1966.1138693.

[128] P. Harms, R. Mittra, and W. Ko, "Implementation of the periodic boundary condition in the finite-difference time-domain algorithm for FSS structures," *IEEE Transactions on Antennas and Propagation*, vol. 42, no. 9, pp. 1317–1324, 1994. DOI: 10.1109/8.318653.

[129] A. Taflove, A. Oskooi, and S. G. Johnson, *Advances in FDTD computational electrodynamics: photonics and nanotechnology*. Artech house, 2013.

[130] W. Ko and R. Mittra, "Implementation of Floquet boundary condition in FDTD for FSS analysis," in *Proceedings of IEEE Antennas and Propagation Society International Symposium*, Ann Arbor, USA, 1993, 14–17 vol.1. DOI: 10.1109/APS.1993.385413.

[131] J. Ji and Y. Ma, "Tunability study of plasma frequency selective surface based on FDTD," *IEEE Transactions on Plasma Science*, vol. 47, no. 3, pp. 1500–1504, 2019. DOI: 10.1109/TPS.2019.2894414.

[132] H. Baudrand, "Application of wave concept iterative procedure in planar circuits," *Recent Res. Devel. Microwave Theory & Tech.*, vol. 1, pp. 187–197, 1999.

[133] S. Aroussi, L. Latrach, N. Sboui, A. Gharsallah, A. Gharbi, and H. Baudrand, "Efficient analysis of complex FSS structure using the WCIP method," *Journal of Electromagnetic Analysis and Applications*, vol. 3, 2011. DOI: 10.4236/jemaa.2011.311071.

[134] E. da Silva Rodrigues Montalvão, A. C. P. da Silva Montalvão, A. G. D'Assunção, L. M. de Mendonça, and A. G. Neto, "Study of the geometric complexity reduction of a quasi-fractal FSS using WCIP," in *SBMO/IEEE MTT-S International Microwave and Optoelectronics Conference*, Natal, Brazil, 2011, pp. 970–974. DOI: 10.1109/IMOC.2011.6169411.

[135] V. P. S. Neto, A. G. D'Assunção, and H. Baudrand, "Analysis of finite size nonuniform stable and multiband FSS using a generalization of the WCIP method," *IEEE Transactions on Electromagnetic Compatibility*, vol. 60, no. 6, pp. 1802–1810, 2018. DOI: 10.1109/TEMC.2017.2785787.

[136] A. Djouimaa, M. Titaouine, and H. Baudrand, "Analysis of double layered frequency selective surface based on WCIP-SM technique," in *Seminar on Detection Systems Architectures and Technologies (DAT)*, Algiers, Algeria, 2017, pp. 1–5. DOI: 10.1109/DAT.2017.7889182.

[137] Y. Wang and A. Zhang, "Dual circularly polarized Fabry–Perot resonator antenna employing a polarization conversion metasurface," *IEEE Access*, vol. 9, pp. 44 881–44 887, 2021. DOI: 10.1109/ACCESS.2021.3062460.

[138] P. Xie, G. Wang, H. Li, X. Gao, and B. Zong, "A novel method for circularly polarized Fabry-Perot cavity antenna," in *International Conference on Microwave and Millimeter Wave Technology (ICMMT)*, Shanghai, China, 2020, pp. 1–3. DOI: 10.1109/ICMMT49418.2020.9386767.

[139] Z.-G. Liu, Z.-X. Cao, and L.-N. Wu, "Compact low-profile circularly polarized Fabry–Perot resonator antenna fed by linearly polarized microstrip patch," *IEEE Antennas and Wireless Propagation Letters*, vol. 15, pp. 524–527, 2016. DOI: 10.1109/LAWP.2015.2456886.

[140] L. Young, L. Robinson, and C. Hacking, "Meander-line polarizer," *IEEE Transactions on Antennas and Propagation*, vol. 21, no. 3, pp. 376–378, 1973. DOI: 10.1109/TAP.1973.1140503.

[141] P. Fei, Z. Shen, X. Wen, and F. Nian, "A single-layer circular polarizer based on hybrid meander line and loop configuration," *IEEE Transactions on Antennas and Propagation*, vol. 63, no. 10, pp. 4609–4614, 2015. DOI: 10.1109/TAP.2015.2462128.

[142] E. Arnieri, F. Greco, L. Boccia, and G. Amendola, "A SIW-based polarization rotator with an application to linear-to-circular dual-band polarizers at K-/Ka-band," *IEEE Transactions on Antennas and Propagation*, vol. 68, no. 5, pp. 3730–3738, 2020. DOI: 10.1109/TAP.2020.2963901.

[143] G. I. Kiani and V. Dyadyuk, "Quarter-wave plate polariser based on frequency selective surface," in *40th European Microwave Conference*, Paris, France, 2010, pp. 1361–1364. DOI: 10.23919/EUMC.2010.5616657.

[144] M. Euler, V. Fusco, R. Cahill, and R. Dickie, "325 GHz single layer sub-millimeter wave FSS based split slot ring linear to circular polarization convertor," *IEEE Transactions on Antennas and Propagation*, vol. 58, no. 7, pp. 2457–2459, 2010. DOI: 10.1109/TAP.2010.2048874.

[145] M. Euler, V. Fusco, R. Cahill, and R. Dickie, "FSS based sub-millimetre wave spatial phase shifter design considerations," in *3rd European Conference on Antennas and Propagation*, Berlin, Germany, 2009, pp. 1648–1650.

[146] J. Bornemann, "Computer-aided design of multilayered dielectric frequency-selective surfaces for circularly polarized millimeter-wave applications," *IEEE Transactions on Antennas and Propagation*, vol. 41, no. 11, pp. 1588–1591, 1993. DOI: 10.1109/8.267362.

[147] L. Li, Y. Li, Z. Wu, F. Huo, Y. Zhang, and C. Zhao, "Novel polarization-reconfigurable converter based on multilayer frequency-selective surfaces," *Proceedings of the IEEE*, vol. 103, no. 7, pp. 1057–1070, 2015. DOI: 10.1109/JPROC.2015.2437611.

[148] W. Zhang, J.-Y. Li, and J. Xie, "A broadband circular polarizer based on cross-shaped composite frequency selective surfaces," *IEEE Transactions on Antennas and Propagation*, vol. 65, no. 10, pp. 5623–5627, 2017. DOI: 10.1109/TAP.2017.2735459.

[149] W. Li, Y. Lan, H. Wang, and Y. Xu, "Microwave polarizer based on complementary split ring resonators frequency-selective surface for conformal application," *IEEE Access*, vol. 9, pp. 111 383–111 389, 2021. DOI: 10.1109/ACCESS.2021.3102942.

[150] A. G. Neto, J. N. de Carvalho, A. N. da Silva, H. de Paiva Almeida Ferreira, I. S. S. Lima, and J. I. Fernandes, "Four arms star: An useful geometry for switchable FSS," in *SBMO/IEEE MTT-S International Microwave Optoelectronics Conference (IMOC)*, Rio de Janeiro, Brazil, 2013, pp. 1–5. DOI: 10.1109/IMOC.2013.6646537.

[151] D. F. Mamedes, A. Gomes Neto, J. Costa e Silva, and J. Bornemann, "Design of reconfigurable frequency-selective surfaces including the PIN diode threshold region," *IET Microwaves, Antennas & Propagation.*, vol. 12, no. 9, 2018-07. DOI: 10.1049/iet-map.2017.0761.

[152] F. Costa, A. Monorchio, and G. Manara, "Efficient analysis of frequency-selective surfaces by a simple equivalent-circuit model," *IEEE Antennas and Propagation Magazine*, vol. 54, no. 4, pp. 35–48, 2012. DOI: 10.1109/MAP.2012.6309153.

[153] S. M. A. Momeni Hasan Abadi and N. Behdad, "Wideband linear-to-circular polarization converters based on miniaturized-element frequency selective surfaces," *IEEE Transactions on Antennas and Propagation*, vol. 64, no. 2, pp. 525–534, 2016. DOI: 10.1109/TAP.2015.2504999.

[154] Ansys. "Ansys HFSS." (2024), [Online]. Available: https://www.ansys.com/products/electronics/ansys-hfss#tab1-1 (visited on 04/12/2024).

[155] T. Kitsuregawa, "Advanced technology in satellite communication antennas: Electrical and mechanical design," *Norwood*, 1990.

[156] Y. Xu and S. Zhang, "An ultra wideband FSS operating at Ka band," in *IEEE International Conference on Computational Electromagnetics (ICCEM)*, Shanghai, China, 2019, pp. 1–3. DOI: 10.1109/COMPEM.2019.8778845.

[157] M. Simruni and S. Jam, "Design of high gain, wideband microstrip resonant cavity antenna using FSS superstrate with equivalent circuit model," *AEU-International Journal of Electronics and Communications*, vol. 112, p. 152 935, 2019. DOI: 10.1016/j.aeue.2019.152935.

[158] N. Kushwaha and R. Kumar, "Design of a wideband high gain antenna using FSS for circularly polarized applications," *AEU-International Journal of Electronics and Communications*, vol. 70, no. 9, pp. 1156–1163, 2016. DOI: 10.1016/j.aeue.2016.05.013.

[159] N. Behdad, M. Al-Joumayly, and M. Salehi, "A low-profile third-order band-pass frequency selective surface," *IEEE Transactions on Antennas and Propagation*, vol. 57, no. 2, pp. 460–466, 2009. DOI: 10.1109/TAP.2008.2011202.

[160] N. Liu, X. Sheng, C. Zhang, and D. Guo, "Design of frequency selective surface structure with high angular stability for radome application," *IEEE Antennas and Wireless Propagation Letters*, vol. 17, no. 1, pp. 138–141, 2018. DOI: 10.1109/LAWP.2017.2778078.

[161] A. Chatterjee and S. K. Parui, "A multi-layered band-pass frequency selective surface designed for Ku band applications," in *IEEE Applied Electromagnetics Conference (AEMC)*, Bhubaneswar, India, 2013, pp. 1–2. DOI: 10.1109/AEMC.2013.7045067.

[162] N. Liu, X. Sheng, C. Zhang, and D. Guo, "Design and synthesis of band-pass frequency selective surface with wideband rejection and fast roll-off characteristics for radome applications," *IEEE Transactions on Antennas and Propagation*, vol. 68, no. 4, pp. 2975–2983, 2020. DOI: 10.1109/TAP.2019.2955665.

[163] F. C. G. d. S. Segundo, A. L. P. d. S. Campos, and A. Gomes Neto, "A design proposal for ultrawide band frequency selective surface," *Journal of Microwaves, Optoelectronics and Electromagnetic Applications*, vol. 12, pp. 398–409, 2013. DOI: 10.1590/S2179-10742013000200012.

[164] A. R. Varkani, Z. H. Firouzeh, and A. Z. Nezhad, "Equivalent circuit model for array of circular loop FSS structures at oblique angles of incidence," *IET Microwaves, Antennas & Propagation*, vol. 12, no. 5, pp. 749–755, 2018. DOI: 10.1049/iet-map.2017.1004.

[165] S. H. Kiani, A. G. Alharbi, S. Khan, M. Marey, H. Mostafa, and M. A. Khan, "Wideband three loop element antenna array for future 5G mmwave devices," *IEEE Access*, vol. 10, pp. 22 472–22 479, 2022. DOI: 10.1109/ACCESS.2022.3152769.

[166] A. Jabbar, R. Ramzan, O. Siddiqui, M. Amin, and F. A. Tahir, "Wave discrimination at C-band frequencies in microstrip structures inspired by electromagnetically induced transparency," *Scientific Reports*, vol. 11, no. 1, pp. 1–11, 2021. DOI: 10.1038/s41598-021-82618-1.

[167] L. Zhu, F.-Y. Meng, L. Dong, J.-H. Fu, F. Zhang, and Q. Wu, "Polarization manipulation based on electromagnetically induced transparency-like (EIT-like) effect," *Optics express*, vol. 21, no. 26, pp. 32 099–32 110, 2013. DOI: 10.1364/OE.21.032099.

[168] K. Kanjanasit, S. Sanesaowarod, and N. Homsup, "EIT-like effect in metamaterials based on two-layer arrays for high-gain antennas," in *17th International Conference on Electrical Engineering/Electronics, Computer, Telecommunications and Information Technology (ECTI-CON)*, Phuket, Thailand, 2020, pp. 304–307. DOI: 10.1109/ECTI-CON49241.2020.9158277.

[169] B. Luk'Yanchuk, N. I. Zheludev, S. A. Maier, *et al.*, "The Fano resonance in plasmonic nanostructures and metamaterials," *Nature Materials*, vol. 9, no. 9, pp. 707–715, 2010. DOI: 10.1038/nmat2810.

[170] K. Karthigeyan, E. Manikandan, E. Papanasam, S. Radha, and B. Sreeja, "Multiband Fano resonance in symmetry broken planar terahertz metamaterial," in *Proc. Int. Conf. Devices for Integrated Circuit (DevIC)*, Kalyani, India, 2021, pp. 1–3. DOI: 10.1109/DevIC50843.2021.9455804.

[171] C. Wu, N. Arju, G. Kelp, *et al.*, "Spectrally selective chiral silicon metasurfaces based on infrared Fano resonances," *Nature Communications*, vol. 5, no. 1, pp. 1–9, 2014. DOI: 10.1038/ncomms4892.

[172] X. Guo, H. Hu, X. Zhu, X. Yang, and Q. Dai, "Higher order Fano graphene metamaterials for nanoscale optical sensing," *Nanoscale*, vol. 9, no. 39, pp. 14 998–15 004, 2017. DOI: 10.1039/C7NR05919A.

[173] M. F. Limonov, M. V. Rybin, A. N. Poddubny, and Y. S. Kivshar, "Fano resonances in photonics," *Nature Photonics*, vol. 11, no. 9, pp. 543–554, 2017. DOI: 10.1038/nphoton.2017.142.

[174] C. Debus and P. H. Bolivar, "Frequency selective surfaces for high sensitivity terahertz sensing," *Applied Physics Letters*, vol. 91, no. 18, p. 184 102, 2007. DOI: 10.1063/1.2805016.

[175] A. Yang, T. B. Hoang, M. Dridi, *et al.*, "Real-time tunable lasing from plasmonic nanocavity arrays," *Nature Communications*, vol. 6, no. 1, pp. 1–7, 2015. DOI: 10.1038/ncomms7939.

[176] M. Amin, R. Ramzan, and O. Siddiqui, "Fano resonance based ultra high-contrast electromagnetic switch," *Applied Physics Letters*, vol. 110, no. 18, p. 181 904, 2017. DOI: 10.1063/1.4982725.

[177] J. He, J. Wang, P. Ding, C. Fan, and E. Liang, "Gain-assisted plasmon induced transparency in T-shaped metamaterials for slow light," *Journal of Optics*, vol. 17, no. 5, p. 055 002, 2015. DOI: 10.1088/2040-8978/17/5/055002.

[178] M. Rahzaani, G. Dadashzadeh, and M. Khorshidi, "New technique for designing wideband one layer frequency selective surface in X-band with stable angular response," *Microwave and Optical Technology Letters*, vol. 60, no. 9, pp. 2133–2139, 2018. DOI: 10.1002/mop.31304.

[179] M. C. Neto, J. P. Araújo, R. J. Mota, *et al.*, "Design and synthesis of an ultra wide band FSS for mm-wave application via general regression neural network and multiobjective bat algorithm," *Journal of Microwaves, Optoelectronics and Electromagnetic Applications*, vol. 18, pp. 530–544, 2019. DOI: 10.1590/2179-10742019v18i41729.

[180] C. Jin, Q. Lv, and R. Mittra, "Dual-polarized frequency-selective surface with two transmission zeros based on cascaded ground apertured annular ring resonators," *IEEE Transactions on Antennas and Propagation*, vol. 66, no. 8, pp. 4077–4085, 2018. DOI: 10.1109/TAP.2018.2839898.

[181] A. Kesavan, R. Karimian, and T. A. Denidni, "A novel wideband frequency selective surface for millimeter-wave applications," *IEEE Antennas and Wireless Propagation Letters*, vol. 15, pp. 1711–1714, 2016. DOI: 10.1109/LAWP.2016.2528221.

[182] A. Chatterjee and S. K. Parui, "A dual layer frequency selective surface reflector for wideband applications," *Radioengineering*, vol. 25, no. 1, pp. 67–72, 2016. DOI: 10.13164/re.2016.0067.

[183] S. Xu, Y. Li, M. Ahmed, *et al.*, "A novel miniaturized ultra-wideband frequency selective surface with rapid band edge," *IEEE Access*, vol. 9, pp. 161 854–161 861, 2021. DOI: 10.1109/ACCESS.2021.3131629.

[184] D. F. Mamedes, J. P. Fernandes da Silva, J. da Silva Souza, T. da Silva Evangelista, T. Rolim de Sousa, and P. Henrique da Fonseca Silva, "Analysis of impedance matching techniques in tapered microstrip patch antenna," in *SBMO/IEEE MTT-S International Microwave and Optoelectronics Conference (IMOC)*, Aguas de Lindoia, Brazil, 2017, pp. 1–4. DOI: 10.1109/IMOC.2017.8121034.

[185] J. Lu, H. C. Zhang, C. Wei, J.-S. Hong, and T. J. Cui, "Design of compact circularly polarized antenna using sunshine-shaped slotted patch," *IEEE Transactions on Antennas and Propagation*, vol. 68, no. 9, pp. 6800–6805, 2020. DOI: 10.1109/TAP.2020.2999663.

[186] C. A. Balanis and P. I. Ioannides, "Introduction to smart antennas," *Synthesis Lectures on Antennas*, vol. 2, no. 1, pp. 1–175, 2007.

[187] J. d. N. Cruz, R. C. S. Freire, A. J. R. Serres, L. C. M. d. Moura, A. P. d. Costa, and P. H. d. F. Silva, "Parametric study of printed monopole antenna bioinspired on the inga marginata leaves for UWB applications," *Journal of Microwaves, Optoelectronics and Electromagnetic Applications*, vol. 16, pp. 312–322, 2017. DOI: 10.1590/2179-10742017v16i1891.

[188] A. Y. Modi, C. A. Balanis, C. R. Birtcher, and H. N. Shaman, "Novel design of ultrabroadband radar cross section reduction surfaces using artificial magnetic conductors," *IEEE Transactions on Antennas and Propagation*, vol. 65, no. 10, pp. 5406–5417, 2017. DOI: 10.1109/TAP.2017.2734069.

[189] M. J. Al-Hasan, T. A. Denidni, and A. R. Sebak, "Millimeter-wave compact EBG structure for mutual coupling reduction applications," *IEEE Transactions on Antennas and Propagation*, vol. 63, no. 2, pp. 823–828, 2015. DOI: 10.1109/TAP.2014.2381229.

[190] A. Artemenko, A. Maltsev, A. Mozharovskiy, A. Sevastyanov, V. Ssorin, and R. Maslennikov, "Millimeter-wave electronically steerable integrated lens antennas for WLAN/WPAN applications," *IEEE Transactions on Antennas and Propagation*, vol. 61, no. 4, pp. 1665–1671, 2013. DOI: 10.1109/TAP.2012.2232266.

[191] D. F. Mamedes, A. G. Neto, and J. Bornemann, "Reconfigurable corner reflector using PIN-diode-switched frequency selective surfaces," in *IEEE International Symposium on Antennas and Propagation and North American Radio*

Science Meeting, Montreal, Canada, 2020, pp. 127–128.
DOI: 10.1109/IEEECONF35879.2020.9329791.

[192] A. Dadgarpour, A. A. Kishk, and T. A. Denidni, "Gain enhancement of planar antenna enabled by array of split-ring resonators," *IEEE Transactions on Antennas and Propagation*, vol. 64, no. 8, pp. 3682–3687, 2016.
DOI: 10.1109/TAP.2016.2565741.

[193] A. Dadgarpour, B. Zarghooni, B. S. Virdee, and T. A. Denidni, "Improvement of gain and elevation tilt angle using metamaterial loading for millimeter-wave applications," *IEEE Antennas and Wireless Propagation Letters*, vol. 15, pp. 418–420, 2016. DOI: 10.1109/LAWP.2015.2449235.

[194] Q.-W. Lin, H. Wong, and C. H. Chan, "A transparent artificial periodic structure for beam-tilting antenna," *IEEE Antennas and Wireless Propagation Letters*, vol. 20, no. 4, pp. 498–502, 2021. DOI: 10.1109/LAWP.2021.3054864.

[195] M. Borhani Kakhki, M. Mantash, A. Kesavan, M. M. Tahseen, and T. A. Denidni, "Millimeter-wave beam-tilting vivaldi antenna with gain enhancement using multilayer FSS," *IEEE Antennas and Wireless Propagation Letters*, vol. 17, no. 12, pp. 2279–2283, 2018. DOI: 10.1109/LAWP.2018.2873113.

[196] J. Gielis, "A generic geometric transformation that unifies a wide range of natural and abstract shapes," *American Journal of Botany*, vol. 90, no. 3, pp. 333–338, 2003. DOI: 10.3732/ajb.90.3.333.

[197] J. L. Coolidge, "The origin of polar coordinates," *The American Mathematical Monthly*, vol. 59, no. 2, pp. 78–85, 1952.
DOI: 10.1080/00029890.1952.11988074.

[198] G. Lamé, *Examen des différentes méthodes employées pour résoudre les problèmes de géométrie: par G. Lamé...* Mme Ve Courcier, rue du Jardinet-Saint-André-des-Arcs, 1818.

[199] G. V. Raviteja and K. Siva Rama Praveen, "Bio-inspired Korean striped maple leaf (Acer Tegmentosum) microstrip monopole design targeting UWB applications," in *International Conference on Advances in Electrical, Computing, Communication and Sustainable Technologies (ICAECT)*, Bhilai, India, 2021, pp. 1–7. DOI: 10.1109/ICAECT49130.2021.9392589.

[200] M. A. de Oliveira, A. P. da Costa, G. G. S. Forte, *et al.*, "Using polar transformation to design a dissimilar antenna array inspired on four-leaf clover," in *IEEE Radio and Wireless Symposium (RWS)*, Anaheim, USA, 2018, pp. 228–230. DOI: 10.1109/RWS.2018.8304994.

[201] S. R. Patre and S. P. Singh, "MIMO antenna using castor leaf-shaped quasi-self-complemetary elements for broadband applications," in *IEEE MTT-S International Microwave and RF Conference (IMaRC)*, Hyderabad, India, 2015, pp. 140–142. DOI: 10.1109/IMaRC.2015.7411400.

[202] J. A. V. Delgado and C. A. V. Mera, "A bio-inspired patch antenna array using Fibonacci sequences in trees," *IEEE Antennas and Propagation Magazine*, vol. 55, no. 5, pp. 192–201, 2013. DOI: 10.1109/MAP.2013.6735514.

[203] H. Ullah and F. A. Tahir, "A novel snowflake fractal antenna for dual-beam applications in 28 GHz band," *IEEE Access*, vol. 8, pp. 19 873–19 879, 2020. DOI: 10.1109/ACCESS.2020.2968619.

[204] H. Wang, M. Yan, S. Qu, L. Zheng, and J. Wang, "Design of a self-complementary frequency selective surface with multi-band polarization separation characteristic," *IEEE Access*, vol. 7, pp. 36 788–36 799, 2019.
DOI: 10.1109/ACCESS.2019.2905416.

[205] X. Liu, R. Lu, A. Zhang, and X. Chen, "Extension of Babinet principle to complementary metallic elements on the interface of different substrates," *IEEE Microwave and Wireless Components Letters*, vol. 32, no. 10, pp. 1151–1154, 2022. DOI: 10.1109/LMWC.2022.3173794.

[206] N. Liu, X.-J. Sheng, J.-J. Fan, and D. Guo, "An angular stable dual-band frequency selective surface with closely spaced resonances," *Progress In Electromagnetics Research Letters*, vol. 70, pp. 1–6, 2017.
DOI: 10.2528/PIERL17070302.

[207] M. Karahan and E. Aksoy, "Design and analysis of angular stable antipodal F-type frequency selective surface with multi-band characteristics," *International Journal of RF and Microwave Computer-Aided Engineering*, vol. 30, no. 12, e22466, 2020. DOI: 10.1002/mmce.22466.

[208] H. Zhou, S.-B. Qu, B.-Q. Lin, *et al.*, "Dual band frequency selective surface based on circular aperture-coupled patches," *Microwave and Optical Technology Letters*, vol. 53, no. 8, pp. 1784–1786, 2011. DOI: 10.1002/mop.26102.

[209] M. Yan, S. Qu, J. Wang, *et al.*, "A miniaturized dual-band FSS with second-order response and large band separation," *IEEE Antennas and Wireless Propagation Letters*, vol. 14, pp. 1602–1605, 2015.
DOI: 10.1109/LAWP.2015.2413942.

[210] H. Wang, L. Zheng, M. Yan, J. Wang, S. Qu, and R. Luo, "Design and analysis of miniaturized low profile and second-order multi-band polarization selective surface for multipath communication application," *IEEE Access*, vol. 7, pp. 13 455–13 467, 2019. DOI: 10.1109/ACCESS.2019.2894013.

[211] Z. He, Y. Shao, J. Huang, C. Zhang, and J. Zhang, "A tri-band highly selective passband frequency selective surface based on multi-layer coupling," in *IEEE International Symposium on Antennas and Propagation and USNC-URSI Radio Science Meeting (APS/URSI)*, Singapore, Singapore, 2021, pp. 1693–1694.
DOI: 10.1109/APS/URSI47566.2021.9704164.

[212] M. Yan, J. Wang, H. Ma, *et al.*, "A tri-band, highly selective, bandpass FSS using cascaded multilayer loop arrays," *IEEE Transactions on Antennas and Propagation*, vol. 64, no. 5, pp. 2046–2049, 2016.
DOI: 10.1109/TAP.2016.2536175.

[213] A. Chatterjee and S. K. Parui, "A triple-layer dual-bandpass frequency selective surface of third order response with equivalent circuit analysis," *International Journal of RF and Microwave Computer-Aided Engineering*, vol. 30, no. 2, e22047, 2020. DOI: 10.1002/mmce.22047.

[214] J. Babinet, "Mémoires d'optique météorologique. ii. sur les couronnes," *CR Hept. Acad. Sci*, vol. 4, pp. 642–645, 1837.

[215] H. G. Booker, "Slot aerials and their relation to complementary wire aerials (Babinet's principle)," *Journal of the Institution of Electrical Engineers-Part IIIA: Radiolocation*, vol. 93, no. 4, pp. 620–626, 1946.
DOI: 10.1049/ji-3a-1.1946.0150.

[216] E. Jordan and K. Balmain, "Electromagnetic waves and radiating systems, prentice hall," *Englewood Cliffs, New Jersey*, 1968.

[217] O. Heaviside, "Iv. the general solution of Maxwell's electromagnetic equations in a homogeneous isotropic medium, especially in regard to the derivation of special solutions, and the formulœ for plane waves," *The London, Edinburgh,*

and Dublin Philosophical Magazine and Journal of Science, vol. 27, no. 164, pp. 29–50, 1889. DOI: 10.1080/14786448908628314.

[218] X.-D. Hu, X.-L. Zhou, L.-S. Wu, L. Zhou, and W.-Y. Yin, "A miniaturized dual-band frequency selective surface (FSS) with closed loop and its complementary pattern," *IEEE Antennas and Wireless Propagation Letters*, vol. 8, pp. 1374–1377, 2009. DOI: 10.1109/LAWP.2009.2039110.

[219] V. Krushna Kanth and S. Raghavan, "Equivalent circuit analysis of complementary FSS for selective EM shielding," in *15th International Conference on ElectroMagnetic Interference Compatibility (INCEMIC)*, Bengaluru, India, 2018, pp. 1–4. DOI: 10.1109/INCEMIC.2018.8704634.

[220] V. K. Kanth and S. Raghavan, "Complementary frequency selective surface array optimization using equivalent circuit model," in *IEEE MTT-S International Microwave and RF Conference (IMaRC)*, Ahmedabad, India, 2017, pp. 1–4. DOI: 10.1109/IMaRC.2017.8449691.

[221] D. F. Mamedes, J. Bornemann, and A. G. Neto, "Linear-to-circular polarization converter based on four-arms star FSS at 5.2 GHz for 5G applications," in *Proc. 16th European Conference on Antennas and Propagation (EuCAP)*, Madrid, Spain, 2022, pp. 1–4. DOI: 10.23919/EuCAP53622.2022.9768954.

[222] D. F. Mamedes and J. Bornemann, "Using an equivalent-circuit model to design ultra-wide band-stop frequency-selective surface for 5G mm-wave applications," *IEEE Open Journal of Antennas and Propagation*, vol. 3, pp. 948–957, 2022. DOI: 10.1109/OJAP.2022.3198290.

[223] V. V. Komarov, T. Zwick, S. Marahrens, and S. Molchanov, "Fano-resonant frequency-selective surface with cross-shaped apertures," *IEEE Microwave and Wireless Components Letters*, vol. 29, no. 12, pp. 775–778, 2019. DOI: 10.1109/LMWC.2019.2948987.

[224] H. Li, Q. Cao, L. Liu, and Y. Wang, "An improved multifunctional active frequency selective surface," *IEEE Transactions on Antennas and Propagation*, vol. 66, no. 4, pp. 1854–1862, 2018. DOI: 10.1109/TAP.2018.2800727.

[225] Y. Rahmani-Shams, S. Mohammd-Ali-Nezhad, A. Nooraei Yeganeh, and S. H. Sedighy, "Dual band, low profile and compact tunable frequency selective surface with wide tuning range," *Journal of Applied Physics*, vol. 123, no. 23, 2018. DOI: 10.1063/1.5023449.

[226] J. R. Reis, R. F. S. Caldeirinha, A. Hammoudeh, and N. Copner, "Electronically reconfigurable FSS-inspired transmitarray for 2-D beamsteering," *IEEE Transactions on Antennas and Propagation*, vol. 65, no. 9, pp. 4880–4885, 2017. DOI: 10.1109/TAP.2017.2723087.

[227] S. C. Bakshi, D. Mitra, and F. L. Teixeira, "Wide-angle broadband rasorber for switchable and conformal application," *IEEE Transactions on Microwave Theory and Techniques*, vol. 69, no. 2, pp. 1205–1216, 2021. DOI: 10.1109/TMTT.2020.3044601.

[228] P. Kong, X.-W. Yu, M. Zhao, Y. He, L. Miao, and J. Jiang, "Switchable frequency selective surfaces absorber/reflector for wideband applications," *Journal of Electromagnetic Waves and Applications*, vol. 29, no. 11, pp. 1473–1485, 2015. DOI: 10.1080/09205071.2015.1049713.

[229] C. Gu, B. S. Izquierdo, S. Gao, *et al.*, "Dual-band electronically beam-switched antenna using slot active frequency selective surface," *IEEE Transactions on Antennas and Propagation*, vol. 65, no. 3, pp. 1393–1398, 2017. DOI: 10.1109/TAP.2016.2647578.

[230] I. Skyworks Solutions. "Skyworks SMP1340-079LF PIN diode." (2019), [Online]. Available: https://www.skyworksinc.com/-/media/SkyWorks/Documents/Products/101-200/SMP1340_Series_200051U.pdf (visited on 11/10/2023).

[231] C. A. Balanis, *Antenna theory: analysis and design*. John wiley & sons, 2016.

[232] M. A. Hossain, I. Bahceci, and B. A. Cetiner, "Parasitic layer-based radiation pattern reconfigurable antenna for 5G communications," *IEEE Transactions on Antennas and Propagation*, vol. 65, no. 12, pp. 6444–6452, 2017. DOI: 10.1109/TAP.2017.2757962.

[233] W.-Q. Deng, X.-S. Yang, C.-S. Shen, J. Zhao, and B.-Z. Wang, "A dual-polarized pattern reconfigurable Yagi patch antenna for microbase stations," *IEEE Transactions on Antennas and Propagation*, vol. 65, no. 10, pp. 5095–5102, 2017. DOI: 10.1109/TAP.2017.2741022.

[234] B. K. Ahn, H.-W. Jo, J.-S. Yoo, J.-W. Yu, and H. L. Lee, "Pattern reconfigurable high gain spherical dielectric resonator antenna operating on higher order mode," *IEEE Antennas and Wireless Propagation Letters*, vol. 18, no. 1, pp. 128–132, 2019. DOI: 10.1109/LAWP.2018.2882871.

[235] J. Ouyang, Y. M. Pan, and S. Y. Zheng, "Center-fed unilateral and pattern reconfigurable planar antennas with slotted ground plane," *IEEE Transactions on Antennas and Propagation*, vol. 66, no. 10, pp. 5139–5149, 2018. DOI: 10.1109/TAP.2018.2860046.

[236] L.-Y. Ji, Z.-Y. Zhang, and N.-W. Liu, "A two-dimensional beam-steering partially reflective surface (PRS) antenna using a reconfigurable FSS structure," *IEEE Antennas and Wireless Propagation Letters*, vol. 18, no. 6, pp. 1076–1080, 2019. DOI: 10.1109/LAWP.2019.2907641.

[237] L.-Y. Ji, P.-Y. Qin, J.-Y. Li, and L.-X. Zhang, "1-D electronic beam-steering partially reflective surface antenna," *IEEE Access*, vol. 7, pp. 115 959–115 965, 2019. DOI: 10.1109/ACCESS.2019.2936237.

[238] A. Chatterjee and S. K. Parui, "Beamwidth control of omnidirectional antenna using conformal frequency selective surface of different curvatures," *IEEE Transactions on Antennas and Propagation*, vol. 66, no. 6, pp. 3225–3230, 2018. DOI: 10.1109/TAP.2018.2819899.

[239] B. A. Decena, J. R. Luzon, and M. C. L. Purisima, "2.4 GHz pattern reconfigurable corner reflector antennas using frequency selective conductor loops and strips," in *TENCON - IEEE Region 10 Conference*, Penang, Malaysia, 2017, pp. 2914–2919. DOI: 10.1109/TENCON.2017.8228360.

[240] R. Alwahishi, M. M. M. Ali, G. Elzwawi, and T. A. Denidni, "Beam-switching antenna using reconfigurable intelligent frequency selective surfaces for internet of things applications," *IEEE Internet of Things Journal*, pp. 1–1, 2023. DOI: 10.1109/JIOT.2023.3298908.

[241] B. Liang, B. Sanz-Izquierdo, E. A. Parker, and J. C. Batchelor, "Cylindrical slot FSS configuration for beam-switching applications," *IEEE Transactions on Antennas and Propagation*, vol. 63, no. 1, pp. 166–173, 2015. DOI: 10.1109/TAP.2014.2367534.

[242] L.-M. Zhang, X. Ding, and W. Shao, "A phase compensation beam switching antenna based on frequency selective surface," *IEEE Antennas and Wireless Propagation Letters*, vol. 20, no. 9, pp. 1741–1744, 2021. DOI: 10.1109/LAWP.2021.3095366.

[243] H. AG. "Huber+Suhner data sheet coaxial cable: EZ_141_TP_M17." (2005), [Online]. Available: https://www.spelektroniikka.fi/kuvat/ez141.pdf.

[244] M. D. Estarki and R. G. Vaughan, "Theoretical methods for the impedance and bandwidth of the thin dipole," *IEEE Antennas and Propagation Magazine*, vol. 55, no. 1, pp. 62–81, 2013. DOI: 10.1109/MAP.2013.6474485.

[245] I. Technologies. "Infineon BAR 64-03 PIN diode datasheet." (2018), [Online]. Available: https://www.infineon.com/dgdl/Infineon-BAR64-03W-DS-v01_01-EN.pdf?fileId=5546d462689a790c01690f0250e138fe (visited on 09/12/2019).

[246] E. F. Harris, "An experimental investigation of the corner-reflector antenna," *Proceedings of the IRE*, vol. 41, no. 5, pp. 645–651, 1953. DOI: 10.1109/JRPROC.1953.274408.

[247] M. Pasian, S. Monni, A. Neto, M. Ettorre, and G. Gerini, "Frequency selective surfaces for extended bandwidth backing reflector functions," *IEEE Transactions on Antennas and Propagation*, vol. 58, no. 1, pp. 43–50, 2010. DOI: 10.1109/TAP.2009.2036185.

[248] I. Agilent Technologies. "Advanced calibration techniques for vector network analyzers." (2006), [Online]. Available: http://anlage.umd.edu/Agilent_Advanced_VNA_calibration.pdf (visited on 09/04/2023).

[249] A-info. "LB-28-25-C-KF datasheet." (), [Online]. Available: ttps://www.ainfoinc.com.cn/en/pro_pdf/new_products/antenna/Standard%20Gain%20Horn%20Antenna/tr_LB-28-25.pdf (visited on 11/04/2020).

[250] A-info. "LB-180400H-KF datasheet." (), [Online]. Available: https://www.ainfoinc.com/amfilerating/file/download/file_id/114/ (visited on 11/04/2020).

[251] Anritsu. "Anritsu 37397C vector network analyzer datasheet." (2001), [Online]. Available: https://dl.cdn-anritsu.com/en-us/test-measurement/files/Manuals/Operation-Manual/10410-00226b.pdf (visited on 07/08/2019).

[252] K. Technologies. "Agilent E5071C vector network analyzer datasheet." (2020), [Online]. Available: https://www.keysight.com/us/en/assets/7018-01423/brochures/5989-5478.pdf (visited on 01/11/2021).

[253] I. A. H. Systems. "SAS-571 datasheet." (), [Online]. Available: https://www.ahsystems.com/datasheets/SAS-571_Horn_Antenna_Datasheet.pdf (visited on 10/07/2019).

[254] K. Technologies. “Agilent E3631A power supply datasheet.” (2018), [Online]. Available: https://www.keysight.com/us/en/assets/7018-06785/data-sheets/5968-9726.pdf (visited on 12/05/2023).

[255] ETS-Lindgren. “ETS-Lindgren 3164-05 datasheet.” (), [Online]. Available: https://www.ets-lindgren.com/datasheet/antennas/open-boundary-quad-ridged-horn/4003/400302 (visited on 05/08/2019).